



COPPE/UFRJ

**DURABILIDADE E PROPRIEDADES MECÂNICAS DE COMPÓSITOS
CIMENTÍCIOS REFORÇADOS POR FIBRAS DE SISAL**

Flávio de Andrade Silva

Tese de Doutorado apresentada ao Programa de Pós-graduação em Engenharia Civil, COPPE, da Universidade Federal do Rio de Janeiro, como parte dos requisitos necessários à obtenção do título de Doutor em Engenharia Civil.

Orientadores: Romildo Dias Toledo Filho
Barzin Mobasher

Rio de Janeiro
Abril de 2009

Livros Grátis

<http://www.livrosgratis.com.br>

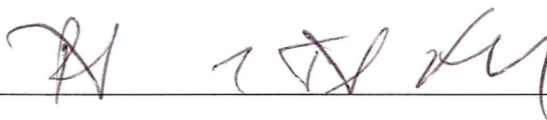
Milhares de livros grátis para download.

DURABILIDADE E PROPRIEDADES MECÂNICAS DE COMPÓSITOS
CIMENTÍCIOS REFORÇADOS POR FIBRAS DE SISAL

Flávio de Andrade Silva

TESE SUBMETIDA AO CORPO DOCENTE DO INSTITUTO ALBERTO LUIZ
COIMBRA DE PÓS-GRADUAÇÃO E PESQUISA DE ENGENHARIA (COPPE) DA
UNIVERSIDADE FEDERAL DO RIO DE JANEIRO COMO PARTE DOS
REQUISITOS NECESSÁRIOS PARA A OBTENÇÃO DO GRAU DE DOUTOR EM
CIÊNCIAS EM ENGENHARIA CIVIL.

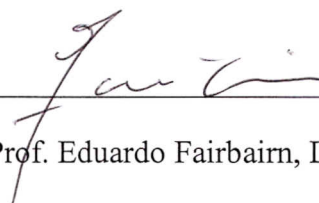
Aprovada por:



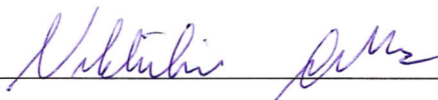
Prof. Romildo Dias Toledo Filho, D.Sc.



Prof. Barzin Mobasher, Ph.D.



Prof. Eduardo Fairbairn, Dr.Ing.



Prof. Nikhilesh Chawla, Ph.D.



Prof. José Roberto Moraes d'Almeida, D. Sc.

RIO DE JANEIRO, RJ - BRASIL

ABRIL DE 2009

Silva, Flávio de Andrade

Durabilidade e Propriedades Mecânicas de
Compósitos Cimentícios Reforçados por Fibras de Sisal /
Flávio de Andrade Silva – Rio de Janeiro: UFRJ/COPPE,
2009.

XI, 243 p.: il.; 29,7 cm.

Orientador: Romildo Dias Toledo Filho

Barzin Mobasher

Tese (doutorado) – UFRJ/ COPPE/ Programa de
Engenharia Civil, 2009.

Referências Bibliográficas: p. 19-22.

1. Compósitos cimentícios. 2. Fibras de sisal. 3.
Durabilidade. 4. Propriedades mecânicas. 5. Fadiga. 6.
Propriedades físicas. I. Toledo Filho, Romildo Dias *et al.*
II. Universidade Federal do Rio de Janeiro, COPPE,
Programa de Engenharia Civil. III. Título.

Agradecimentos

Reconhecimento, gratidão e apreciação são conferidos àqueles indivíduos e/ou instituições com os quais eu tive o prazer de conhecer e trabalhar durante o curso da presente pesquisa. Primeiro gostaria de expressar minha mais sincera gratidão ao Prof. Romildo Dias Toledo Filho (COPPE/UFRJ), meu orientador, que acreditou na minha capacidade de desenvolver esse trabalho, colaborando com conselhos e idéias que refletiram nos bons resultados obtidos. O seu encorajamento e suporte para que eu pudesse participar em congressos e comitês científicos internacionais foram, com toda certeza, importantes para que eu me tornasse um cientista com uma visão mais ampla. A sua orientação contribuiu, indubitavelmente, para o perfeito desenvolvimento da presente pesquisa.

Durante o curso desse trabalho eu tive o privilégio de trabalhar com o Prof. Eduardo Fairbairn (COPPE/UFRJ). Nossas discussões e suas aulas me deram um grande conhecimento nos fundamentos da mecânica dos materiais, nanotecnologia de materiais cimentícios, reações álcali-agregado e fluência.

O grupo de pesquisa do Prof. Toledo Filho e do Prof. Fairbairn do Departamento de Engenharia Civil da COPPE/UFRJ proporcionaram um perfeito ambiente para o trabalho e para troca de conhecimentos o que reflete no crescimento profissional e avanço de todos os seus pesquisadores. Foi um grande prazer em poder trabalhar nesse grupo. Especial reconhecimento é feito à João Melo Filho pela sua ajuda nas moldagens e ensaios dos compósitos realizados na COPPE/UFRJ. Obrigado aos colegas do grupo pela amizade e ajuda durante o decorrer desse trabalho: Dra. Cíntia Fontes, Ederli Marangon, Prof^{ta}. Eugenia Silva, Prof. Guilherme Cordeiro, Guilherme Romano, Dr. Marcos Silvano, Margareth Magalhães, Dra. Reila Velasco e Vivian Balthar. A ajuda dos técnicos Clodoaldo Santos da Costa e Flavio Justino Nascimento Costa nas moldagens dos compósitos e preparação das matérias primas é também apreciada. Agradeço às secretárias do laboratório, Luzidelle da Conceição Peixoto e Sandra Maria da Silva Mendonça, pelo auxílio na compra de materiais e nas questões burocráticas.

Agradecimentos ao Departamento de Materiais e Metalurgia da COPPE/UFRJ pela utilização do Microscópio Eletrônico de Varredura.

Especial reconhecimento ao Dr. Reiner Neumann do CETEM pela disponibilização do seu laboratório para preparação de amostras de microscopia, uso de microscópio ótico e eletrônico de varredura e análise termogravimétrica.

Agradeço ao Prof. José Roberto Moraes d'Almeida (PUC-Rio) pela participação na banca do exame de qualificação e pelas sugestões dadas ao presente trabalho.

Parte da presente pesquisa foi realizada na Arizona State University sob a supervisão do Prof. Barzin Mobasher. Profundos agradecimentos são manifestados ao Departamento de Engenharia Civil e Ambiental da ASU e ao Prof. Mobasher pelo convite.

Aos alunos do Grupo do Prof. Mobasher - Amir Bonakdar, Dr. Chote Soranakom, Deju Zhu, Juan Erni, Masoud Yekani-Fard, Mehdi Bakhshi - pela amizade, ajuda em minha adaptação, ajuda nos ensaios mecânicos e nos modelos analíticos.

Aos funcionários do Departamento de Engenharia Civil e Ambiental da ASU, Peter Goguen (gerente de laboratório), Jeffrey Long (técnico de pesquisa) e Danny C. Clevenger (técnico de pesquisa) pela ajuda técnica no laboratório de estruturas durante a minha estada na ASU.

Em 2007 tive o grande prazer de conhecer o Prof. Nikhilesh Chawla com quem comecei a pesquisar sobre a resistência mecânica das fibras de sisal. A ele sou bastante grato pela colaboração e por permitir que trabalhasse em seu grupo e utilizasse os equipamentos do seu laboratório (Mechanical Behavior of Materials Facility). Agradeço aos seus alunos, ex-alunos e pesquisadores que foram sempre cordiais e amigos: Dr. Jason Willians, Rob Adams, Martha Dudek, Danny Singh e Dr. G. Crawford. Reconhecimento especial é dado ao Dr. Willians pela grande ajuda nos ensaios mecânicos e microscopia.

Agradeço ao Dr. Dallas Kingsbury (ITML-ASU) por permitir e auxiliar na utilização de equipamentos do Integrated Mechanical Testing Laboratory.

Reconhecimento ao LeRoy Eyring Center for Solid State Science da ASU pelo uso do ESEM, TGA, microscópio ótico e facilidades de preparação de amostras para microscopia.

Agradecimentos ao Dr. Zhenquan Liu e Sisouk Phrasavath pelo treinamento e auxílio no uso de microscopia eletrônica de varredura.

Os ensaios de TGA feitos na ASU foram realizados por Timothy Karcher ao qual sou muito grato.

Agradeço a David Wriarth (ASU) por permitir o uso de facilidades para preparação de amostras de microscopia.

Reconhecimento ao W. M. Keck Bioimaging Laboratory da School of Life Sciences (ASU) pelo uso do Nikon Elipse TE300 Inverted Video Microscope e Leica SP2 Multiphoton Scanning Laser Microscope. Muito obrigado a Dra. Debra Page Baluch por sua cordialidade e atenção no treinamento para o uso dos microscópios.

Reconhecimento é feito ao Center for Solid State Electronics Research (ASU) pelo uso do FESEM.

Essa pesquisa foi parcialmente financiada pelo CNPq durante o período de 10/2004 à 09/2008.

Resumo da Tese apresentada à COPPE/UFRJ como parte dos requisitos necessários para a obtenção do grau de Doutor em Ciências (D.Sc.)

DURABILIDADE E PROPRIEDADES MECÂNICAS DE COMPÓSITOS CIMENTÍCIOS REFORÇADOS POR FIBRAS DE SISAL

Flávio de Andrade Silva

Abril/2009

Orientadores: Romildo Dias Toledo Filho

Barzin Mobasher

Programa: Engenharia Civil

O presente trabalho tem como objetivo o desenvolvimento e a caracterização mecânica de compósitos cimentícios duráveis reforçados por fibras longas de sisal. Com a finalidade de aumentar a durabilidade dos compósitos uma matriz com 50 % de substituição parcial de cimento por argilas calcinadas foi utilizada. A nova matriz foi desenvolvida de forma a se obter uma mistura livre de hidróxido de cálcio. As fibras de sisal apresentam estrutura hierárquica, morfologia variável e seção transversal irregular. Para sua caracterização morfológica uma investigação sistemática foi realizada no nível micro e meso estrutural. As fibras foram caracterizadas mecanicamente através de ensaios de tração direta e fadiga. Os compósitos desenvolvidos apresentaram comportamento à tração direta com múltipla fissuração e resistência pós primeira-fissura média de 12 MPa com deformação de 1,5 %. Processos de envelhecimento acelerado através de molhagem e secagem e imersão em água quente foram realizados nos compósitos. Ensaios de tração e flexão além de investigação micro-estrutural foram realizados após o processo de envelhecimento acelerado. Compósitos com substituição parcial do cimento por 50 % de argila calcinada não apresentaram sinal de degradação após 100 ciclos de molhagem e secagem quando ensaiados por flexão. Ensaios de fadiga, impacto, tração em alta velocidade, análise da interface fibra-matriz e investigação dos mecanismos de fissuração foram executados para completa caracterização mecânica do compósito.

Abstract of Thesis presented to COPPE/UFRJ as a partial fulfillment of the requirements for the degree of Doctor of Science (D.Sc.)

DURABILITY AND MECHANICAL PROPERTIES OF SISAL FIBER
REINFORCED CEMENT COMPOSITES

Flávio de Andrade Silva

April/2009

Advisors: Romildo Dias Toledo Filho

Barzin Mobasher

Department: Civil Engineering

In the present work a new composite system reinforced with long aligned sisal fibers with increased durability was developed and mechanically characterized. To improve the composite durability a matrix with partial cement replacement by 50 % of calcined clays was used. This matrix was developed in order to achieve a mix free of calcium hydroxide. The sisal fibers presented a hierarchical structure, diverse morphology and irregular cross sectional area. A systematic characterization was performed in the meso and micro scale to characterize the fiber morphology. Monotonic tensile and fatigue tests were performed to mechanically characterize the sisal fiber. The developed composite presented a multiple cracking behavior with strain hardening under direct tension. An average ultimate tensile stress of 12 MPa with an ultimate strain of 1.5 % was observed. The composites were submitted to accelerate aging processes of wetting and drying cycles and hot water immersion. A microstructural and mechanical investigation was performed in aged specimens. Composites with 50 % partial cement replacement by calcined clays presented no signal of degradation after 100 wet/dry cycles when tested under bending loads. Fatigue, impact, high speed tension tests, interface investigation by pull-out tests and an investigation on the cracking mechanisms of the composite was performed.

Sumário

LISTA DE FIGURAS	xi
CAPÍTULO 1. INTRODUÇÃO	1
CAPÍTULO 2. REVISÃO BIBLIOGRÁFICA	4
CAPÍTULO 3. METODOLOGIA E RESULTADOS	12
3.1 MORFOLOGIA E PROPRIEDADES MECÂNICAS DA FIBRA DE SISAL (ARTIGOS A E B)	12
3.2 DURABILIDADE DE COMPÓSITOS REFORÇADOS POR FIBRAS DE SISAL (ARTIGOS C, D E F)	13
3.3 COMPORTAMENTO ESTÁTICO DE COMPÓSITOS REFORÇADOS POR FIBRAS DE SISAL (ARTIGOS D E E)	14
3.4 ESTUDO DA INTERFACE FIBRA-MATRIZ (ARTIGO G)	14
3.5 COMPORTAMENTO DINÂMICO DE COMPÓSITOS REFORÇADOS POR FIBRAS DE SISAL (ARTIGOS H, I E J)	15
CAPÍTULO 4. CONCLUSÕES.....	17
REFERÊNCIAS	19
ANEXOS	23
ARTIGO A - Silva F.A., Chawla N. and Toledo Filho R.D. Tensile behavior of high performance natural (sisal) fibers. <i>Composites Science and Technology</i> 68 (2008) 3438-3443	24
ARTIGO B - Silva F.A., Chawla N. and Toledo Filho R.D. An Experimental Investigation of the fatigue behavior of sisal fibers. <i>Materials Science and Engineering A</i> , in press, 2009.	42
ARTIGO C - Toledo Filho, R.D. Silva F.A., Fairbairn E.M.R., Melo Filho J.A. Durability of compression molded sisal fiber reinforced mortar laminates. <i>Construction and Building Materials</i> 23 (2009) 2409-2420.	59
ARTIGO D - Silva F.A., Toledo Filho R.D., Fairbairn E.M.R., Melo Filho J.A. Physical and mechanical behavior of durable sisal fiber cement composites. <i>Construction and Building Materials</i> , submitted, 2009.	89
ARTIGO E - Silva F.A., Mobasher B. and Toledo Filho R.D. Cracking mechanisms in durable sisal fiber reinforced cement composites. <i>Cement and Concrete Composites</i> , in press, 2009.....	114
ARTIGO F - Silva F.A., Mobasher B. and Toledo Filho R.D. Degradation Mechanisms in Sisal fiber Cement Composites Systems with Low Contents of Calcium Hydroxide. To be submitted, 2009.	138
ARTIGO G -Silva F.A., Mobasher B. and Toledo Filho R.D. Pull-out mechanism in sisal fiber cement composites. To be submitted, 2009.....	159
ARTIGO H - Silva F.A., Mobasher B. and Toledo Filho R.D. Fatigue behavior of sisal fiber cement composites. To be submitted, 2009.....	180
ARTIGO I - Silva F.A., Zhu D., Mobasher B. and Toledo Filho R.D. Impact behavior of sisal fiber cement composites under flexural load. <i>Composites Part A</i> , submitted, 2009.....	197

ARTIGO J - Silva F.A., Zhu D., Mobasher B. and Toledo Filho R.D. High speed tensile behavior of sisal fiber cement composites. To be submitted, 2009.....222

LISTA DE FIGURAS

Figura 1. Construção em Berlin, Alemanha mostrando placas pré-moldadas de concreto fabricadas pela Florack Bauunternehmung GMBH. Compósitos cimentícios reforçados por fibras longas de sisal podem ser uma alternativa sustentável para esse tipo de material.	2
Figura 2. Comparação entre comportamento à flexão em quatro pontos e tração direta de um compósito reforçado por 10% em volume de fibras longas de sisal.	9
Figura 3. Comportamento mecânico de compósito cimentício reforçado por tecido de juta: (a) comparação entre comportamento à tração e flexão em quatro pontos de um compósito reforçado por 5 camadas de tecido de juta e (b) micrografia mostrando pouca penetração da matriz no fio de juta.	10

Capítulo 1.

Introdução

Fibras naturais vem sendo utilizadas como reforços em matrizes cimentícias e poliméricas como uma alternativa sustentável às fibras sintéticas [1][2][3][4]. Os tipos e arranjos de reforços fibrosos mais utilizados podem ser divididos em 4: fibras longas alinhadas [4][5][6][7][8][9], fibras curtas (< 50 mm) [10][11][12][13][14][15][16][17] e fibras de polpa [18][19][20][21][22][23][24][25][26][27][28][29][30] distribuídas aleatoriamente e tecidos bidirecionais [31]. Para que se possa produzir um compósito cimentício reforçado por fibras naturais, com comportamento mecânico adequado ao seu uso como elemento semi-estrutural ou estrutural, é necessário a utilização de reforços contínuos uni ou bi-direcionais [32]. Tais compósitos podem ser utilizados como painéis estruturais, divisórias internas e externas, telhados, fôrmas, material de reparo estrutural e reforço de paredes de alvenaria, entre outros. A Figura 1 mostra uma construção feita com painéis pré-moldados de concreto. Esses painéis do tipo sanduíche possuem reforços de aço entre as duas placas de concreto como mostrado na Figura 2b. Tais painéis podem ser substituídos pelos compósitos reforçados por fibras longas de sisal, objeto da presente pesquisa. Esse tipo de construção gera uma economia em tempo e mão de obra além de diminuir os desperdícios comumente observados na construção civil.



Figura 1. Construção em Berlin, Alemanha mostrando placas pré-moldadas de concreto fabricadas pela Florack Bauunternehmung GMBH. Compósitos cimentícios reforçados por fibras longas de sisal podem ser uma alternativa sustentável para esse tipo de material.

O uso de fibras naturais como reforço em matrizes de cimento Portland apresenta um problema de durabilidade quando expostos a ambientes úmidos o qual acarreta uma redução na resistência pós-primeira fissura e de tenacidade. Esse problema está associado com o aumento de fratura de fibras e diminuição de arrancamento devido a mineralização das fibras. Esse processo de mineralização é resultado da migração de produtos de hidratação do cimento (principalmente o CaOH_2) para a estrutura da fibra.

A presente pesquisa tem como objetivo desenvolver e caracterizar mecanicamente um compósito cimentício reforçado por fibra natural (sisal) com elevada durabilidade e desempenho mecânico compatível ao seu uso como elemento estrutural. O compósito em questão é reforçado por fibras longas de sisal alinhadas em uma só direção. Para o aumento da durabilidade, uma matriz com substituição de cimento por argila calcinada foi desenvolvida. Essa matriz apresenta 50% de substituição de cimento resultando em uma baixa quantidade de hidróxido de cálcio.

O presente trabalho foi escrito na forma de artigos dos quais alguns já foram publicados em jornais internacionais indexados e outros estão em revisão para posterior submissão e possível publicação. Os referidos artigos se encontram no anexo do documento. Cada

artigo trata sobre uma propriedade específica do reforço ou do compósito como apresentado abaixo:

Artigo A : Morfologia e resistência à tração da fibra de sisal.

Artigo B: Comportamento à fadiga da fibra de sisal.

Artigo C: Durabilidade do compósito.

Artigo D: Propriedades físicas e mecânicas do compósito.

Artigo E: Mecanismos de fissuração do compósito.

Artigo F: Mecanismos de degradação do compósito.

Artigo G: Propriedades de interface fibra-matriz.

Artigo H: Comportamento a fadiga do compósito.

Artigo I: Resistência ao impacto do compósito.

Artigo J: Resistência à tração em alta velocidade do compósito.

A estrutura do documento é composta, além do presente capítulo introdutório, de uma revisão bibliográfica, metodologia/resultados e conclusão. O capítulo sobre revisão bibliográfica dá uma visão geral das pesquisas encontradas na literatura que tratam sobre o uso de fibras naturais como reforço em matrizes de cimento. A lacuna do conhecimento é evidenciada mostrando a importância da presente pesquisa. Revisões bibliográficas sobre assuntos específicos tratados nos diferentes artigos são encontrados nas introduções dos respectivos artigos. O capítulo sobre metodologia e resultados resume as metodologias utilizadas para se atingir o objetivo da presente pesquisa e os resultados obtidos fazendo dessa forma uma ponte para os artigos. Uma conclusão com os resultados mais relevantes do trabalho é feita no último capítulo. Conclusões de cada assunto específico são apresentadas nos artigos.

Capítulo 2.

Revisão Bibliográfica

O uso de fibras naturais como reforço em concreto é um desafio para a indústria da construção civil, particularmente em países não industrializados, uma vez que esse tipo de reforço é barato e disponível no formato a ser utilizado precisando de um processamento de baixo grau de industrialização. Se comparada a um peso equivalente de uma fibra de reforço sintética a energia necessária para obtenção da fibra natural é baixa e dessa forma os custos de produção são bastante reduzidos.

Fibras naturais tem sido utilizadas para reforçar materiais inorgânicos por milhares de anos porém apenas durante a segunda guerra mundial, a devida atenção foi dada para o uso de fibras celulósicas como reforço em materiais a base de cimento. Quando a reserva da fibra de asbesto começou a diminuir, a fibra de celulose começou a ser empregada como substituto parcial ou total do asbesto. No começo dos anos 70, quando foi descoberto que o asbesto é prejudicial à saúde humana, outra vez, foi dada atenção às fibras naturais. De acordo com Gram [9], iniciaram-se no final da década de 60, investigações sobre a possibilidade do uso de fibras naturais orgânicas como reforço em placas finas de concreto. Um método para a manufatura de placas finas, feitas por concreto reforçado com fibras naturais, para uso como cobertura foi rapidamente desenvolvido e disseminado para países na América central, África e Ásia [9]. Mais recentemente o uso de polpas celulósicas como reforço em matrizes de cimento vem sendo pesquisado para fabricação de elementos de cobertura e outros elementos não estruturais [33].

Entretanto, compósitos cimentícios reforçados por fibras naturais sofrem um processo de envelhecimento em ambientes úmidos o qual gera uma redução na resistência pós-primeira fissura e na tenacidade do material. Esse problema de durabilidade está associado com um aumento da fratura da fibra e na diminuição do arrancamento devido

a um processo de mineralização da fibra. Tal processo está relacionado com a migração de produtos de hidratação (principalmente o CaOH_2) para a estrutura da fibra.

As fibras naturais apresentam uma estrutura hierárquica de grande complexidade. Cada fibra é composta por várias fibro-células. Cada fibro-célula, por sua vez, é formada por quatro partes principais: parede primária, parede secundária, parede terciária e o lúmen. As fibro-células são ligadas umas as outras pela lamela central, a qual consiste de hemicelulose e lignina. O lumen possui tamanho variado porém a sua geometria é bem definida. As paredes celulares são formadas por varias camadas de estrutura fibrilar a qual é constituída por fibrilas conectadas por lignina. Na parede primaria, as fibrilas possuem uma estrutura reticulada. Na parede secundaria exterior (S_1) as fibrilas são arranjadas em espirais com um ângulo de 40° em relação ao eixo longitudinal da fibra. As fibrilas na parede secundaria interna (S_2) possuem uma inclinação de 18 a 25° . A parede terciária possui estrutura fibrilar paralela e engloba o lumen. As fibrilas são formadas por micro-fibrilas com uma espessura de 20 nm. As micro-fibrilas são compostas de cadeias moleculares de celulose com uma espessura de 0.7 nm e são conectadas por hemicelulose. Toda essa complexidade da estrutura das fibras naturais transformam o seu estudo em um desafio. As fibras naturais possuem seção transversal irregular o que dificulta o cálculo de sua área e consequentemente das tensões de tração. Esse fato aumenta a variabilidade dos resultados encontrados na literatura sobre o comportamento mecânico de fibras naturais. As seções irregulares apresentam formas diferentes dependendo do tipo de fibra natural e no caso das fibras extraídas de folhas, do seu posicionamento. As diferentes geometrias podem afetar a aderência fibra matriz e devem ser levadas em consideração quando do cálculo da adesão.

Várias pesquisas foram realizadas para estudar a durabilidade das fibras naturais como reforço em concreto. Essas pesquisas podem ser divididas em relação ao tipo de reforço: fibras longas [4][5][6][7][8][9], fibras curtas [10][11][12][13][14][15][16][17] e fibras de polpa [18-30]. Diversos tipos de ensaios foram desenvolvidos e utilizados: ciclos de molhagem e secagem, imersão em água quente, envelhecimento natural e modificações dos ciclos de secagem e molhagem. Gram [5][7][9] desenvolveu o método CBI que consiste em armazenar os compósitos em um cubículo no qual os materiais são umedecidos e resfriados por um borrifador de água. A água é transportada no cubículo por 30 minutos a uma temperatura de 10°C . Depois do umedecimento dos compósitos uma resistência e um ventilador são acionados até que o cubículo atinja uma

temperatura de 105 °C. A resistência permanece ligada por cinco horas e meia antes que a água seja, mais uma vez, borrifada no cubículo. Silva et al. [4][6][8] desenvolveu a câmara de ventilação forçada (CVF), equipamento que permite a simulação da velocidade do vento e temperatura do processo de secagem durante os ciclos de molhagem e secagem. Estudos de degradação em fibras naturais sendo essas submetidas a diferentes soluções alcalinas [11][15] e investigações sobre a água dos poros do compósito assim como o teor de lignina presente em fibras naturais antes e após processo de envelhecimento [14] também foram estudados.

Para aumentar o desempenho da durabilidade de compósitos cimentícios reforçados por fibras naturais vários estudos foram feitos incluindo impregnação da fibra com agentes repelentes e bloqueadores de água, selagem do sistema de poros da matriz, redução da alcalinidade da matriz e combinação da impregnação da fibra e modificação da matriz.

Um dos primeiros e mais completos trabalhos referentes à durabilidade de fibras naturais como reforço em matrizes cimentícias foi realizado por Gram [7]. De acordo com este autor o processo principal de degradação da fibra de sisal está relacionado à decomposição química da lignina e da hemicelulose na lamela central da fibra. Nesse processo de degradação a água alcalina presente nos poros do concreto dissolveria a lignina e a hemicelulose quebrando assim a ligação entre as fibro-células. Gram desenvolveu um extenso trabalho experimental testando varias técnicas as quais podem ser divididas em dois grupos: tratamento da fibra e modificação da matriz cimentícia. As técnicas são descritas de forma sumária a seguir: utilização de um feixe de fibras ao invés de filamentos individuais, impregnação da fibra com agentes bloqueadores, impregnação da fibra com agentes repelentes de água, impregnação da fibra com agentes bloqueadores e repelentes de água, selagem do sistema de poros da matriz, redução da alcalinidade da matriz e combinação de impregnação da fibra e modificações na matriz de cimento. Os resultados são descritos a seguir. Nenhum dos agentes bloqueadores aumentaram a durabilidade da fibra. Para os agentes repelentes de água utilizados, somente nitratos de bário, esteárico e formine levaram a um retardamento do processo de enrijecimento do compósito. O uso de glóbulos de cera e estearato de zinco como agentes para selar o sistema poroso mostraram resultados promissores. O resultado mais promissor alcançado por Gram foi a substituição de 45% do cimento por fumo de sílica. Tal tratamento diminuiu a perda de tenacidade do compósito. O uso de

pozolanas naturais como substituto do cimento não foi tão efetivo quanto o uso de fumo de sílica, entretanto demonstraram um efeito positivo no aumento da durabilidade.

Canovas et al. [12][13] investigaram a impregnação da fibra de sisal com compostos orgânicos derivados da madeira como taninas, colophony e óleos vegetais. Os resultados indicaram uma diminuição no processo de mineralização das fibras de sisal. A selagem dos poros com colophony, tanina e montan também foi investigado por Canovas et al. Os resultados indicaram que a absorção de água e a porosidade relativa do compósito cimentício reduziram, diminuindo assim o processo de enrijecimento do compósito.

Toledo Filho et al. [10][11] investigaram o problema de durabilidade das fibras de sisal como reforço em matrizes de cimento. As técnicas utilizadas na referida pesquisa foram a carbonatação da matriz, imersão das fibras de sisal em solução de fumo de sílica e substituição parcial do cimento Portland por fumo de sílica e escória de alto forno. A substituição de cimento por 40%, em massa, de escória não reduziu o processo de enrijecimento do compósito. A adição de 10 % de fumo de sílica foi efetivo no retardamento da perda de resistência e enrijecimento do compósito reforçado por fibras de sisal. Os resultados de Toledo Filho corroboram com aqueles obtidos por Gram. A imersão da fibra de sisal em solução de fumo de sílica e carbonatação da matriz mostraram ser alternativas promissoras para um incremento da durabilidade dos compósitos.

Mohr et al. [34] investigaram o envelhecimento acelerado de compósitos cimentícios reforçados por polpas de madeira até 25 ciclos de molhagem e secagem. Misturas binárias, ternárias e quaternárias de fumo de sílica, escória, cinza volante classe C e F, metacaulim e cinzas vulcânicas foram estudadas como substituto parcial do cimento. Somente misturas com substituição parcial do cimento por 90% de escória, 30% de metacaulim, ou mais de 30% de fumo de sílica não apresentaram degradação após 25 ciclos de secagem e molhagem. A quantidade de hidróxido de cálcio foi determinada para as diversas matrizes utilizadas. Foi visto que quando o conteúdo de hidróxido de cálcio era superior a 2 % a tenacidade do compósito depois da ciclagem era mínimo. Quando a quantidade de hidróxido de cálcio foi inferior a 2%, a tenacidade calculada foi consideravelmente superior.

Silva et al. [4][6][8] propuseram que o principal processo de degradação de compósitos reforçados por fibras de sisal seria a mineralização da fibra de sisal devido a

precipitação de hidróxido de cálcio na estrutura da fibra. Para combater esse processo de degradação uma matriz com reduzida quantidade de hidróxido de cálcio foi desenvolvida. Essa matriz é composta pela substituição de 50 % de cimento Portland por 30 % de metacaulinita e 20 % de tijolo cerâmico moído calcinado. Ciclos de molhagem e secagem foram efetuados e foi observado que 100 ciclos de molhagem e secagem não afetaram a resistência à flexão e a tenacidade do compósito. Nenhum sinal de mineralização foi observado através de investigação microscópica [4][6][8].

O uso de fibras longas e alinhadas como reforço demonstram ser uma boa alternativa para o desenvolvimento de compósitos cimentícios duráveis reforçados por fibras naturais. A modificação da matriz através da substituição parcial do cimento por pozolanas demonstra ser uma melhor alternativa em relação ao tratamento da fibra. Matrizes cimentícias com baixa quantidade de hidróxido de cálcio demonstraram ser uma boa alternativa para o desenvolvimento de compósitos cimentícios reforçados por fibras naturais.

Apesar do relevante número de trabalhos sobre durabilidade de compósitos reforçados por fibra natural é necessário ainda a caracterização desses compósitos por um número mais elevado de ciclos e da realização de ensaios de tração além dos de flexão. Em relação ao sistema de reforço apenas Gram [7] pesquisou a durabilidade em compósitos reforçados por fibras longas. O referido estudo foi realizado no início da década de 80 e não foi dada continuação ao mesmo.

O estudo do comportamento mecânico de compósitos cimentícios reforçados por fibras naturais pode ser dividido em 3 famílias: as reforçadas por polpa, fibras curtas (< 50 mm) e fibras longas alinhadas unidirecionalmente. Compósitos reforçados com polpas de sisal com fração de massa variando de 0,5 a 12 % foram investigadas por Coutts et al. [35]. A resistência máxima à flexão foi obtida para um compósito com 8% de reforço. Módulo de ruptura de 18 MPa e tenacidade de 2,49 kJ/m² foram obtidos para tais compósitos. Savastano et al. [36] obtiveram resultados semelhantes. Silva et al. [37] investigaram o uso de polpa de sisal como reforço em compósitos cimentícios em frações de massa de 8 e 14 %. O maior resultado foi obtido para um compósito com fração de massa de 14 % o qual obteve módulo de ruptura e tenacidade de 14,26 MPa e 0,97 kJ/m². Mohr et al. [34] obtiveram módulo de ruptura variando de 3,94 a 12,92 MPa para compósitos reforçados por 4 % de polpa de madeira (para diferentes tipos de matrizes). Compósitos cimentícios reforçados com polpas apresentam comportamento à

flexão com formação de apenas uma fissura com posterior queda da capacidade portante. A capacidade de absorção de energia nesses materiais é normalmente inferior a 3 kJ/m^2 .

Compósitos cimentícios reforçados por fibras curtas de juta e coco foram estudados por Aziz et al. [38]. Testes de flexão e tração direta foram realizados para compósitos reforçados por 2, 3 e 4% de fibras em volume e comprimentos de fibra de 25 e 38 mm. Foi observado um comportamento tanto na tração quanto na flexão de formação de uma só fissura com amolecimento de deformação. Valores de resistência à tração e módulo de ruptura para compósitos reforçados por juta variaram de 2,30 a 2,36 MPa e 3,92 a 4,50 MPa, respectivamente. Para compósitos reforçados com fibras de coco a resistência à tração variou de 2,04 a 2,74 MPa.

O uso de fibras de sisal com 25 mm de comprimento como reforço em uma matriz com 50 % de substituição parcial do cimento por metacaulim foi estudado por Melo Filho et al. [39]. Foi observado um comportamento de múltipla fissuração na flexão para compósitos reforçados por 6 % de fibras em volume. Foram observados valores médios de resistência à flexão de 7,20 MPa e tenacidade de $3,86 \text{ kJ/m}^2$.

Compósitos reforçados por fibras longas de sisal alinhadas unidirecionalmente foram desenvolvidos por Silva et al. [3][4][6][8] e Melo Filho [40]. Esses compósitos apresentam comportamento de múltipla fissuração na tração direta e na flexão (ver Figura 2).

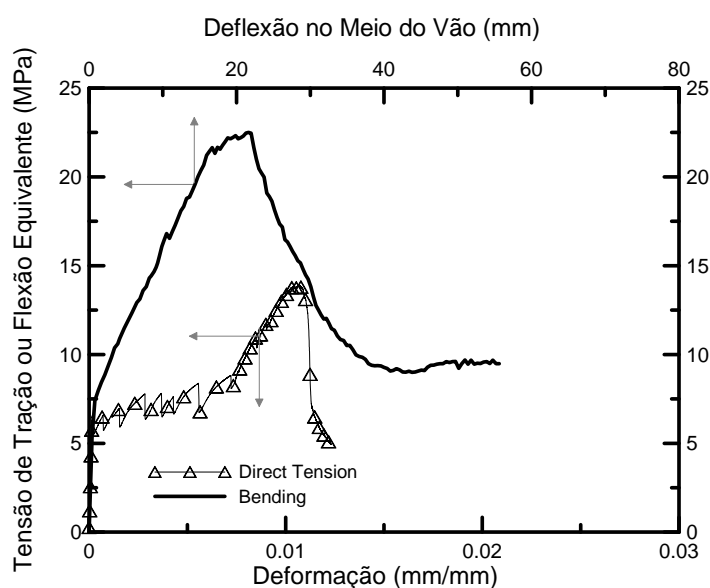
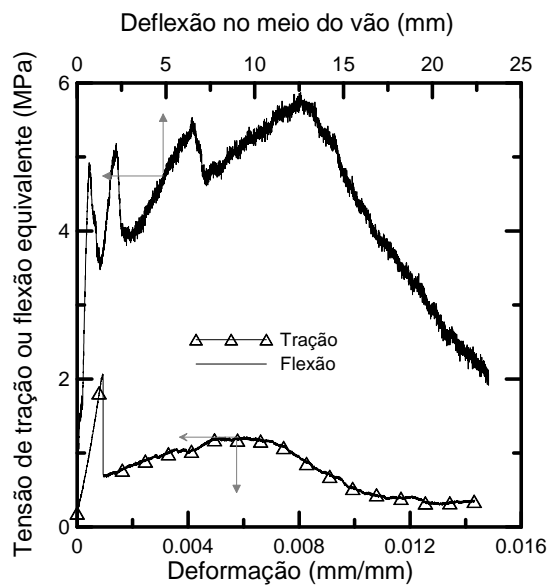


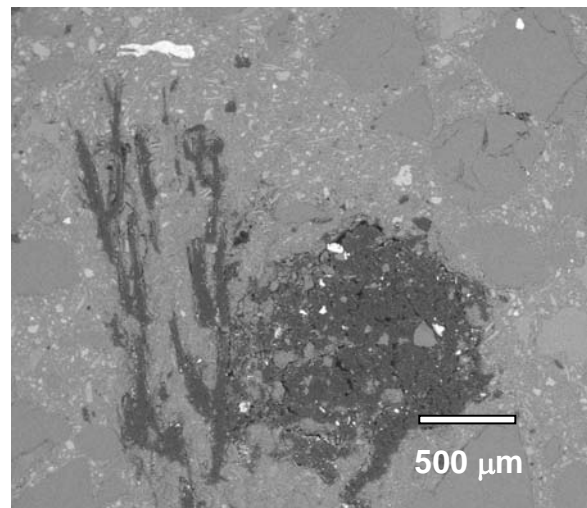
Figura 2. Comparação entre comportamento à flexão em quatro pontos e tração direta de um compósito reforçado por 10% em volume de fibras longas de sisal.

Resistência à tração média de 12 MPa com deformação última de 1,5 % e módulo de ruptura médio de 25 MPa com deslocamento referente a carga última de 20 mm foram obtidos.

Para o desenvolvimento de compósitos reforçados por fibras longas em escala industrial se faz necessário a fabricação de um tecido bi-direcional. Esse tipo de tecido facilitaria o processo de produção do compósito o qual poderia ser feito através de pultrusão. Existem no mercado alguns tipos de tecidos naturais usados, em sua maior parte, para a produção de tapetes e sacos. Recentemente Silva et al. [31] usaram o tecido de juta como reforço em uma matriz cimentícia. Como mostrado na Figura 3 foi observado um comportamento de múltipla fissuração na flexão com módulo de ruptura de 7 MPa e deflexão última de 12,5 mm. O comportamento à tração apresentou a formação de duas fissuras com tensão máxima de 2 MPa.



(a)



(b)

Figura 3. Comportamento mecânico de compósito cimentício reforçado por tecido de juta: (a) comparação entre comportamento à tração e flexão em quatro pontos de um compósito reforçado por 5 camadas de tecido de juta e (b) micrografia mostrando pouca penetração da matriz no fio de juta.

Observa-se uma baixa penetração da matriz no fio de juta (Figura 3b). Dessa forma se faz necessário a produção de um tecido composto de fios com uma quantidade menor de filamentos para que se obtenha uma maior eficiência das fibras.

Estudos sobre o comportamento dinâmico de compósitos cimentícios reforçados por fibras natural são de grande importância. Entretanto, pesquisas referentes a tal comportamento não foram encontradas na literatura disponível. O presente trabalho contribui para o avanço do conhecimento no referido assunto com investigações em relação ao comportamento mecânico sob cargas de impacto, tração em alta velocidade e fadiga.

Capítulo 3.

Metodologia e Resultados

3.1 Morfologia e Propriedades Mecânicas da Fibra de Sisal (Artigos A e B)

As fibras de sisal possuem uma estrutura hierárquica, com morfologia variável e seção transversal irregular. Testes de tração em fibras naturais de pequeno diâmetro não é tarefa trivial. As áreas irregulares das fibras devem ser consideradas assim como a contribuição da flexibilidade do sistema de ensaios. Elevada resolução na medida da carga e deslocamento é, também, bastante importante para se obterem valores precisos de módulo de elasticidade, resistência à tração e deformação.

Ensaio de tração foram realizados em fibras com diferentes comprimentos utilizando uma MTS Tytron. A área da seção transversal de todas as fibras ensaiadas foi medida usando MEV e posterior análise de imagens. O módulo de elasticidade medido através de ensaio de tração foi corrigido para a flexibilidade do sistema de teste utilizado. Estatística de Weibull foi empregada para quantificar o grau de variabilidade da resistência à tração da fibra para diferentes comprimentos. O módulo Weibull diminuiu de 4,6 para 3,0 com o aumento do comprimento da fibra de 10 mm para 40 mm, respectivamente.

O módulo de elasticidade médio das fibras de sisal obtido, corrigido para flexibilidade do sistema, foi em torno de 18 GPa. O módulo não foi influenciado pelo comprimento das fibras. A deformação última da fibra de sisal diminuiu de aproximadamente 5,2 % para 2,6% quando o comprimento aumentou de 10 mm para 40 mm. A resistência à tração não depende do comprimento de fibra.

O modo de falha das fibras foi investigado através do MEV. Os mecanismos de falha são descritos e analisados em termos da microestrutura e defeitos das fibras. Foi

observado delaminação da parede primária e terciária da fibro-célula e delaminação entre as fibro-células.

O comportamento de fadiga em tração das fibras de sisal foi investigado em termos de tensão versus ciclos e tensão-deformação. As fibras foram testadas em níveis de tensão variando de 80 e 400 MPa. As fibras de sisal não apresentaram fadiga para uma tensão máxima abaixo de 320 MPa. Os gráficos de tensão-número de ciclos foram normalizados pela resistência à tração estática das fibras de sisal, sendo observado que abaixo de uma razão de 0,5 não houve fratura da fibra antes de 10^6 ciclos.

Testes de tração direta foram realizados em fibras que sobreviveram 10^6 ciclos para determinação da resistência residual. Não foi observada diminuição em resistência, mas sim um aumento no módulo de elasticidade com um aumento da tensão de fadiga. Os mecanismos para o aumento do módulo assim como os mecanismos de degradação microestrutural foram investigados.

3.2 Durabilidade de Compósitos Reforçados por Fibras de Sisal (Artigos C, D e F)

Para o desenvolvimento de um compósito cimentício de elevada durabilidade reforçado por fibra de sisal foi desenvolvida uma nova matriz. A metodologia utilizada foi a de substituição parcial do cimento por argilas calcinadas para se produzir uma matriz livre de hidróxido de cálcio. O conteúdo de hidróxido de cálcio foi determinado através de análise térmica realizada aos 28 dias de idade. Matrizes livres de hidróxido de cálcio foram obtidas para substituições de 50 % de cimento. Ciclos de molhagem e secagem e imersão em água quente foram realizados para acelerar o envelhecimento dos compósitos. A durabilidade foi investigada pela determinação dos efeitos do envelhecimento acelerado na microestrutura, ensaios de flexão e tração direta. Testes de termogravimetria foram realizados em fibras retiradas de dentro do compósito após envelhecimento. Foi avaliada a deterioração de celulose e hemicelulose das fibras extraídas de compósitos envelhecidos.

Os resultados indicaram que a matriz desenvolvida evita a mineralização das fibras mantendo a tenacidade dos compósitos a níveis elevados.

3.3 Comportamento Estático de Compósitos Reforçados por Fibras de Sisal (Artigos D e E)

O comportamento mecânico estático de compósitos cimentícios reforçados por fibras de sisal foi determinado através de ensaios de tração direta e flexão em quatro pontos. Os compósitos apresentaram formação de múltiplas fissuras sob cargas de tração e flexão. A formação dessas fissuras foi investigada através de um processo de captura de imagens de alta resolução. O espaçamento das fissuras foi determinado através de análise de imagens e correlacionado com a deformação do compósito. Vários estágios de carregamento correspondentes a iniciação, propagação, distribuição, abertura e localização das fissuras foram analisados. O efeito da formação de fissuras sob carga de flexão na localização da linha neutra foi determinado utilizando “strain gages”.

O espaçamento de fissuras em tração, medido na zona de saturação, foi quase duas vezes maior do que o correspondente à flexão. Enquanto que o módulo pós-fissuração diminuiu significativamente de 35 GPa para 1,32 GPa, o compósito alcançou resistências máximas à tração e flexão de 12 e 25 MPa, respectivamente.

3.4 Estudo da Interface Fibra-Matriz (Artigo G)

A interface fibra-matriz foi caracterizada por meio de ensaios de arrancamento. O efeito do tempo de cura e do comprimento de embebimento foi investigado. O efeito da geometria irregular na adesão fibra-matriz foi avaliado. Microscopia eletrônica de varredura acoplada à análise de imagens foi utilizada para medir a área de cada fibra testada e para posterior classificação morfológica. Os resultados foram correlacionados com a morfologia da fibra. Ensaio de tração direta foram realizados em compósitos reforçados por 10 % em volume de fibras de sisal. Modelo de diferenças finitas desenvolvido por Soranakom e Mobasher foi utilizado para determinar a relação constitutiva da interface a partir de dados experimentais e para prever o comportamento à tração e espaçamento entre fissuras do compósito.

A adesão fibra-matriz atingiu sua capacidade máxima aos 14 dias de cura e nenhum aumento foi verificado para idades de 21 e 28 dias. A tensão adesional média após 15 dias de cura foi variou de 0,59 à 0,67 MPa.

Foi observado que com o aumento do comprimento de embebedimento a carga de arrancamento aumentou de 2 para 8 N. Para comprimentos de 40 mm nenhum aumento significativo foi observado. O comprimento de embebedimento não influenciou a tensão de adesão.

O modelo de diferenças finitas se mostrou eficiente para prever o comportamento de fibras de sisal embebidas em matrizes de cimento. A simulação do comportamento à tração dos compósitos mostrou boa correlação com a resposta do “strain gage” até a primeira fissura. A partir desse ponto até uma deformação de 0,4 % a simulação apresentou boa correlação com valores experimentais mais baixos. Após deformação de 0,4 % o modelo simulou bem valores mais elevados superestimando a resistência máxima à tração.

3.5 Comportamento Dinâmico de Compósitos Reforçados por Fibras de Sisal (Artigos H, I e J)

O comportamento mecânico dos compósitos quando sujeitos a cargas dinâmicas foi abordado nos artigos H, I e J. Ensaio de fadiga (artigo H), impacto (artigo I) e tração em alta velocidade (artigo J) foram realizados.

O comportamento à tração em fadiga do compósito foi examinado em termos de tensão versus ciclos de fadiga e comportamento tensão-deformação. Os compósitos foram testados em níveis de tensão máxima variando de 4 à 9,8 MPa. Não foi observada fadiga antes de 10^6 ciclos para um nível máximo de tensão de 6 MPa. Ensaio de tração direta foram realizados em compósitos que sobreviveram 10^6 ciclos. O espaçamento entre fissuras foi determinado através de análise de imagens. Não foi observada diminuição na resistência à tração porém houve um decréscimo no módulo de elasticidade e aumento na tensão de primeira fissura. Microscopia ótica fluorescente foi utilizada para investigar a formação de fissuras de compósitos sujeitos à cargas de fadiga.

Testes de impacto baseados na queda livre de um martelo instrumentado com configuração de flexão em três pontos foram realizados. Quedas variando de alturas de 1 a 2000 mm foram controladas através de mecanismos eletrônicos. Compósitos reforçados por fibras de sisal foram ensaiados em alturas de 101,6 mm (4”), 152,4 mm (6”) e 203,2 mm (8”). Os resultados indicaram que a aceleração do compósito após o

impacto atingiu valores de até 100 m/s^2 com carregamento de 850 N para uma energia de impacto de 10,55 J. Para energias de impacto mais elevadas (15,83 e 21,1 J) a aceleração do compósito aumentou para 170 m/s^2 , entretanto, a diferença em termos da força de impacto não foi significativa. Tensões de impacto variaram de 22,97 MPa (energia de impacto de 10,55 J) à 18,06 MPa (energia de impacto de 21,1 J) com desvio padrão variando de 3,3 à 4,6 MPa. A rigidez inicial do compósito diminuiu de 4,4 para 2,2 kN/mm com o incremento da energia de impacto de 10,55 à 21,1 J. A degradação da rigidez acontece após a formação da primeira fissura e não existe diferença significativa para as diferentes energias de impacto estudadas. A morfologia do dano consistiu de fissuras na matriz e delaminação. O processo de dano teve início com a formação de fissuras. Dois tipos de fissuras foram observadas: de tração e cisalhamento. Delaminação resultando na ruptura total do compósito foi observada apenas para energias de impacto de 21,1 J.

Ensaio de tração direta dinâmica foram conduzidos utilizando uma máquina de testes universais servo-hidráulica MTS para ensaios de alta velocidade. A velocidade do atuador foi controlada pela abertura da servo-válvula que controla o suprimento de óleo. Os ensaios foram realizados com uma velocidade de aproximadamente 1180 m/s o que gerou uma taxa de deformação de $24,6 \text{ s}^{-1}$ e um tempo de ensaio de 20 ms.

Imagens do compósito durante o teste foram obtidas por uma máquina de alta velocidade Phantom. Um programa escrito em MATLAB usando o método de correlação digital de imagens foi usado para a determinação do campo de deslocamentos e para o cálculo das deformações durante o ensaio. Foi observado um incremento significativo na resistência à tração dinâmica. Um fator de incremento dinâmico para resistência à tração de 1,26 foi calculado. Foi observada uma dependência da resistência de primeira fissura à taxa de deformação. Um incremento na tensão de primeira fissura de 5,94 à 8,06 MPa foi calculado quando comparados ensaios estáticos e dinâmicos. A deformação correspondente a máxima resistência à tração aumentou de 3 % à 10 % para ensaios dinâmicos. O mecanismo de falha principal foi o de arrancamento. O método de correlação digital de imagens provou ser uma ferramenta poderosa para a determinação do campo de deslocamento em compósitos cimentícios.

Capítulo 4.

Conclusões

Fibras de sisal foram caracterizadas mecânica e morfologicamente. As fibras apresentaram uma estrutura hierárquica, com morfologia variada e seção transversal irregular. Foi comprovado que os fatores citados influenciam no comportamento mecânico e na adesão interfacial fibra-matriz. A fibra de sisal apresentou um módulo médio de elasticidade de aproximadamente 18 GPa e resistência à tração média de 400 MPa. As fibras de sisal não apresentaram fadiga para uma tensão máxima abaixo de 320 MPa quando submetidas até 10^6 ciclos.

Compósitos cimentícios duráveis reforçados por fibras longas de sisal foram desenvolvidos. Para isso uma matriz foi desenvolvida a partir da substituição parcial do cimento em 50 % por metacaulim e tijolo moído calcinado. Essa matriz foi caracterizada a partir de análises térmicas sendo que, aos 28 dias de idade, não foi observada a presença hidróxido de cálcio. Ensaios de envelhecimento acelerado foram realizados. Não foi notada perda de tenacidade ou resistência à flexão para compósitos submetidos a 100 ciclos de molhagem e secagem e imersão em água à 60 °C por seis meses.

O compósito desenvolvido apresentou comportamento de endurecimento com múltipla fissuração sob tração direta. O compósito alcançou resistências máximas à tração e flexão de 12 e 25 MPa, respectivamente. Deformações máximas de tração da ordem de 1,5% foram observadas o que demonstra a ductilidade do material.

A adesão fibra-matriz atingiu sua capacidade máxima aos 14 dias de cura e nenhum aumento foi verificado para idades de 21 e 28 dias. A tensão adesional média após 15 dias de cura variou de 0,59 à 0,67 MPa. Modelos de diferença finita foram utilizados para simular o comportamento à tração direta do compósito e distância entre fissuras a partir de um modelo constitutivo de adesão fibra-matriz.

Os compósitos foram testados à fadiga em níveis de tensão máxima variando de 4 à 9,8 MPa. Não foi observada fadiga antes de 10^6 ciclos para um nível máximo de tensão de 6 MPa. Testes de impacto e tração em alta velocidade foram realizados nos compósitos demonstrando a elevada capacidade de absorção de energia sob cargas dinâmicas.

REFERÊNCIAS

- [1] LARBIG, H., SCHERZER, H., DAHLKE, B., POLTROCK R., 1998, “Natural fibre reinforced foams based on renewable resources for automotive interior applications”, **Journal of Cellular Plastics**, v.34, pp.361–79.
- [2] MAGURNO, A., 1999, “Vegetable fibres in automotive interior components”, **Die Angewandte Makromolekulare Chemie**, v. 272, pp. 99–107.
- [3] SILVA, F. A., MOBASHER, B., TOLEDO FILHO R.D., 2008, “Recent Advances in High Performance Natural (Sisal) Fiber Cement Composites”. In: *Seventh International Rilem Symposium on Fibre Reinforced Concrete: Design and Applications (BEFIB 2008)*, pp. 105-113, Chennai. Rilem Publications S.A.R.L.
- [4] TOLEDO FILHO, R.D., SILVA, F.A., FAIRBAIRN, E.M.R., MELO FILHO, J.A., 2009, “Durability of Compression Molded Sisal Fiber Reinforced Mortar” **Construction & Building Materials**, no prelo.
- [5] GRAM, H.-E., 1988, “Durability of natural fibres in concrete”, In: *Swamy (Ed.) Natural Fibre Reinforced Cement and Concrete*, pp. 143-172, Blackie and Son Ltd.
- [6] SILVA, F.A., TOLEDO FILHO, R.D., FAIRBAIRN E.M.R., 2006, “Accelerated aging characteristics of sisal fiber-cement based composites made with a CH free cementitious matrix”, In: *Brazilian Conference Non-Conventional Materials and Technologies in Ecological and Sustainable Construction – Brasil Nocmat*.
- [7] GRAM, H.-E., 1983, “Durability of natural fibres in concrete”, Swedish Cement and Concrete Research Institute, pp.1-255, S-100 44 Stockholm, CBI Fo 1:83.
- [8] SILVA, F.A., MELO FILHO, J.A., TOLEDO FILHO, R.D., FAIRBAIRN, E.M.R., 2006, “Mechanical behavior and durability of compression moulded sisal fiber cement mortar laminates (SFCML)”, In: *1st International RILEM Conference on Textile Reinforced Concrete (ICTRC)*, pp. 171-180, Aachen, Germany.
- [9] BERGSTROM, S.G., GRAM, H.-E., 1984, “Durability of alkali-sensitive fibres in concrete”, **The International Journal of Cement Composites and Lightweight concrete**, v.6, n.2, pp. 75-80.

- [10] TOLEDO FILHO, R.D., GHAVAMI, K., ENGLAND, G.L., SCRIVENER, K., 2003, “Development of vegetable fibre-mortar composites of improved durability”, **Cement and Concrete Composites**, V. 25, pp. 185-196.
- [11] TOLEDO FILHO, R.D., SCRIVENER, K., ENGLAND, G.L., GHAVAMI, K., 2000, “Durability of alkali-sensitive sisal and coconut fibres in cement mortar composites”, **Cement and Concrete Composites**, v. 22, pp. 127-143.
- [12] CANOVAS, M. SELVA, KAWICHE, G.M., 1992, “New economical solutions for improvement of durability of portland cement mortars reinforced with sisal fibers”, **Materials and Structures**, v. 25, pp. 417-422.
- [13] CANOVAS, M.F., KAVICHE, G.M., SELVA, N.H., 1990, “Possible ways of preventing deterioration of vegetable fibres in cement mortars”, *In: Sobral H.S. (Ed.) Vegetable plants and their fibres as building materials*, pp. 120-129, Chapman & Hall.
- [14] JOHN, V.M., CINCOTTO, M.A., SJOSTROM, C., AGOPYAN, V., OLIVEIRA, C.T.A., 2005, “Durability of slag mortar reinforced with coconut fibre”, **Cement and Concrete Composites**, v. 27, pp. 565-574.
- [15] RAMAKRISHNA, G., SUNDARARAJAN, T., 2005, “Studies on the durability of natural fibres and the effect of corroded fibres on the strength of mortar”, **Cement and Concrete Composites**, v. 27, pp. 575-582.
- [16] GUIMARÃES, S.S., 1990, “Vegetable fiber cement composites”, *In: Sobral H.S. (Ed.) Vegetable plants and their fibres as building materials*, pp. 98-107, Proceedings of the second international Rilem Symposium, Chapman & Hall.
- [17] JOHN, V.M., AGOPYAN, V., DEROLLE, A., 1990, “Durability of blast furnace-slag-based cement mortar reinforced with coir fibres”, *In: Sobral H.S. (Ed.) Vegetable plants and their fibres as building materials*, pp. 87-97, Proceedings of the second international Rilem Symposium, Chapman & Hall.
- [18] MOHR, B.J., BIERNACKI, J.J., KURTIS, K.E., 2006, “Microstructural and chemical effects of wet/dry cycling on pulp fiber-cement composites”, **Cement and Concrete Research**, v.36, pp.1240-1251.
- [19] MOHR, B.J., NANKO, H., KURTIS, K.E., 2005, “Durability of thermomechanical pulp fiber-cement composites to wet/dry cycling”, **Cement and Concrete Research**, v.35, pp. 1646-1649.

- [20] MOHR, B.J., NANKO, H., KURTIS, K.E., 2005, "Durability of kraft pulp fiber-cement composites to wet/dry cycling", **Cement and Concrete Composites**, v.27, pp. 435-448.
- [21] MOHR, B.J., *Durability of Pulp Fiber Cement Composites*, Ph.D. Dissertation, Georgia Institute of Technology, 2005.
- [22] SOROUSHIAN, P., MARIKUNTE, S., 1992, "Long-term durability and moisture sensitivity of cellulose fiber reinforced cement composites", *In: Swamy (Ed.) Fibre Reinforced Cement and Concrete*, pp. 1166-1184, E & FN Spon, London.
- [23] SARIGAPHUTI, M., SHAH, S.P., VINSON, K.D., 1993, "Shrinkage cracking and durability characteristics of cellulose fiber reinforced concrete", **ACI Materials Journal**, v.90, n. 4, pp. 309-318.
- [24] MACVICAR, R., MATUANA, L.M., BALATINECZ, J.J., 1999, "Aging mechanisms in cellulose fiber reinforced cement composites", **Cement and concrete Composites**, v. 21, pp. 189-196.
- [25] PIRIE B.J., GLASSER F.P., SCHMITT-HENCO C., AKERS S.A.S. Durability studies and characterization of the matrix and fibre-cement interface of asbestos-free fibre-cement products. **Cement and Concrete Composites**, v.12, 1990, p. 233-244.
- [26] KIM, P.J., WU, H.C., LIN, Z., LI, V.C., DELHONEUX, B., AKERS, S.A.S., 1999, "Micromechanics-based durability study of cellulose cement in flexure", **Cement and Concrete Research**, v. 29, pp.201-208.
- [27] BENTUR, A., AKERS, S.A.S., 1989, "The microstructure and ageing of cellulose fibre reinforced cement composites cured in a normal environment", **The International Journal of Cement Composites and Lightweight Concrete**, v.11, n.2, pp. 99-109.
- [28] TAIT, R.B., AKERS, S.A.S., 1989, "Micromechanical studies of fresh and weathered fibre cement composites. Part 2: wet testing", **The International Journal of Cement Composites and Lightweight Concrete**, v.11, n.2, pp.125-131.
- [29] FISHER, A.K., BEAL, F.B., 2001, "The durability of cellulose fibre reinforced concrete pipes in sewage applications", **Cement and Concrete Research**, v.31, pp. 543-553.

- [30] SAVASTANO JR., H, WARDEN, P.G., COUTTS, R.S.P., 2001, “Performance of low-cost vegetable fibre-cement composites under weathering”, *In: CIB World Building Congress: Performance in Product and Practice*, pp.1-11, Wellington, New Zealand.
- [31] SILVA, F.A., MELO FILHO, J.A. E TOLEDO FILHO, R.D., 2005, “Development of a new natural textile reinforced concrete”. Trabalho não publicado.
- [32] SILVA, F.A., MOBASHER, B., TOLEDO FILHO, R.D., 2009, “Cracking mechanisms in sisal fiber reinforced composite”, **Cement and Concrete Composites**, no prelo.
- [33] ROMA JR, L.C., MARTELLO, L.S., SAVASTANO JR., H., 2008, “Evaluation of mechanical, physical and thermal performance of cement-based tiles reinforced with vegetable fibers” , **Construction and Building Materials**, v. 22, pp. 668–674.
- [34] MOHR, B.J., BIERNACKI, J.J., KURTIS, K.E., 2007, “Supplementary cementitious materials for mitigating degradation of kraft pulp fiber-cement composites”, **Cement and Concrete Research**, v.37, pp. 1531-1543.
- [35] COUTTS, R.S.P., WARDEN, P.G., 1992, “Sisal Pulp Reinforced Cement Mortar”, **Cement and Concrete Composites**, v. 14, pp.17-21.
- [36] SAVASTANO JR., H., WARDEN, P.G., COUTTS, R.S.P., 2003, “Mechanically pulped sisal as reinforcement in cementitious matrices”, **Cement and Concrete Composites**, v.25, pp. 311-319.
- [37] SILVA, F.A. *Tenacidade de Materiais Compósitos Não Convencionais*, Dissertação de Mestrado, PUC-Rio, 2004.
- [38] AZIZ, M.A., PARAMASIVAM, P., LEE, S.L., 1987, “Natural Fibre Reinforced Composite Building Materials for Low-Income Housing”, *In: Symposium on Building Materials for Low Incoming Housing*, Banckok, Thailand, pp. 129-137.
- [39] MELO FILHO, J.A., SILVA, F.A., TOLEDO FILHO, R.D., FAIRBAIRN, E.M.R., 2007, “Effect of Reinforcement Ratio and Molding Pressure on the Mechanical Performance of Short Sisal FRC”, *In: 4th International Conference on Science and Technology of Composite Materials*, Rio de Janeiro – RJ.
- [40] MELO FILHO, J.A. *Desenvolvimento e Caracterização de Laminados Cimentíceos Reforçados com Fibras Longas de Sisal*, Dissertação de mestrado, COPPE/UFRJ, 2005.

ANEXOS

ARTIGO A - Silva F.A., Chawla N. and Toledo Filho R.D. Tensile behavior of high performance natural (sisal) fibers. Composites Science and Technology 68 (2008) 3438-3443.

Tensile Behavior of High Performance Natural (Sisal) Fibers

Flávio de Andrade Silva^a, Nikhilesh Chawla^b, and Romildo Dias de Toledo Filho^a

^aCivil Engineering Department, COPPE, Universidade Federal do Rio de Janeiro, P.O.
Box 68506, CEP 21941-972, Rio de Janeiro – RJ, Brazil.

^bSchool of Materials, Arizona State University, Tempe, AZ 85287-8706

Composites Science and Technology

2008

Abstract

Environmental awareness and an increasing concern with the greenhouse effect have stimulated the construction, automotive, and packing industries to look for sustainable materials that can replace conventional synthetic polymeric fibers. Natural fibers seem to be a good alternative since they are readily available in fibrous form and can be extracted from plant leaves at a very low costs. In this work we have studied the monotonic tensile behavior of a high performance natural fiber: Sisal fiber. Tensile tests were performed on a microforce testing system using four different gage lengths. The cross-sectional area of the fiber was measured using scanning electron microscope (SEM) micrographs and image analysis. The measured Young's modulus was also corrected for machine compliance. Weibull statistics were used to quantify the degree of variability in fiber strength, at the different gage lengths. The Weibull modulus decreased from 4.6 to 3.0 as the gage length increased from 10 mm to 40 mm, respectively. SEM was used to investigate the failure mode of the fibers. The failure mechanisms are described and discussed in terms of the fiber microstructure as well as defects in the fibers.

Keywords: A. Natural fibers; B. Mechanical properties; C. Probabilistic methods; D. Fractography; SEM.

1. Introduction

Sisal fiber is one of the most widely used natural fibers in yarns, ropes, twines, cords, rugs, carpets, mattresses, mats, and handcrafted articles. During the past two decades sisal fibers have also been used as reinforcement in cement and polymer based composites [1-7]. The sisal reinforcement can be used as short randomly distributed fibers, long oriented fibers, or as a fiber fabric. Sisal fibers (*Agave sisalana*) are extracted from sisal plant leaves (see Fig. 1a) in the form of long fiber bundles. A sisal plant produces between 200 to 250 leaves before flowering [8], each of which contains approximately 700-1400 fiber bundles with a length of about 0.5-1.0 m [2]. The sisal leaf consists of a sandwich structure composed of approximately 4% fiber, 1% cuticle, 8% dry matter, and 87% water [8].

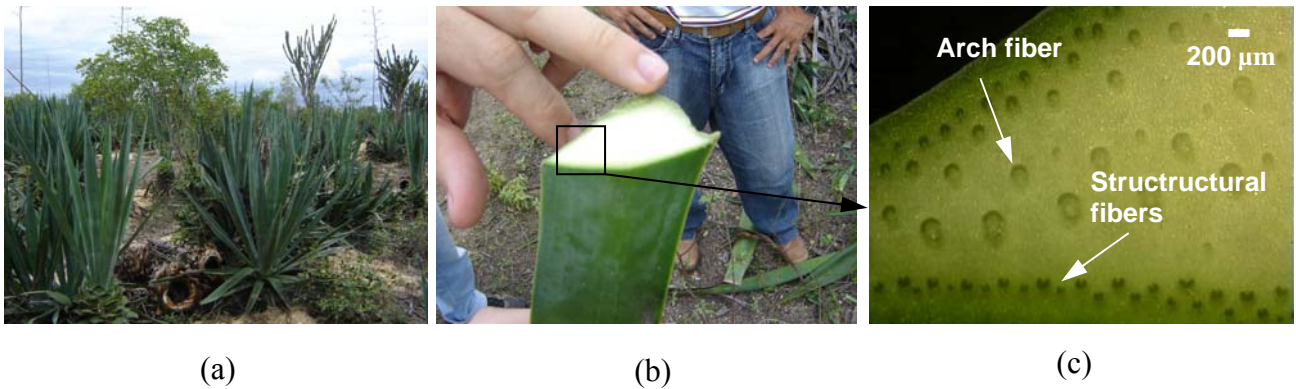


Fig. 1. The sisal: (a) its plant, (b) cross section view and (c) optical microscopy of region selected in (b).

Within the leaf, there are three basic types of fibers: structural, arch, and xylem fibers. The structural fibers give the sisal leaf its stiffness and are found in the periphery of the leaf (see Figures Fig. 1b and 1c). The equivalent diameter of the fibers is around 200 μm and the cross-section is rarely circular and usually has a “horse-shoe” shape (see Fig. 2a). The structural fibers are of great importance commercially because they almost never split during the process of extraction. The arch fibers grow in association with the conducting tissues of the plant (see Fig. 2b) and are usually found in the middle of the leaf (see Fig. 2c). These fibers run from base to tip of the plant and have good mechanical strength [9]. The xylem fibers grow opposite to the arch fibers and are connected to them through the conducting tissues. According to Nutman [9], they are composed of thin walled cells, and are invariably broken up and lost during the process of fiber extraction.

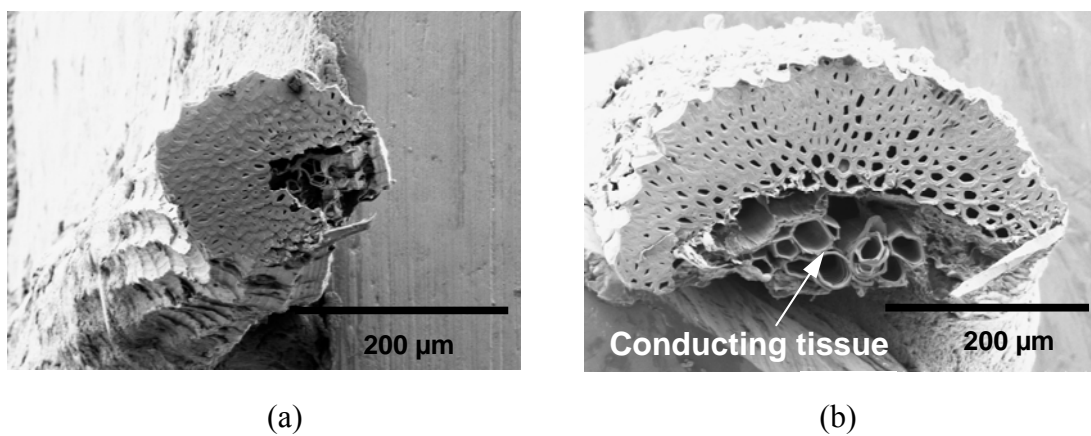


Fig. 2. Different sisal fiber types: (a) structural fiber with a horse shoe shape geometry and (b) arch fiber.

It is interesting to note that the sisal fiber has a hierarchical structure. Every fiber contains numerous elongated individual fibers, or fiber-cells, which are about 6 to 30 μm in diameter [8]. Each fiber-cell is made up of four main parts, namely the primary wall, the thick secondary wall, the tertiary wall, and the lumen (see Fig. 3). The fiber-cells are linked together by means of the middle lamellae (ML), which consist of hemicellulose and lignin (see Fig. 3). The lumen varies in size but is usually well-defined. The walls consist of several layers of fibrillar structure consisting of fibrillae which are linked together by lignin. In the primary wall, the fibrillae have a reticulated structure, while in the outer secondary wall the fibrillae are arranged in spirals. The thin, innermost, tertiary wall has a parallel fibrillar structure and encloses the lumen. The fibrillae are, in turn, built of micro-fibrillae with a thickness of about 20 nm. The microfibrillae are composed of cellulose chains with a thickness of around 0.7 nm and a length of a few μm and are linked together by means of hemicellulose [3].

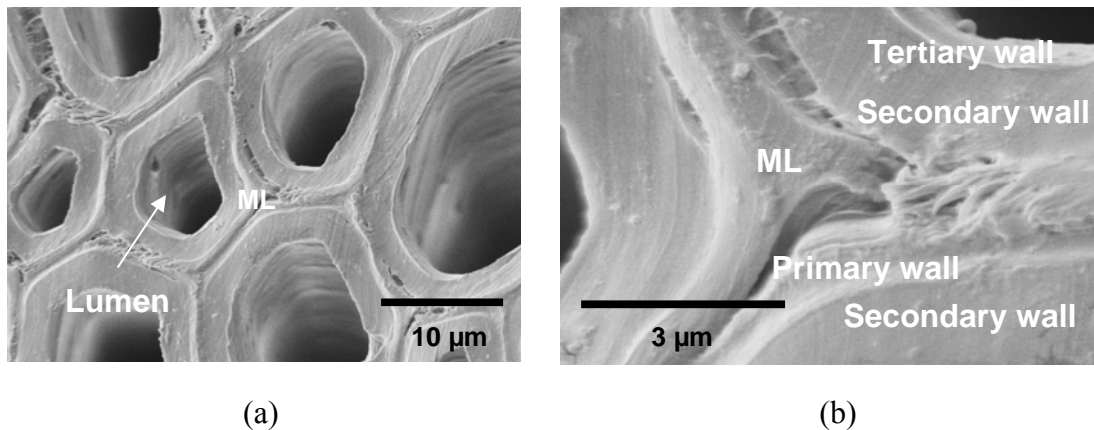


Fig. 3. Sisal fiber microstructure showing (a) fiber-cells with lumen and middle lamellae and (b) detail of ML and cell-walls.

A limited number of studies have been conducted on the tensile behavior of sisal and other natural fibers [8, 10-14] and even fewer studies on the fatigue behavior of natural fibers [15]. The main difference between the various lies in the equipment used for tensile testing, methodology for measuring the fibers' area, and methodology for computing the Young's modulus. Rao et al. [11], for example, used an optical laser beam to measure the sisal fiber diameter at different angles. While the technique for testing and measuring modulus is not reported, they report a tensile strength of about 567 MPa and Young's modulus of 10.4 GPa. Munawar et al. [10] determined the cross-

sectional area of several natural fibers, including sisal, by measuring the average of five diameters, at angular intervals of 36° , obtained from a SEM micrograph. The variability in each measured diameter was very small, although it should be noted that the cross-section was close to circular. One would expect a higher degree of variability for irregularly shaped fibers, such as those shown in Fig. 2b. They performed their experiments in a Universal Testing Machine, and obtained an average tensile strength and modulus of 375 MPa and 9.1 GPa, respectively. d'Almeida et al. [14] investigated the tensile strength of piassava fiber. The actual area was measured at 5 different points along the gage length by using a micrometer. A mechanically driven machine, with 10 kN capacity, was used and the tensile strength and modulus, at a 25 mm gage length, were 147 MPa and 2 GPa, respectively (uncorrected for compliance of the load train). Gage lengths ranging from 15-150 mm were used, and the machine compliance computed. The corrected modulus was then reported as approximately 6 GPa for the 25 mm gage length.

The use of sisal fibers in high performance composites requires an understanding of the mechanical behavior of the fibers themselves. The review of the literature shows that there is a large discrepancy in reported tensile strength and Young's modulus of natural fibers. This may be due in part to uncertainties in the measurement of the fiber's cross-sectional area (due to the non-circular cross-section), as well as not using high resolution load and displacement measurement techniques. In this work we present a systematic study of the tensile and fracture behavior of the sisal fibers. These experiments were conducted on a state-of-the art micromechanical testing system ideally suited for fiber testing. Since the fiber cross-section is not perfectly circular and exhibits some variability, the cross-sectional areas for each fiber were measured using a field emission scanning electron microscope (FESEM), coupled with image analysis. This provided an accurate means of quantifying the cross-sectional area of the fibers. The variability in fiber strength was also quantified over various gage lengths. These set of experiments enabled us to subtract the contribution of the machine compliance, and to accurately determine the Young's modulus of the fibers. Finally, the variability of the fibers was quantified using Weibull statistics, and a relationship between fiber microstructure and strength is discussed.

2. Materials and Experimental Procedure

The sisal fibers used in this study were obtained from a farm located in the city of Valente in the northeast state of Bahia, Brazil. The fibers were extracted from its leaf by a mechanical process called decortication. In the process of decortication, the leaves are crushed by a rotating wheel with blunt knives, so that only the fibers remain. The decorticated fibers were washed before drying in the sun. Proper drying is important as fiber quality depends largely on reduced moisture content. Dry fibers were combed by a machine and sorted into various grades, largely on the basis of in-field separation of leaves into different size groups.

The as-received fibers were tested, in a natural dry condition, under tensile loading at four different gage lengths (GL): 10, 20, 30, and 40 mm. Testing was conducted on a microforce testing system (Tytron 250, MTS Systems, Minneapolis, MN) (see Fig. 4a). A steel “V” shaped mechanical clamping grip was used to grip the fibers (see Fig. 4b).

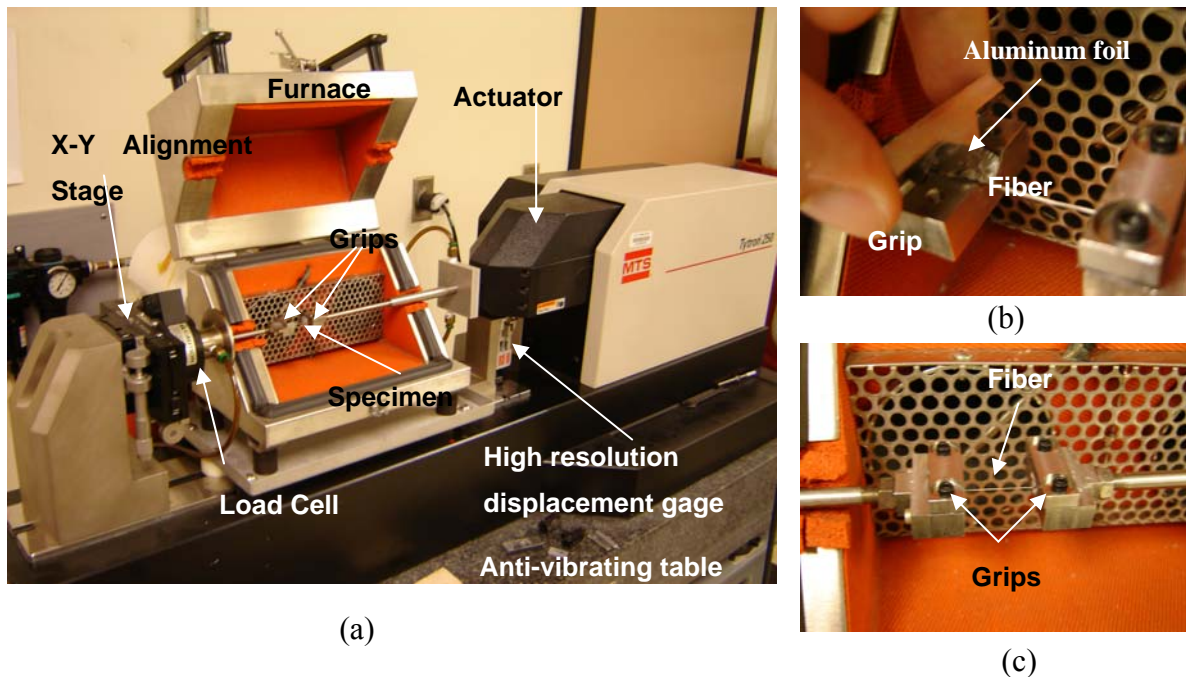


Fig. 4. Tytron microforce testing system used for the tensile test: (a) general view (b) and (c) detail of the grip and fiber.

A 250 N load cell was used to measured load. The displacement of the fiber was measured using a short-stroke transducer with a resolution of about 0.1 μm . Tensile tests were conducted in displacement control at a rate of 0.1 mm/min. This displacement rate corresponded to a nominal strain rate range, in the linear region of the stress-strain curve, of about 0.15 s^{-1} (GL = 40mm) to 0.6 s^{-1} (GL = 10mm). Strain rate effects were not observed in this range of strain rates. All testing was conducted at ambient temperature ($\sim 22^\circ\text{C}$) and a relative humidity of about 20%.

The compliance of the loading and gripping system was determined by obtaining the force versus displacement behavior of the fiber at various gage lengths following the methodology used by Chawla et al. [16]. The total cross-head displacement during fiber testing, δ_t , can be expressed by:

$$\frac{\delta_t}{F} = \left[\frac{1}{EA} \right] \ell + c \quad (1)$$

where c is the machine compliance, F is the applied force, E is the Young's modulus of the fiber, and A is the cross-sectional area of the fiber. Thus, a plot of δ_t/F versus gage length, ℓ , will yield a straight line of slope $1/(EA)$ and intercept c , the compliance of the load train.

The fiber's microstructure, before and after fracture, was investigated using a FESEM (Hitachi S-4700, Minato-ku, Tokyo, Japan). The FESEM was operated in secondary electron mode, under an accelerating voltage of 3-5 kV, and a working distance of 15 mm. The fibers were pre-coated with a thin layer of gold. In order to measure the fiber's cross-sectional area, for each tested fiber, an adjacent piece of the fiber (immediately next to the one tested) was kept for future measurement using the FESEM. To evaluate the variability of the cross section area through the length, a fiber with 40 mm was cut in four parts of 10 mm length and four micrographs were taken. The obtained images were post-processed using ImageJ (National Institutes of Health, Bethesda, Maryland), a Java-based image processing program. A contour line was drawn to delineate the fiber cross section (see Fig. 5) and the area was computed.

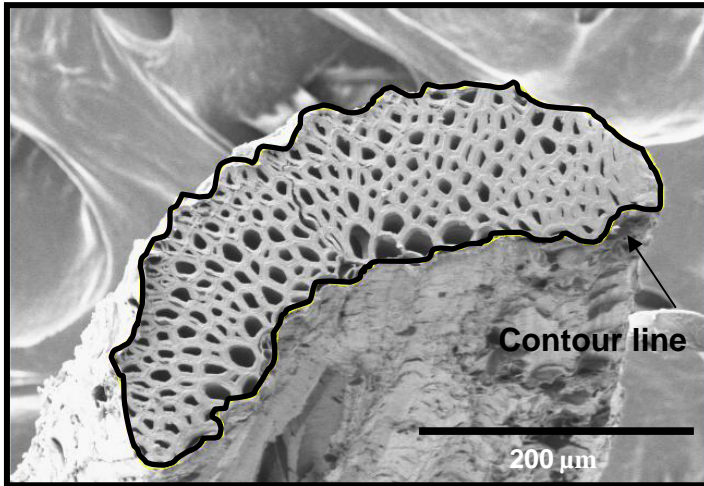


Fig. 5. Area calculation using ImageJ. The area was calculated as an integral of the whole cross-section of the fiber from a FESEM image. This included the lumens and the micro pores that exist inside the cell-walls.

3. Results and Discussion

A total of 15 fibers were randomly chosen from a given batch and tested at each gage length. The Young's modulus was calculated in the elastic portion of the stress-strain curve and then corrected for compliance by measuring force versus displacement, at various gage lengths, using Equation 1 (Fig. 6). These results are shown in Table 1.

Table 1. Summary of the tensile tests (displacement rate of 0.1 mm/min; strain rate ranged from 0.15 s⁻¹ to 0.16 s⁻¹).

Gage Length (mm)	Tensile Strength (MPa)	As-measured Young's Modulus (GPa)	Young's Modulus Corrected for Compliance (GPa)	Strain-to-Failure (%)	Weibull Modulus	Area (mm ²)
10	391 ± 89	10.7 ± 4.0	17.7 ± 9.4	5.2 ± 2.5	4.6	0.046 ± 0.008
20	392 ± 105	10.4 ± 3.0	13.7 ± 3.7	3.8 ± 1.1	3.7	0.050 ± 0.020
30	385 ± 99	14.8 ± 6.2	18.8 ± 7.5	2.8 ± 0.6	3.6	0.040 ± 0.004
40	400 ± 126	15.7 ± 6.0	19.0 ± 6.9	2.6 ± 0.8	3.0	0.046 ± 0.013

The gage length does not seem to influence the modulus of the fiber. The variability in modulus, for a given gage length, is likely due to the variability in the microstructure of the sisal fibers and possible damage that occurred during the extraction process. The current results are similar to those found in the literature, as seen in Table 2. Fig. 7 shows the “as-measured” versus corrected stress-strain response of the sisal fiber. At a given stress the contribution of the machine compliance resulted in larger displacements. It should also be noted that the calculation of the modulus from the corrected curve resulted in similar values compared to the modulus computed from the displacement/force versus gage length procedure. A non-linear region, following the initial portion of the stress-strain curve, was observed for some of the tested fibers. This behavior has been hypothesized to be due to a collapse of the weak primary cell walls and delaminate between fiber cells [8]. The strain-to-failure of the fibers decreased with increasing gage length. This behavior is related to the average size and distribution of flaws in the volume of the fiber and is described later in this section.

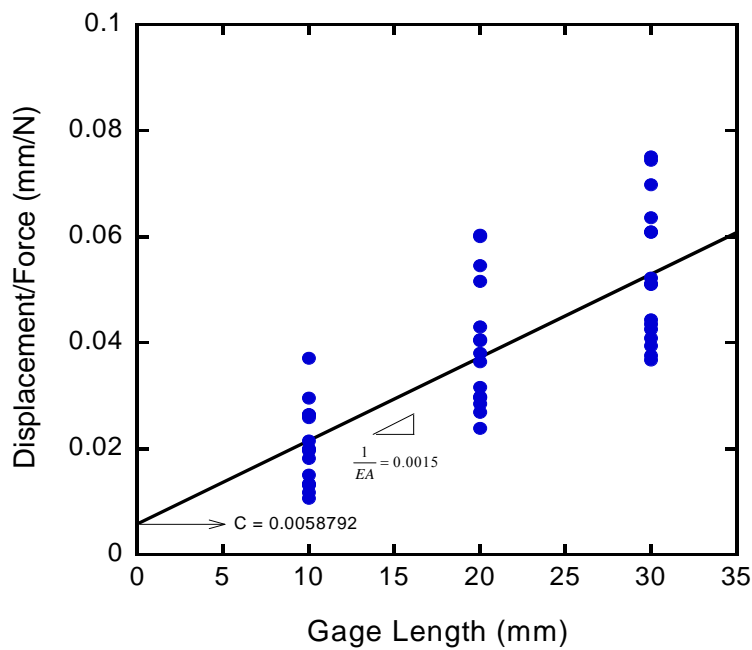


Fig. 6. Normalized displacement versus gage length plot that yields a linear relationship with slope $1/(EA)$, where E is the Young’s modulus and A is the cross-sectional area. The machine compliance, given by the intercept ($c=0.0058792$), was also determined from this plot.

As with the Young's modulus, the tensile strength of the fiber does not appear to be a function of the gage length, as shown in Table 1. Our results are in the range of those found in the literature. Table 2 shows a summary of studies that described their entire testing methodology. The Young's modulus varies between 9-19 GPa and the tensile strength from 347-577 MPa.

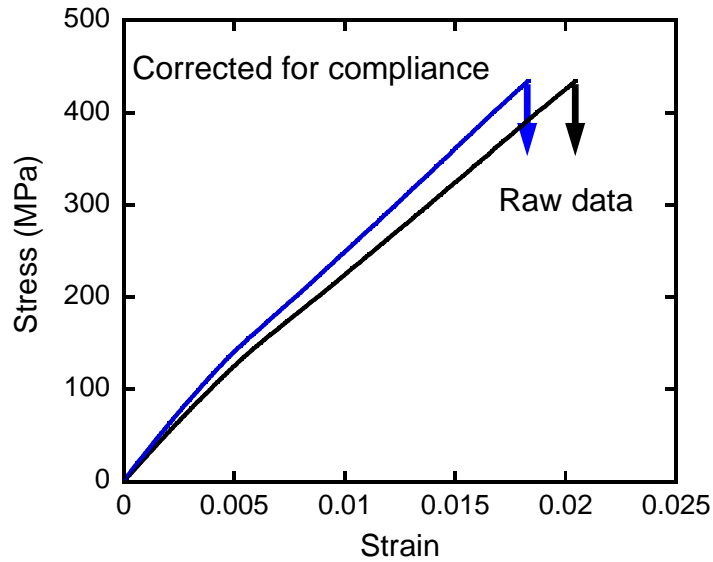


Fig. 7. Stress-strain behavior of a sisal fiber tested at a 30 mm gage length, showing the “as measured” data and that corrected for compliance.

As described in the introduction, this variability can be explained by three main factors: (i) test parameters/conditions, (ii) plant characteristics, and (iii) area measurements. The test parameters that could influence the results can be summarized as follows: Precision of the instrumentation, gage length, strain rate, type of grips, and compliance of the machine. Concerning the plant characteristics the mechanical behavior of the sisal fiber is dependent on its plant source, age, type of processing (mechanism of fiber extraction) as well as the fiber microstructure. For the studied sisal fiber the source and processing was discussed under Materials and Experimental process. The fiber microstructure presented in the introduction corresponds to that of the fiber used in the present investigation.

Table 2. Summary of literature values of the sisal fiber's tensile properties.

Gage length (mm)	Tensile strength (MPa)	Young's modulus (GPa)	Strain-to-Failure (%)	Cross head speed (mm/min)	Strain rate (s ⁻¹)	Reference
10	375	9.1	-	1	6	[10]
-	567	10.4	5.5	-	-	[11]
65	577	19.0	3.0	0.2	0.2	[12]
50	481	8.4	3.2-4.1	1	1.2	[8]
-	347	14.0	5	-	-	[13]

Some reports in the literature assume the fiber to be of circular cross-section. Since the sisal has an irregular cross section, simply measuring diameter at a given location will result in an erroneous measurement of the cross-sectional area of the fiber. We believe that the use of image analysis from an SEM micrograph to measure the area is a very precise method. Area measurements at four points, equally spaced, through a 40 mm sisal fiber resulted in values of 0.031, 0.033, 0.031, and 0.037 mm². Therefore, measuring the area at the end of the tested fiber resulted in more accurate determination of the average area.

Sisal fibers exhibited variability in tensile strength which is quite characteristic of natural fibers. This variability can be explained by distribution of defects within the fiber or on the fiber surface. Slight differences in microstructure associated with the different types of sisal fibers could also result in some variability. Weibull statistics were used to rank the relative fiber strength versus probability of failure of the fibers to obtain a measure of the variability in fiber strength [17-18]. According to the Weibull analysis, the probability of survival of a fiber at a stress, σ , is given by the following relation:

$$P(\sigma) = \exp \left[- \left(\frac{\sigma}{\sigma_0} \right)^m \right] \quad (2)$$

where σ is the fiber strength for a given probability of survival, and m is the Weibull modulus. σ_0 is defined as the characteristic strength, which corresponds to $P(\sigma) = 1/e = 0.37$. The higher the value of “ m ” the lower the variability in strength. Ranking of the fiber strengths is performed by using an estimator given by:

$$P(\sigma)_i = 1 - \frac{i}{N+1} \quad (3)$$

where $P(\sigma)_i$ is the probability of survival corresponding to the i th strength value and N is the total number of fibers tested. Substituting Equation (3) into Equation (2) yields:

$$\ln \ln \left[\frac{N+1}{N+1-i} \right] = m \ln \left(\frac{\sigma}{\sigma_0} \right) \quad (4)$$

Thus, a plot of $\ln \ln \left[\frac{N+1}{N+1-i} \right]$ versus $\ln \left(\frac{\sigma}{\sigma_0} \right)$ yields a straight line with slope of m .

The Weibull modulus values for the sisal fiber are in the same range of some synthetic fibers. For example, Chawla et al. [16] obtained a Weibull modulus of 4.6 for an aluminosilicate ceramic fiber (Nextel 312). Figure 8 shows the influence of gage length on the Weibull modulus “ m ”. Increasing gage length resulted in a decrease in the Weibull modulus. It can be seen from Fig. 8 that even though the curves have different slopes (e.g., different values of “ m ”) they all intercept at the same point (e.g., they have the same mean strength). According to Chawla [19], this behavior of different materials having the same mean strength but different Weibull modulus can be explained as follows. The mean defect size for all materials controls the mean strength, but the number of defects controls the Weibull modulus. Thus, while the fibers with a lower gage length have a smaller number of defects, the average defect size is the same as that of the other gage lengths. The question of why strength is not affected by gage length, while the ductility is affected by gage length, may now be explained as follows. The mean flaw size controls the strength, as described above. This mean flaw size does not change with gage length. Once a crack is formed at the largest flaw, how quickly the linkage between flaws occurs will determine the ductility. Thus, if a larger number of flaws exists, the linkage between flaws will be quicker, and the ductility lower (as observed in the highest gage length of 40 mm).

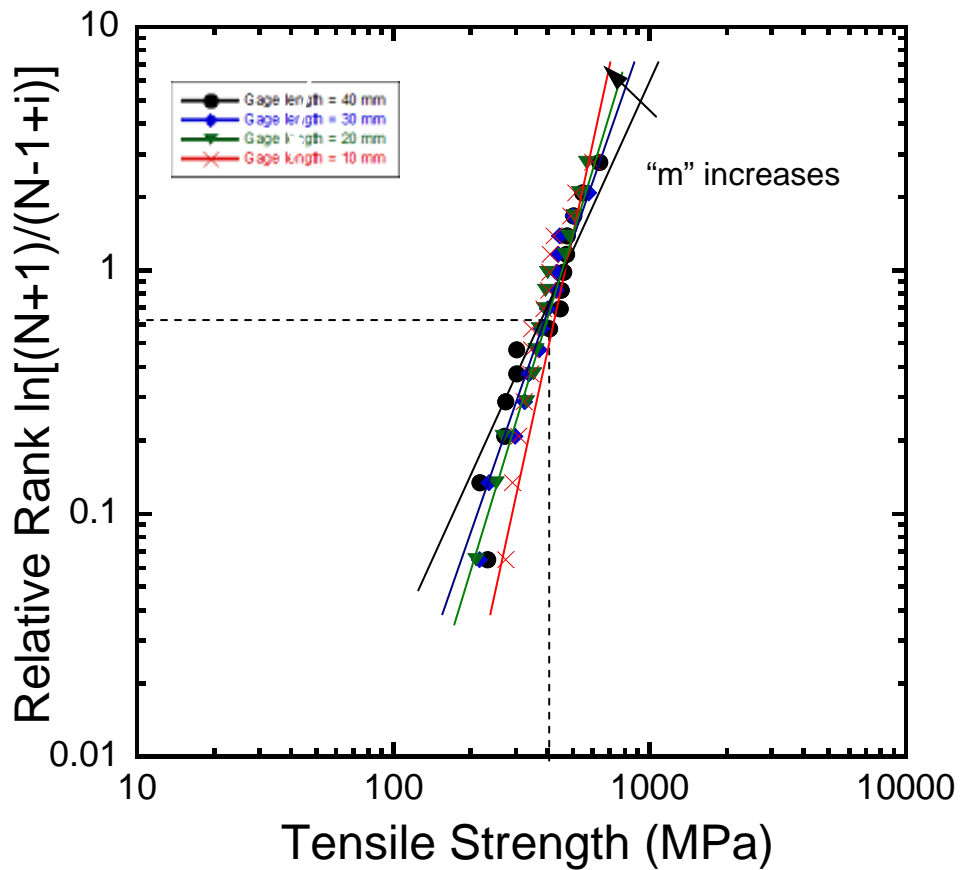


Fig. 8. Weibull distribution of the sisal fiber tensile strength for different gage lengths.

Examination of the fracture surfaces of the fiber, Fig. 9, shows that fiber fracture occurred by three different processes: (i) fracture of the fiber cells, (ii) delamination within the fiber cells, and (iii) delamination between fiber cells. Fig. 9 shows that the different fiber cells have fractured in different planes, possibly due to variability in strength of the individual fiber cells. The authors believe that the non-linear stress-strain portion prior to fracture is due to the delamination of one or more fiber-cells (see Fig. 9b) due to the weakening of the lignin and hemicellulose during the loading process. Delamination of the tertiary and primary wall is observed in the fiber cells in Fig. 9b and c, respectively. This process of delamination may occur before or after the fracture of the various fiber-cells and may contribute to the change in the slope of the stress-strain curve.

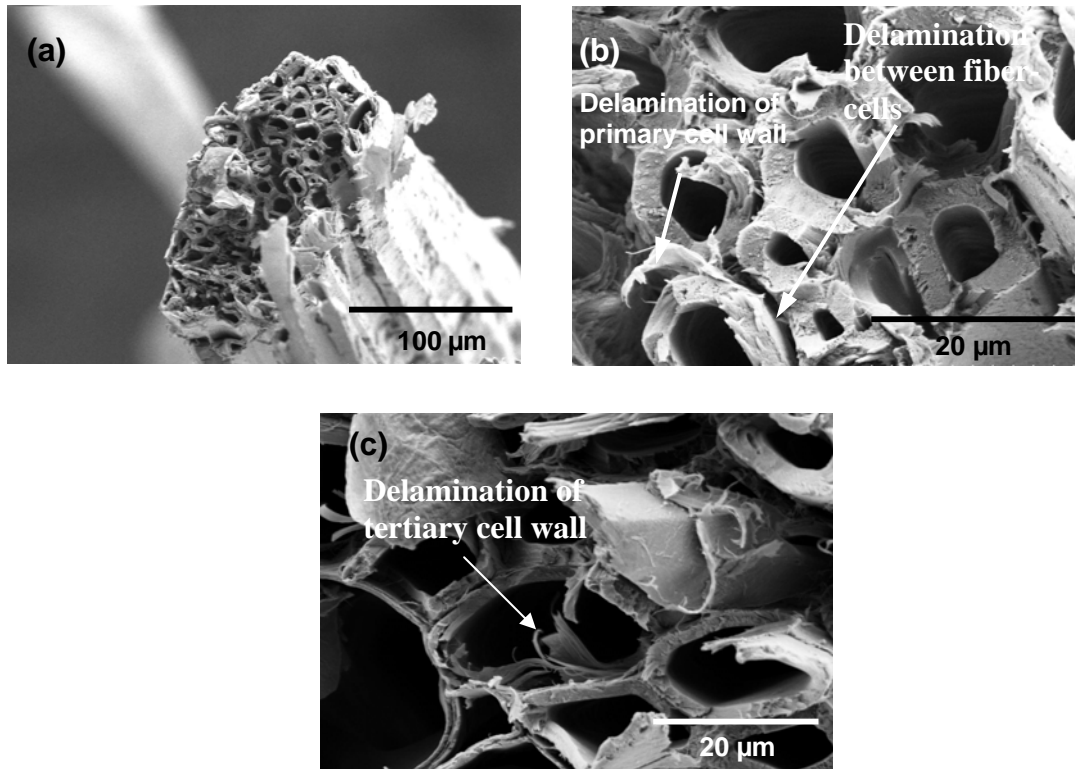


Fig. 9. Fractography of the sisal fibers: (a) overall view, (b) and (c) details of fiber cell fracture, fiber cell and fiber cell/wall delamination.

4. Conclusions

We have investigated the monotonic tensile behavior of high performance sisal fibers. The following conclusions can be drawn from this work:

- Mechanical testing of small diameter fibers is not trivial. The irregular area of the fibers needs to be considered, as well as the contribution of compliance of the load train. High resolution measurement of load and displacement is also very important in obtaining accurate values of Young's modulus, strength, and strain-to-failure.
- The Young's modulus of sisal fibers, corrected for machine compliance, was around 18 GPa. The modulus was not influenced by the gage length.

- The strain-to-failure decreased from approximately 5.2 % to 2.6 % when the gage length was increased from 10 mm to 40 mm. The tensile strength, on the other hand, was found to be independent of the gage length. The Weibull modulus decreased from 4.6 to 3.0 when the gage length was increased from 10 mm to 40 mm, respectively. This can be explained by the fact that the average flaw size is independent of gage length, but that the number of flaws increases with increasing volume. Thus, while average flaw size controls strength, the number of flaws may play a more important role in controlling the strain-to-failure, since the linking of cracks at flaws determines the strain-to-failure. It follows that at larger gage lengths, the linking of flaws is easier, because of the larger number of flaws.
- The fracture mode of the sisal fiber was studied using SEM. Both delamination of the primary and tertiary wall (within the fiber cell) and delamination between fiber cells was observed. This delamination between fiber cells likely resulted in the small non-linear region, in the stress-strain curve, prior to failure of the fiber. Fracture of the individual fiber-cells, at different planes, was also observed.

Acknowledgements

The authors gratefully acknowledge the Conselho Nacional de Desenvolvimento Científico e Tecnológico, CNPq, (Brazilian National Science Foundation), for partial financial support for this work. We also thank Dr. Jason Williams from ASU for assistance with SEM and tensile testing.

References

- [1] Silva FA, Toledo Filho RD. Sisal Fiber Reinforcement of Durable Thin Walled Structures – A New Perspective. In: Proceedings of International Workshop on Cement Based Materials & Civil Infrastructure, Karachi, Pakistan, 2007, p. 575-586.
- [2] Oksman K, Wallstrom L, Toledo Filho RD. Morphology and mechanical properties of unidirectional sisal-epoxy composites. *Journal of Applied Polymer Science* 2002; 84(13): 2358-2365.

- [3] Gram HE. Durability of natural fibers in concrete. Swedish Cement and Concrete Research Institute, Research Fo. 1983, p. 225.
- [4] Bisanda ETN, Ansell MP. Properties of sisal-CNSL composites. *Journal of Materials Science* 1992; 27:1690-1700.
- [5] Toledo Filho RD, Ghavami K, England GL, Scrivener K. Development of vegetable fiber-mortar composites of improved durability, *Cement & Concrete Composites* 2003; 25: 185-196.
- [6] Toledo Filho RD, England GL, Scrivener K, Ghavami K. Durability of alkali-sensivite sisal and coconut fibers in cement mortar composites, *Cement & concrete composites* 2000; 22: 127-143.
- [7] Towo AN, Ansell MP. Fatigue of sisal fiber reinforced composites: constant life diagrams and histeresis loop capture. *Composites Science and Technology* 2008; 68: 915-924.
- [8] Murherjee PS, Satyanarayana KG. Structure properties of some vegetable fibers, part 1. Sisal fibre. *Journal of Materials Science* 1984; 19:3925-34.
- [9] Nutman FJ. Agave fibres Pt. I. Morphology, histology, length and fineness; frading problems. *Empire Journal of Experimental Agriculture* 1936; 5(75) 75-95.
- [10] Munawar SS, Umemura K, and Kawai S. Characterization of the morphological, physical, and mechanical properties of seven nonwood plant fiber bundles. *J. Wood Sci.* 2007;53:108–113.
- [11] Rao KMM, Rao KM. Extraction and tensile properties of natural fibers: vakka, date and bamboo. *Composite Structures* 2007; 77: 288-295.
- [12] Toledo Filho RD, Natural fiber reinforced mortar composites: experimental characterization. Ph.D. Thesis, PUC-Rio, Brazil, Department of Civil Engineering, 1997.
- [13] Bessell TJ, Mutuli SM. The interfacial bond strength of sisal-cement composites using a tensile test. *Journal of Materials Science Letters* 1982;1:244-6.
- [14] d’Almeida JRM, Aquino RCMP, Monteiro SN. Tensile Mechanical Properties, morphological aspects and chemical characterization of Piassava (*Attalea funifera*) Fibers. *Composites Part A: applied science and manufacturing* 2006; 37: 1473-1479.

- [15] Kerr M, Chawla N, Chawla KK. The Cyclic Fatigue of High Performance Fibers. JOM, 2005, p. 67-70.
- [16] Chawla N, Kerr M, Chawla KK. Monotonic and Cyclic Fatigue Behavior of High-Performance Ceramic Fibers. Journal of American Ceramic Society 2005; 88: 101-108.
- [17] Chawla KK., Fibrous Materials. Cambridge University Press, Cambridge, 1998.
- [18] Weibull W. A Statistical Distribution Function of Wide Applicability. J. Appl. Mech 1951; 18: 293.
- [19] Chawla KK. Ceramic Matrix Composites. Chapman & Hall, London, 1993.

ARTIGO B - Silva F.A., Chawla N. and Toledo Filho R.D. An Experimental Investigation of the fatigue behavior of sisal fibers. Materials Science and Engineering A, in press, 2009.

An Experimental Investigation of the Fatigue Behavior of Sisal Fibers

Flávio de Andrade Silva^a, Nikhilesh Chawla^b, and Romildo Dias de Toledo Filho^a

^aCivil Engineering Department, COPPE, Universidade Federal do Rio de Janeiro, P.O.
Box 68506, CEP 21941-972, Rio de Janeiro – RJ, Brazil.

^bSchool of Materials, Fulton School of Engineering, Arizona State University, Tempe,
AZ 85287-8706

Materials Science and Engineering A

2009

Abstract

The tensile fatigue behavior of individual sisal fibers was investigated. The fatigue behavior was examined in terms of the stress versus cycles and stress-strain hysteresis behavior of the fibers. Fibers were tested at stress-levels ranging between 80 to 400 MPa. The sisal fibers did not fatigue below a maximum fatigue level of 320 MPa. The stress-versus cycles curve was normalized by dividing the maximum fatigue stress over the ultimate tensile strength of each individual tested fiber and it was found that below a ratio of 0.5 there was no fiber failure below 10^6 cycles. Monotonic tensile testing was performed for fibers that survived 10^6 tests to determine its residual strength. There was no observed loss in strength, but an increase in Young's modulus was observed with increasing fatigue stress. The mechanisms for increase in modulus as well as microstructural degradation mechanisms after fatigue were investigated and are discussed.

Keywords: A. Natural fibers; Sisal; B. Fatigue; D. Fractography; SEM.

1. Introduction

Sisal fibers extracted from sisal plant leaves in the form of long fiber bundles have been used extensively as ropes and twines [1]. After cotton, these fibers have the second highest volume of production, among natural fibers. Sisal fiber has also been used as reinforcement for composite materials due to its high strength, durability, and strain-to-failure [2-5]. Some automotive components have already been produced using polymer matrix composites reinforced with sisal fibers [2]. Door trim panels made from thermoplastic polymer reinforced by vegetable fibers are being commercially produced and used by companies such as Volkswagen-Audi and OPEL-GM among others [3]. Silva et al. [4,5] have recently used long sisal fibers to reinforce durable cement composites. These composites exhibited tensile strengths comparable to those of polypropylene, polyethylene, and glass fabric reinforced cement composites [6]. If compared to synthetic fibers such as carbon, glass, and aramid, natural fibers present numerous advantages. They are biodegradable, renewable, recyclable, do not present any health risk, consume very low energy, can be produced with low investment at low cost, and CO_2 is used while oxygen is given back to the environment.

While the mechanical behavior of natural fiber reinforced composites has been examined [2-5], little attention has been paid to the deformation behavior of the fibers themselves. Natural fibers such as sisal [7], piassava [8], coir [9], caroa [10], curaua [11] have been characterized through monotonic tensile tests. A fair amount of scatter in ultimate tensile and Young's modulus is observed. This is due to the different approaches in measuring the cross-sectional area and to the fact that, in some cases, the machine and grip compliance is not accounted for in the calculation of the modulus. In addition to the tensile behavior, the fatigue behavior of composites is of great importance since they will be subjected by cyclic loads in a variety of applications. Furthermore, the behavior of the fibers themselves, under fatigue loading, can control the fatigue behavior of the composite. A reasonable amount of work on the cyclic behavior of synthetic fibers has been conducted [12-17]. Bunsell et al. have performed fatigue tests on aramid [14] and carbon fibers [16]. They found that no noticeable fatigue damage seems to occur in carbon fibers at room temperature and that the failure of the aramid fiber under cyclic conditions may be induced by a combination of creep and fatigue mechanisms. Limited work on the fatigue behavior of natural fibers has been conducted on wood pulp [18,19] and cotton [20]. Hkarlk and Sparrow [20] investigated the fatigue behavior of cotton fibers and observed that the cotton fiber fractured due to splitting of the fibrils. This behavior was also noticed under static tension but the degree of splitting was greater in fatigue. More recently, Hamad investigated the fatigue behavior of wood-pulp fibers [19]. The described damage mechanisms included delamination of fiber layers and peeling off of external walls after the formation of microcracks.

In this paper we investigate the stress versus cycles fatigue behavior of single sisal fibers. The tensile behavior of these fibers is reported elsewhere [7]. Sisal fibers were subjected to tensile fatigue load with maximum stresses ranging from 80 to 400 MPa at a frequency of 2 Hz. The fatigue tests were stopped either at 10^6 cycles or complete failure of the fiber, whichever occurred first. Fibers that survived 10^6 cycles were tested under monotonic tension to establish the residual strength of the fiber. Field emission scanning electron microscopy (FESEM) was used to study the fatigue fracture mechanisms.

2. Materials and Experimental Procedure

The sisal fibers used in this study were obtained from a farm located in the city of Valente in the northeast state of Bahia, Brazil. The fibers were extracted from its leaf by a mechanical process called decortication. Figure 1a shows a micrograph of the sisal fiber. The sisal fiber has a hierarchical structure.

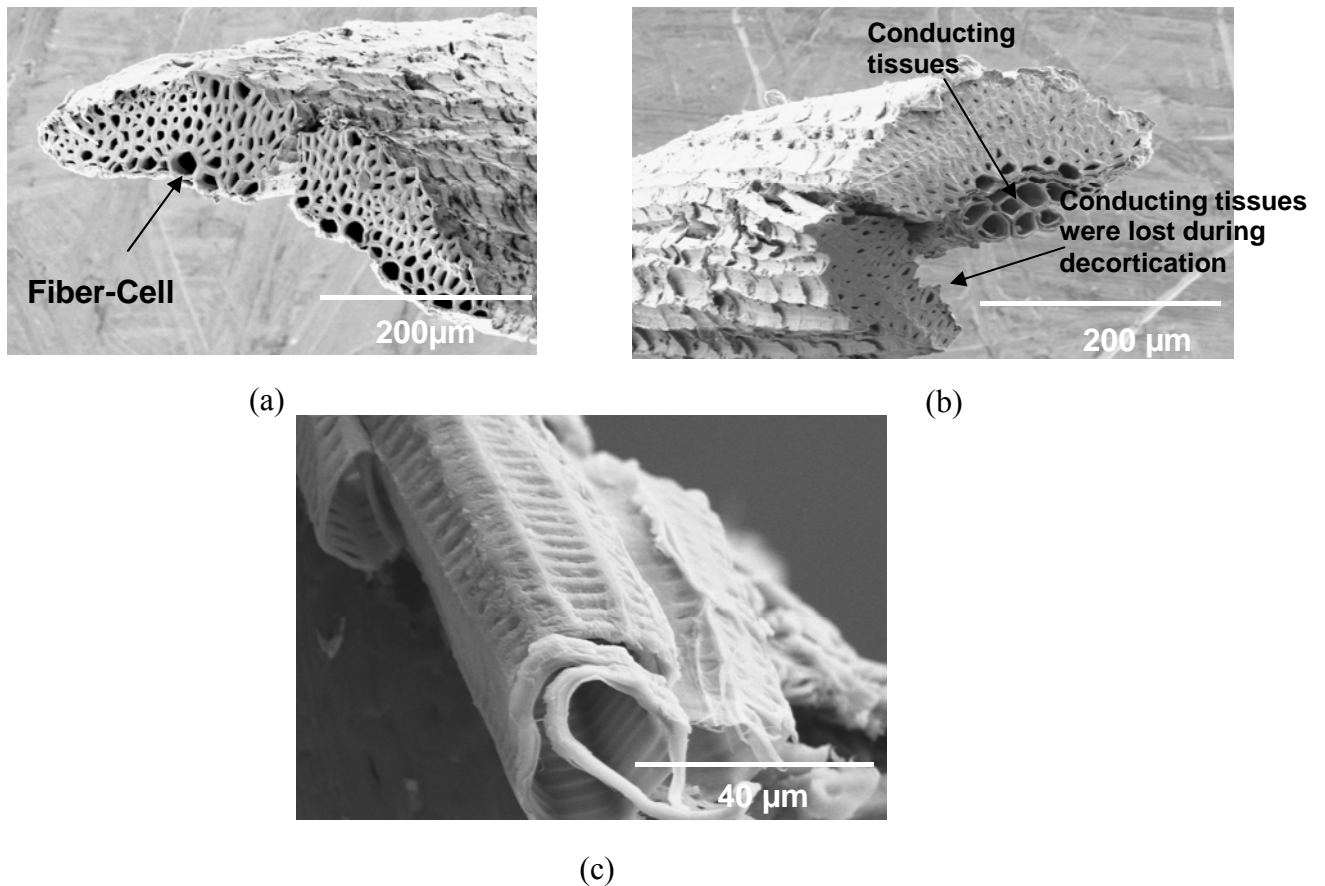


Figure 1. Various types of sisal fiber: (a) structural fiber, (b) arch fiber with conducting tissues, and (c) conducting tissue.

Every fiber contains numerous elongated individual fibers, or fiber-cells, which are about 6 to 30 μm in diameter. Each fiber-cell is made up of four main parts, namely the primary wall, the thick secondary wall, the tertiary wall, and the lumen [7]. The fiber-cells are linked together by means of the middle lamellae (ML), which consist of hemicellulose and lignin. The walls consist of several layers of fibrillar structure consisting of fibrillae which are linked together by lignin. The fibrillae are, in turn, built of micro-fibrillae with a thickness of about 20 nm. The microfibrillae are composed of cellulose chains with a thickness of around 0.7 nm and a length of a few μm and are

linked together by means of hemicellulose [21]. Three different types of fibers can be found: structural, arch, and xylem fibers [7]. The arch fibers grow in association with the conducting tissues of the plant (see Figure 1b). A micrograph of a conducting tissue, which itself is a fiber-cell, is shown in Figure 1c. We believe that the strength of the conducting tissue is lower in comparison to the conventional fiber-cells because they are invariably broken during the decortication process. It can be seen their structure is also quite different, see Figure 1.

The as-received fibers were tested, in a natural dry condition, under tensile fatigue loading at a stress ratio (R ratio = $\sigma_{\min}/\sigma_{\max}$) of 0.2 and frequency of 2 Hz. Testing was conducted on a microforce testing system (Tytron 250, MTS Systems, Minneapolis, MN) under force control. Figure 2 shows a typical sinusoidal waveform of force versus time measured from the microforce testing system. Note the high accuracy and control of the applied loading.

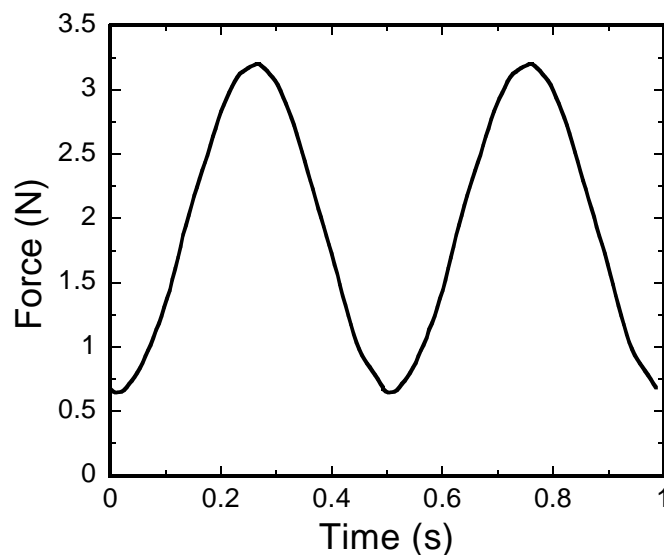


Figure 2. Force vs. time plot, from the Tytron 250 system, during fatigue of a single Sisal fiber showing the high accuracy and control of the applied loading.

All tested fibers, including those that failed on loading, are included in the data set, i.e., no screening of fibers was conducted. The experiment was conducted in fibers with a 20 mm gage length at five different stress levels: 80, 160, 240, 320 and 400 MPa. The tests were stopped after 10^6 cycles or after fiber failure, whichever occurred first. A steel “V” shaped mechanical clamping grip was used to grip the fibers and a 25 N load cell was used to measure the load. All testing was conducted at ambient temperature (~ 22 °C) and relative humidity of about 20%.

The fiber's microstructure, before and after fracture, was investigated using a field emission scanning electron microscope (FESEM, Hitachi S-4700, Minato-ku, Tokyo, Japan). The FESEM was operated in secondary electron mode, under an accelerating voltage of 3-5 kV, and a working distance of 15 mm. The fibers were pre-coated with a thin layer of gold. In order to measure the fiber's cross-sectional area, for each tested fiber, an adjacent piece of the fiber (immediately next to the one tested) was measured using the FESEM. The cross-sectional area of the fibers was determined as follows. Images obtained were post-processed using ImageJ (National Institutes of Health, Bethesda, Maryland), a Java-based image processing program. A contour line was drawn to delineate the fiber cross section and the area was computed. This computed area was used to calculate the load required for each individual fiber in order to apply stress levels ranging from 80 to 400 MPa.

3. Results and Discussion

We first present the stress versus cycles data. This is followed by an analysis of the Young's modulus and proportional limit stress of fibers that exhibited fatigue runout. Finally we show stress-strain hysteresis information, followed by fatigue fractography. Figure 3 shows the stress versus cycles behavior of the sisal fibers tested at various maximum stresses (80 MPa-400 MPa).

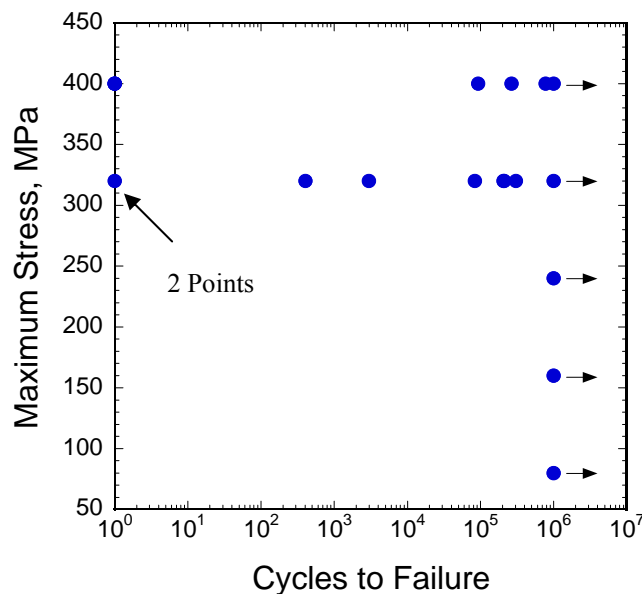


Figure 3. Stress versus cycles fatigue curve for sisal fibers subjected to maximum stress levels ranging from 80 to 400 MPa at constant R ratio of 0.2. Fatigue runout was taken at 10⁶ cycles.

It can be seen that below a maximum stress level of 320 MPa all the fibers have survived 10^6 cycles. Above 320 MPa there was a significant spread of data. This is due to the fact that the monotonic tensile strength of the sisal fiber varies from 300 to 500 MPa [7]. Because of this behavior it was decided to test, under monotonic tension, the individual fibers adjacent to the ones tested under fatigue. Figure 3 was then re-plotted by normalizing the maximum fatigue stress level by the individual monotonic tensile strength (see Figure 4). This new plot shows that when the maximum monotonic stress is close to the maximum applied stress, the fibers failed at the 1st cycle or below 1000 cycles. When the ratio between maximum applied fatigue stress and ultimate tensile stress (UTS) ranges from 0.5 to 0.8, fibers failed between 3000 to 10^6 cycles, while below 0.5 all the fibers survived 10^6 cycles.

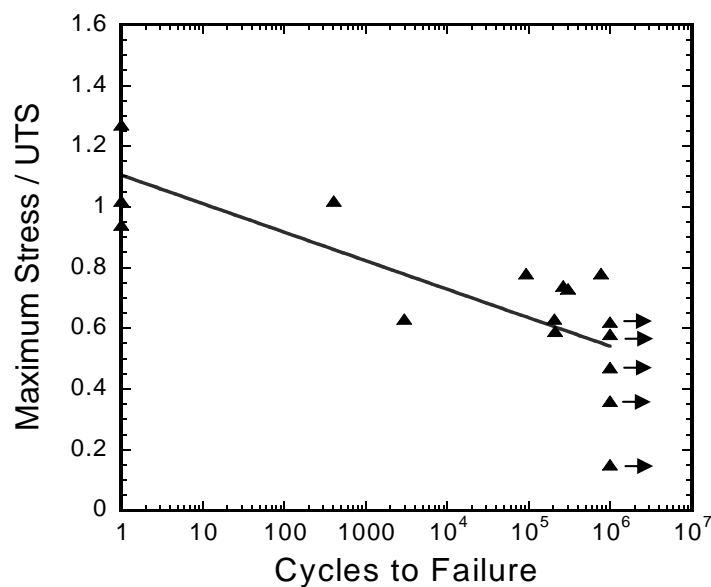


Figure 4. Normalized stress versus cycles curve. The maximum stress was normalized by the fiber ultimate tensile strength (UTS) of the fibers. Note that normalizing by UTS the S-N curve decreases with decreasing stress.

All sisal fibers that survived 10^6 cycles were tested under monotonic tensile load. Figure 5 shows the stress-strain curves for these experiments. It can be seen that the cycles did not affect the UTS of the fibers. Actually all of these fibers had an UTS superior than those obtained for average UTS in our previous work [7]. Bunsell and Somer reported that a carbon fiber which survived 3×10^7 cycles (max load = 9.2 g or 0.0902 N; 98% of

the UTS) failed in tension at 9.4g (0.0921 N) [16]. In a similar way the sisal fiber that was cycled at 400 MPa (100% of the average UTS) had a post-fatigue UTS of 690 MPa.

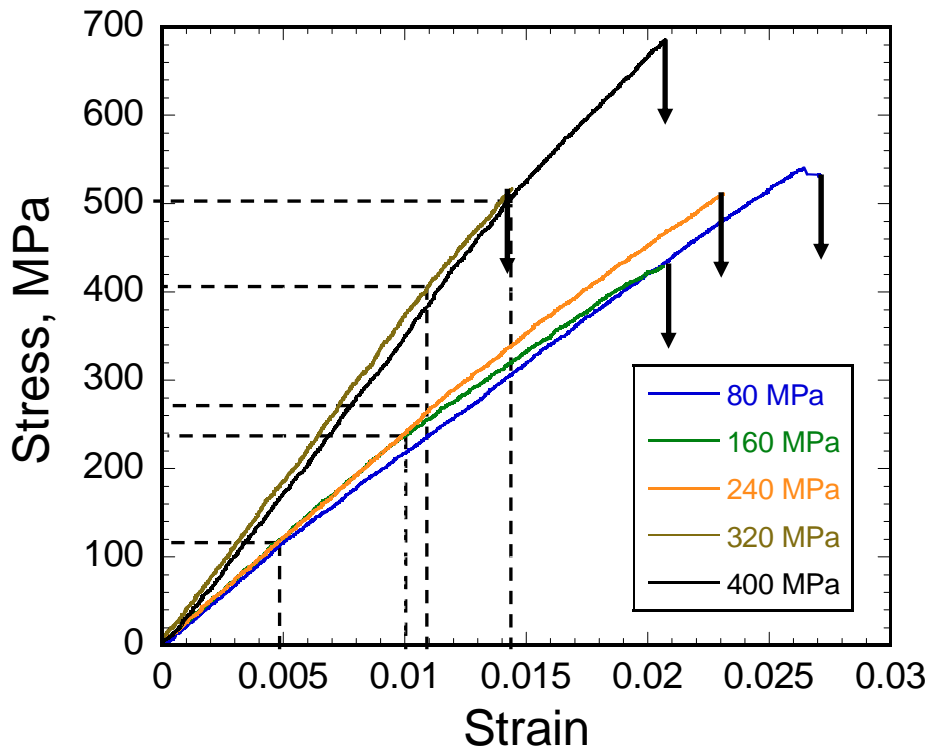


Figure 5. Monotonic tensile behavior of fibers that have survived 10^6 cycles. The dotted lines show the proportional limit stress (σ_{pl}).

The proportional limit stress (σ_{pl}) also increased with increasing fatigue stress. This points to an interesting correlation between the maximum fatigue stress and σ_{pl} . An increase in Young's modulus with fatigue stress was also observed. Figure 6 illustrates this behavior. This plot shows the trend of increase in modulus and σ_{pl} with increasing fatigue stress. Bunsell and Somer [16] also reported a slightly increase in modulus with the cycles in carbon fibers which was suggested by an improvement in alignment of the layered graphitic structure. As explained in the section 2 the sisal fiber presents a hierarchical structure. The walls of the fiber cells are formed by fibrillar structures consisting of fibrillae linked together by lignin. The fibrillae are arranged in spirals with a certain angle to the longitudinal axis and built up of micro-fibrillae which is composed by cellulose molecular chains. Some degree of alignment of the cellulose molecular chains in the sisal fiber seems to be taking place, which would explain the increase in Young's modulus. The increase in σ_{pl} can be explained by the damage level induced

during fatigue. In the post-fatigue tensile test, the new limit for permanent deformation, σ_{pl} , is dictated by the prior level of fatigue damage.

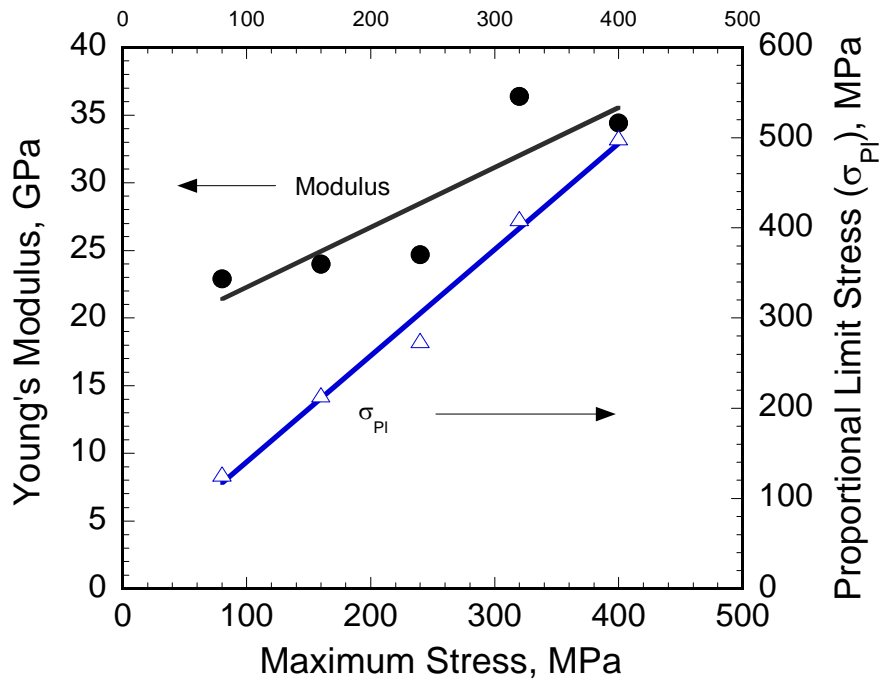
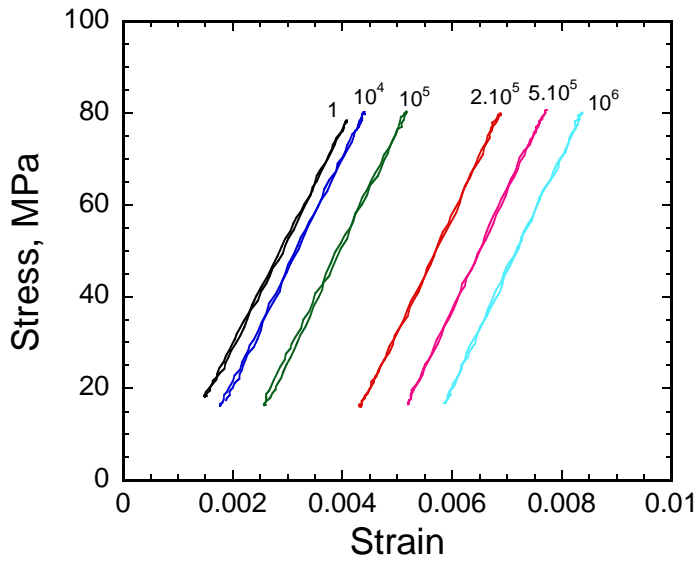
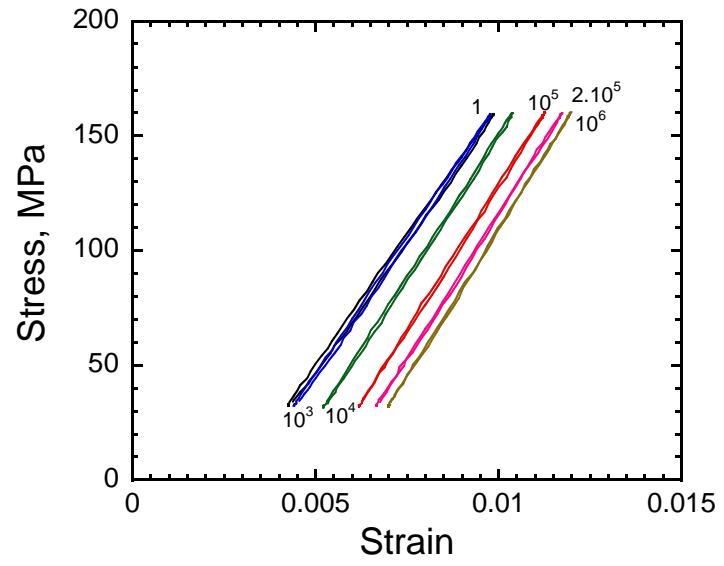


Figure 6. Relationship between Young's modulus and proportional limit stress vs. maximum applied stress for samples that survived 10^6 cycles and were tested under monotonic tension. The modulus and proportional limit stress increase with fatigue stress.

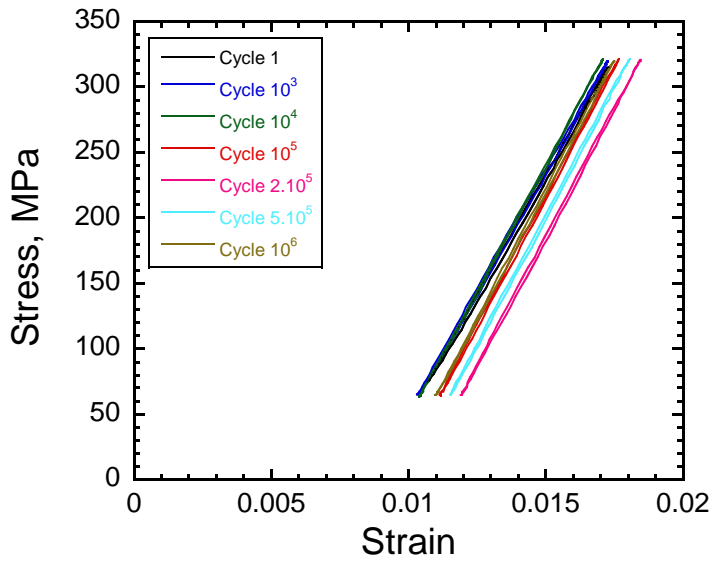
To understand the evolution of damage, stress-strain hysteresis measurements were conducted at various stress levels, these are shown in Figure 7. These plots were obtained from fibers that survived 10^6 cycles at maximum stress levels ranging from 80 to 400 MPa. The Young's modulus was computed from the unloading portion of the cycle for the first and last cycle. A slightly increase in modulus was observed from the 1st to the last cycle, but a more considerable increase was measured with increasing fatigue stress levels (see Figure 8). This same trend was observed when computing the modulus from monotonic tension tests in fibers that survived 10^6 cycles. The thickness of the individual hysteresis loops, a measure of inelastic damage or energy during a given cycle, was not significant. Averett et al. [22] observed a decrease both in hysteresis loop width and modulus on Nylon. This lower modulus was explained as a temporary rupture of hydrogen bonds and does not represent a permanent decrease in modulus.



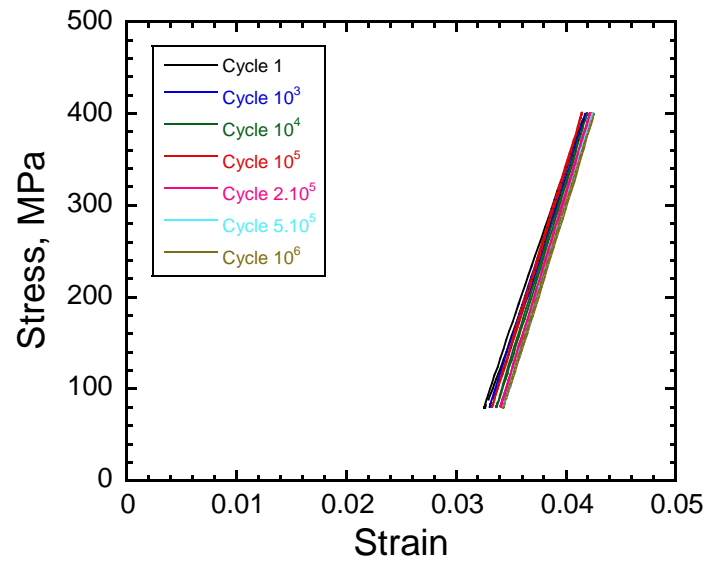
(a)



(b)



(c)



(d)

Figure 7. Effect of maximum stress level on the stress-strain response of sisal fibers during fatigue cycles: (a) 80 MPa (b) 160 MPa (c) 320 MPa and (d) 400 MPa. Very little hysteresis is observed, although an increase in modulus with cycles is measurable.

It can be seen from the stress-strain hysteresis loop in Figure 7 that by increasing the number of cycles the permanent strain also increases. This damage increases when increasing the maximum fatigue stress levels.

The fracture surfaces of the fibers were examined to better understand the underlying damage mechanisms during fatigue. It can be seen that alignment of the micro-fibrillae structure that compose the fiber-cell walls takes place during fatigue (see Figure 9). This alignment that occurs during the cycles appears to be responsible for the increase in Young's modulus. A similar behavior has been reported for carbon fibers, although the alignment in those fibers is due to the graphitic plates [16]. The cyclic fracture surface is also quite different from what we observed in pure tension [7]. The monotonic tensile fracture of the sisal fiber was characterized by fracture of the fiber cells, delamination within the fiber cells, and delamination between fiber cells. Different fiber cells can fracture in different planes, possibly due to variability in strength of the individual fiber cells. No alignment in the fibrillar structure was observed during tensile testing as was observed for the cyclic tests.

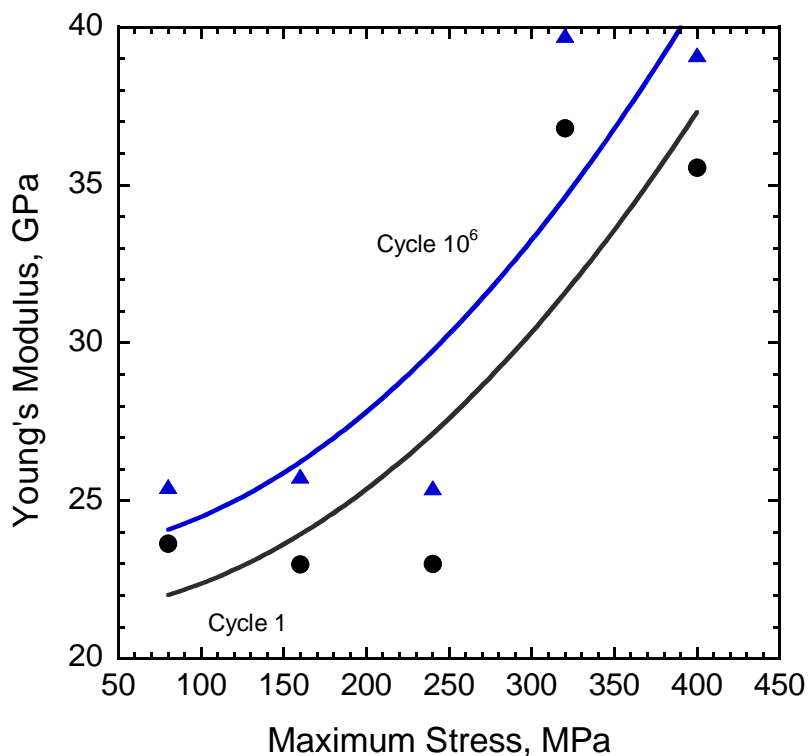


Figure 8. Effect of the maximum fatigue stress on the Young's modulus. The modulus increases due to alignment of the fibrillar structure during fatigue.

To understand the micro damage mechanisms due to fatigue it's important to elucidate the particular morphological phenomena involved. Three main micro-damage mechanisms were observed under fatigue loading: (i) The change in volume and, thus, a re-shaping of the fiber cells. From Figure 9 and 10 it can be seen that after fatigue the fiber-cells have more of an oval shape than a more circular shape which was observed in non-tested fibers and fibers tested under monotonic tension; (ii) formation of microcracks perpendicular to the load in the secondary wall, followed by subsequent propagation to the middle lamellae and delamination between adjacent fiber-cells, and pelling off of the external cell wall layers (see Figure 10); (iii) mechanical degradation of the cellulosic fibrillar structure with increasing number of cycles resulting in a weakening in the link between lignin, hemicellulose and these structural systems. This leads to a removal of parts in the secondary layer resulting in a complete failure of the fiber (see Figure 11).

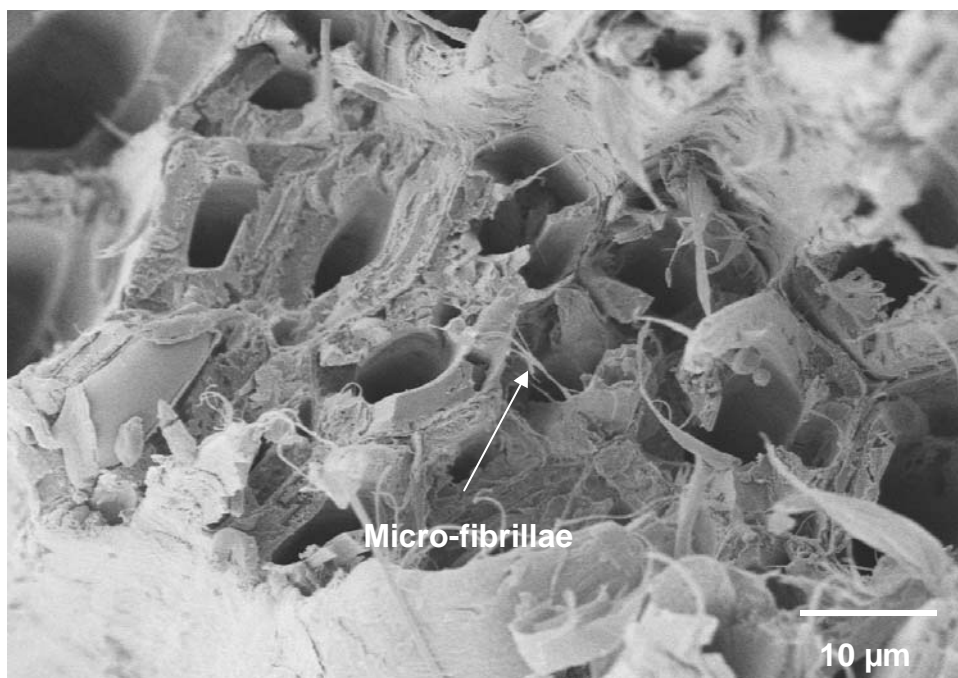


Figure 9. Fatigue fracture surface showing alignment of the fibrillar structure (nanofibers) that compose the fiber-cell walls.

The formation of microcracks and posteriori propagation leading to delamination and pelling off mechanisms have also been reported by Hamad [19] for wood pulp. The authors stated that the strength of the filamentary fiber are largely dictated by the

strength of the cellulosic fibrillar structure. Once the latter becomes structurally degraded, the amorphous hemicellulose and lignin (that act as a matrix) can no longer hold the layers of the laminated tube together. For cotton fibers it was described by Hkarlk and Sparrow [20] that the failure mechanisms were due to fibril splitting, which was no different from that observed in monotonic tensile load.

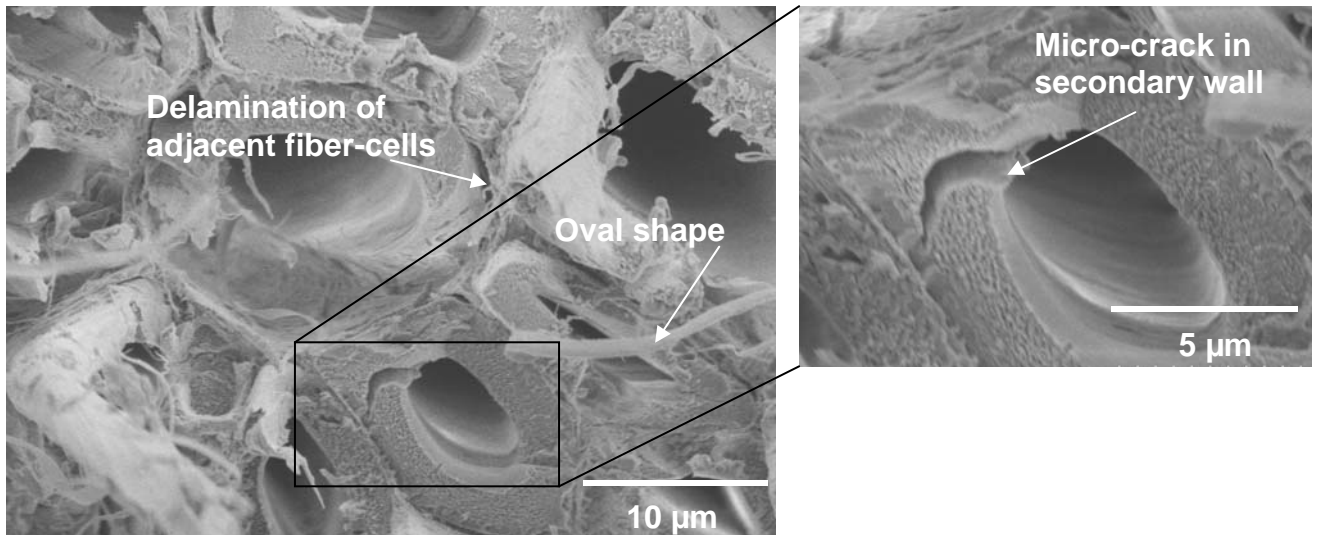


Figure 10. Fatigue fracture surface showing the formation of microcracks in the secondary wall and propagation to the middle lamellae.

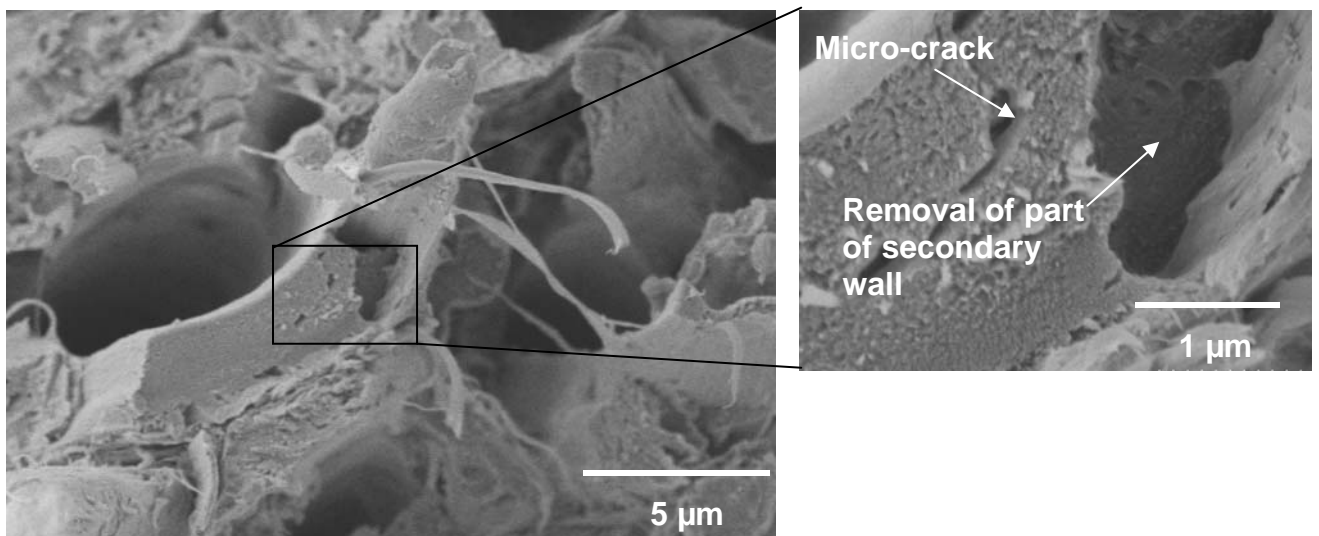


Figure 11. Fatigue fracture surface showing the formation of microcracks in the secondary wall and removal of part of the secondary wall material.

4. Conclusions

The tensile fatigue behavior of sisal fibers has been investigated. The following conclusions can be drawn from this work:

- Fibers subjected to a ratio of maximum applied fatigue stress to ultimate tensile strength of 0.5 have survived 10^6 cycles. Sisal fibers failed in fatigue when the ratios ranged between 0.6 to 0.8, and fatigue lives of between 10^3 and 10^6 cycles, respectively.
- Monotonic tensile tests was performed on fibers that survived 10^6 cycles. An increase in the Young's modulus was observed with an increase in the maximum fatigue stress. In additional, the proportional limit stress, σ_{pl} , also increased with maximum fatigue stress. This can be attributed to an alignment of the fibrillar structure of the fiber during fatigue at these intermediate stresses.
- No significant stress-strain hysteresis was observed during fatigue, although an increase in Young's modulus with the increase of maximum fatigue stress was detected.
- Fractographic analysis after fatigue shed light on three main fatigue micro-damage mechanisms: (a) a change in volume and therefore the shape of the fiber cells, (b) formation of micro-cracks perpendicular to the load in the secondary wall of the cells, with subsequent propagation to the middle lamellae causing delamination between adjacent fiber-cells and pelling of the external cell wall layers, and (c) mechanical degradation of the cellulosic fibrillar structure with an increasing number of fatigue cycles.

Acknowledgements

The authors gratefully acknowledge the Conselho Nacional de Desenvolvimento Científico e Tecnológico, CNPq, (Brazilian National Science Foundation), for partial financial support for this work. We also thank Dr. Jason Williams, ASU, for assistance with SEM and fatigue testing.

References

- [1] O.R.R.F Silva and N.E.M. Beltrão (Edited), *O agronegócio do sisal no Brasil*, first ed., EMBRAPA, Brasília, 1999. (in Portuguese).
- [2] H. Larbig, H. Scherzer, B. Dahlke, R. Poltrock, *J. Cell. Plast.* 34 (1998) 361–79.
- [3] A. Magurno, *Die Angewandte Makromolekulare Chemie* 272 (1999) 99–107.
- [4] F. A. Silva, B. Mobasher, R.D. Toledo Filho. Recent Advances in High Performance Natural (Sisal) Fiber Cement Composites. In: *Seventh International Rilem Symposium on Fibre Reinforced Concrete: Design and Applications (BEFIB 2008)*, Chennai. Rilem Publications S.A.R.L., (2008), p. 105-113.
- [5] R.D. Toledo Filho, F.A. Silva, E.M.R. Fairbairn, J.A. Melo Filho, *Constr. Build. Mater.* (2008), doi:10.1016/j.conbuildmat.2008.10.012.
- [6] B. Mobasher, J. Pahilajani, A. Peled, *Cem. Concr. Compos.* 28 (2006) 77-89.
- [7] F.A. Silva, N. Chawla, R.D. Toledo Filho, *Compos. Sci. and Tech.* 68 (2008) 3438-3443.
- [8] J.R.M. d’Almeida, R.C.M.P. Aquino, S.N. Monteiro, *Compos. Part A: Appl. Sci. Manuf.* 37 (2006) 1473–1479.
- [9] A.G. Kulkarni, K.G. Satyanarayana, K. Sukumaran and P.K. Rohatgi, *J. Mater. Sci.* 16 (1981) 905-914.
- [10] J.R.M. d’Almeida, A.L.F.S. d’Almedia, and L.H. Carvalho, *Polym. Polym. Compos.*, 16 (2008) 589-595.
- [11] A. Gomes, K. Goda, J. Ohgi, *JSME International Journal Series A* 47 (2004) 541-546.
- [12] M. Kerr., N. Chawla and K.K. Chawla, *JOM* (2005) 67-70.

- [13] A.R. Bunsell, J.W.S. Hearle, and R.D. Hunter, *J. Phys. E. Sci. Inst.* 4 (1971) 868.
- [14] M.H. Lafitte and A.R. Bunsell, *J. Mater. Sci.* 17 (1982) 2391-2397.
- [15] A.R. Bunsell, J.W.S. Hearle, *J. Appl. Polym. Sci.* 18 (1974) 267-291.
- [16] A.R. Bunsell, A. Somer, *Plast. Rubber Compos. Process. Appl.* 18 (1992) 263-267.
- [17] A.R. Bunsell, *J. Mater. Sci.* 10 (1975) 1300-1308.
- [18] W.Y. Hamad, J.W. Provan, *Cellulose* 2 (1995) 159-177.
- [19] W.Y. Hamad, *Cellulose* 4 (1997) 51-56.
- [20] J.W.S. Hkarlk and J.T. Sparrow, *Textile Research Journal* 49 (1979) 242-243.
- [21] H-E. Gram, *Durability of natural fibers in concrete*. Swedish Cement and Concrete Research Institute, Research Fo; (1983).
- [22] R.D. Averett, M.L. Realff, S. Michielsen, W.N. Richard, *Compos. Sci. and Tech.* 66 (2006) 1671–1681.

*ARTIGO C - Toledo Filho, R.D. Silva F.A., Fairbairn E.M.R., Melo Filho J.A.
Durability of compression molded sisal fiber reinforced mortar laminates. Construction
and Building Materials 23 (2009) 2409-2420.*

Durability of Compression Molded Sisal Fiber Reinforced Mortar Laminates

Romildo Dias Toledo Filho^a, Flávio de Andrade Silva^a, E.M.R. Fairbairn^a and João de Almeida Melo Filho^a

^aCivil Engineering Department, COPPE, Universidade Federal do Rio de Janeiro, P.O. Box 68506, CEP 21941-972, Rio de Janeiro – RJ, Brazil.

Construction and Building Materials

2009

Abstract

This paper presents an experimental research on the durability performance of compression molded sisal fiber-cement mortar composites (SFRMC). To obtain a material with enhanced performance, the used methodology was to replace the Portland cement (PC) by calcined clay (metakaolin and calcined waste crushed clay brick) in order to produce a matrix totally free of calcium hydroxide (CH). The content of calcium hydroxide in the matrix was determined by thermal analysis. SFRMC were then produced using both a PC and a CH free PC-calcined clay matrix and the composites were submitted to accelerated aging through cycles of wetting and drying. The durability of the SFRMC was investigated by determining the effects of accelerated aging on the microstructures and flexural behavior of the composites. The results indicate that the newly developed CH-free matrix avoided the fiber embrittlement process keeping the toughness in time even after 100 cycles of wetting and drying.

Keywords: durability (C), cement (D), sisal fiber, composites (E), metakaolin (D), calcined clay brick.

1. Introduction

Academic institutions and fiber cement producers have been engaged for the past 25 years in intensive research to find substitutes and to develop processes for the industrial production of asbestos free fiber materials. Some products are already produced on a commercial basis using cellulose pulp [1] and fibrillated polypropylene networks-glass fibers as reinforcement [2]. Polyvinyl alcohol (PVA) fibers and a combination of cellulose and short PVA fibers have also been proposed for asbestos replacement [3]. A considerable effort has also been directed toward the application of vegetable fibers such as sisal and coconut to replace asbestos fibers because of their availability in the tropical and subtropical parts of the world, low cost and low consumption of energy [4-9].

The use of vegetable fibers in concrete provides an exciting challenge to the housing construction industry, particularly in developing countries, since they are an economic and readily available kind of reinforcement, require only a low degree of industrialization for their processing and, in comparison with an equivalent weight of

the most common synthetic reinforcing fibers, the energy required for their production is small and hence, the cost of fabricating these composites is also low.

Cement pastes and mortars can be reinforced with vegetable fibers for manufacturing thin section building components with variable shapes. However, vegetable fiber cement composites undergo an aging process in humid environments in which they may suffer a reduction in post-cracking strength and toughness. This durability problem is associated with an increase in fiber fracture and decrease in fiber pull-out due to a combination of weakening of the fibers by alkali attack, fiber mineralization, due to migration of hydration products to lumens and to the middle lamella, and volume variation in these fibers due to their high water absorption.

To enhance the durability performance of vegetable fiber reinforced cement-based composites several approaches have been studied including fiber impregnation with blocking agents and water-repellent agents, sealing of the matrix pore system, reduction of matrix alkalinity and combinations of fiber impregnation and matrix modification [4,6,10].

Fiber impregnation with blocking agents (ex: sodium silicate, sodium sulphite and magnesium sulphate) have been studied by Gram [4] but none of them improved the durability of the sisal fiber in a PC matrix. Fiber impregnation with water repellent agents (ex: formine and stearic acid) led to a retardation of the embrittlement tendency of the composites but failed to prevent the fiber from being mineralized [4]. Impregnation of sisal fibres with organic compounds derived from timber (ex: tannins, colophony and vegetable oils) were studied by Canovas et al. [6]. Their results indicated a slight slow down in the embrittlement process, but it was not avoided completely.

Sealing the matrix pores, admixing small beads of wax or zinc stearate powder in the fresh mortar, or impregnating the hardened product with sulphur showed promising results [5]. Pore sealing with colophony, tannin or montan wax reduced the water absorption and relative porosity of sisal fibre-mortar composites, decreasing, but not hindering, the embrittlement process [10]. Reduction of matrix alkalinity through the use of pozzolanic materials has been studied in the last two decades [4,7,9,10]. The cementitious materials studied included high alumina cement and modified PC-based materials containing silica fume, slag, fly ash or natural pozzolanas such as rice husk ash, pumice and diatomite. Replacing 45% of the cement with silica fume significantly reduced the loss in toughness of the composite. A marked improvement was also observed when using high alumina cement and natural pozzolanas. With partial

replacement of PC by fly ash or slag, however, no significant improvement was obtained. Carbonation of the matrix and immersion of sisal fibers in slurried silica fume also presented a promising alternative for increasing the composite durability.

The approach used in this study in order to improve the durability performance of Portland cement (PC) based composites incorporating sisal fibers was to produce a matrix completely free of calcium hydroxide (CH). To achieve this objective the PC in the matrix was partially replaced by metakaolin (MK) and crushed waste calcined clay bricks (CWCCB). The composites were submitted to accelerated aging through cycles of wetting and drying in order to verify the efficiency of this concept. The durability of the composites is discussed based on the flexural strength and toughness obtained before and after 25, 50, 75 and 100 cycles of aging and on observations of the fibers in a scanning electron microscope (SEM). The results indicate that the newly developed CH-free matrix avoided the fiber embrittlement process keeping the toughness in time even after 100 cycles of wetting and drying.

2. Sisal Fibers

2.1 Chemical composition

Chemically the sisal fibers comprise cellulose (~70%), hemicellulose (~18%), lignin (~10%) and a small amount of pectin, waxes and fat (~2%). Cellulose $(C_6H_{10}O_5)_n$ is a linear polysaccharide polymer formed by glucose monosaccharide $(C_6H_{12}O_6)$ [11]. The degree of polymerization of cellulose in sisal fiber is about 25000 and therefore there will be few chain-ends to disrupt the crystalline arrangement [4].

Hemicellulose are amorphous short-chained isotropic polysaccharides and polyuronides, often of very similar sugars, e.g. galactose and mannose and rarely if ever crystalline [11]. The polysaccharide hemicellulose are chemically linked or partly intermingled and oriented with cellulose molecules. The hemicelluloses present a relatively low degree of polymerization and are soluble in alkalis. According to Gram [4] hemicelluloses occur mainly in the primary wall and their degree of polymerization in sisal fibers lies between 50 and 200.

Lignin is a short chain isotropic and non-crystalline made up of units from phenylpropane. It is found in the middle lamella of the fiber and in the walls of the fibrillae [12]. About 25% of the total lignin is to be found in the middle lamella. Since

the middle lamella is very thin, the concentration of lignin is correspondingly high (~70%). Their degree of polymerization is 60 [12]. According to Gram [4] and Velpari et al. [13] lignin can be broken down or leached out in alkaline environment.

2.2. Morphology

The sisal fibers (*Agave sisalana*) are extracted from the sisal plant leaves in the form of long fiber bundles called technical fibers. A sisal plant produces from 200 to 250 leaves before flowering [14]. Each of them contains approximately 700-1400 fiber bundles with a length of 0.5-1.0 m [15]. The sisal leaf is a sandwich structure composed of 4% fiber, 0.75 % cuticle, 8% dry matter and 87.25% water [14]. Three types of fibers reinforce the leaf: structural, arch and xylem. The structural fibers give the sisal leaf its stiffness and they are found in the periphery of the leaf. They present a rarely circular and usually horse shoe shaped cross-section and a rough surface (see Figure 1).

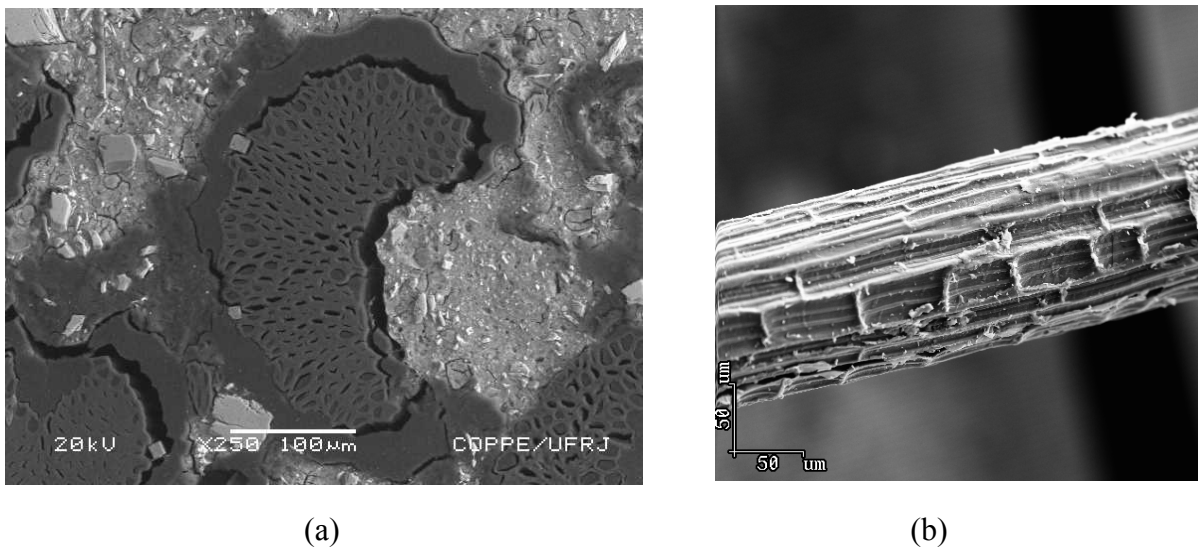


Figure 1 – Structural Fiber geometry: (a) horse shoe shape and (b) rough surface.

The arch fibers occur in association with the conducting tissues (see Figure 2) and they are usually developed in the median line of the leaf. The xylem occurs opposite to the arch fibers. According to Nutman [16], they are composed of thin walled cells, and are invariably broken up and lost during the process of fiber extraction.

Every technical fiber contains numerous elongated individual fibers (fiber-cells) which are about 6 to 30 μm in diameter [14]. The microstructure of the fiber-cell is shown in Figure 3. The individual fiber-cells are linked together by means of the middle lamella,

which consist of hemicellulose and lignin. The lumen varies in size but is usually well-defined (see Figure 3b). Each individual fiber-cell is made up of four main parts, namely the primary wall, the thick secondary wall, the tertiary wall and the lumen (see Figure 3c).

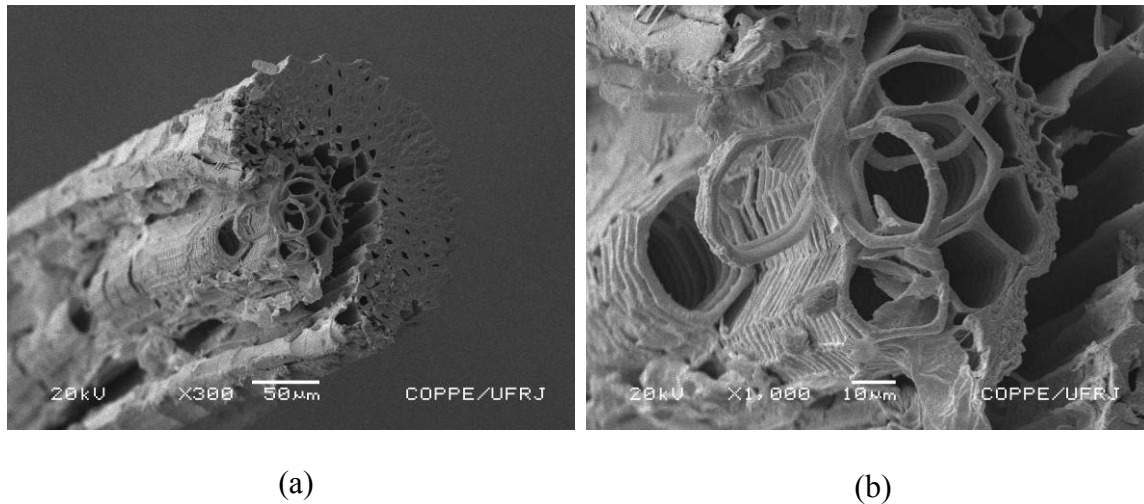


Figure 2 - Arch fiber morphology: (a) arch fiber connected with its conducting tissues and (b) conducting tissues detail.

The walls consist of several layers of fibrillar structure consisting of fibrillae which are linked together by lignin. In the primary wall, the fibrillae have a reticulated structure. In the outer secondary wall (S_1) the fibrillae are arranged in spirals with a spiral angle of 40° in relation to the longitudinal axis of the individual fiber. The fibrillae in the inner secondary wall (S_2) have a sharper slope (18 to 25°). The thin, innermost, tertiary wall has a parallel fibrillar structure and encloses the lumen. The fibrillae are, in turn, built up of micro-fibrillae with a thickness of about 20 nm. The microfibrillae are composed of cellulose molecular chains with a thickness of 0.7 nm and a length of a few μm and are linked together by means of hemicellulose [4].

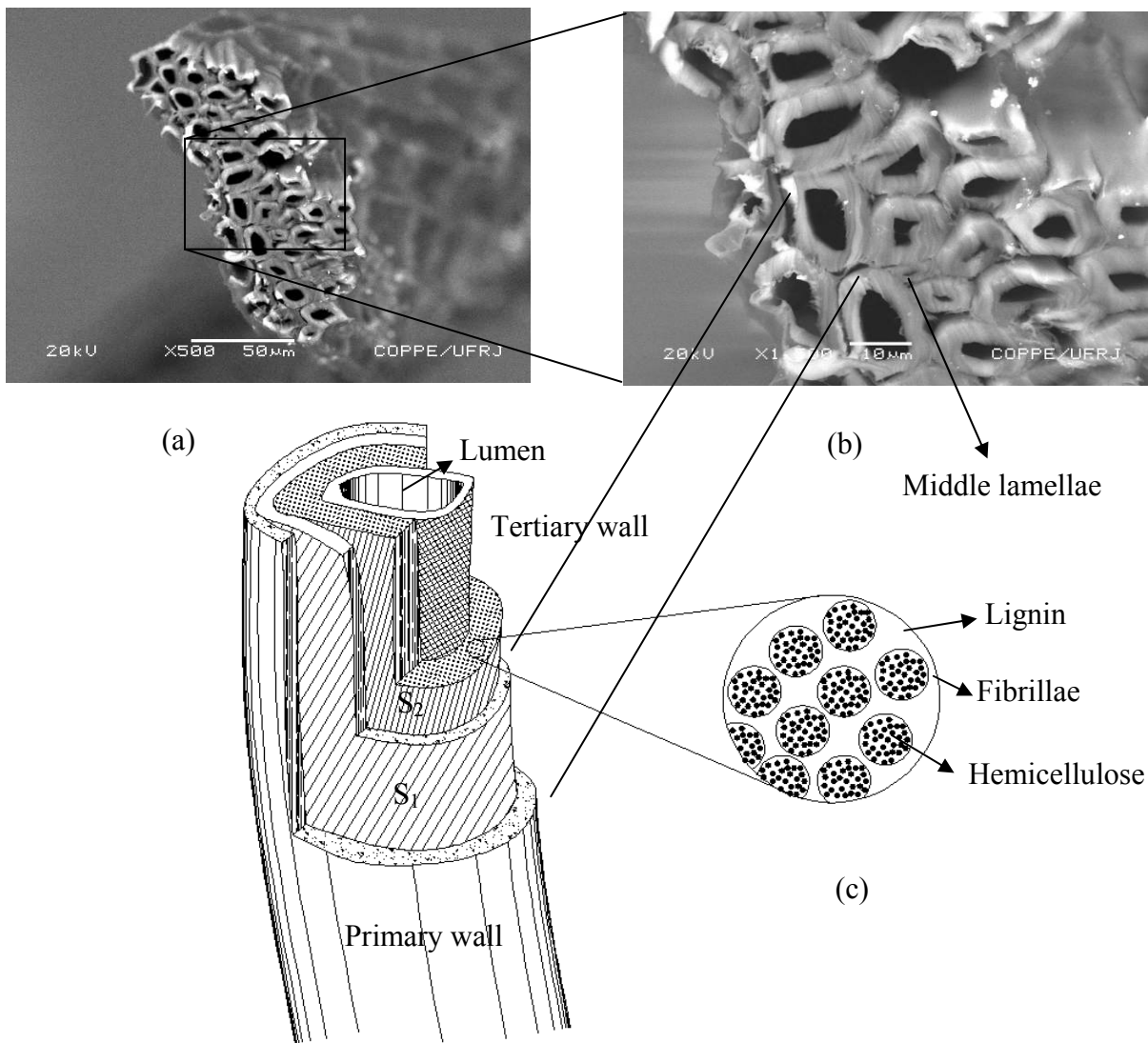


Figure 3 – Fiber-cell microstructure: (a) cross section view showing the fiber-cells, lumens and middle lamellae (b) magnification of the cross section and (c) schematic drawing showing the different layers of an individual fiber cell.

3. Composition and Hydration of Cementitious Materials

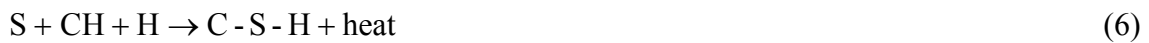
Typical cement chemistry notation will be used throughout this section: C=CaO, S=SiO₂, F=Fe₂O₃, A=Al₂O₃, N=Na₂O, K=K₂O, \bar{S} =SO₃ and H=H₂O; C-S-H represents calcium silicate hydrate, where the symbol '-' indicates no exact stoichiometric proportions; CH represents calcium hydroxide, or Ca(OH)₂; AFt is the abbreviation of ettringite Ca₆Al₂(SO₄)₃(OH)₁₂.26H₂O, and AFm is the abbreviation of monosulfate, Ca₄Al₂O₆(SO₄).14H₂O.

In fact, what is called cement hydration reaction (cement + water → hydrates + calcium hydroxide + heat) is the combination of hydration reactions that takes place when the cement matrix is becoming mature. For Portland cement hydration, the main reactions are based on the mineral compounds of the clinker. They can be written in a simplified form as:



All these reactions have its own kinetics [17], and the reagents, i.e., the clinker minerals, have different heats of hydration at complete reaction (Q_∞), which are, approximately, in kJ/kg: $Q_\infty^{C_3S} = 505$; $Q_\infty^{C_2S} = 260$; $Q_\infty^{C_3A} = 870$ and $Q_\infty^{C_4AF} = 420$ [18].

Mineral additions strongly influence the hydration of cementitious materials. If pozzolans are added to cement, they react with calcium hydroxide forming C-S-H in an exothermic reaction. If the pozzolan is composed mainly by silica oxide, the following reaction equation can be written:



The pozzolanic reaction tends to proceed more slowly than the reaction of the clinker compounds. However, depending on the chemical composition and surface area, some pozzolans can be highly reactive. A typical example of a pozzolan that can present this characteristic is metakaolinite ($Al_2O_3 \cdot 2SiO_2$). The reaction between metakaolin and CH generates new cementitious products including C-S-H and alumino-silicates hydrates

(ex: C_2ASH_8 , C_4AH_{13} and C_3AH_6) [19]. In this paper, calcined clays (metakaolin and crushed waste calcined clay brick) were used to eliminate calcium hydroxide from the cement matrix.

4. Mechanisms of Sisal Fibers Degradation in PC Matrices

Technical sisal fibers can suffer various degrees of degradation when exposed to an alkaline environment. The extent of the attack, as determined by strength loss of the fibers, depends on the kind of alkaline solution. The possible causes of the deterioration of sisal fibers in the alkaline solutions are associated with two different mechanisms. One is the chemical decomposition of the lignin and hemicellulose in the middle lamella which breaks the link between the individual fibers and then its reinforcing capacity. According to Gram [4] this effect only take place at a high rate above a temperature of 75 °C. This happens because the degree of polymerization in sisal cellulose is high (~25000). The other possibility is the cristallization of lime in the lumen, walls of the individual fibers and middle lamellae leading to a decrease in the technical fiber flexibility and strength [4,9,20].

5. Experimental Program

5.1 Materials

The sisal fibers used in this investigation were of Brazilian production and had a mean density, elastic modulus and tensile strength of 0.90 g/cm³, 19 GPa and 577 MPa, respectively [7]. Wollastonite fiber (JG class), obtained from Energyarc, were used as a micro-reinforcement in the composite production.

The matrix was produced using the Portland cement CII F-32 defined by the Brazilian standard [21] as composed with filler (in mass: 85%<clinker<91%; 3%<gypsum<5%; 6%<filler<10%) with 32 MPa of compressive strength at 28 days, Metakaolin (MK) from Metacaulim do Brasil Industria e Comércio LTDA, calcined waste crushed clay brick (CWCCB) from an industry located in Itaborai – RJ, Brazil, burned at 850 °C, river sand with maximum diameter of 1.18 mm and density of 2.67g/cm³ and a naphthalene superplasticizer Fosroc Reax Conplast SP 430 with content of solids of

44%. The physical and chemical characteristics of the cementing materials are presented in Table 1.

Table 1 - Chemical properties of the cementing material.

Chemical properties	Portland cement	CWCCB	MK
SiO ₂ (wt%)	19.98	63.89	51.20
Fe ₂ O ₃ (%)	3.12	7.73	4.00
Al ₂ O ₃ (%)	3.70	25.49	35.30
CaO (%)	62.80	0.29	2.62
MgO (%)	3.10	0.04	0.40
Na ₂ O (%)	0.07	Traces	-
K ₂ O (%)	0.80	0.95	0.97
TiO ₂	-	-	0.41
Insoluble residue (%)	1.50	Traces	Traces
% retained on mesh 325 (45 μm)	22	35	0

X-ray diffraction results from the pozzolanic materials and grading curves of the cementing materials are presented, respectively, in Figure 4 and Figure 5.

In terms of chemical composition both pozzolanic materials have a content of SiO₂ + Al₂O₃ + Fe₂O₃ above 90% which is in accordance with ASTM C 618-01 [22]. The fineness of the cementing materials is also in accordance with the mentioned standard (100% of the grains of MK are smaller than 45 μm whereas for the CWCCB, 62% of their particles were found below 45 μm).

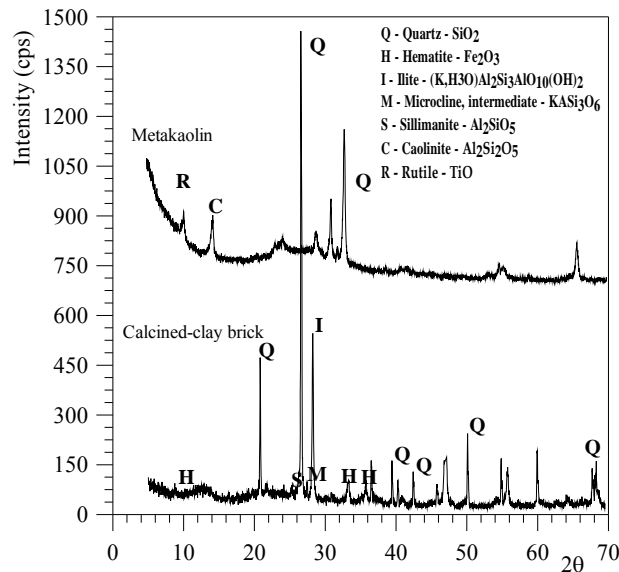
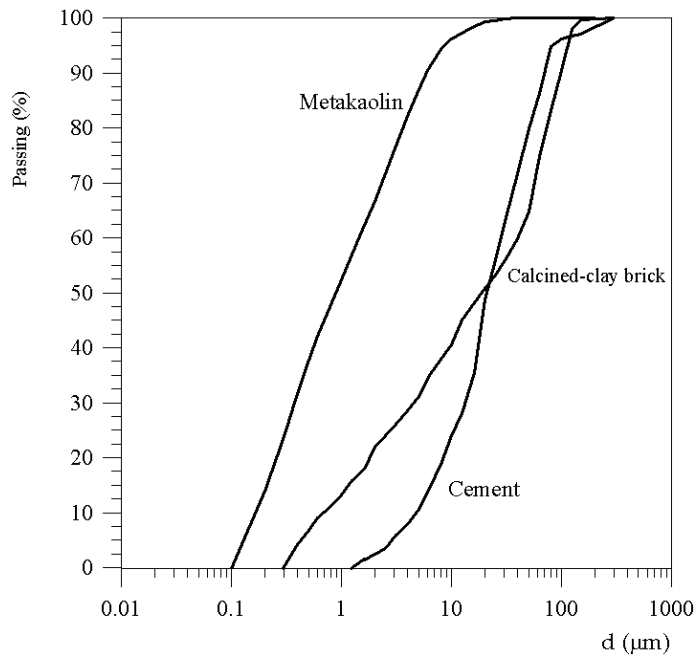


Figure 4 – X-ray diffraction of the pozzolanic materials.

The X-ray powder diffraction results showed that the metakaolin presents peaks of quartz, rutile and caolinite. Using the Rietveld's method it was found that the amount of amorphous phase was about 87 %. Analyzing the results of the x-ray diffraction of the CWCCB it was observed peaks of quartz, hematite, sillimanite, microcline and illite. The Rietveld's method indicated that the amount of amorphous phase in the CWCCB was about 62 %.



The calcium hydroxide (Ca(OH)_2) chemically decomposes when exposed to temperatures between 420°C and 550°C and loses water in a dehydration process. Through a thermogravimetric analysis (TGA) it was possible to determine the mass loss in the dehydration region that corresponded to the water loss which was chemically combined to the Ca(OH)_2 .

The chemical reaction occurred during the dehydration process of the Ca(OH)_2 is shown in Equation 7 [23]:



From Equation 7 it can be seen that the weight loss correspondent to one molecule gram of water (18g) is originated from the dehydration of one molecule gram of Ca(OH)_2 (74g) hence, the mass of free Ca(OH)_2 is equal to 74/18 times the mass of water loss in the chemical reaction shown in Equation 8. The Equation 8 was then used to compute the CH amount present in each mixture:

$$\text{CH}(\%) = \frac{74.09}{18.01} \times \frac{(M_s^{T_0} - M_s^{T_f})}{M_c} \quad (8)$$

Where: $M_s^{T_0}$ - is the mass obtained from the TGA test for the temperature corresponding to the initial CH dehydroxilation; $M_s^{T_f}$ - is the mass obtained in the TGA tests for the temperature corresponding to the final CH dehydroxilation observed in the DTGA and M_c - is the sample initial mass.

Considering that the used MK presents a higher capacity to retain water, probably due to its high specific area and internal lamellar structure, and that the used CWCCB did not change the rheological behavior of mortar matrices up to a level of PC replacement of 40% [24], it was decided to develop a blend of both pozzollans (MK and CWCCB) as cement replacement.

The partial replacement of PC by MK and CWCCB ranged from 10 to 55% by weight. A total of 10 cement pastes were produced: (i) the OPC control mixture; (ii) 10, 30 and 40% of replacement of Portland cement by MK; (iii) 10, 30 and 40% of replacement of Portland cement by CWCCB and (iv) 3 blends of metakaolin and calcined waste

crushed clay brick as cement replacement: 25% MK + 25% CWCCB, 30% MK + 20% CWCCB and 30% MK + 25% CWCCB.

Based on the CH content, mechanical performance and rheology the matrix composed by 20% of CWCCB and 30% of MK was selected to produce the composites (see section 6.1).

5.3 Composite production

The mortar matrix used in this study presented a mix design 1:1:0.4 (cementitious material:sand:water by weight). The matrix was produced using a bench-mounted mechanical mixer of 20 liters capacity. The cementitious materials were dry mixed during 30 seconds (for homogenization) with the subsequent addition of sand and then a volume fraction of 5% wollastonite. The powder material was mixed for more 30 seconds when the superplasticizer diluted in water were slowly poured in the running mixer and then mixed for 3 minutes. For the production of the laminates, the mortar mix was placed in a steel mould, one layer at a time, followed by one layer of long unidirectional aligned fibers (up to 5 layers) and vibration resulting in a sisal fiber volume fraction of 10%. The vibrating table was used at a frequency of 65 Hz. After casting the composites were compressed at 3 MPa during 5 minutes. Figure 6 illustrates the whole molding process. The specimens were covered in their molds for 24 hours and after this time they were demolded and fog cured for 28 days in a cure chamber with 100% RH and 23 ± 1 °C.



Figure 6 - Composite molding process.

The PC composites were named as follows: M0-0, M0-25, M0-50, M0-75 and M0-100. Where M0-0 is the reference PC mixture tested after 180 days of fog cure and 25, 50, 75 and 100 stands for the number of wetting and drying cycles. Therefore, M0-25 means the PC composite fog cured for 180 days tested after 25 cycles of wetting and drying. The free CH composites were named following the same methodology as of the PC composites: M1-0, M1-25, M1-50, M1-75 and M1-100.

5.4. Microstructural analysis

The scanning electron microscopy was performed in a Jeol JSM 6460 LV operating under low vacuum chamber to remove the high vacuum constraint in the sample environment. The microscope was operated under an accelerating voltage ranging from 10 kV to 20 kV. No precoating with carbon or gold, as is done for standard high vacuum SEM, was required. The specimen chamber pressure was adjusted to values ranging from 25 to 80 Pa. All the micrographs were taken under the backscattered electrons mode.

5.5. Evaluation of the composite durability

The durability was evaluated on the basis of four point bending tests that were performed before and after controlled cycles of wetting and drying. For the drying cycles a forced air flow chamber (FAFC) was used. The FAFC was designed in order to allow the control of the wind velocity and air temperature enabling a simulation of the environmental conditions to which the material can be subjected in real life (see Figure 7). In the present study the FAFC was set to a temperature of 36 ± 1 °C and wind velocity of 0.5 m/s.

In order to define the length of the wetting and drying cycles a sample was completely saturated in water at 30 °C and left to dry in the FAFC. Considering that after 24 hours of water immersion the sample absorbed about 90 % of its total saturation capacity and that after 48 hours it lost about 70% of the gained mass, a three day cycle was chosen (1 day under water followed by 2 days of drying under the FAFC condition).

A Shimadzu UH-F 1000 kN testing machine was used to perform the four point bending tests as can be seen in Figure 8.

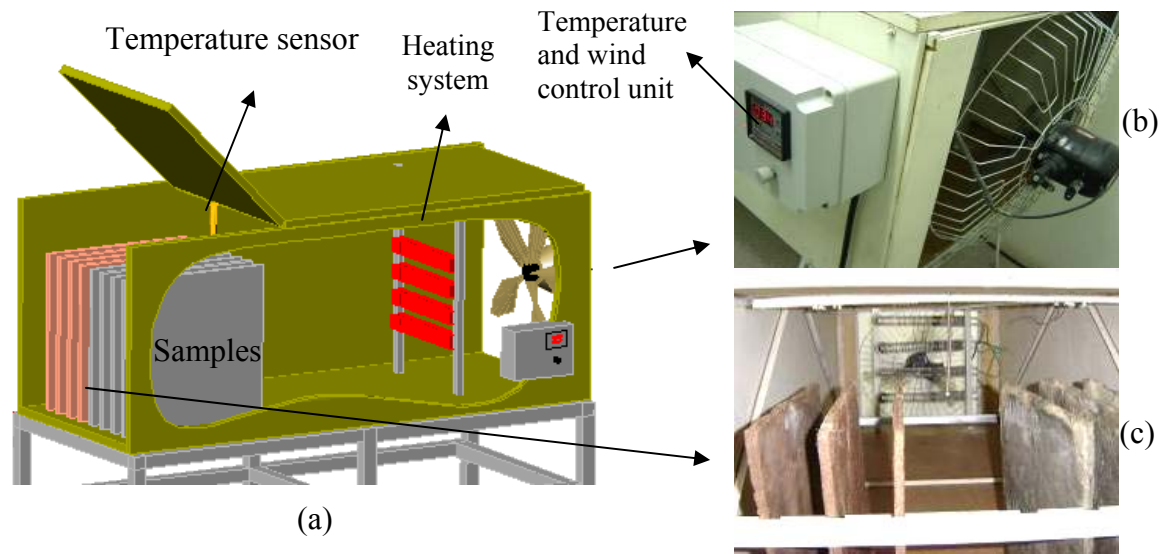


Figure 7 - Forced air flow chamber (FAFC): (a) schematic view, (b) fan, temperature and wind velocity control unit and (c) specimen holder and temperature sensor.

The tests were carried out at a crosshead rate of 0.5 mm/min. Three specimens with geometry of 400 mm x 100 mm x 12 mm (length x width x thickness) were tested under bending (300 mm span). Displacements at mid span were measured using electrical transducers (LVDT) and were continuously recorded, together with the corresponding loads, using a 32-bit data acquisition system taking four readings per second.

From the load-deflection curves three parameters were calculated to evaluate the reinforcing effect of the fibre and consequently its durability or embrittlement with time for the cases studied:

(i) The post-cracking flexural strength of the composite (PCS) - determined from the maximum load using the bending formula given by equation 9:

$$PCS = 6M/bd^2 \quad (9)$$

where M is the failure moment of the test specimen and d and b are the depth and width of the specimen, respectively.

(ii) The toughness of the composites - calculated from the area under the load-deflection curves obtained under bending up to a post-peak deflection corresponding to 40% of the peak load [25].

(iii) The French and Belgian load ratios $P^* = P_n/P_f$. The applied load at deflections of 0.5 mm, 1.0 mm, 2.0 mm and 2.8 mm is defined as P_n and that at the first visible crack is defined as P_f [26,27]. Considering that some mixtures presented deflections considerable higher than those used in the mentioned standards, it was also calculated the load ratios at deflection values of 10.0 mm, 20.0 mm and 40.0mm.

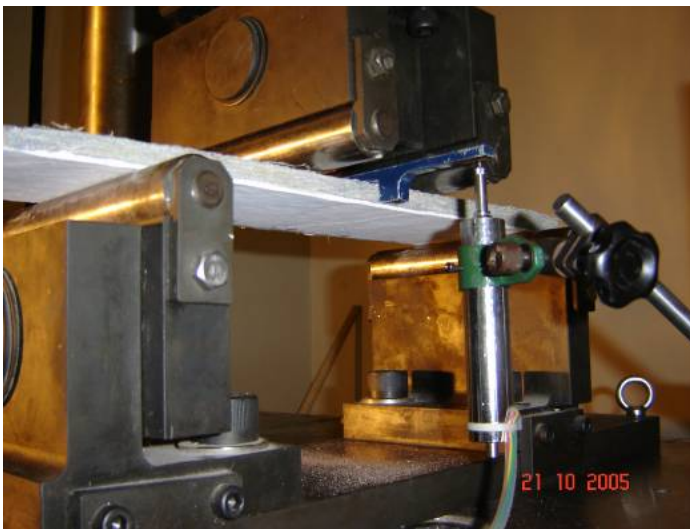


Figure 8 - Four point bending test set-up.

6. Results And Discussion

6.1 The CH free matrix

Figure 9 shows the TGA and DTGA curves for the PC cement paste and for the mixtures containing CWCCB or MK. The CH consume calculated according to Equation 8 is shown in Table 2. The results indicated that 10%, 30% and 40% of PC substitution by MK shows a drop in CH content from 14.92 % (reference matrix) to 1.41 %. When CWCCB was used as the partial substitute of PC a lower CH consume was noticed for the same amount of replacement (reduction of the CH content from 14.92% to 4.15%). This result demonstrates the higher reactivity of the MK. However, since the CH was not completely consumed by the used pozzolans a higher ratio of cement replacement would be needed. Figure 10 shows the TGA and DTGA curves for

the studied blends. It can be seen that for all blends a complete consume of CH was achieved.

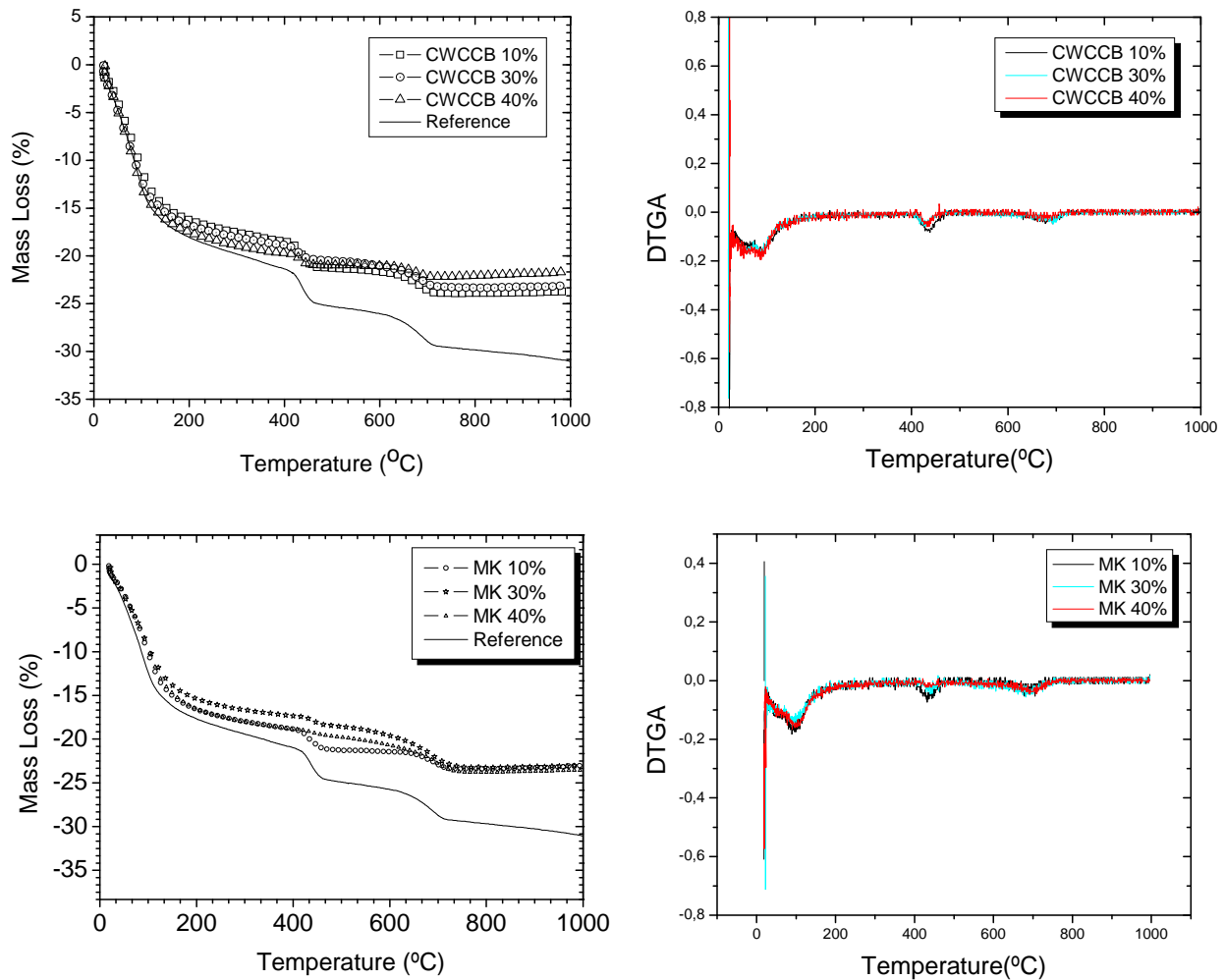


Figure 9 - TGA and DTGA curves for the OPC cement paste (reference) and for the mixes containing 10, 30 and 40% of CWCCB or MK as cement replacement.

To select the blend for the composite production, mortar mixtures were cast and tested to determine its workability (using the flow table test) and compressive strength. Considering that the mixture containing 30% of MK + 20% of CWCCB was the one that presented higher spreading (38 cm) and compressive strength (65 MPa) it was chosen to continue this study. Details of afore mentioned study can be found elsewhere [28, 29].

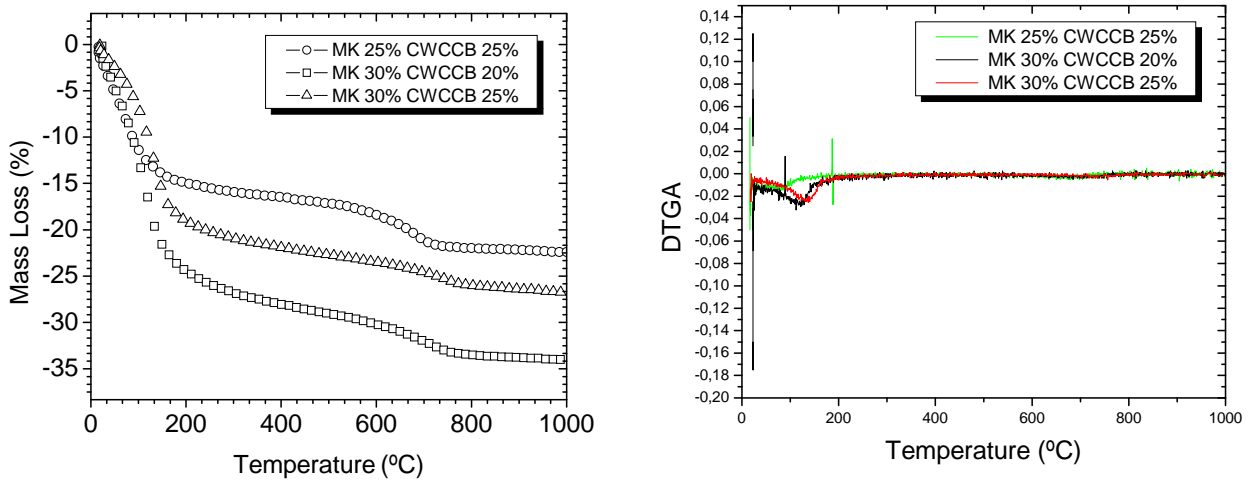


Figure 10 - TGA and DTGA curves for the cement pastes containing both CWCCB and MK as cement replacement.

Table 2 - Calculation of CH consume.

Cement Paste Mixture No	Composition of the pastes (PC:MK: CWCCB:water by weight)	CH content at 28 days (%)
1	1.00:0.00:0.00:0.40	14.94
2	0.90:0.10:0.00:0.40	8.02
3	0.70:0.30:0.00:0.40	3.04
4	0.60:0.40:0.00:0.40	1.41
5	0.90:0.00:0.10:0.40	9.57
6	0.70:0.00:0.30:0.40	5.25
7	0.60:0.00:0.40:0.40	4.15
8	0.50:0.25:0.25:0.40	0
9	0.50:0.30:0.20:0.40	0
10	0.45:0.30:0.25:0.40	0

6.2. Durability of the composites after accelerated aging

Figure 11 presents typical equivalent flexural stress-displacement curves obtained from M0-0 (reference) and M0-25, M0-50, M0-75 and M0-100 composites. It can be observed that first crack strength (FCS) of the reference specimens was increased up to 44% (see Table 3). The reference specimen presented a ductile behavior which was drastically decreased by the aging process (see Table 3). It is important to observe that the deterioration in the PC-composite toughness is already complete after 25 cycles of wetting and drying. The same trend can be observed from the P^* parameters. For

example, values of $P_{2.8}^*$ ranging from 0.06 to 0.30 were observed for aged specimens in contrast with a value of 1.52 observed for the reference specimens.

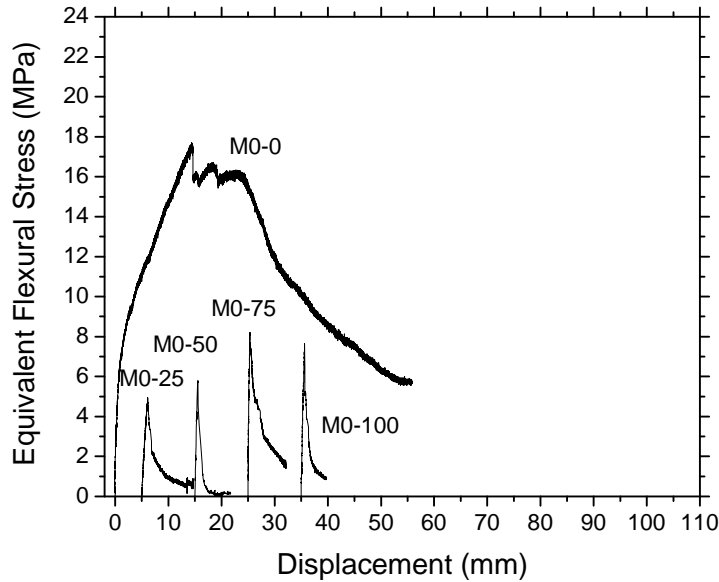


Figure 11 – Typical four point bending curves of aged and non-aged PC composites.

Figure 12 shows the typical cracking patterns for M0-0-specimens and for M0-25 specimens. It was observed that whereas the non-aged specimens presented a multiple cracking behavior under bending loads, all specimens submitted to cycles of wetting and drying presented a single crack formation similar to M0-25. The failure surface presented in Figure 13 shows that the fiber pull-out length was severely affected by the accelerated aging processing (visual inspections indicated fiber pull-out lengths ≤ 3 mm for specimens subjected to 25-100 cycles of wetting and drying).

Figure 14 presents typical examples of equivalent flexural stress-displacement curves obtained from M1-0 and M1-25, M1-50, M1-75 and M1-100 specimens. A ductile behavior is observed not only for the reference specimens but also for the aged ones. For the free CH composites, it was also observed an increase in the FCS, up to 65% after 100 cycles (calculated from Table 3). The obtained results indicate that the increase in FCS was higher for the specimens containing pozzolans. This behavior may be related to a twofold action that combines the degradation of the sisal fibers in the OPC mixtures with the aging process and the late pozzolanic reaction in the CH-free mixtures. It is well known that sisal fibers mineralization leads to a complete reduction in its strength and strain capacity [4–9] and, therefore, it can be considered that a

reduction in the homogenized session of the OPC composites occurs after submitting the specimens to the wetting and drying cycles. Pozzolanic reactions can also contribute in some extent to the increase of the FCS values once the hydration reactions of the OPC still progress at late ages and the CH produced is consumed by the pozzolan along with the evolution of these reactions. Studies carried out by [26,27] indicate that the use of 50% of calcined clay as cement replacement, as used in the present study, is enough to consume all CH formed at late ages.

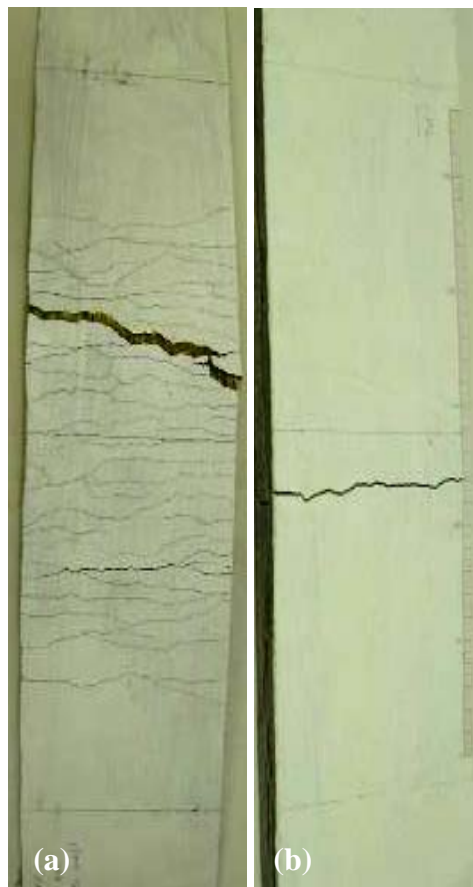


Figure 12 - Typical cracking patterns: (a) non aged PC specimens (b) aged PC specimens submitted to 25 cycles of wetting and drying.

Considering that all specimens have been cured for 180 days before starting the accelerated aging process, it is the authors' opinion that the elevated increase in FCS experienced by both composites can not be only related to the thermo-activated hydration process and that the understanding of this behavior demands further and deeper investigations. The PCS of the reference specimens have increased up to 29% with the accelerated aging regime.

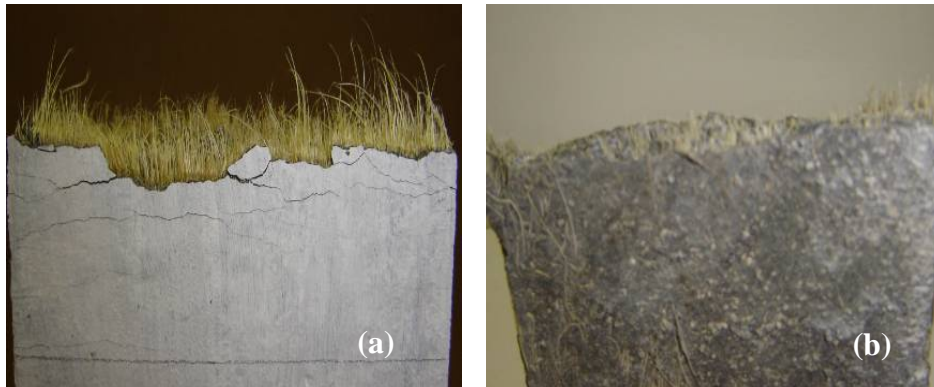


Figure 13 - Failure surface of the composites before and after aging. Pull-out length of the fibers in non aged PC specimens (a) and in aged PC specimens submitted to 25 cycles of wetting and drying.

Regarding to the bending toughness parameter calculated according to the RILEM recommendation [25] it can be observed a slightly tendency in its reduction which lies in the same range of its standard deviation. The P^* parameters clearly indicates the deflection hardening behavior of the non-aged and aged composites. Values of P^* as high as 2.0-2.6 were reported for the aged composites at deflection ranging from 10-20 mm. Observing the stress-displacement curves it can be noted an increase in the slope of the curves between the FCS and PCS as well as in its descending branch with the wet/dry cycling process. This behavior may indicate an increase in the fiber-matrix adhesion with the wetting and drying cycles. The fibers, however, were not deteriorated during the used accelerated aging process. The multiple cracking patterns of the aged specimens shown in Figure 15 and the long fiber pull-out lengths (≥ 30 mm) shown in Figure 16 for specimens M1-25 and M1-100 indicates that the CH free matrix was capable of keeping the sisal fibers integrity with the aging process. Visual observation

of the fibers extracted from aged specimens indicates that they kept their original flexibility.

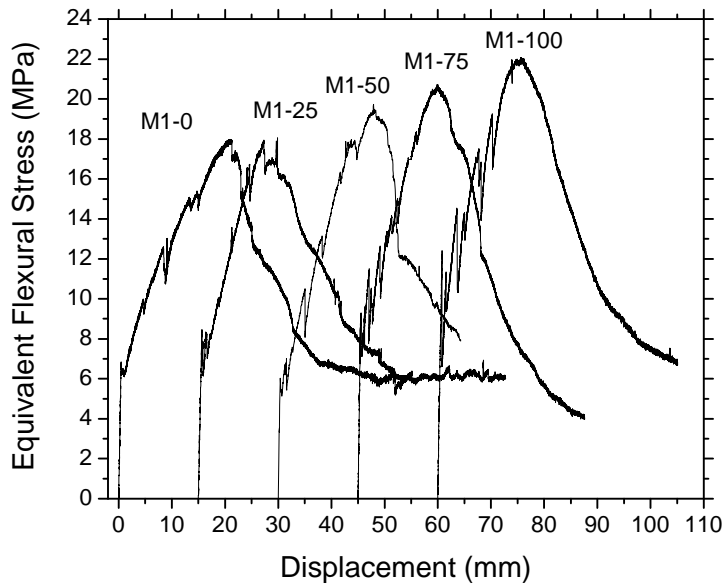


Figure 14 – Typical four point bending curves of non-aged and aged free CH composites.

Table 3 - Summary of results (mean \pm standard deviation) of first crack strength (FCS), post crack strength (PCS), toughness, and P^* indexes.

Mix	Ageing time	FCS (MPa)	PCS (MPa)	Toughness (kJ/m ²)	$P_{2.5}^*$	$P_{1.0}^*$	$P_{2.0}^*$	$P_{2.8}^*$	P_{10}^*	P_{20}^*	P_{40}^*
M0	Reference	5.33 \pm 0.93	19.32 \pm 2.07	22.54 \pm 4.39	0.72	0.99	1.39	1.52	2.37	2.87	1.07
	25 cycles	5.80 \pm 1.08	-	0.36 \pm 0.048	0.69	0.69	0.30	0.22	-	-	-
	50 cycles	5.46 \pm 1.04	-	0.10 \pm 0.018	0.75	0.35	0.08	0.06	-	-	-
	75 cycles	7.50 \pm 1.42	-	0.42 \pm 0.15	0.91	0.63	0.41	0.30	-	-	-
	100 cycles	7.70 \pm 0.39	-	0.31 \pm 0.03	0.73	0.69	0.39	0.26	-	-	-
M1	Reference	6.23 \pm 0.23	17.82 \pm 0.66	21.70 \pm 3.36	0.96	1.01	1.16	1.26	2.05	2.74	1.26
	25 cycles	7.88 \pm 0.52	19.70 \pm 3.03	19.26 \pm 3.98	0.79	0.82	1.00	1.12	2.05	1.96	0.67
	50 cycles	6.81 \pm 1.01	19.25 \pm 4.28	17.84 \pm 1.50	0.91	0.99	1.15	1.33	2.16	2.64	1.12
	75 cycles	9.5 \pm 1.37	21.08 \pm 3.77	16.10 \pm 4.22	0.83	1.04	1.14	1.20	2.04	1.51	0.58
	100 cycles	10.28 \pm 1.86	22.99 \pm 1.09	18.28 \pm 3.59	0.82	0.89	1.04	1.21	1.95	1.53	0.61

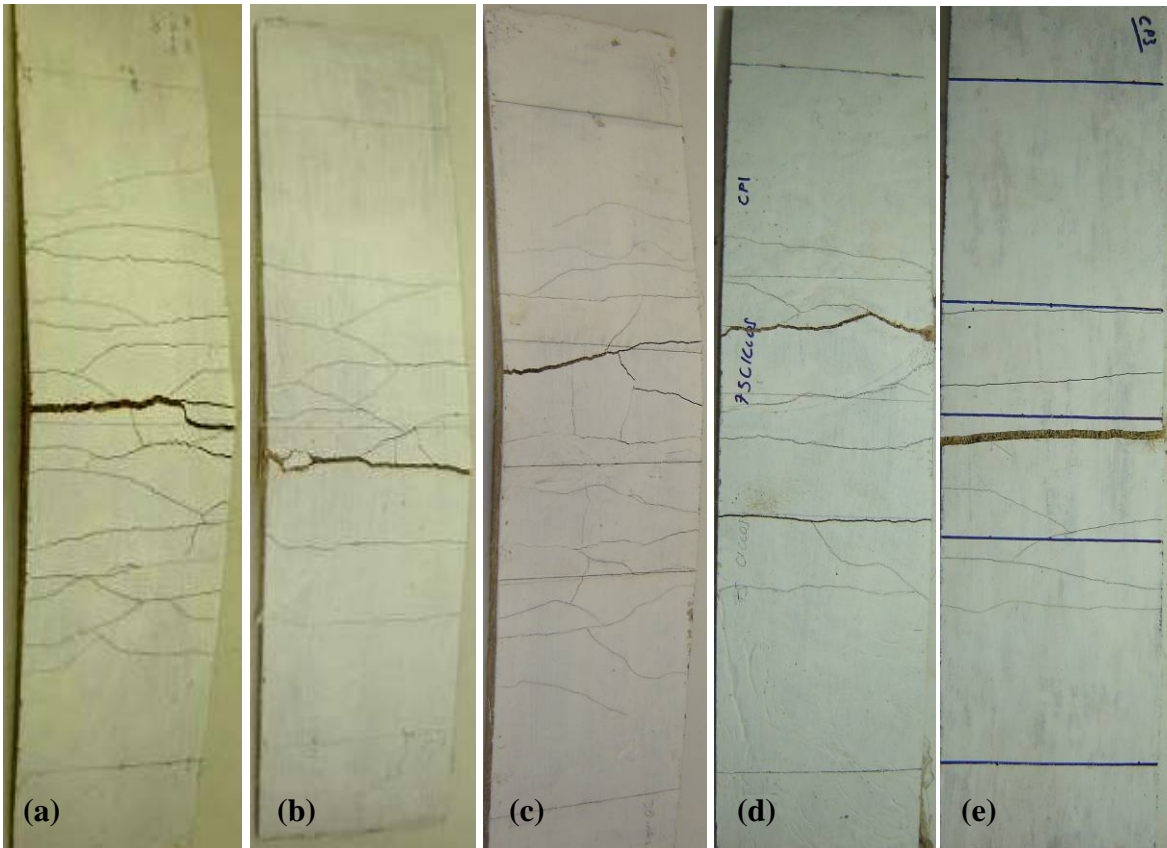


Figure 15 - Typical cracking patterns of CH free composites: (a) non-aged, (b) aged for 25 cycles, (c) aged for 50 cycles, (d) aged for 75 cycles and (e) aged for 100 cycles.

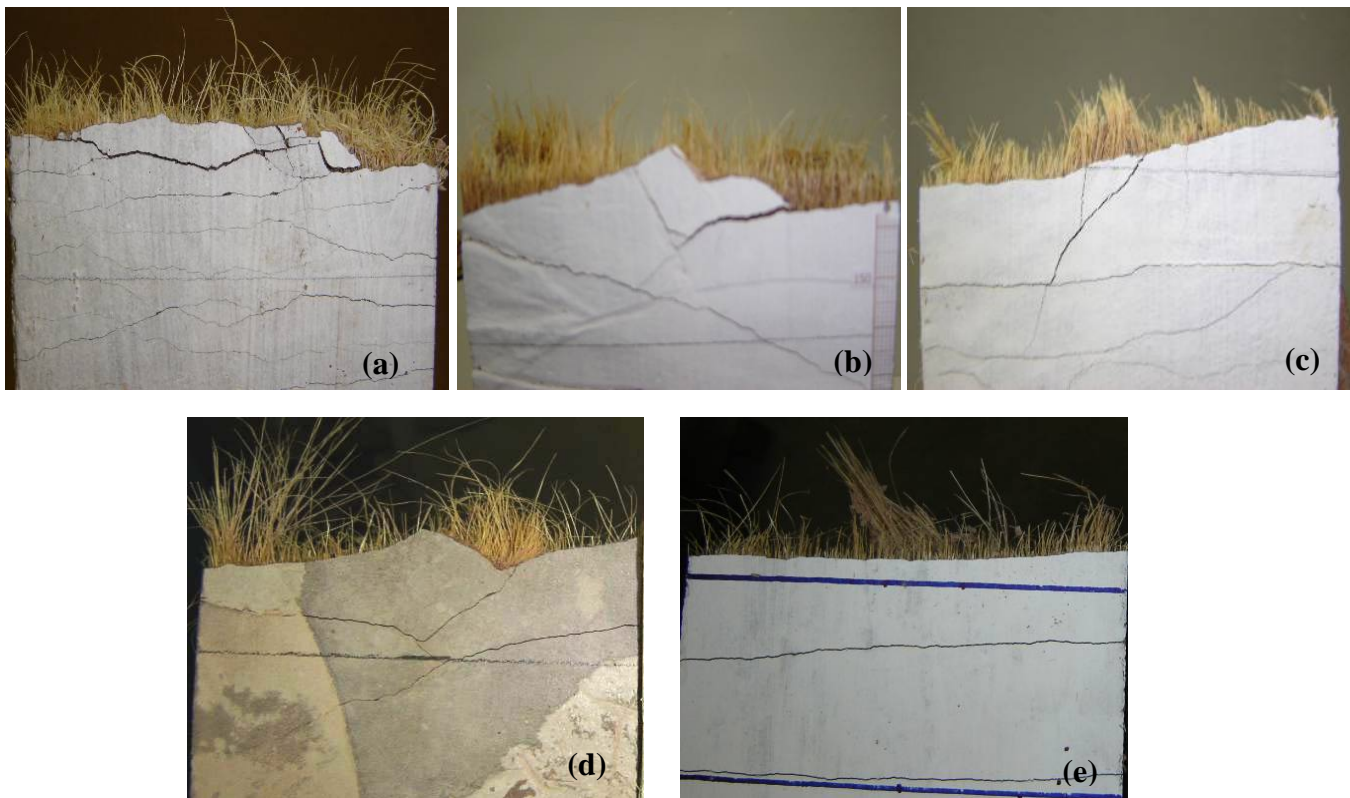


Figure 16 - Failure surface of the CH free specimens before and after aging. Pull-out length of the fibers for the reference specimens (a), for specimens submitted to 25 (b), 50(c), 75 (d) and 100 cycles of wetting and drying (e).

6.3. Micro-structure of aged PC and CH free composites

Figure 17 shows micrographs of PC composites after 25 cycles of wetting and drying. The cavities presented in Figure 17 parts (a) and (b) appeared as a result of the specimens sawing during sample preparation for SEM analysis. This behavior indicates that the fibers have lost their strength and flexibility due to the attack by calcium hydroxide. Signs of fiber mineralization are evident in Figure 17(c). The same behavior was observed in the specimens subjected to 50, 75 and 100 cycles of wetting and drying.

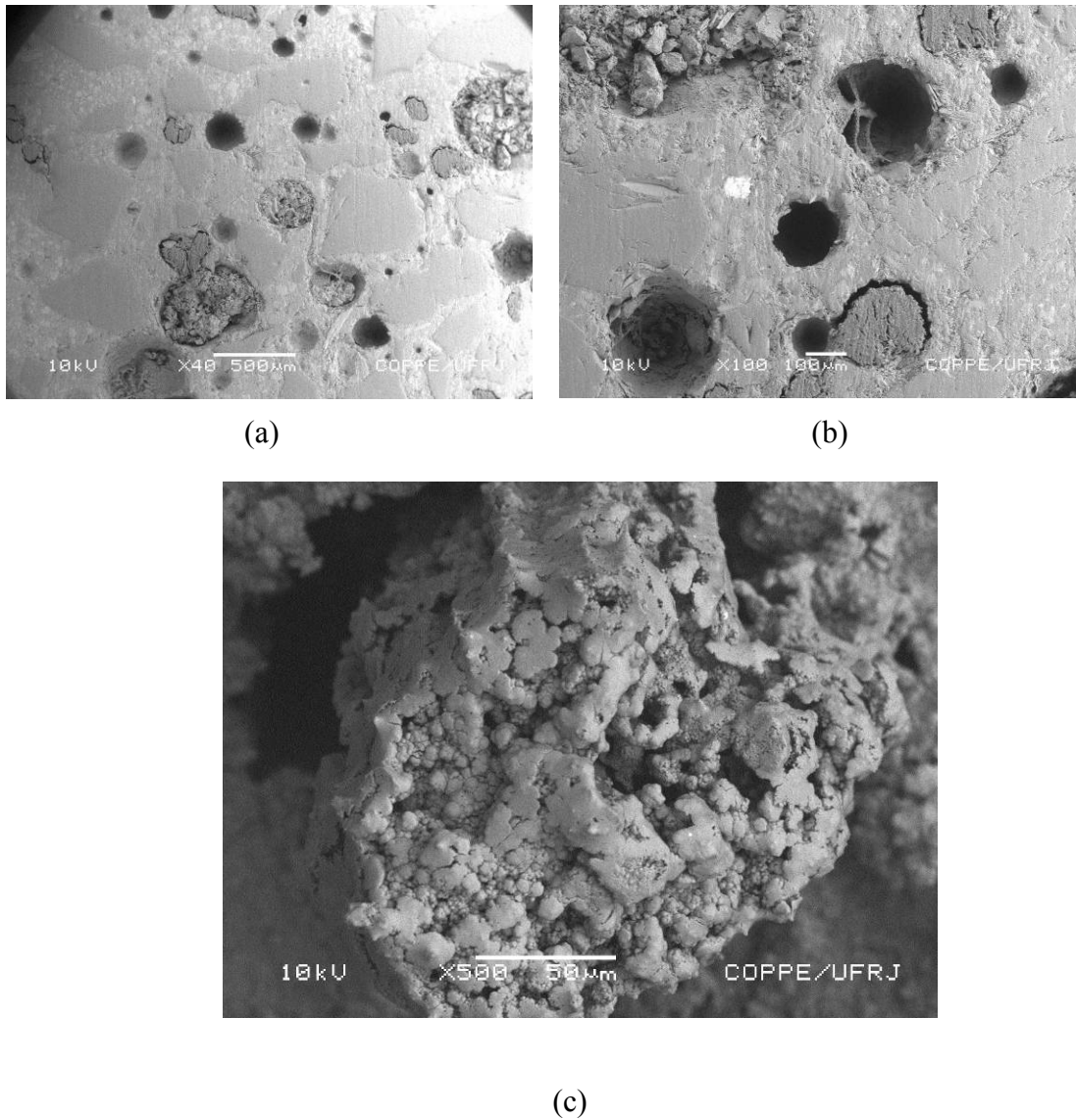


Figure 17 - Micrographs of aged PC specimens subjected to 25 cycles of wetting and drying: (a) and (b) cavities in the matrix due to fibers breaking and pull-out; (c) mineralized fiber inside the specimen.

There was no indication of fiber mineralization in all the micrographs taken from the aged free CH composites. No signs of fiber degradation can be seen in Figure 18(a) and (b). A close up view of the sisal fiber cells in specimens subjected to 50 cycles of wetting and drying are shown in Figure 18(c) and (d) and clearly indicates that the fibers did not suffer any process of mineralization.

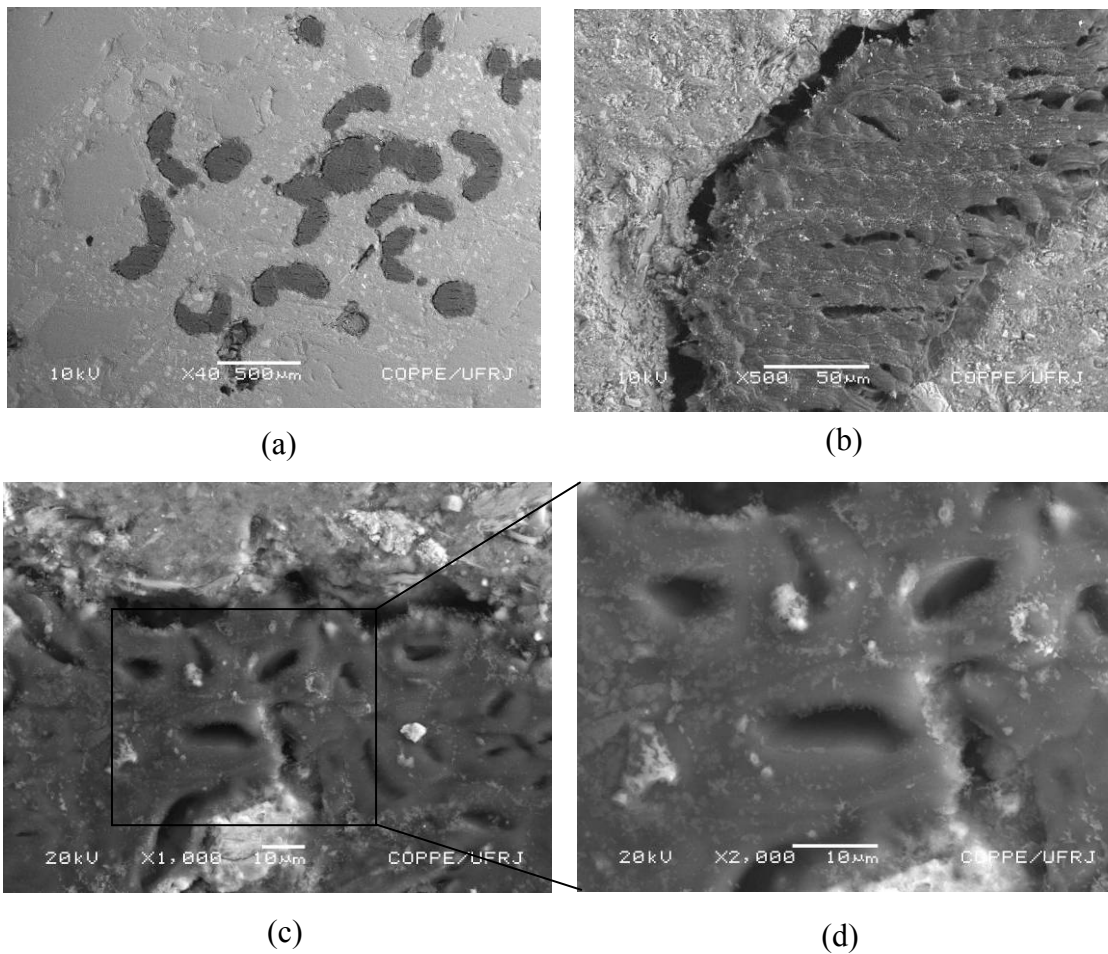


Figure 18 - Micrographs of CH free specimens: (a) specimen subjected to 25 cycles of wetting and drying (b) zoom in a sisal fiber subjected to 25 cycles (c) and (d) close up view of the sisal fiber cells in specimens subjected to 50 cycles of wetting and drying.

7. Conclusions

Based on the results presented in this paper it can be concluded that the long-term embrittlement of sisal fiber-cement based composites can be completely avoided through the use of a cement matrix free of calcium hydroxide. The use of 50% of calcined clay as partial replacement of Portland cement resulted in a CH free matrix that promoted an adequate environment for the sisal fiber reinforcement. The specimens of the free CH composites subjected up to 100 cycles of wetting and drying presented post-cracking strength and bending toughness as high as those of the reference specimens. The multiple-cracking formation observed in the specimens during the bending tests, the

long fiber pull-out length in the surface of fracture of the tested specimens and the micro-structural analysis indicated that the sisal fibers did not suffer any process of mineralization when used as reinforcement in the CH-free matrix. A complete mineralization was observed, however, when the fibers were used as reinforcement in the PC composites. Therefore, the use of a CH-free matrix seems to be a promising alternative for increasing the durability of sisal fiber cement based composites with aging.

Acknowledgements

The authors would like to acknowledge the financial support given by Brazilian CNPq, CAPES and FAPERJ.

References

- [1] R.S.P. Coutts, Wood fibre reinforced cement composites, in: R.N. Swamy (Editor) *Natural Fibre Reinforced Cement and Concrete*, Vol. 5, Blackie and Son Ltd., London, 1988, pp.1-62.
- [2] G. Xu, S. Magnani, G. Mesturini, D.J Hannant, Hybrid polypropylene-glass/cement corrugated sheets, *Composites: Part A* 27 (6) (1996) 459-466.
- [3] J. Hikasa, and T. Genba, Replacement for asbestos in reinforced cement products – “Kuralon” PVA fibers, properties, structure, in: *International Man-Made Fibers Congress*, Austria, 1986.
- [4] H.-E Gram, *Durability of natural fibers in concrete*, Swedish Cement and Concrete Research Institute, Research Fo. 1983.
- [5] Z. Berhane, Performance of natural fiber reinforced mortar roofing tiles, *Materials and Structures* 27 (1999) 347-352.
- [6] M.F. Canovas, N.H. Selva and G.M. Kawiche, New economical solutions for improvement of durability of portland cement mortars reinforced with sisal fibers. *Materials and Structures* 25 (1992) 417-422.
- [7] R.D. Toledo Filho, *Natural fiber reinforced mortar composites: experimental characterisation*, Ph.D. Thesis, DEC-PUC-Rio, Brazil, 1997, 472 p.
- [8] R. D. Toledo Filho, K. Joseph, K. Ghavami, G.L. England, *The use of sisal fiber as*

reinforcement in cement based composites. *Brazilian Journal of Agricultural and Environmental Engineering* 3 (1999) 245-256.

[9] R.D. Toledo Filho, K. Scrivener, G.L. England, K. Ghavami, Durability of alkali-sensitive sisal and coconut fibers in cement mortar composites, *Cement & concrete composites* 22 (2000) 127-143.

[10] R.D. Toledo Filho, K. Ghavami, G.L. England, K. Scrivener, Development of vegetable fiber-mortar composites of improved durability, *Cement & Concrete Composites* 25 (2003) 185-196.

[11] J.C.F. Walker, *Primary Wood Processing: Principles and Practice*. Chapman and Hall, 1993.

[12] Wayne's Word. <http://waynesword.palomar.edu/chemid2.htm#lignin>. Major Part of Chemical Compounds in Plants & Animals – Part II Phenolic Compounds Glycosides & Alkaloids, Access in April 17th 2006.

[13] V. Velpari, B.E. Ramchandran, T.A. Bashkaron, B.C. Pai, and N. Balasubramanian, Alkali resistance of fibres in cement. *Journal of Materials Science* 15 (1980) 1570-1584.

[14] K.G. Mukherjee, and K.G. Satyanarayana, Structure and properties of some vegetable fibres. Part 1: Sisal Fibre. *Journal of Materials Science* 19 (1984) 3925-3934.

[15] K. Oksman, L. Wallstrom, L.A. Berglund, R.D. Toledo Filho, Morphology and mechanical properties of unidirectional sisal-epoxy composites. *Journal of Applied Polymer Science* 84 (13) (2002) 2358-2365.

[16] F.F. Nutman, Agave Fibers Pt. I. Morphology, histology, length and fineness; frading problems. *Empire Journal of Experimental Agriculture* 5 (75) (1936) 75-95.

[17] P.C. Hewlett, *Lea's chemistry of cement and concrete*, Oxford, BH, 2001.

[18] K. Maekawa, R. Chaube, T. Kishi, *Modeling of concrete performance: hydration, microstructure formation and mass transport*, London, E & FN Spon, 1999.

[19] B. B. Sabir, S. Wild, J. Bai, Metakaolin and calcined clays as pozzolans for concrete: a review. *Cement and Concrete Composites* 23 (2001) 441-454.

[20] S.M. Singh, Alkali resistance of some vegetable fibers and their adhesion with portland cement, *Research and Industry* 15 (1985) 121-126.

[21] NBR 11578, Cimento Portland Composto. Associação Brasileira de Normas Técnicas (ABNT), Julho, 1991 (In Portuguese).

- [22] ASTM C 618-01, Standard Test Method for Specification of Coal Fly Ash and Raw or Calcined Natural Pozzolan for Use as a Mineral Admixture in Concrete. ASTM International, 2001.
- [23] J.G. Cabrera, and C.J. Lynsdale, The effect of superplasticizers on the hydration of normal Portland cement . *L'industria Italiana del Cimento* 7-8 (1996) 532-541.
- [24] J.P.Gonçalves, Development and Characterization of low environmental impact concretes containing calcined clays and artificial sand, Doctoral Thesis, Universidade Federal do Rio de Janeiro, 2005.(In portuguese)
- [25] Rilem Technical Committee 49 TFR. Testing methods for fiber reinforced cement based composites, *Materiaux et Constructions* 17 (1984).
- [26] AFNOR Normalisation Française P18-409, Béton Avec Fibres Métalliques-Essai de Flexion, P18-409, L'association Française de Normalisation (AFNOR), France, 1993. p. 8.
- [27] Norme Belge NBN B 15 238, Essais de Béton Renforcé de Fibres-Essai de Flexion sur Éprouvettes Prismatiques, Institut Belge de Normalisation (IBN), Brussels, 1992. p. 9.
- [28] R.V. Velasco, M.C.R. Farage, J.P. Gonçalves, R.D. Toledo Filho and E.M.R. Fairbairn, Development and mechanical characterization of cement based matrices for the production of low environmental impact laminates, in: *Proceedings of the XXXI Jornadas Sud-Americanas de Ingenieria Estructural 2003*. (in portuguese).
- [29] J. A. Melo Filho, Development and experimental characterization of flat and corrugated thin-section cement based laminates, M.Sc. thesis, COPPE/UFRJ, Rio de Janeiro, Brazil, 2005. (in portuguese).

ARTIGO D - Silva F.A., Toledo Filho R.D., Fairbairn E.M.R., Melo Filho J.A. Physical and mechanical behavior of durable sisal fiber cement composites. Construction and Building Materials, submitted, 2009.

Physical and Mechanical Properties of Durable Sisal Fiber Cement Composites

Flávio de Andrade Silva^a, João de Almeida Melo Filho^a, Romildo Dias Toledo Filho^a
and E.M.R. Fairbairn^a

^aCivil Engineering Department, COPPE, Universidade Federal do Rio de Janeiro, P.O.
Box 68506, CEP 21941-972, Rio de Janeiro – RJ, Brazil.

Journal of Construction and Building Materials

2009

Abstract

Sisal fiber cement composites reinforced with long unidirectional aligned fibers were developed and their physical-mechanical behavior was characterized in the present study. Flat and corrugated sheets were cast by a manual lay-out of the fibers in a self-compacted cement matrix and compressed with a pressure of 3 MPa. Direct tensile and bending tests were performed to determine the first crack, post-peak strength and toughness of the composites. Drying shrinkage, capillary water absorption and water tightness tests were performed to characterize the physical properties of the composites. To ensure the composite durability, the ordinary Portland cement matrix was modified by adding metakaolin and calcined waste crushed clay brick to consume the calcium hydroxide generated during Portland cement hydration. The durability of the newly developed composite was determined through accelerated aging conditions using the hot water immersion test. The developed material presented a multiple cracking behavior under bending, even when subjected to six months of hot water immersion under 60 °C. Scanning Electron Microscopy was used to investigate the microstructure of the composites before and after aging.

Keywords: sisal fibers; physical properties; mechanical properties; durability.

1. Introduction

The use of vegetable fibers such as sisal, jute and coconut in concrete poses an exciting challenge to the construction industry since they are a cheap and readily available form of reinforcement and require only a low degree of industrialization for their processing. In comparison to an equivalent weight of the most common synthetic reinforcing fibers, the energy required for their production is small and therefore, their costs are also low.

Usually vegetable fibers have been used as reinforcement of cementitious matrices in the form pulp or short filament fibers [1-7]. These composite systems present a tension softening behavior with low tensile ultimate strength, resulting in products which are more suitable for non-structural applications. Multiple cracking behavior under direct tension cannot be achieved up to this moment for non continuous vegetable cement composites due to the difficulty in dispersing fiber volume fractions greater than 3-4% with fiber length higher than 25-30mm [8,9]. For pulp fibers cement based composites,

although volume fractions as high as 8-10% can be used, the composites still present a tension softening behavior under direct tension due to the short fiber length [3,4,6,7]. In addition, the matrix that is normally used in pulp fiber reinforced composites is a cement paste which presents high consume of cement, hence, elevated emission of CO₂ to the atmosphere and high shrinkage.

In order to produce a composite reinforced with vegetable fibers that present tension hardening behavior under direct tension, long sisal fibers were employed in the present study. The continuous sisal fiber reinforced composites (SCFRC) allows the design of thin walled elements with high strength in tension and compression. These composites can be used in various fields of applications such as permanent formworks, facades, tanks, pipes, long span roofing elements, strengthening of existing structures and structural building members. The SCFRC presents enhanced strength and ductility which is primarily governed by the composite action when matrix cracks and the fibers bridge them to transfer the loads, allowing a distributed microcrack system to develop [10]. These materials are strong enough to be used as load bearing structural members, in applications such as structural panels, impact & blast resistance, repair and retrofit, earthquake remediation, strengthening of unreinforced masonry walls, and beam-column connections.

Vegetable fiber cement composites produced with ordinary Portland cement matrices undergo an aging process in humid environments during which they may suffer a reduction in post-cracking strength and toughness. The aging process is due to fiber mineralization and results in reducing the tensile strength of fibers and decreasing the fiber pull-out ligament after fracture. This mineralization process is a result of migration of hydration products (mainly Ca(OH)₂) to the fiber structure. Efforts to develop durable and structural cement composite laminates reinforced with long sisal fibers has shown much promise recently [11, 12]. To guarantee the durability of the composites, a free calcium hydroxide matrix was developed using high contents of pozzolanic materials (up to 50% of cement replacement by mass) therefore, reducing the CO₂ emissions associated to cement production. The low environmental impact of this material is achieved by both the use of a renewable reinforcement and a green cementitious matrix.

In order to characterize this newly developed material physical-mechanical tests were carried out in the present study. Direct tension and bending tests were performed to

determine their mechanical behavior under quasi-static loads. Flat and corrugated sheets were produced and tested under three-point bending configuration. The composite's physical characteristics were evaluated through drying shrinkage, capillary water absorption and water tightness. Accelerated aging test through hot water immersion ($T = 60\text{ }^{\circ}\text{C}$) was performed during six months to evaluate the durability of the composites. Scanning Electron Microscopy was used to investigate the microstructure of the composites before and after aging.

2. Experimental program

2.1. Materials and processing

2.1.1. Sisal fiber

The sisal fibers (*Agave sisalana*) were obtained from farms in Bahia state, Brazil. They were extracted from the sisal plant leaves in the form of long fiber bundles. The fiber extraction from the leaf was done by semi-automatic raspadors. From a 100 kg of sisal leaves about 3.5 kg extractable fiber is obtained. These fibers were characterized mechanically by Silva et al. [13, 14]. Monotonic tension tests were performed in fibers with gage lengths ranging from 10 to 40 mm. The sisal fibers presented mean elastic modulus and tensile strength around 19 GPa and 400 MPa, respectively. The Young's modulus and ultimate tensile strength were not influenced by the gage length. The strain-to-failure decreased from approximately 5.2 % to 2.6 % when the gage length was increased from 10 mm to 40 mm. The Weibull modulus decreased from 4.6 to 3.0 when the gage length was increased from 10 mm to 40 mm, respectively. More details can be found elsewhere [13]. Fatigue tensile tests showed that sisal fibers subjected to a ratio of maximum applied fatigue stress to ultimate tensile strength of 0.5 have survived 10^6 cycles. Sisal fibers failed in fatigue when the ratios ranged between 0.6 to 0.8, and fatigue lives of between 10^3 and 10^6 cycles, respectively [14].

Regarding to the sisal fiber microstructure it is formed by numerous individual fibers (fiber-cells) which are about 6 to 30 μm in diameter (Figure 1a). The individual fiber-cells are linked together by means of the middle lamella (Figure 1b), which consist of hemicellulose and lignin. The chemical composition of the sisal fiber comprehends

approximately 54-66% cellulose, 12-17% hemicellulose, 7-14% lignin, 1% pectin and 1-7% ash.

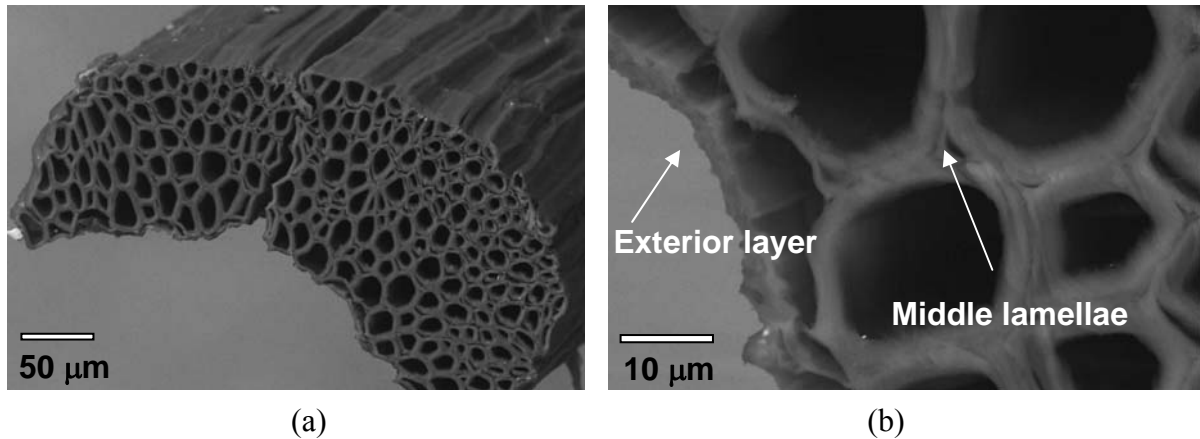


Figure 1. Sisal fiber morphology showing: a) fiber composed of several fiber-cells linked by the middle lamellae and b) detail of middle lamellae (composed of lignin and hemicellulose) and exterior layer.

To be used as reinforcement in the developed composite, the sisal fibers were washed in hot water, brushed to separate the individual fibers and cut to the size of the molds (400 mm). The fibers were weighted and separated into five different layers resulting in a total volume fraction of 10%. The sisal fibers were stitched by three cotton fibers to make a homogeneous spacing between the fibers so as to facilitate the molding process.

2.1.2. Matrix

The matrix was designed using the Portland cement CII F-32 defined by the Brazilian standard [15] as composed with filler (in mass: 85%<clinker<91%; 3%<gypsum<5%; 6%<filler<10%) with 32 MPa of compressive strength at 28 days. Following the recommendations of previous studies, in order to increase the durability of the composites, the Portland cement was replaced by 30% of MK and 20% of CWCCB metakaolin (MK) [11, 12]. By replacing 50% of cement by the calcined clays it was possible to develop a matrix that was free of calcium hydroxide (CH) at 28 days of age. The metakaolin was obtained from Metacaulim do Brasil Industria e Comércio LTDA, and calcined waste crushed clay brick (CWCCB) from an industry located in Itaborai – RJ, calcined at 850 °C. The mortar matrix used in this study presented a mix design of

1:1:0.4 (cementitious material : sand : water by weight). The physical and chemical characteristics of the cementing materials are presented in Table 1. In the present work two matrices were used: one free of calcium hydroxide denominated M1 (CH free composite) and the other made of Portland cement with no additions and denominated M0 (PC composite).

Mineral micro-fiber of wollastonite JG obtained from Energyarc was used as micro-reinforcement ($V_f = 5\%$). The wollastonite fiber featured a density of 2.9 g/cm^3 . The Flow Table Spread (FTS) test was used to determine the content of superplasticizer to be added to matrices in order to guarantee a fluidity index (FI) higher than 70%. This index is defined by $FI = (S_f - S_i)/S_i$, where S_f and S_i are the final and initial spread, respectively. The matrix free of CH (M1) presented a fluidity index of 73% whereas the OPC matrix (M0) presented a FI of 76%. Both matrices present characteristics of self compacting mixes. The optimum fiber volume fraction (V_f) of the sisal fiber was determined as 10 % based on results of previous works [16, 17].

Table 1. Physical and chemical characteristics of the Portland cement, calcined waste crushed clay brick and metakaolin.

Chemical properties	Portland Cement	CWCCB	MK
SiO ₂ (wt%)	19.98	63.89	51.20
Fe ₂ O ₃ (%)	3.12	7.73	4.00
Al ₂ O ₃ (%)	3.70	25.49	35.30
CaO (%)	62.80	0.29	2.62
MgO (%)	3.10	0.04	0.40
Na ₂ O (%)	0.07	Traces	-
K ₂ O (%)	0.80	0.95	0.97
TiO ₂	-	-	0.41
Insoluble residue (%)	1.50	Traces	Traces
% retained on mesh 325 (45 μm)	22	35	0

2.1.3 Processing

The matrix was produced using a bench-mounted mechanical mixer with a capacity of 20 liters. The cementitious materials were dry mixed for 30 seconds (for homogenization) with the subsequent addition of sand and wollastonite. The powder

material was mixed for 30 seconds more and the superplasticizer diluted in the water was slowly poured into the running mixer and subsequently mixed for 3 minutes.

For the production of the flat and corrugated laminates, the mortar mix was placed in a steel mould by a manual lay-out technique, one layer at a time, followed by one layer of fibers and vibration. Corrugated and flat composites were produced with the dimensions of 400 mm x 400 mm x 12 mm to investigate the influence of the corrugation on the bending behavior of the material, see Figure 2.

The vibrating table was used at a frequency of 65 Hz. Composites with five layers were produced using the technique described and then compressed at a pressure of 3 MPa for 5 minutes. The pressure of 3 MPa was chosen after an optimization process in which pressures ranging from 0 to 4 MPa were tested. Details of this study can be found elsewhere [17]. The composites were fog cured for 28 days in a cure chamber with 100 % relative humidity (RH) and 23 ± 1 °C.

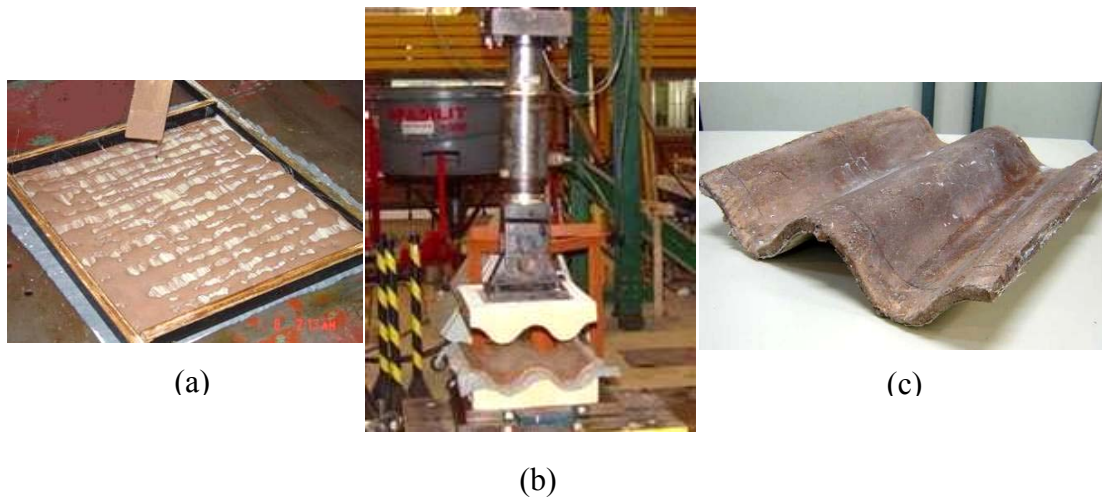


Figure 2. Production of the corrugated and flat laminates: (a) Placement of the matrix and fiber layers, (b) compression molding and (c) final product.

2.2. Test Methods

2.2.1 Mechanical properties

To determine the mechanical properties of the studied composites at 28 days of age, a Shimadzu UH-F 1000 kN was used. Direct tension and bending tests were performed.

The direct tension and bending tests were carried out under displacement control at a crosshead rate of 0.1 mm/min and 0.5 mm/min, respectively.

Three specimens with the dimensions of 400 mm x 100 mm x 12 mm (length x width x thickness) were tested under a four-point bending (300 mm span). Corrugated and flat sheets (with dimensions of 400 mm x 400 mm x 12 mm) were tested under a three-point bending configuration. Deflections at mid-span were measured using an electrical transducer (LVDT) and the loads and corresponding deflections were continuously recorded using a 32-bit data acquisition system taking four readings per second.

For the direct tension tests specimens were cast producing samples of 400 mm x 50 mm x 12 mm (200 mm span between grips). Hinged-hinged boundary conditions were used. The displacement measurements were realized using two LVDT's mounted apart in the central part of the specimen on a base of 100 mm. The crosshead displacements were also recorded. Data acquisition follows the same procedure as per the bending tests. The specimens were cured for 28 days in a fog chamber with 100% RH.

2.2.3. Physical properties

The rate of capillary absorption was obtained using a rectangular specimen of 25 mm × 25 mm × 12 mm. The specimens were initially dry in an oven ($T = 100\text{ }^{\circ}\text{C}$) until constant mass was reached. Afterwards they were placed in contact with the water in a shallow tray. The lateral faces of the specimens were sealed and the water was absorbed through the 25 mm × 25 mm bottom face.

The water tightness was determined following the Brazilian standard NBR 5642 [18]. In the tightness test a hollow cylindrical tube with 35 mm diameter and enough height to allow a water column of 250 mm is set over the specimen flat surface in the vertical position. The cylinder was filled with water to 250 mm and rested for 7 days. Visual inspections were carried out during the test duration to monitor the appearance of water marks and leak in the bottom face of the specimens. The tests were carried out in square flat specimens (150mm x 150mm x 12mm) after being cured for 60 days in a fog chamber with 100% RH.

To determine the drying shrinkage of the CH free composite and its matrix, a frame (see Figure 3) was fabricated and two strain indicators were used to measure the

deformations. Flat plates with dimensions of 400 mm x 400 mm x 12 mm were tested after being cured for 60 days in a fog chamber with 100% RH. The tests were performed in a room with controlled temperature (19 ± 0.5 °C) and humidity (53 ± 5 %).



Figure 3. Drying shrinkage test set-up. The strains were measured by two strain indicators located at the top of the frame.

2.2.2. Durability

The durability of the composites was evaluated through accelerated aging tests. The samples were cured for 28 days in a cure chamber with 100 % relative humidity (RH) and 23 ± 1 °C, and then immersed in hot water at 60 °C for 6 months. Three specimens of each type of matrix (M1 and M0) were tested under four point bending after the aging process.

The scanning electron microscopy was performed in a Jeol JSM 6460 LV operating under a low vacuum chamber to remove the high vacuum constraint in the sample environment. The microscope was operated under an accelerating voltage ranging from 10 kV to 20 kV. No precoating with carbon or gold, as is done for standard high vacuum SEM, was required. The specimen chamber pressure was adjusted to 30 Pa. All the micrographs were taken under the Backscattered electrons mode.

3. Results and Analysis

3.1. Mechanical Properties

Typical curves obtained from the direct tensile tests for the composites made of PC matrix and blended PC + MK + CWCCB (CH free) matrix are presented in Figure 4a. The initial stress-strain response in tension (figure 4a) is linear elastic as the specimen exhibits a high stiffness, but a low first crack strain capacity. From a macroscopic perspective, the bend over point (BOP) corresponds to the formation of matrix cracking. CH free composites presented average BOP ranging from 6.06 to 6.78 MPa whereas the PC composites presented slightly lower BOP's which varied from 5.16 to 5.43 MPa (refer to Table 2).

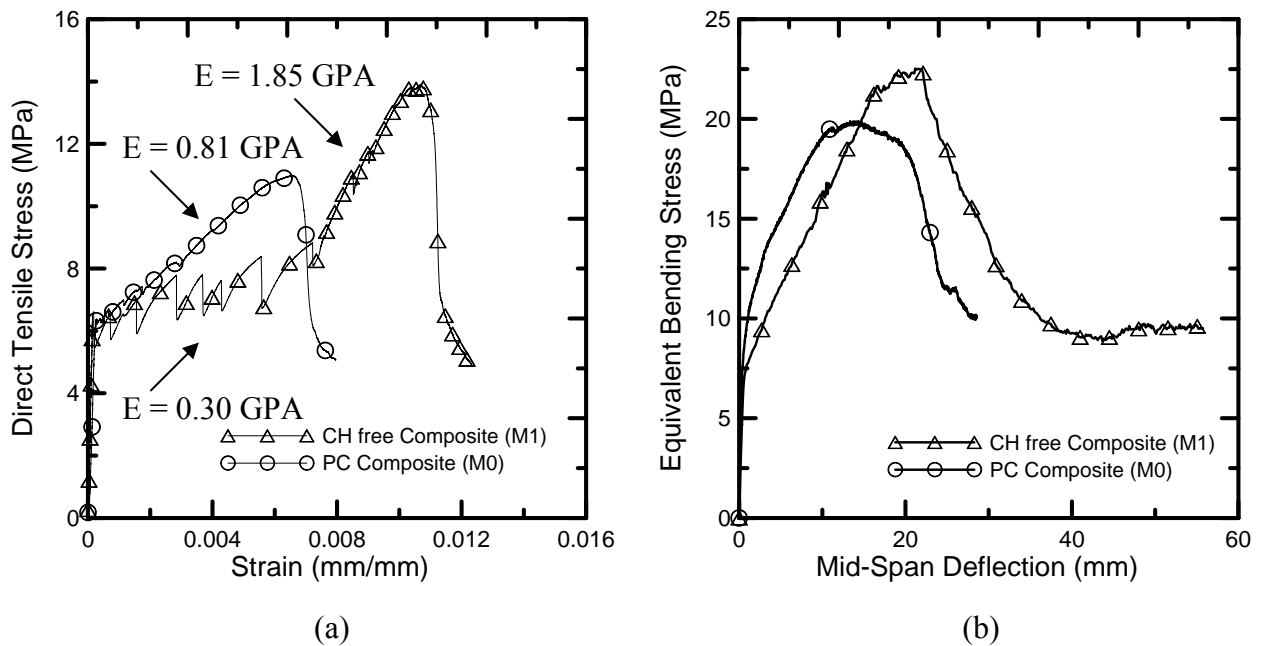


Figure 4. Mechanical response of CH free and PC non aged composites: (a) direct tension test (note the difference in the post-cracking modulus) and (b) four-point bending test.

The standard deviation was around ± 1 MPa. At this linear range the response is dominated by the matrix and the Young's modulus measured from LVDT data was found to be approximately 24 GPa for the CH free and 19 GPa for the PC composite (see Table 2). The stage after the BOP was characterized by a multiple cracking formation for both composites. The stiffness of the sisal fiber reinforced cement

composite system is sufficiently high to keep the newly formed cracks from widening and thus promoting a multiple cracking behavior observed in Figure 4. The modulus after the BOP and during the multiple cracking formation decreased to 0.30 GPa in the CH free composites and to 0.81 GPa for the PC composites. As can be seen in Figure 4a the two composite systems present a distinct behavior after the BOP zone. It was observed a superior number of cracks with lower width for the PC composites in comparison to the CH free. This behavior may indicate higher bond strength for the PC composite therefore, resulting in a stiffer Post-BOP region. The multiple cracking behavior reached a saturation level at about 0.8 % for CH free composites and 0.6 % for PC composites (refer to Figure 4a). For the CH free composites, after the crack saturation level the response is dominated by progressive damage and characterized by a crack widening stage ultimately leading to failure by fiber pullout. At this level the sisal fiber is taking most of the load. The Young's modulus was computed and found to be 1.85 GPa. If using the rule of mixtures to calculate the modulus ($E_f V_f = 19 \times 0.1 = 1.9$ GPa) a good agreement is obtained for the CH free composite. For the PC composite it was observed a combined failure mechanism characterized by fiber pull-out and fiber fracture. A distinction between the multiple cracking stage and fiber widening is not observed in the stress-strain response (see Figure 4a). The ultimate tensile strength (UTS) for the CH free and PC composites were 13.95 MPa at 1% strain and 9.24 MPa at 0.45%, respectively.

Table 2. Summary of direct tension tests of non-aged composites (Mean values and standard deviation in parenthesis).

Composite	*E _{initial} (GPa)	**E _{initial} (GPa)	σ _{BOP(-)} (MPa)	σ _{BOP(+)} (MPa)	ε _{BOP(-)} (%)	ε _{BOP(+)} (%)	UTS (MPa)	ε _{ultimate} (%)	Toughness (kJ/m ²)
CH free	24.25	2.17 (0.52)	6.06 (0.71)	6.78 (1.13)	0.021 (0.0078)	0.023 (0.0062)	13.95 (1.6)	1.00 (0.05)	20.03 (2.79)
PC	18.61	1.67 (0.27)	5.16 (1.13)	5.43 (1.09)	0.027 (0.004)	0.039 (0.01)	9.24 (1.52)	0.45 (0.15)	10.06 (4.84)

*Young's modulus measured from LVDT data. **Young's modulus measured from cross-head displacement data.

Tension toughness was calculated as the area under the load vs. displacement curve. CH free composites presented toughness twice as much as of the PC composite (see Table 2). The better performance obtained in tension by the CH free composite indicates that the partial substitution of cement by the calcined clays may have resulted in a lower bond strength thus, promoting an interface transition zone for the composites that allowed a fiber pull out failure mechanism with a longer multiple cracking stage and higher UTS.

Four-point bending typical curves are shown in Figure 4b. An elastic-linear range where both matrix and the fiber behave linearly is observed up to a point where the matrix cracks. The end of the linear elastic range is delimited by lower and upper bounds of the limit of proportionality (LOP). CH free composites presented average LOP ranging from 6.0 to 7.16 MPa while for PC composites the LOP ranged from 6.27 to 8.58 MPa (see Table 3).

Table 3. Summary of bending tests of aged and non-aged composites (Mean values and standard deviation in parenthesis).

Aging	Composites	$\sigma_{LOP(-)}$ (MPa)	$\sigma_{LOP(+)}$ (MPa)	$\delta_{LOP(-)}$ (mm)	$\delta_{LOP(+)}$ (mm)	MOR (MPa)	$\delta_{ultimate}$ (mm)	Toughness (kJ/m ²)
Non-aged	CH free	6.00 (0.74)	7.16 (0.92)	0.43 (0.04)	0.64 (0.07)	23.21 (2.86)	19.75 (6.29)	29.66 (7.60)
	PC	6.27 (1.01)	8.58 (1.83)	0.52 (0.21)	1.01 (0.15)	21.08 (6.78)	13.25 (2.62)	18.12 (9.22)
Aged (6 months at 60 °C)	CH free	7.26 (0.42)	8.00 (0.95)	0.42 (0.04)	0.50 (0.10)	23.25 (2.71)	18.00 (1.36)	28.00 (3.34)
	PC	-	-	-	-	6.06 (0.60)	0.53 (0.10)	0.66 (0.48)

Standard deviations varied from 0.7 to 1.8 MPa. The post LOP range was characterized by a multiple cracking formation. The failure of the composites occurred after a mid-span deflection around 13 mm (PC composite) and 19 mm (CH free composite). Failure of the composites were followed by a strain softening response due to the localization and widening of one of the existing cracks. Modulus of rupture (MOR) were in the same range for both composites (21MPa for PC and 23MPa for CH free composites) but the energy absorption capacity was approximately 50 % higher for the CH free composite (see Table 3).

The bending and tensile responses are compared in Figure 5 and 6. The inset plot shows the relationship between LOP vs. BOP and MOR vs. UTS. It can be seen that under bending, loads associated with the formation of the first crack (BOP^+ and LOP^+) occur at stress levels similar than those observed for the direct tension tests in CH free composites and higher for PC composites. It is important to mention that some data scatter was observed at this stress level (see inset plots of Figure 5 and 6). The values reported for MOR is approximately two times greater than that of the UTS; such response has been theoretically and experimentally shown to exist for a variety of strain hardening cement composite systems [19].

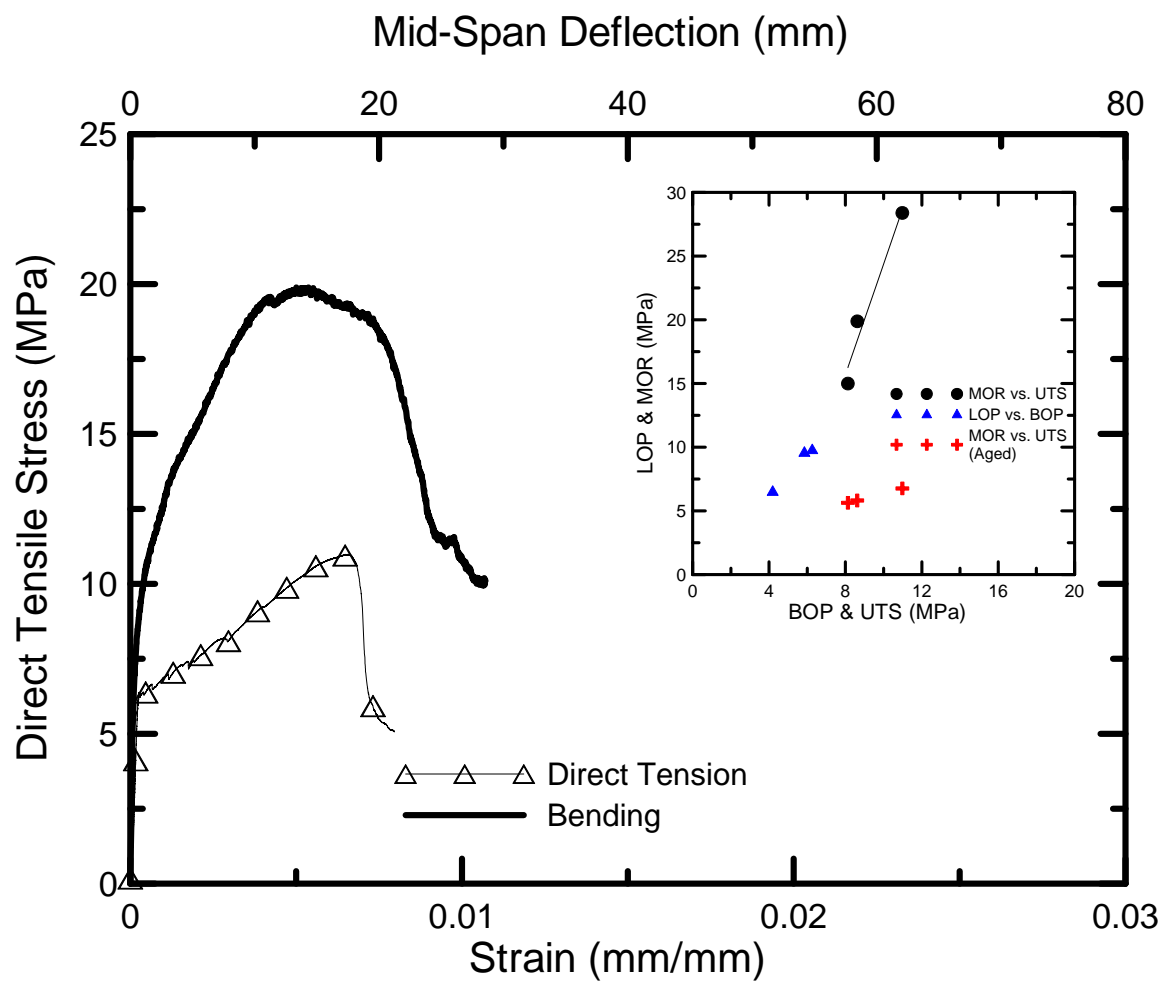


Figure 5. Comparison of direct tension and four-point bending behavior of PC composites. The inset shows a comparison of MOR vs. UTS and LOP vs. BOP.

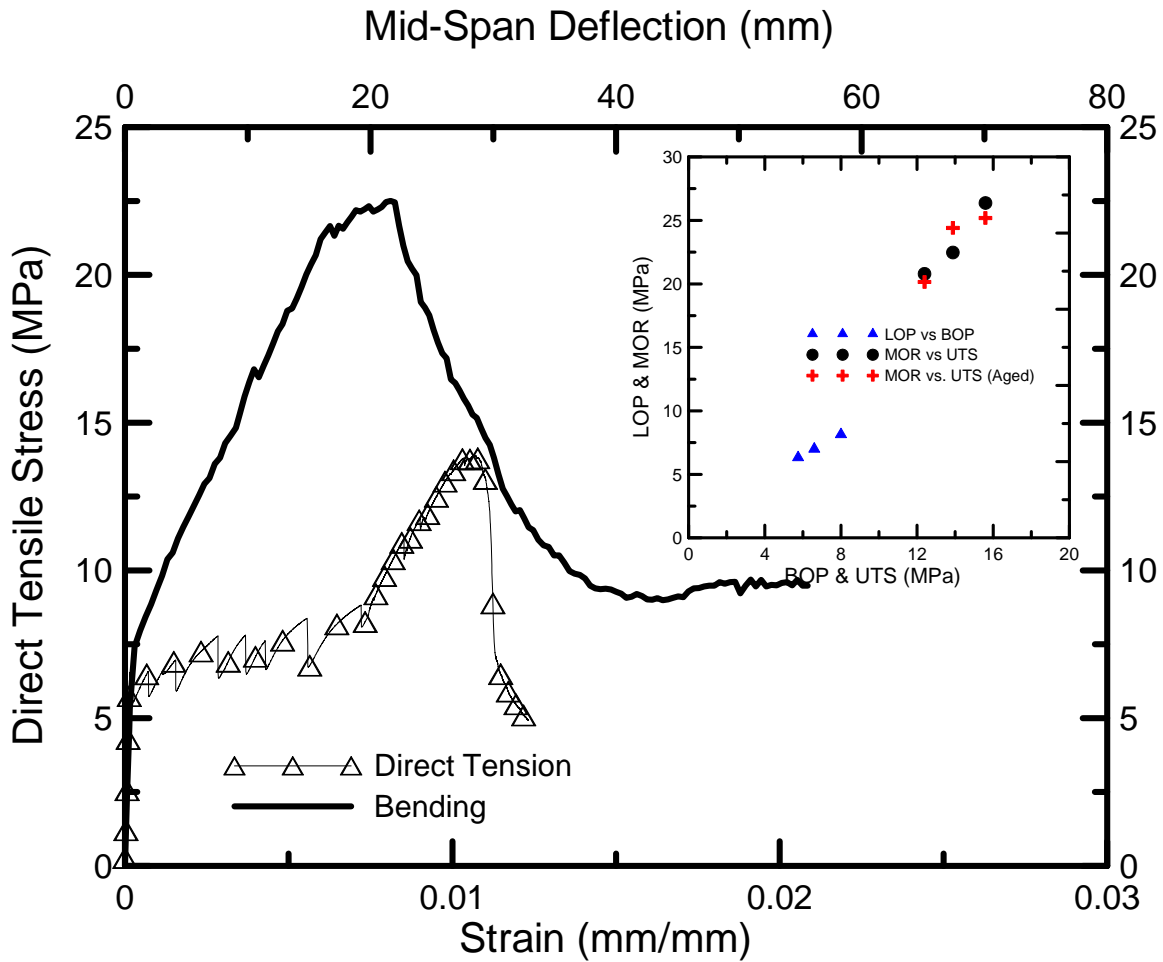


Figure 6. Comparison of direct tension and four point bending tests of CH Free Composites. A correlation of LOP vs. BOP and MOR vs. UTS is shown in the right upper corner.

The load-displacement typical curves of the corrugated and flat laminates as well as their corresponding cracking patterns are presented in Figure 7. The flat composites featured an average first crack load of 1.24 kN and an ultimate load of 3.91 kN. The corrugation increased the stiffness which resulted in higher first crack and ultimate load values of 6.81 and 10.26 kN, respectively (see Figure 7a). Both structures showed a multiple cracking behavior. However, the cracking pattern in the plain sheet was more concentrated in the center while in the corrugated, it was more randomly distributed over the material, see Figure 7 (b) and (c). The displacement values which referred to

the ultimate strength amounted to approximately 10 mm for the corrugated and to 24 mm for the flat sheet, respectively, which results from the higher stiffness promoted by the corrugation.

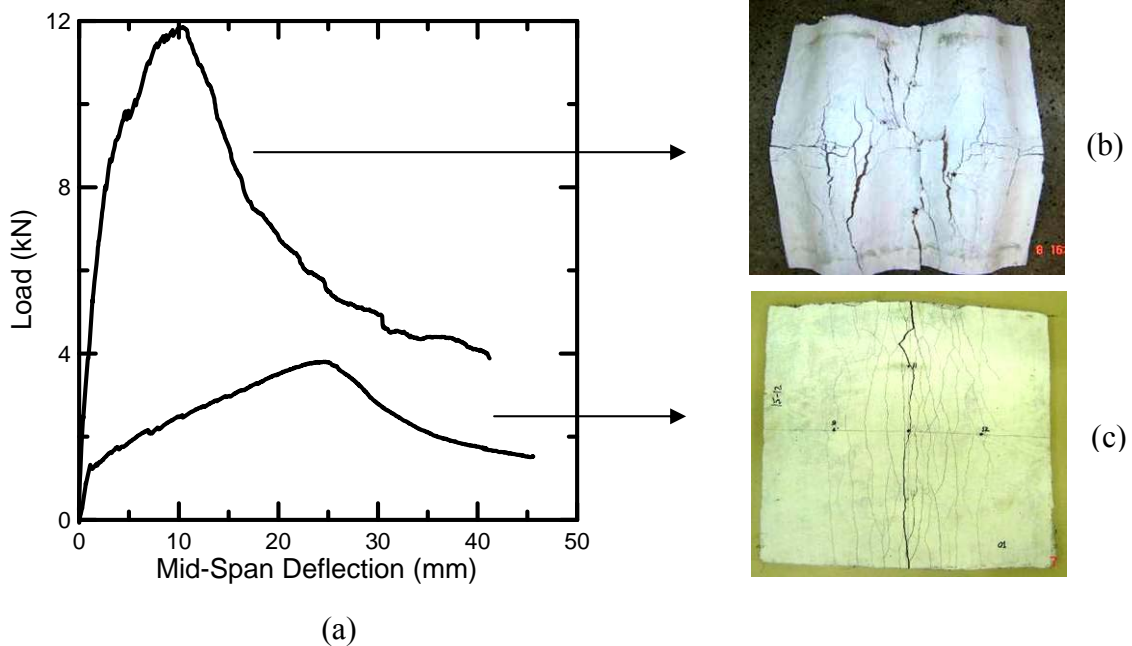


Figure 7. Effect of corrugation on the mechanical performance of the composites: (a) typical three-point bending curves of corrugated and flat laminates, (b) and (c) cracking pattern of the corrugated and flat laminates, respectively.

3.2. Physical Properties

The drying shrinkage curves for the CH matrix and the CH free composite are presented in Figure 8. It was observed that the drying shrinkage increases with the presence of sisal fiber. When comparing the shrinkage presented by the matrix M1 to the composite it was noticed an increment of 40%. A difference of 5 % was noticed when measuring the shrinkage parallel and perpendicular to the fiber which suggests that the fiber orientation does not affect the shrinkage for the developed composite. The drying shrinkage of a cement matrix is mainly related to the magnitude of its porosity and to the size, shape and the continuity of the capillary system in the hydrated cement paste. The addition of the sisal fibers increased the matrix porosity, therefore contributing to the higher drying shrinkage of the composite that was observed in this work. The porous nature of the used fibers at the micro-structure level created more moisture paths into the matrices which contributed to the increased drying shrinkage. A similar behavior was observed for short sisal and coconut fiber-cement based composites [20].

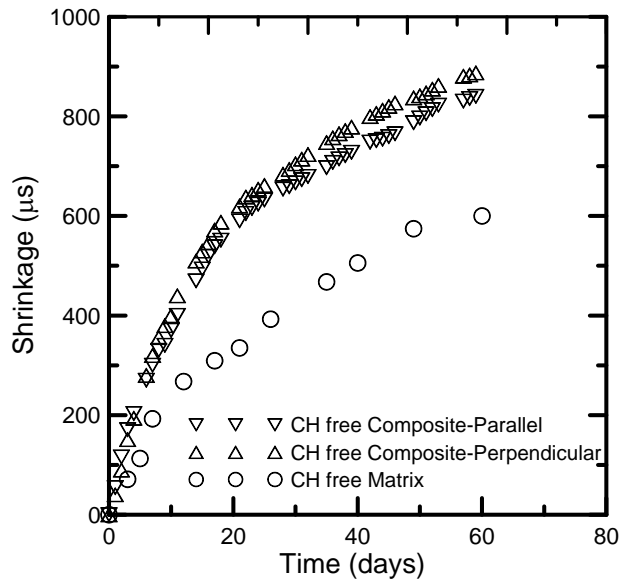


Figure 8. Drying shrinkage curves of CH free composite and CH free matrix fog cured for 60 days (measured parallel and perpendicular to the fibers).

In the water tightness test, after 24 hours, it was noticed no water marks in the back of the sample. After 48 hours a new verification was made and again no water marks or leaks were seen. The last inspection has been done after 7 days and once more no water leaks or marks were noticed in the opposite face of the composite. The absence of marks maybe an indication of a reduced and disconnected pore structure of the composite system.

The capillary water absorption curve is presented in Figure 9. There are three defined stages for the CH free and PC composites: (i) initial stage where i is linear in $t^{1/2}$, with slope S_m which defines the composite sorptivity; (ii) transitional stage which deviates from $t^{1/2}$ kinetics and ends at the beginning of the terminal stage; (iii) a terminal stage at which the wet front has reached the end of the specimen and further absorption is much slower or do not take place. It can be seen from Figure 9 that water absorption of both composites follows an exponential decay function. The composites presented sorptivity values of $0.025 \text{ cm min}^{-1/2}$ for CH free and $0.019 \text{ cm min}^{-1/2}$ for the PC composites. The obtained sorptivity values are in the range of those found by Hall [21] for cement based construction materials. For example, cement mortars and concrete presented sorptivities values ranging from $0.019 \text{ cm min}^{-1/2}$ $0.19 \text{ cm min}^{-1/2}$.

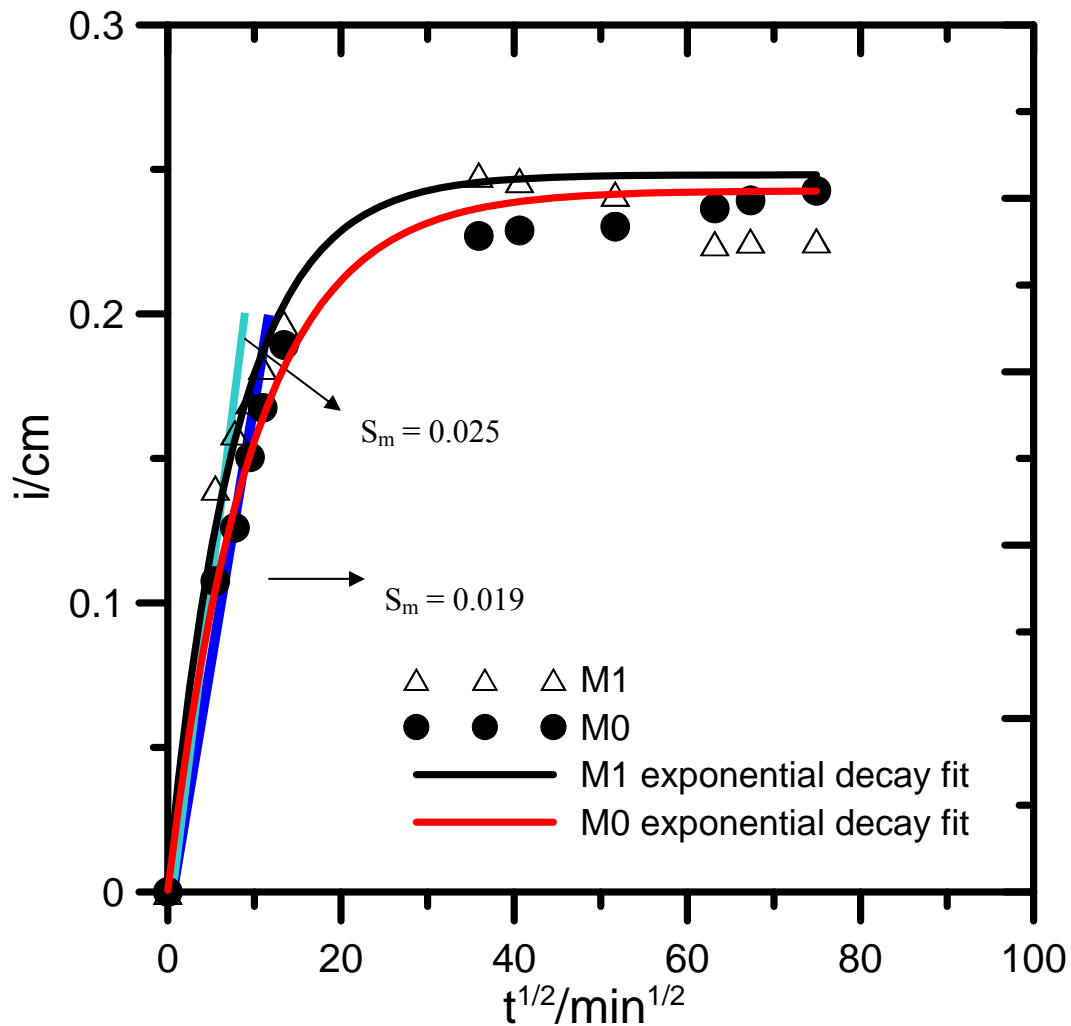


Figure 9. Capillary water absorption: Cumulative absorption i vs. $t^{1/2}$; experimental points are marked by triangles for CH free (M1) and circles for PC (M0) composites. The sorptivity S_m is defined by the main linear portion of the figure.

3.3. Durability

Figure 10 presents typical four-point bending curves of CH free and PC based composites after 6 months of hot water immersion (at 60°C). In opposition to the PC, the CH free composite did not suffer any mechanical degradation with the accelerated aging as can be seen in Figure 10 and 11. A multiple cracking behaviour still can be observed for the aged CH free composite. Average toughness and MOR values of 28 kJ/m² and 23.25 MPa were reported for the aged CH free composite, respectively. These values are in the same magnitude as the ones observed in the non-aged CH free composite (see Table 3). The high deformation capacity of the aged CH free composite can be seen in the insight of Figure 10. The picture shows the deflected specimen at the ultimate load.

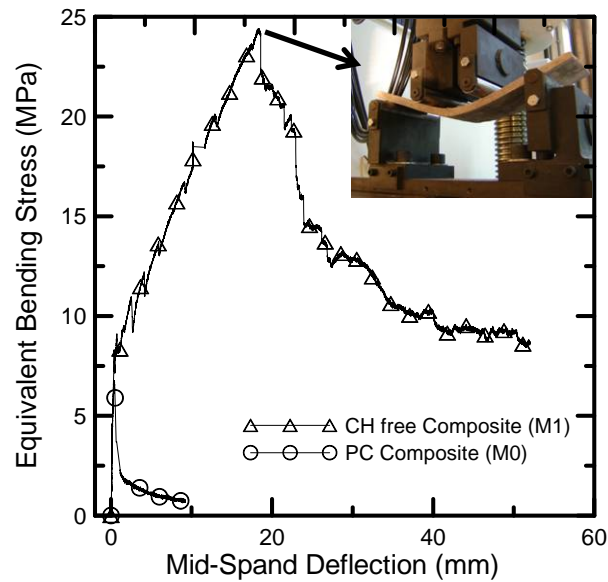


Figure 10. Effect of hot water immersion at 60 °C in the four-point bending response of CH free and PC composites.

The aged PC composite presented a single cracking formation with a fragile post-peak behavior. The average toughness value of this composite decreased from 18.12 to 0.66 kJ/m² with the aging process whereas the MOR decreased from 21.08 to 6.06 MPa. A correlation between degraded MOR vs. UTS for aged PC and CH free composites is shown in the inset of Figure 5 and 6, respectively. It can be seen that after aging the relationship for PC composites drops from 2 to about 0.7 whereas the correlation for the CH free composite remains the same.

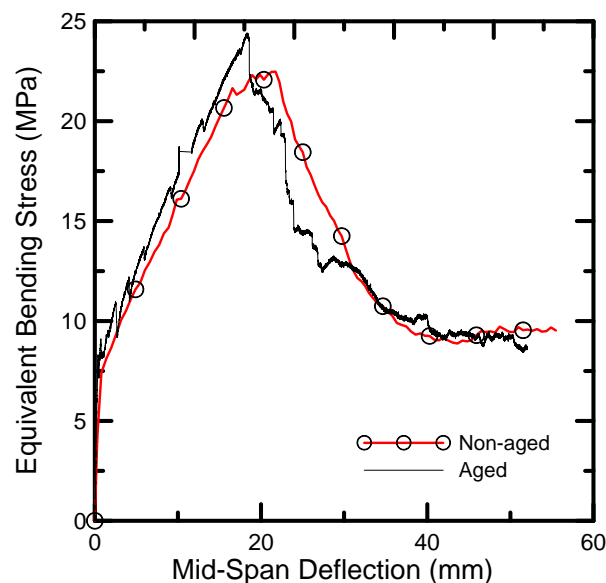


Figure 11. Effect of hot-water immersion on aged CH-Free composite. The plot shows a non-aged CH free composite tested at 28 days and a CH Free composite tested after being subjected to 6 months under hot water immersion at 60 °C.

A microstructural investigation was performed in the CH free and PC aged-composites to investigate the fiber degradation process. Figure 12 shows SEM images of the CH free aged composite. The fiber structure remains intact with no signs of mineralization as can be seen in Figure 12. A calcium (Ca) X-ray mapping was performed in the fiber-matrix interface to verify if leached calcium, from the CH, could have migrate to the interior of the sisal. It was observed a light red color that indicates low amount of Ca.

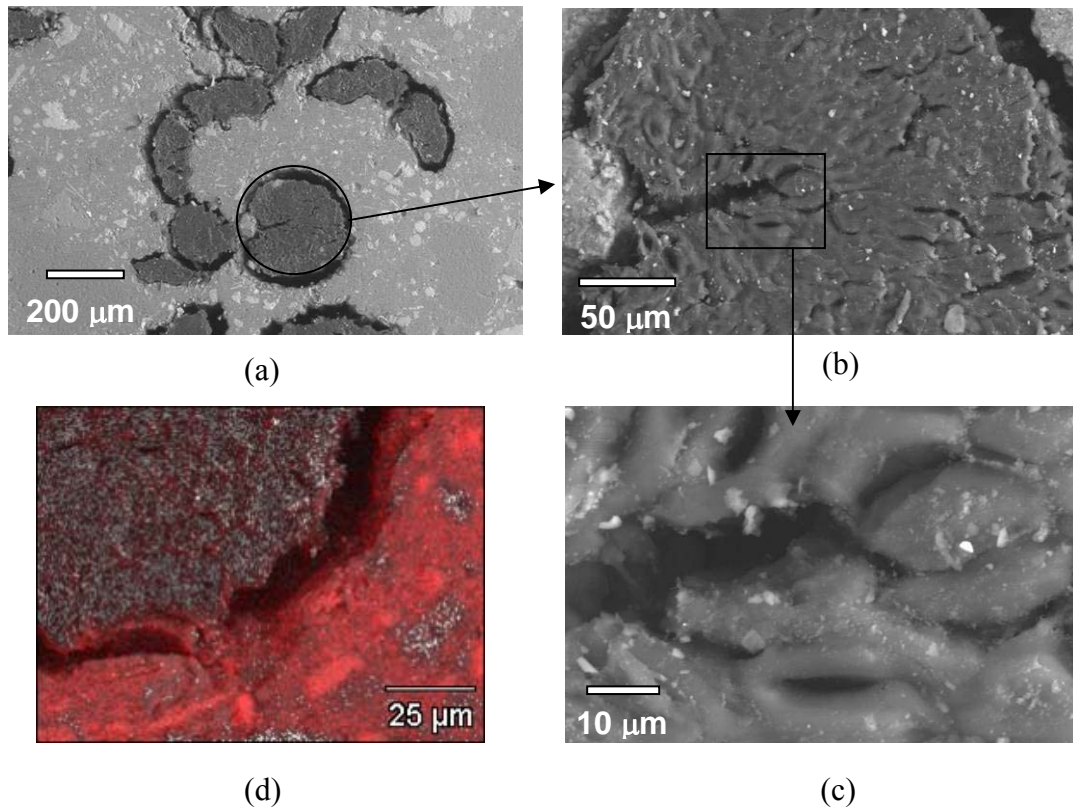


Figure 12. SEM images of the aged CH free composite: (a) Overall view of the composite (b) sisal fiber (c) X-ray mapping for Ca in the fiber-matrix interface and (d) detail of fiber cells.

Figure 13 shows SEM images of the PC aged composite. The sisal fiber microstructure was found to be mineralized as can be seen in Figure 13b. An Energy Dispersive Spectroscopy (EDS) analysis was performed inside the sisal fiber which showed high Ca concentration (see Figure 13 (c) and (d)). A Ca X-ray mapping was performed in the fiber matrix interface and its results have shown a high Ca concentration as can be seen in Figure 13 (e) and (f). This microstructure analysis confirms that in the PC composite the fiber cells are mineralized possible due to high Ca concentration. In the Free CH

composite it was observed no signs of fiber deterioration and much lower Ca concentration inside the fiber cells.

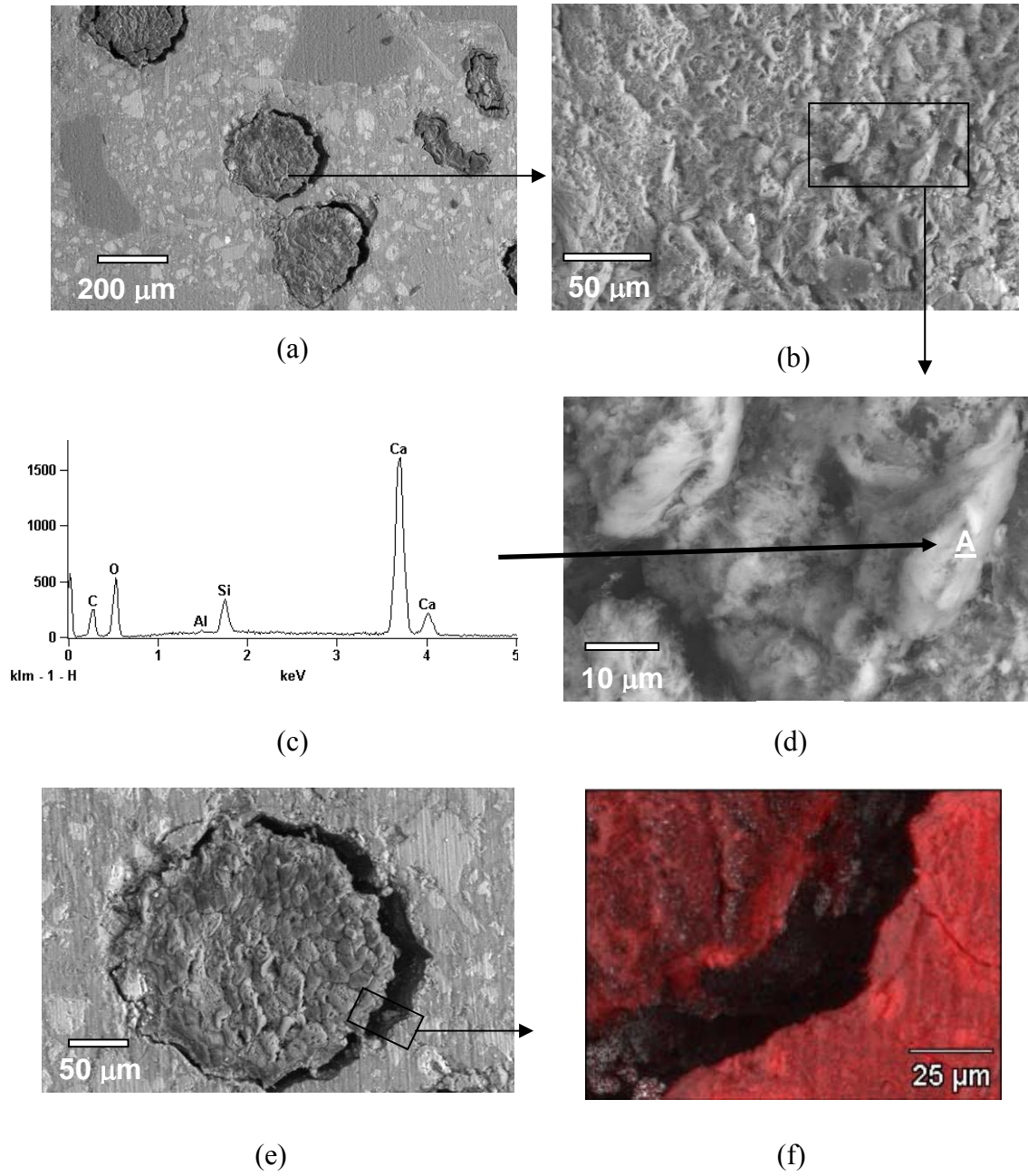


Figure 13. SEM images of PC aged composite: (a) Overall view of the composite (b) Sisal fiber (c) EDS analysis of point A (d) region analyzed by EDS (e) detail of X-ray mapped region (f) X-ray mapping for Ca in the fiber-matrix interface.

The addition of MK and CWCCB have successfully sustained the capacity of energy absorption of the CH free composite, increased its first crack strength and maintained its ultimate strength through accelerated aging, proving to be a good solution for the durability issues of natural fiber as reinforcement in cement composites. The obtained results using the accelerated technique are in accordance with those obtained with wetting and drying accelerated aging presented by the authors previous work using the same materials [11].

4. Conclusions

This work demonstrated the potential of the use of long aligned sisal fibers as reinforcement in thin cement based laminates for semi-structural and structural applications. The material presented a multiple cracking process with a strain hardening behavior both in tension and bending. CH free and PC composites presented UTS of 13.95 and 9.24 MPa, respectively. Toughness of CH free composites under tensile loads were twice as that of the PC composites.

The failure of the composites under bending occurred after a mid-span deflection around 13 mm (PC composite) and 19 mm (CH free composite). Failure of the composites were followed by a strain softening response due to the localization and widening of one of the existing cracks. Modulus of rupture (MOR) were in the same range for both composites (21MPa for PC and 23MPa for CH free composites). It was found that the corrugation of the flat sheets increased its ultimate bending load by about 260%.

Physical tests indicated that both composite systems were quite impermeable with no water leaks or marks being noticed in the opposite face of the specimens even after 7 days of test. Low values of sorptivity ($0.025 \text{ cm min}^{-1/2}$ for CH free and $0.019 \text{ cm min}^{-1/2}$ for the PC composites) were obtained which are in the range of those found in the literature for cement based materials.

The CH free composites, subjected to accelerated aging through hot water immersion, have shown an ultimate bending strength 3.8 times higher and a toughness 42.4 times higher than the PC based composite subjected to the same conditions. The obtained

results indicate the high potentiality of the developed material for the use in the construction industry.

Acknowledgment

The authors would like to acknowledge the CNPq, CAPES, FAPERJ and FINEP for their financial support.

References

- [1] Toledo Filho RD, Scrivener K, England GL and Ghavami K. Durability of alkali-sensivite sisal and coconut fibers in cement mortar composites, *Cement and concrete composites* 2000;2(22):127-143.
- [2] Ramakrishna G. and Sundararajan T. Impact strength of a few natural fibre reinforced cement mortar slabs: a comparative study. *Cement and Concrete Composites* 2005;27:547-553.
- [3] Silva FA, Ghavami K, and d'Almeida JRM. Bamboo-Wollastonite Hybrid Cementitious Composites: Toughness Evaluation. In: Joint ASME/ASCE/SES Conference on Mechanics and Materials, Baton Rouge, 2005.
- [4] Silva FA, Ghavami K, and d'Almeida JRM. Toughness of cementitious composites reinforced by randomly distributed sisal pulps. In: Eleventh International Conference on Composites/Nano Engineering (icce - 11), Hilton-Head Island, 2004.
- [5] Silva FA, Ghavami K, and d'Almeida JRM. Behavior of CRBP-AL subjected to impact and static loading. In: 17th ASCE Engineering Mechanics Conference (EM 2004), Delaware, 2004.
- [6] Mohr BJ, Nanko H, and Kurtis KE. Durability of Kraft Pulp Fiber-Cement Composites to Wet/Dry Cycling. *Cement and Concrete Composites* 2005;27(4): 435-448.
- [7] Roma Jr LC, Martello LS ; Savastano Jr H. Evaluation of mechanical, physical and thermal performance of cement-based tiles reinforced with vegetable fibers. *Construction and Building Materials* 2008;22: 668-674.

- [8] Toledo Filho RD. Composite Materials Reinforced with Natural Fibers: Experimental Characterization, Ph.D. Dissertation, Department of Civil Engineering, Pontifical Catholic University of Rio de Janeiro, 1997.
- [9] Lima PRL. Theoretical Analysis and Experimental Characterization of Composites Reinforced with Sisal Fibers. Ph.D. Dissertation, Department of Civil Engineering, Federal University of Rio de Janeiro, 2004.
- [10] Silva FA, Mobasher B, Toledo Filho RD. Cracking Mechanisms in Durable Sisal Fiber Reinforced Cement Composites. *Cement and Concrete Composites* 2009, In Press.
- [11] Toledo Filho RD, Silva FA, Fairbairn EMR, Melo Filho JA. Durability of compression molded sisal fiber reinforced mortar laminates. *Construction and Building Materials* 2009;23:2409-2420.
- [12] Silva FA, Melo Filho JA, Toledo Filho RD, Fairbairn EMR. Mechanical Behavior and Durability of Compression Moulded Sisal Fiber Cement Mortar Laminates (SFCML). In: 1st International RILEM Conference on Textile Reinforced Concrete (ICTRC), Rilem Publications S.A.R.L., 2006, p. 171-180. doi:10.1617/2351580087.017.
- [13] Silva F.A., Chawla N., Toledo Filho R.D. Tensile behavior of high performance natural (sisal) fibers. *Composites Science and Technology* 2008;68:3438-3443.
- [14] Silva F.A., Chawla N., Toledo Filho R.D. An Experimental Investigation of the Fatigue Behavior of Sisal Fibers. *Materials Science and Engineering A* 2009, In Press. doi:10.1016/j.msea.2009.03.026.
- [15] NBR 11578, Cimento Portland Composto. Associação Brasileira de Normas Técnicas (ABNT), Julho, 1991 (In Portuguese).
- [16] Silva, F.A., Melo Filho, J.A., Toledo Filho, R.D., and Fairbairn, E.M.R. Effect of Reinforcement Ratio on the Mechanical Response of Compression Molded Sisal Fiber Textile Reinforced Concrete. In: High Performance Fiber Reinforced Cement Composites (HPFRCC 5), Mainz, Germany, 2007.

- [17] Melo Filho JA. Development and experimental characterization of cement based laminates reinforced with long sisal fibers. M.Sc. Thesis, Department of Civil Engineering, Federal University of Rio de Janeiro, 2005.
- [18] NBR 5642, Telha de Fibrocimento – Verificação da Impermeabilidade. Associação Brasileira de Normas Técnicas (ABNT), 1993. (In Portuguese)
- [19] Soranakom C. and Mobasher B. Correlation of tensile and flexural responses of strain softening and strain hardening cement composites. *Cement and Concrete Composites* 2008;30:465-477.
- [20] Toledo Filho RD, Ghavami K, Sanjuan M, England G. Free, restrained and drying shrinkage of cement mortar composites reinforced with vegetable fibres. *Cement and Concrete Composites* 2005;27:537-546.
- [21] Hall C., Hoff W. *Water Transport in Brick, Stone and Concrete*. Spon Press, London and New York, 2002.

ARTIGO E - Silva F.A., Mobasher B. and Toledo Filho R.D. Cracking mechanisms in durable sisal fiber reinforced cement composites. Cement and Concrete Composites, in press, 2009.

Cracking Mechanisms in Durable Sisal Fiber Reinforced Cement Composites

Flávio de Andrade Silva^a, Barzin Mobasher^b, and Romildo Dias Toledo Filho^a

^aDepartment of Civil Engineering, COPPE/ Universidade Federal do Rio de Janeiro,
P.O. Box 68506, CEP 21941-972, Rio de Janeiro – RJ, Brazil.

^bDepartment of Civil and Environmental Engineering, Arizona State University, Tempe,
Arizona.

Cement and Concrete Composites

2009

Abstract

Fiber reinforced cement composite laminates with long sisal fibers were manufactured using a cast hand lay up technique. A matrix with partial cement replacement by metakaolin and calcined waste crushed clay brick was used in order to improve the durability aspects. Mechanical response was measured under tension and bending tests while crack formation was investigated using a high resolution image capturing procedure. Crack spacing was measured using image analysis and correlated with the applied strain under both the tensile and bending response. Various stages of loading corresponding to initiation, propagation, distribution, opening, and localization of a crack system in the specimen are discussed. The effect of flexural cracking on the location of neutral axis during the bending tests was measured using strain gages.

Keywords: natural fiber; cement composites; crack formation; image analysis.

1. Introduction

The need for economical, sustainable, safe, and secure shelter is an inherent global problem and numerous challenges remain in order to produce environmentally friendly construction products which are structurally safe and durable. This paper addresses the development of strain hardening cement composites using sisal, a natural fiber with an average tensile strength of 400 MPa and strain at failure of 3% as reinforcement in concrete. These composites provide an exciting opportunity to the housing construction industry and may generate economic incentives particularly in developing countries since the availability and production of composite reinforcement requires a low degree of industrialization. Furthermore, in comparison to the most common synthetic reinforcing fibers, natural fibers require less energy to produce and are the ultimate green products.

Natural fibers have been traditionally used as a substitute of asbestos in the form of chopped, short, and or in a pulp form for the production of thin elements for roofing and cladding. An increased use of these materials for applications such as cladding, internal, and external partitioning walls is possible and may lead towards the development of low cost-sustainable materials [1-8]. Natural fiber cement composites have been mainly reinforced by short or pulp cellulose fibers. Nevertheless, their

application in the construction industry is still quite limited due to the lack of understanding in how to improve the durability while making ductile materials.

Continuous fiber reinforced cement based composites are a new class of sustainable construction materials with superior tensile strength and ductility [9,10]. The enhanced strength and ductility is primarily governed by the composite action that exists such that the fibers bridge the matrix cracks and transfer the loads, allowing a distributed microcrack system to develop. These materials are strong enough to be used as load bearing structural members, in applications such as structural panels, impact & blast resistance, repair and retrofit, earthquake remediation, strengthening of unreinforced masonry walls, and beam-column connections [11].

Vegetable fiber cement composites produced with ordinary Portland cement matrices undergo an aging process in humid environments during which they may suffer a reduction in post-cracking strength and toughness. The aging process is due to fiber mineralization and results in reducing the tensile strength of fibers and decreasing the fiber pull-out ligament after fracture. This mineralization process is a result of migration of hydration products (mainly $\text{Ca}(\text{OH})_2$) to the fiber structure. Efforts to develop durable and structural cement composite laminates reinforced with long sisal fibers has shown much promise recently [12,13]. A recently developed matrix that lowers Calcium Hydroxide production (only 50% Portland cement as compared to conventional systems) increases the long term durability of natural fiber, reduces CO_2 emissions, and presents an economical and sustainable approach. The modified matrix has shown no strength and toughness reduction in accelerated aging tests [13]. The present study is focused on the implementation of this matrix in lieu of a Portland cement matrix which invariably results in a low durability performance record [13].

A fundamental understanding in toughening mechanisms and how cracks form and propagate in the brittle matrix composites is important for optimization, analysis, and design. The cracking mechanism in a multilayer sisal fiber reinforced composite is addressed in this paper. An experimental procedure was used to monitor and analyze the distributed cracking formation, the stiffness degradation, and the crack spacing distribution functions during flexural bending and tensile tests. Photographs of the crack formation at periodic strain levels were processed by image-analysis techniques and correlated with the applied stress levels. The differences between the flexural results and tensile results were studied by comparing the strain distribution profiles in the

loading configuration. In the tension test, the strain distribution was verified by the uniform nature of cracking across the specimen, whereas in the flexural test, the movement of the neutral axis was experimentally determined by strain-gages attached to compression and tensile composite surfaces. Analysis of the flexural strains allows a direct comparison between material properties obtained from tensile and flexural data.

2. Experimental Program

2.1. The sisal Fiber

The sisal fibers used in this investigation were extracted from the sisal plant in a farm located in the city of Valente, state of Bahia – Brazil. The sisal plant leaf is a functionally graded composite structure which is reinforced by three types of fibers: structural, arch, and xylem fibers. The first occurs in the periphery of the leaf providing resistance to tensile loads (see Figure 1). The others present secondary reinforcement, occurring in the middle of the leaf, as well as, a path for nutrients. The fibers were characterized earlier to have an irregular cross section with mean area ranging from 0.04 to 0.05 mm² and a mean density, elastic modulus, and tensile strength of 0.9 g/cm³, 19 GPa and 400 MPa, respectively [14].

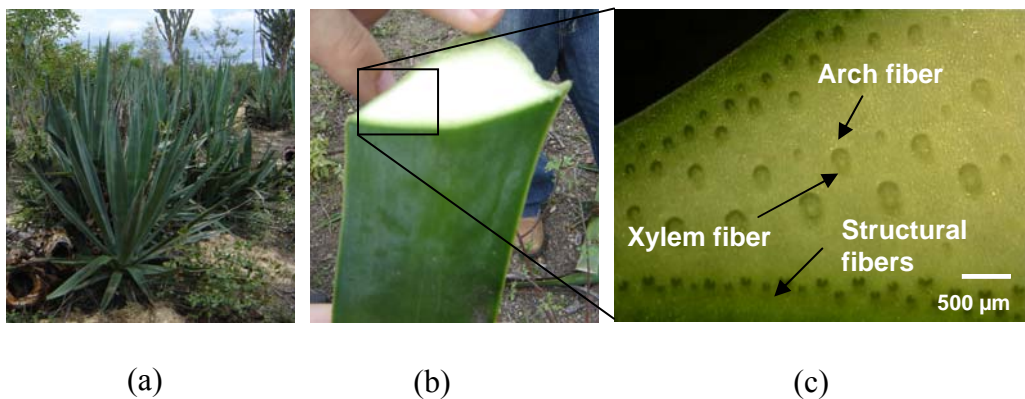


Figure 1. The sisal plant (a), leaf (b) and leaf cross section showing different fiber types (c).

Sisal fibers contain numerous elongated fiber-cells which are about 6 to 30 μm in diameter [15]. The microstructure of the fiber-cell is shown in Figure 2. The individual fiber-cells are linked together by means of the middle lamella, which consist of

hemicellulose and lignin. The lumen varies in size but its shape is usually well-defined (see Figure 2b). Each individual fiber-cell is made up of four main parts, namely the primary wall, the thick secondary wall, the tertiary wall and the lumen (see Figure 2c). After receiving the sisal fibers they were washed and cut to the size of the molds (400 mm). The fibers were weighted and separated into five different layers resulting in a total volume fraction of 10% (see section 2.3). The sisal fibers were stitched by three cotton fibers to make a homogeneous spacing between the fibers so as to facilitate the molding process.

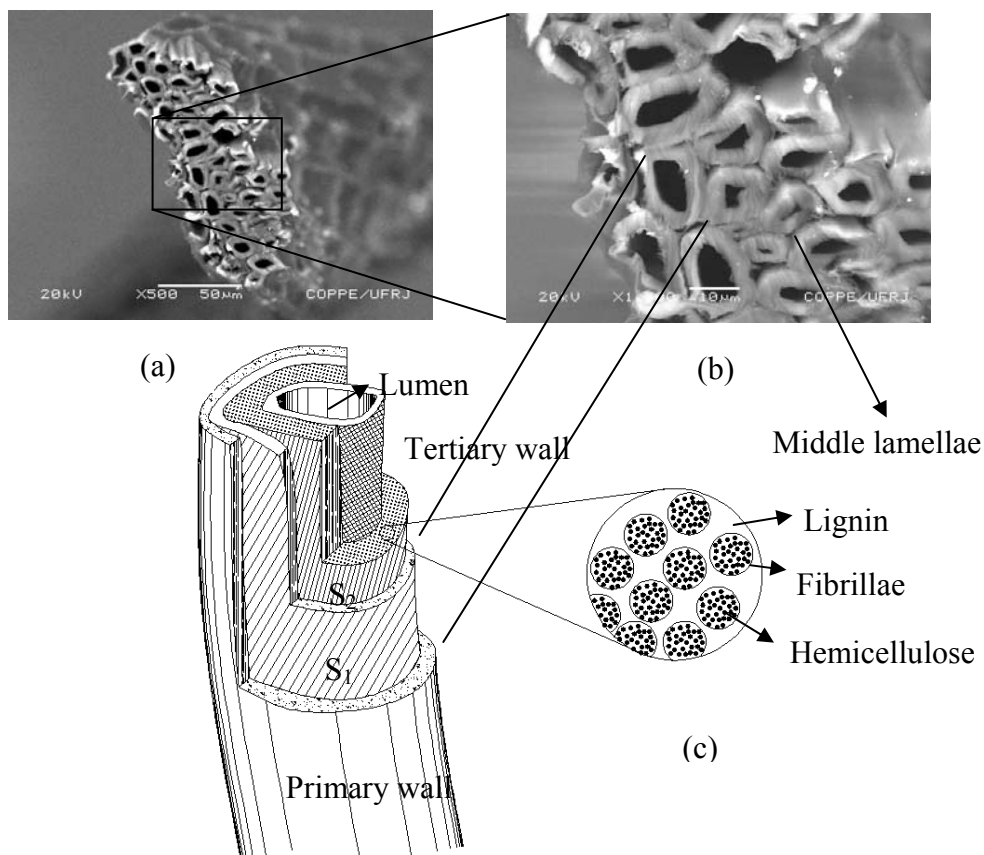


Figure 2. Fiber-cell microstructure: (a) cross section view showing the fiber-cells, lumens and middle lamellae (b) magnification of the cross section and (c) schematic drawing showing the different layers of an individual fiber-cell.

2.2. Matrix Modification

To increase the durability of the composites, the cementitious matrix consisted on 50% Portland cement, 30% metakaolin (MK) and 20% calcined waste crushed clay brick (CWCCB) [12,13]. Portland cement CII F-32 defined by the Brazilian standard [16] as

composed with filler (in mass: 85%<clinker<91%; 3%<gypsum<5%; 6%<filler<10%) with a 28 days compressive strength of 32 MPa was used. The metakaolin (MK) was obtained from Metacaulim do Brasil Industria e Comércio LTDA, and calcined waste crushed clay brick (CWCCB) from an industry located in Itaboraí – RJ, Brazil, calcined at 850 °C. The mortar matrix used a mix proportion of 1:1:0.4 (cementitious material:sand:water by weight). River sand with a maximum diameter of 1.18 mm and density of 2.67g/cm³ and a naphthalene superplasticizer Fosroc Reax Conplast SP 430 with content of solids of 44% were used.

Wollastonite is a naturally occurring white, non-metallic mineral with an acicular morphology. Wollastonite fiber (JG class, CaSiO₃), obtained from Energyarc, with an average equivalent diameter of 40 µm and an aspect ratio of 15 was used as a micro-reinforcement in the composite production ($V_f = 5\%$).

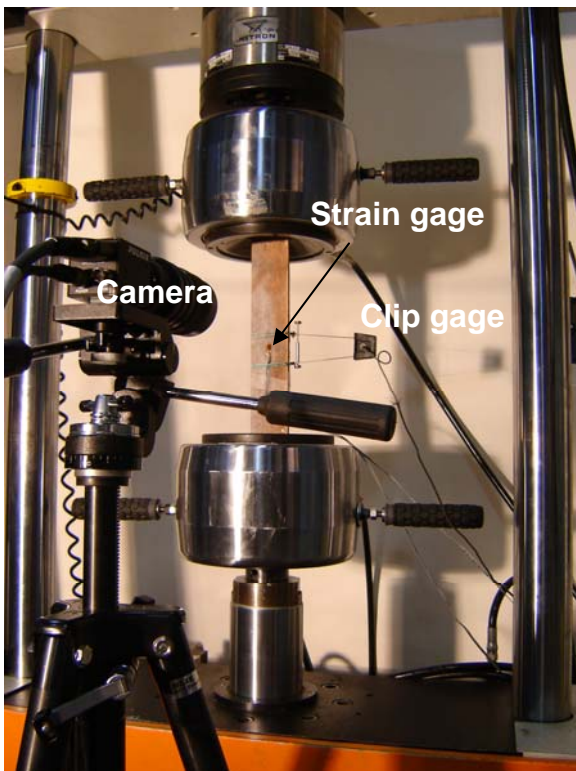
2.3. Composite manufacturing

The matrix was produced using a bench-mounted mechanical mixer of 20 liters capacity. The cementitious materials were homogenized by dry mixing for 30 seconds prior to addition of sand and 5% by volume of wollastonite. The powder material was mixed for an additional 30 seconds prior to addition of superplasticizer and water. The mixture was blended for 3 minutes. For the production of the laminates, the mortar mix was placed in a steel mold, one layer at a time, followed by single layers of long unidirectional aligned fibers (up to 5 layers). The samples were consolidated using a vibrating table operated at a frequency of 65 Hz, resulting in a sisal fiber volume fraction of 10%. After casting the composites were compressed at 3 MPa for 5 minutes. The compression load was applied in the face that the matrix was placed. The specimens were covered in their molds for 24 hours prior to moist curing for 28 days in a cure chamber with 100% RH and 23±1 °C.

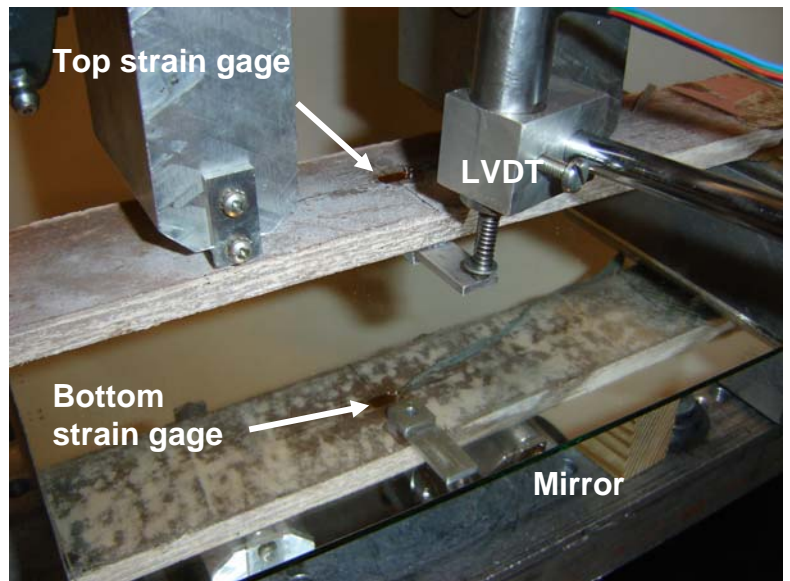
3. Testing

3.1. Mechanical Performance

Direct tensile tests were performed in a closed loop servohydraulic testing machine with a capacity of 500 kN (see Figure 3a). The tests were controlled by the cross-head displacement at a rate of 0.1 mm/min. Six specimens measuring 400 mm x 50 mm x 12 mm (length x width x thickness) were tested using a gage length of 300 mm with fixed–fixed boundary conditions. Aluminum thin sheets were glued on both ends of the specimen and the pressure of the hydraulic grips was adjusted to 1.37 MPa (200 psi) in order to minimize stress concentration and damage. The tensile load, cross head displacement and strain were recorded. Tensile strains were also measured by a strain gage glued on the center of the specimen.



(a)



(b)

Figure 3. Mechanical tests set-up: (a) direct tension and (b) four point bending.

Four point bending tests were performed in a MTS 810 universal testing machine with a capacity of 100 kN. The tests were controlled by the cross-head displacement at a rate of 0.5 mm/min. Six specimens measuring 400 mm x 70 mm x 12 mm (length x width x thickness) were tested under a span of 300 mm. Strain gages were glued at the center bottom and top surface of the specimen in order to compute the extreme fiber strain and the neutral axis (see Figure 3b). The bending load, cross head displacement and strains were recorded.

3.2. Crack Spacing Measurements

By evaluating cracking patterns at regular time intervals, crack development throughout the loading cycle of tensile and bending test were recorded. A digital Pulnix camera with a 10X macro zoom lens and frame grabber captured images of 480x640 in resolution at 60 second intervals. Images were used to measure the crack formation during bending and tension tests. Photos of the tension face in bending tests were taken using a mirror positioned at 45° with respect to the specimen as shown in Figure 3b.

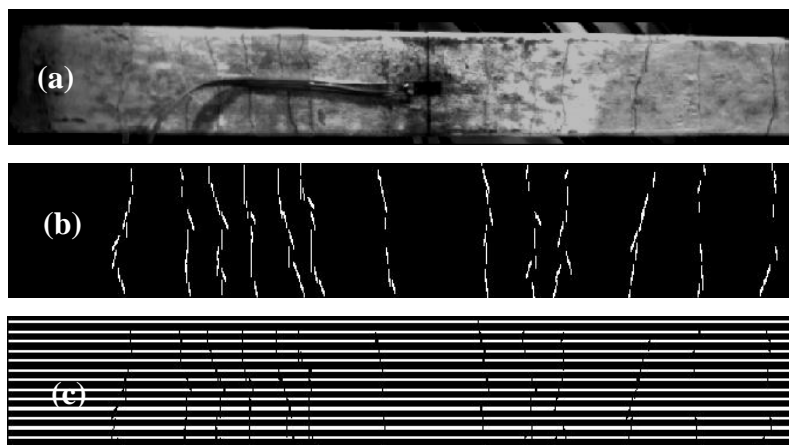


Figure 4. Image analysis methodology: (a) image during tensile test, (b) trace lines of cracking and (c) horizontal line segments representing the distribution of crack spacing.

Image processing was done by the digital processing toolbox of MATLAB. To quantitatively measure the crack spacing as a function of the applied strain, a two step approach was used. During the first step, newly formed cracks of each image were

traced and added to data from previous loading increment. Figure 4a represents the crack development at a strain of 0.0068 mm/mm. The trace profiles of these cracks are shown in Figure 4b. The second step measured the crack spacing from the traced cracks as shown in Figure 4c using the following procedure:

An image consisting of a series of parallel lines was generated. The crack spacing was measured in pixels, and the image was calibrated using conventional techniques to convert the size of a pixel to length measures. By conducting a binary “AND” operation the points of intersection of the series of parallel lines with the cracks were identified. A second binary operation of “OR” between the intersection points and the parallel spacing lines, broke up the straight lines into segments representing crack spacing distribution as shown in Figure 4c. The distribution of the length segments and statistical parameters of crack spacing were computed next [17,18,19].

4. Results and Discussion

4.1. Mechanical Tests

Figure 5 shows a typical tensile stress strain response of the sisal fiber reinforced composite system. Two measures of tensile strain are used including the localized strain measured from the electrical resistance gage and the nominal strain defined by dividing the cross head stroke displacement by the specimen length. Comparison of the two strain measurements allows one to evaluate the early age cracking phase and make a distinction among all stages of cracking. These responses differ at various stages of loading as they correspond to crack initiation, propagation, distribution, opening, and localization.

From a macroscopic perspective, the bend over point (BOP) corresponds to the formation of matrix cracking. Five distinct zones are identified using roman numerals with two zones prior to and three zones after the bend over point (BOP). Figure 5b shows both the initial response and also the overall response of the stress strain curve using a multi-scale axis representation. Figure 6 shows the relationship between the strain gage reading and the strain measured by the stroke. Note that the measurements of these two gages allow differentiation of the response ranges. Zone I corresponds to the elastic-linear range where both matrix and the fiber behave linearly. Due to low

volume fraction of fibers ($\leq 10\%$) the stiffness of the composite is dominated by matrix properties and this zone is limited to strain measures of up to 150-175 μstr as shown by the inset of Figure 6. The initial stress-strain response is marked by a limited range of linear elastic portion as the two strain measures are almost the same, and the specimen exhibits the highest stiffness. The deviation from linearity occur at around 150 microstrains due to initiation and propagation of first cracks. Note that the sensitivity of the stroke displacement in this range is within the instrumentation error, therefore, the strain gage response is far more reliable than the stroke in this range. The linear zone is terminated by initial crack formation in the matrix phase (reported as of $\sigma_{\text{BOP-}}$ from experiments) as shown in Figure 5a. After the initiation of cracks in the matrix, its load carrying capacity does not vanish as the cracks are bridged by the longitudinal fibers.

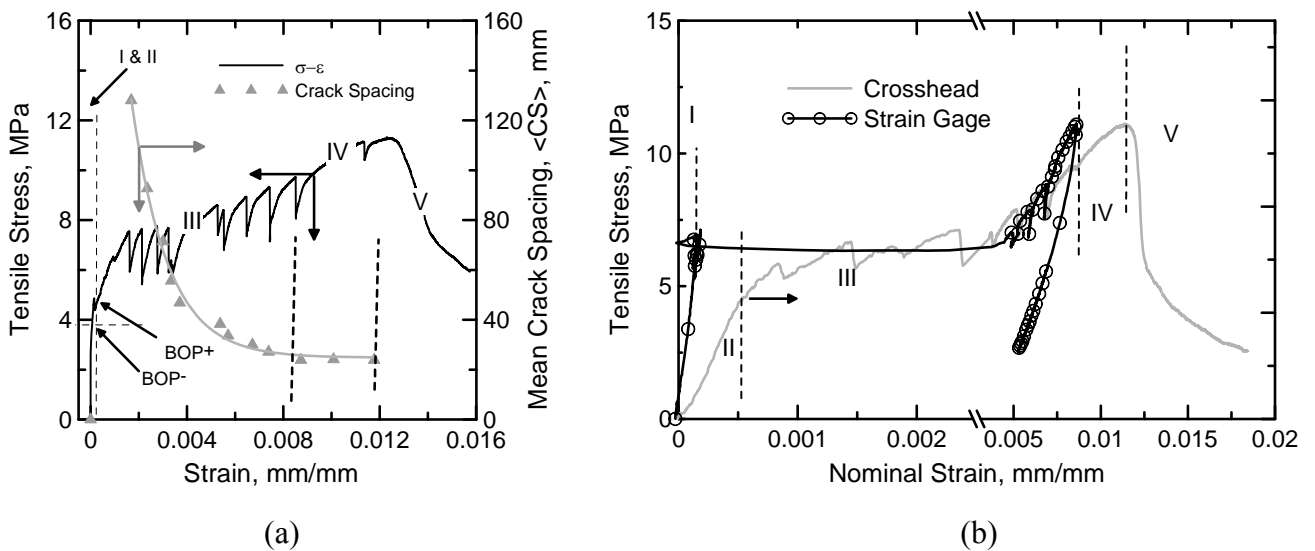


Figure 5. Tensile response of the sisal fiber reinforced composite system: (a) tensile stress and crack spacing vs. strain and (b) comparison of tensile stress vs. strain from strain gage measurements and cross-head displacement.

Immediately after the initiation of the first matrix crack, other matrix cracks also initiate throughout the specimen at approximately regular intervals and begin to propagate across the width [20]. The strain recorded by the resistance gage remains relatively constant in this range which indicates a steady state condition of several cracks that initiate and propagate across the width of the specimen. The strain range within Zone II is associated with formation of matrix cracks, however, no single crack has traversed

the entire width. The term defined as BOP+ corresponds to the stress level at which the first matrix crack completely propagates across the width. As indicated in the experimental results shown in Figure 5a and 5b the linear behavior terminates at the $\sigma_{BOP-} = 3.63-4.80$ MPa. The bend over point ranges from the beginning of non-linearity at 4.80 MPa to a point where the slope drastically decreases ($\sigma_{BOP+}=4.80-5.59$ MPa). Zone II is therefore defined as the stable cracking range between the two stress levels of σ_{BOP-} and σ_{BOP+} .

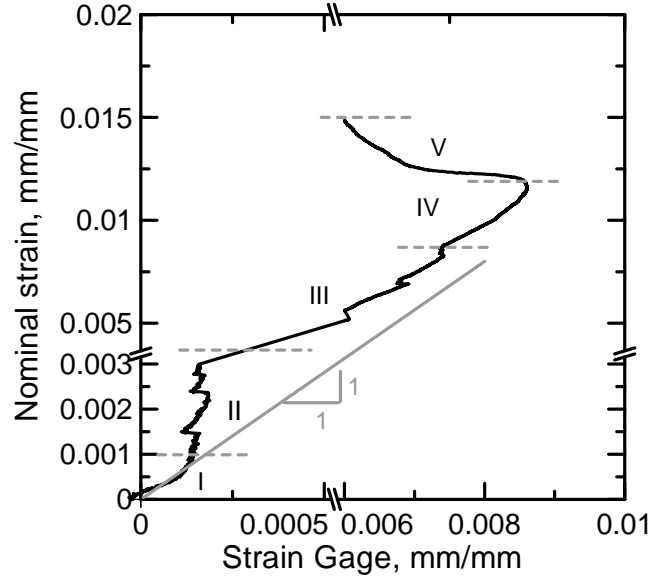


Figure 6. Relationship between the strain gage and strain measured by the stroke.

The post BOP stage is characterized by formation of distributed cracking in Zone III. In this homogenization phase, as the applied strain increases, more cracks form and the spacing decreases in an exponential manner as presented empirically by equation 1. The strain measured by the strain gage remains constant while several cracks form throughout the section as shown in Figure 5b. The decrease in crack spacing can be empirically represented as a function of three parameters and its initiation is represented by parameters S_0 , S_1 , α , and ϵ_{mu} (Equation 1).

$$S(\epsilon_i) = S_1 + S_0 e^{-\alpha(\epsilon_i - \epsilon_{mu})} \quad \epsilon_i > \epsilon_{mu} \quad (1)$$

where, $S(\epsilon_i)$ = crack spacing as a function of strain, ϵ_{mu} = average strain at the BOP level, or where the first set of measurements were obtained, ϵ_i = independent parameter representing strain in the specimen, S_0 and α = constants representing the initial length

of the specimen and rate of crack formation as a function of strain, and S_1 = Saturation crack spacing. The stiffness of the sisal fiber reinforced cement composite system is sufficiently high and keeps the newly formed cracks from widening; thus promoting multiple cracking behavior as shown in Figure 5. This stiffness affects the rate of reduction of crack spacing, or α parameter. Individual, mean and standard deviations values of the S_1 , S_0 , ϵ_{mu} and α for the composites studied under tension and bending loads are presented in Table 1. The mentioned parameters were computed from four different specimens. Significant variations in the value of the α parameter were observed in the tensile tests. Less variability was obtained for S_1 , S_0 , and α from the bending tests.

Table 1. Crack spacing versus strain parameters for tension and bending tests. Parameters were computed for four different specimens. Identification of specimens (i.e. specimen #) corresponds to the same as of Table 2. (S.D. = standard deviation).

Tests	Specimen #	$S_1 + S_0 e^{-\alpha(\epsilon_i - \epsilon_{mu})}$			
		S_1	S_0	α	ϵ_{mu} (mm/mm) - tension δ_{mu} (mm) - bending
Direct Tension	2	24.8	318.63	666.66	0.0015
	4	25.64	324.93	680.27	0.0016
	5	13.79	135.8	288.18	0.0013
	6	24.23	539.18	1204.81	0.0015
	Mean ± S.D.	22.1 ± 5.5	329.6 ± 164.9	709.7 ± 376.2	0.00155 ± 0.000153
Bending	1	38.05	126.82	0.25	0.99
	2	41.58	171.95	0.24	0.99
	3	54.57	289.83	0.41	1.49
	5	23.74	346.47	0.26	4.5
	Mean ± S.D.	39.5 ± 11.1	233.8 ± 101.8	0.26 ± 0.07	1.99 ± 1.68

The crack spacing measurements as shown in Figure 5a show a general reduction in spacing during loading until a steady state condition is reached. This zone covers a large range at the end of Zone II, and III and remains constant throughout Zone IV. This constant level of crack spacing is defined as saturation crack spacing. Beyond this point, reduction in crack spacing is not observed since no new cracks form, while, as verified by the pictures of the specimen under the load, additional imposed strain results in widening of the existing cracks.

It can be seen from Figure 5a that at the strain of 0.0016 mm/mm (Zone III) the cracking spacing drastically decreases from an initial value of 130 mm to 45 mm. During the multiple crack formation the crack spacing decreases until a point (beginning of Zone IV) where it becomes constant at 23 mm.

Zone IV corresponds to the completion of cracking phase and initiation of debonding. Note that the strain gage recording fails to increase as the same rate of the overall strain measure and no additional cracks are formed. As the cracking saturates in the specimen, Zone IV is dominated by progressive damage and characterized by a crack widening stage ultimately leading to failure by fiber pullout. This zone is asymptotically terminated at the saturation crack spacing represented by parameter S_1 . The dominant mechanism of failure during stage IV is crack widening which is associated with fiber debonding and pullout. The post peak response occurs in Zone V where a residual strength of approximately 2 MPa is observed. As shown in Table 2 a considerable difference between the initial (E_{initial}) and post-crack (E_{pc}) moduli from cross-head displacement data and strain-gages are observed. Results for E_{initial} and E_{pc} from strain gages are, respectively, 3.6 and 2.60 times greater than that of the cross-head. This discrepancy is attributed to the spurious deformation, slipping, and localized damage at the grips, indicating that initial stiffness computation from the cross head displacement is significantly erroneous.

The average ultimate tensile strain of the composite is 1.53% (measured from cross-head displacement) which shows the capacity of the sisal fibers to cause crack distribution. Strain values ranging from 1.15% to 2.2% was obtained for individual tests. The average ultimate tensile strength of 12 MPa and an initial modulus of 34.17 GPa (computed from strain gage measurements) is indicative that sisal fiber reinforced cement composite presents a mechanical performance high enough for structural level applications. Nevertheless, a small variability was observed when addressing individual tensile tests. Ultimate strength ranged from 10.56 to 14.70 MPa as can be seen in Table 2.

Table 2. Summary of tensile and four-point bending results (C.H.D = cross head displacement, S.G. = strain gage, and S.D. = standard deviation).

Tests	Instrumentation	Specimen #	E_{initial} (GPa)	$\sigma_{\text{BOP}(-)}$ $\sigma_{\text{LOP}(-)}$ (MPa)	$\sigma_{\text{BOP}(+)}$ $\sigma_{\text{LOP}(+)}$ (MPa)	$\epsilon_{\text{BOP}(-)}$ $\epsilon_{\text{LOP}(-)}$ (%)	$\epsilon_{\text{BOP}(+)}$ $\epsilon_{\text{LOP}(+)}$ (%)	E_{pc} (GPa)	σ_{ultimate} (MPa)	$\epsilon_{\text{ultimate}}$ (%)	Total Toughness (kJ/m ²)	First Crack Toughness (kJ/m ²)	
Direct Tension	C.H.D.	1	9.23	3.63	4.8	0.023	0.043	0.40	12.40	2.2	49.14	1.66	
		2	8.26	4.25	4.87	0.074	0.098	0.49	10.61	1.35	40.74	1.82	
		3	12.58	4.50	5.08	0.021	0.049	0.59	14.70	1.73	66.00	1.77	
		4	8.38	4.34	4.85	0.038	0.067	0.43	11.32	1.27	39.35	1.74	
		5	9.44	4.86	5.59	0.053	0.076	0.56	12.74	1.53	46.22	1.79	
		6	9.05	4.60	5.15	0.071	0.085	0.52	10.56	1.15	34.20	1.41	
			Mean	9.49	4.36	5.10	0.046	0.069	0.50	12.00	1.53	45.95	1.70
			± (S.D.)	(1.58)	(0.41)	(0.30)	(0.023)	(0.021)	(0.07)	(1.57)	(0.38)	(11.15)	(0.15)
		S.G.	6	34.17	-	-	0.015	0.017	1.32	-	0.80	-	-
	Bending	C.H.D.	1	-	10.1	10.2	-	-	-	28.47	-	15.45	0.25
2			-	9.58	9.64	-	-	-	29.31	-	26.84	0.11	
3			-	7.78	8.94	-	-	-	29.85	-	34.43	0.28	
4			-	8.58	10.08	-	-	-	20.88	-	17.51	0.71	
5			-	9.24	10.07	-	-	-	23.67	-	19.85	0.92	
6			-	8.06	8.65	-	-	-	18.26	-	18.68	0.62	
			Mean	-	8.89	9.60	-	-	-	25.07	-	22.13	0.48
			± (S.D.)		(0.90)	(0.51)				(4.86)		(7.16)	(0.31)
		S.G.	2	35.32	-	-	-	-	-	-	-	-	-
			3	28.72	-	-	-	-	-	-	-	-	-
	4		16.15	-	-	0.04	0.07	*0.50	-	0.60	-	-	
	5		24.61	-	-	0.02	0.03	*0.51	-	1.00	-	-	
		6	18.07	-	-	-	-	-	-	-	-	-	
		Mean	29.55	-	-	0.03	0.05	0.50	-	0.80	-	-	
		± (S.D.)	(8.02)	-	-	(0.014)	(0.028)	(0.006)	-	(0.28)	-	-	

* Computed at zone II (refer to Figure 8a).

Figure 7a shows the typical bending response of the sisal fiber reinforced composite and its cracking spacing measurements.

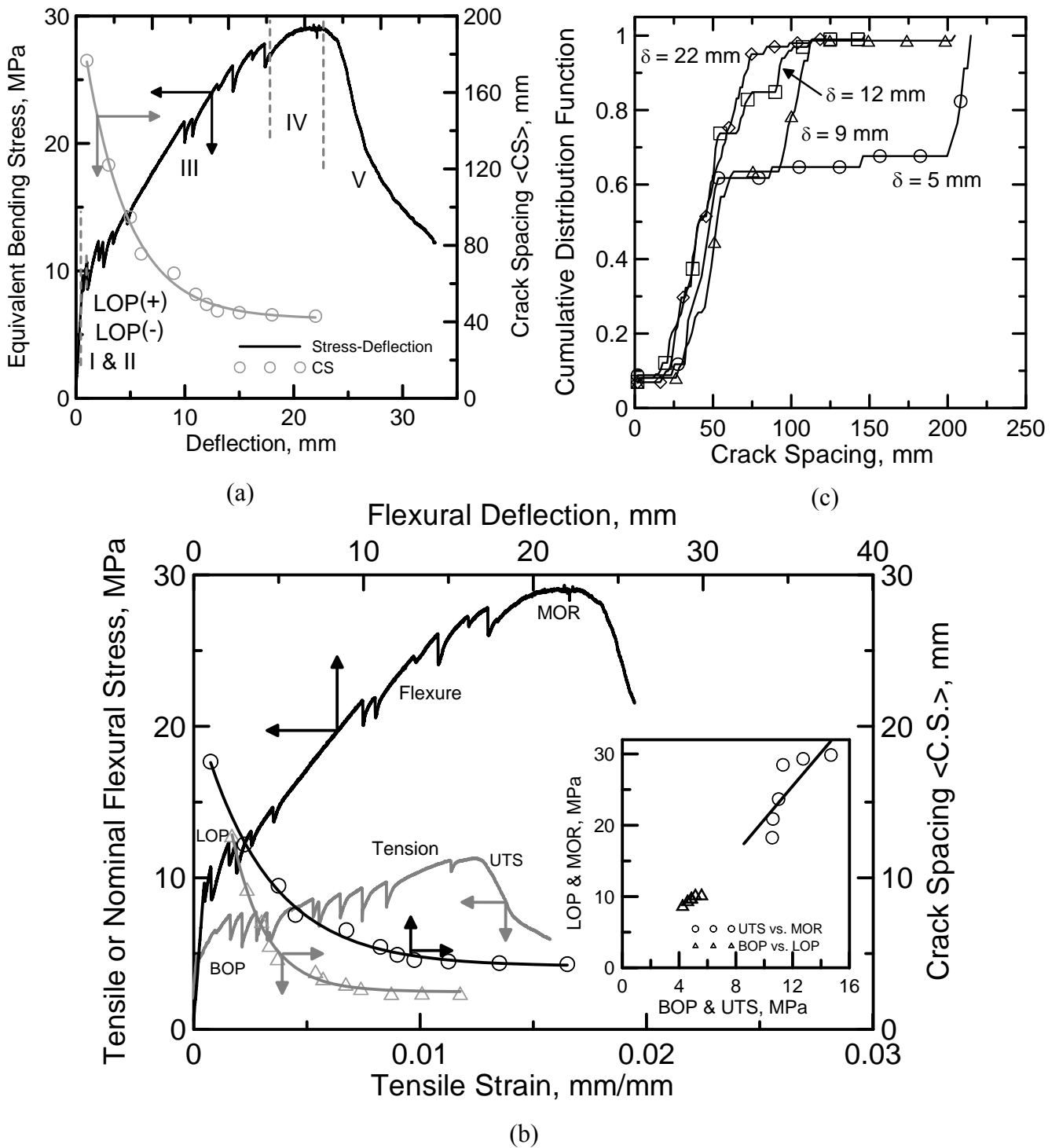


Figure 7. Bending response of the sisal fiber reinforced composite system: (a) Bending stress and crack spacing vs. displacement, (b) comparison of flexural vs. tensile response, and (c) cumulative distribution function for crack spacing.

Using the same methodology as for the direct tension, the bending curve was divided into 5 regions identified by roman numerals. Zone I corresponds to the elastic-linear range where both matrix and the fiber behave linearly. The lower and upper bounds of the limit of proportionality (LOP) delimit the Zone II. Mean values of 8.89 and 9.60 MPa for σ_{LOP}^- and σ_{LOP}^+ , respectively, were obtained. The post LOP range (zone III) is characterized by a multiple cracking formation which can be represented by an exponential decay function similar to equation 1 (see Table 1). Figure 7a shows that the crack spacing initially drops abruptly from 180 mm to 60 mm up to the deflection of 10 mm. The crack spacing saturates at the end of Zone IV (40 mm) which happens at a deflection of approximately 23 mm. Zone V is characterized by the strain softening response due to the localization and widening of a major crack. No new cracks appear at this stage and crack spacing remains constant. The initial elastic modulus of 29.55 GPa shows that the replacement of cement by calcined clays resulted in a matrix of sufficiently high stiffness.

The bending and tensile responses with their respective crack distribution are compared in Figure 7b. The inset plot shows the relationship between LOP vs. BOP and MOR (modulus of rupture) vs. UTS (ultimate tensile stress). It can be seen that under bending, loads associated with the formation of the first crack occur at stress levels twice as those observed for the direct tension tests. The correlation of tensile and bending test results has been documented through theoretical modeling [21]. It has been shown that the flexural results are affected by tension stiffening effects and normalization of the flexural load with an elastic section modulus may result in apparent tensile strength which are as high as 2.8 times the tensile strength. At these stress levels a homogeneous response was observed for all composites. A greater variability was noticed under both testing conditions at ultimate stress states. The values reported for MOR is approximately two times greater than that of the UTS. A procedure to theoretically validate this ratio has been shown for a variety of strain hardening cement composite systems [21]. Under flexural loads, the saturation crack spacing is twice as large as that of tensile loads.

Figure 7c shows the cumulative distribution function for crack spacing under bending at four different levels of displacement beyond the LOP range. As the displacement level increases from 5 to 12 mm, the variability in measured crack widths decreases. As the displacement level approaches the crack saturation level, a more homogenized set of

data with less scatter is observed. At this level 99% of the measurements are below 75 mm.

The composite toughness was determined as the area under the load-displacement curve for tension and bending tests. Elevated toughness values of 45.95 and 22.13 kJ/m² in tension and bending, respectively, demonstrated the high ductility capacity of the sisal fiber composite. Toughness at first crack strength was computed for tensile and bending tests as 1.70 and 0.48 kJ/m², respectively. These values represent a ratio of total to first crack toughness of 27 and 46.1, respectively.

The compressive and tension strains during a four point bending test are shown in Figure 8a. A distinct behavior is observed after the first crack formation. Three different zones are identified for the compressive strain. Zone I is the linear-elastic region which yields the same stiffness (29.55 GPa) as the tension strain. Zone II begins after the first crack formation and is characterized by an increase in stiffness during the multiple cracking. Although not shown, the unloading process is defined by Zone III. At this range a modulus of 8.0 GPa is reported.

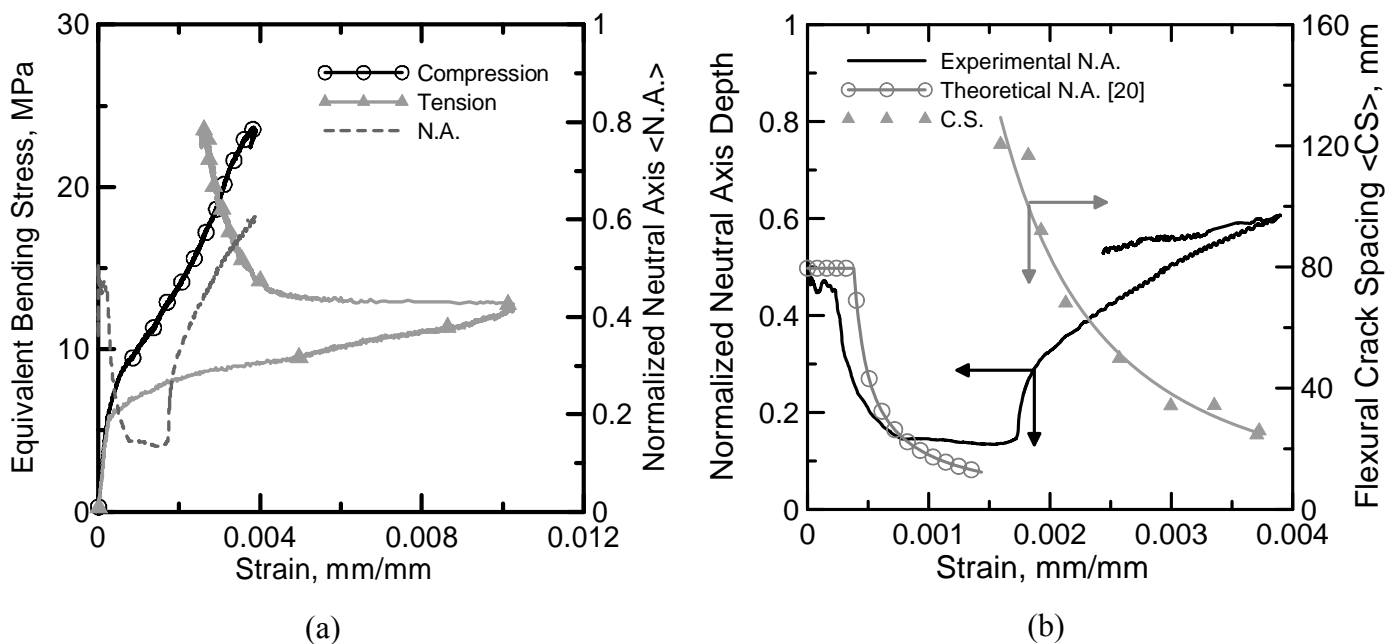


Figure 8. Neutral axis computation: (a) compression and tension strains under four bending loading and (b) crack spacing versus neutral axis.

The tensile region of the flexural sample experiences five ranges of behavior. Zone I is characterized by a linear-elastic response. After the complete formation of the first

crack, Zone II begins. Stiffness degradation is caused by the crack formation, and results in a significant drop in the modulus from 29.55 to 0.50 GPa. A decrease in tensile strain occurs in zone III and IV as a result of crack formations in the vicinity of the strain gage and shear lag mechanisms which result in stress decay in matrix. Note that the resistance type strain gage measurements are not uniquely related to the uncracked material as the strain recorded in the matrix is dependent on the relative position of a strain gage between two parallel cracks. At Zone IV the strain gage response of the matrix between two cracks results in a stiffness of 10.7 GPa. This stage characterizes the degraded matrix's contribution to the composite overall response. Finally, Zone V is the unloading region that presents a stiffness of 22.94 GPa which is similar to Zone I. The data acquisition of strains from the compression and tension faces during the bending test allowed the computation of the neutral axis (normalized with specimen depth, d) as seen in Figure 8a and b. During the elastic-region zone the normalized neutral axis depth (N.A.) remains constant at centroidal location ($0.5d$) until the beginning of the first crack formation which happens at 0.00023 mm/mm. A sudden drop of the N.A. to $0.18d$ is observed as tensile cracking results in load redistribution across the thickness. This N.A. value indicates that assuming plane sections remaining plane, 82% of the sample is in tension while the rest is in compression for strains up to 0.002 mm/mm. At this strain level the first crack has already been formed and the crack spacing starts to decrease with an increase in the N.A. until a strain level of 0.004 mm/mm (see Figure 8b).

Analysis of tensile and compressive stress and strain distribution are important since they provide an insight into the role that cracking plays in redistributing the forces applied onto the member. Flexural loads are carried by means of tensile cracking and redistribution of stresses. Simplifying assumptions which are based on uncracked section modulus leading to an equivalent elastic stresses are unconservative and significantly overestimate the strength of the material.

4.2. Microstructure

Figure 9 shows an optical micrograph cross section view of the sisal fiber reinforced composite with two layers of sisal fibers embedded in the matrix. The matrix has

sufficiently penetrated within and is surrounding all the fibers, indicating that the matrix rheology was adequate for the manufacturing of the composite system.

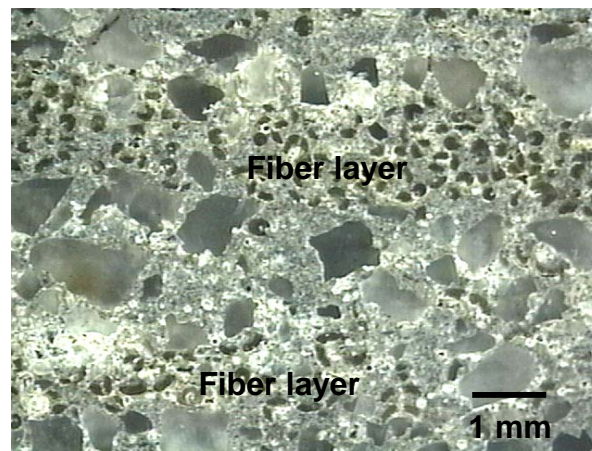
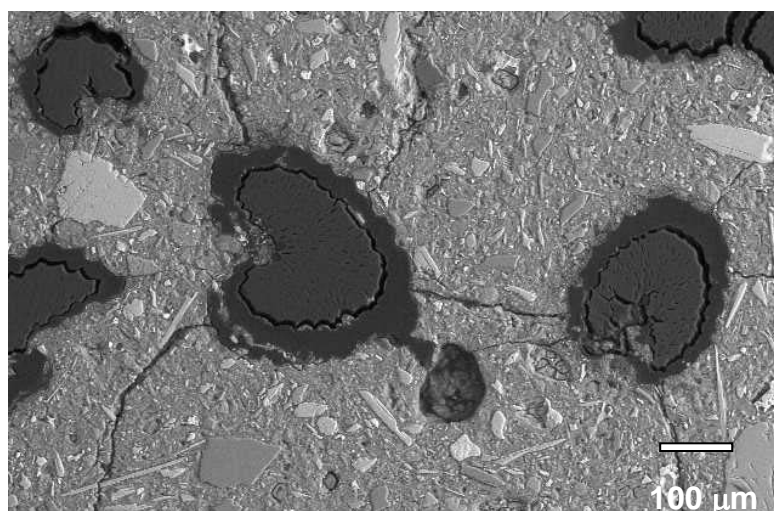
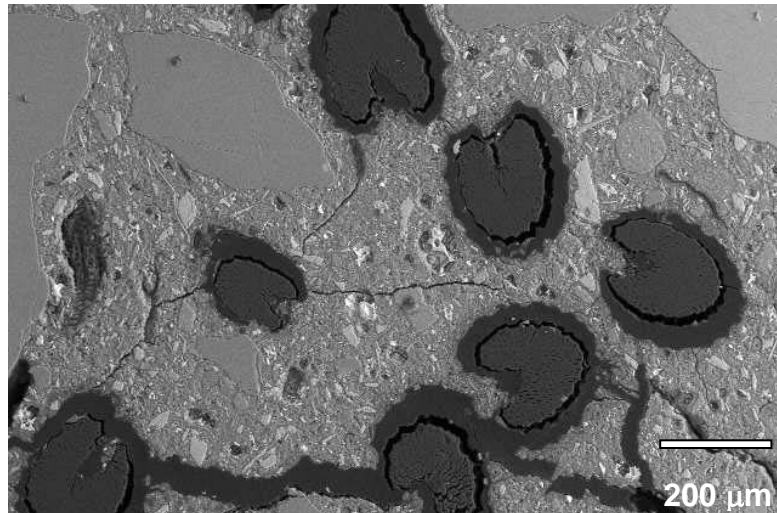


Figure 9. Optical micrograph showing the cross section view of a sisal fiber reinforced composite before testing.

A SEM micrograph showing the sisal fiber composite at the end of the tensile test is presented in Figure 10. The contribution of the sisal fibers to crack arrest and bridging mechanism is observed. The crack propagates through the thickness of the specimen from one fiber layer to the next (Figure 10a and b). Crack deflection mechanism occurs due to interface delamination and changes in the crack path. Such crack arresting and bridging mechanisms lead to a ductile composite as shown by the tensile and bending responses (Figures 5 and 7).



(a)



(b)

Figure 10. SEM micrographs showing crack arresting and bridging in a sisal fiber reinforced composite after a tensile test.

5. Conclusion

A study on the cracking formation under tensile and bending load of continuous sisal fiber cement composites was presented and mechanisms of crack formation and toughening were addressed. Use of continuous sisal fabrics that are formed by aligning and stitching the fibers in a multilayer cement composite system present a new perspective for the use of natural fiber reinforced composites in the construction industry. A matrix with a low content of Portland cement and Calcium Hydroxide was used to reduce the potential aging of sisal fibers.

The composites showed high modulus at linear-elastic zones ranges with elastic moduli in the range of: 30-34 GPa under flexural and direct tension, respectively.

Multiple cracking behavior was observed under both tensile and bending loads. The crack spacing as a function of applied strain was characterized using an exponential decay function under both loading conditions. The crack saturation spacing in tension was almost half of its corresponding values in flexure. While the post-crack modulus decreased significantly compared to the elastic response, the composite was able to

reach average ultimate strengths of 12 and 25 MPa under tension and bending loads, respectively.

The high energy absorption capacity of the developed composite system was reflected in high toughness values under tension and bending loads of approximately 45 and 22 kJ/m², respectively.

Microstructural analysis indicated that the sisal fibers were able to bridge and arrest the cracks within the tensile region of response leading to a high mechanical performance and energy absorption capacity.

Acknowledgements

The authors would like to acknowledge the Brazilian Agency CNPq for its partial financial support.

References

- [1] Swift D.F., Smith R.B.L. The Flexural Strength of Cement-Based Composites using Low Modulus (sisal) Fibers. *Composites* 1979;6(3):145-148.
- [2] Coutts R.S.P., Warden P.G. Sisal Pulp Reinforced Cement Mortar. *Cement & Concrete Composites* 1992;14(1):17-21.
- [3] Toledo Filho R.D., Ghavami K., England G.L., Scrivener K. Development of Vegetable Fiber-Mortar Composites of Improved Durability. *Cement & Concrete Composites* 2003;25(2):185-196.
- [4] Toledo Filho R.D., Scrivener K., England G.L., Ghavami K. Durability of Alkali-Sensitive Sisal and Coconut Fibers in Cement Mortar Composites. *Cement & Concrete Composites* 2000;22(2):127-143.
- [5] Toledo Filho R. D., Joseph K., Ghavami K., England G.L. The use of Sisal Fiber as Reinforcement in Cement Based Composites. *Brazilian Journal of Agricultural and Environmental Engineering* 1999;3(2):245-256.

- [6] Silva F.A., Ghavami K., d'Almeida J.R.M. Toughness of Cementitious Composites Reinforced by Randomly Sisal Pulps. In: Eleventh International Conference on Composites Engineering. Hilton Head Island, 2004.
- [7] Silva F.A., Ghavami K., d'Almeida J.R.M. Bamboo-Wollastonite Hybrid Cementitious Composites: Toughness Evaluation. In: Joint ASME/ASCE/SES Conference on Mechanics and Materials, Baton Rouge, 2005.
- [8] Silva F.A., Ghavami K., d'Almeida J.R.M. Behavior of CRBP-AL Composites Subjected to Impact Load. In 17th ASCE Engineering Mechanics Conference, Delaware, 2004.
- [9] Mobasher B., Pivacek A., and Haupt G. J. Cement Based Cross-Ply Laminates. *Journal of Advanced Cement Based Materials* 1997;6:144-152.
- [10] Silva F.A., Melo Filho J.A., Toledo Filho R.D., Fairbairn E.M.R. Effect of Reinforcement Ratio on the mechanical response of compression molded sisal fiber textile reinforced concrete. In: High Performance Fiber Reinforced Cement Composites (HPRFRC5), Mainz, p. 175-182, 2007.
- [11] Hagger J., Will N., Aldea C., Brameshuber W., Brockmann T., Curbach M., Jesse J. Applications of Textile Reinforced Concrete. In: Brameshuber, W. (edited) State-of-the-Art Report of Rilem Technical Committee 201-TRC: Textile Reinforced Concrete. 2006, p.237-266.
- [12] Silva F.A., Melo Filho J.A., Toledo Filho R.D., Fairbairn E.M.R. Mechanical behavior and durability of compression moulded sisal fiber cement mortar laminates (SFCML). In: 1st International RILEM Conference on Textile Reinforced Concrete (ICTRC), Aachen, Proceedings, p. 171-180, 2006.
- [13] Toledo Filho R.D., Silva F.A., Fairbairn E.M.R., Melo Filho J.A. Durability of compression molded sisal fiber reinforced mortar laminates. *Construction and Building Materials* 2008, in Press. doi:10.1016/j.conbuildmat.2008.10.012
- [14] Silva F.A., Chawla N., and Toledo Filho R.D. Tensile behavior of high performance natural (sisal) fibers. *Composites Science and Technology* 2008;68:3438-3443.
- [15] Mukherjee K.G. and Satyanarayana K.G. Structure and properties of some vegetable fibres. Part 1: Sisal Fibre. *Journal of Materials Science* 1984;19:3925-3934.

- [16] Brazilian Standard NBR 11578, Cimento Portland Composto. Associação Brasileira de Normas Técnicas (ABNT), 1991 (In Portuguese).
- [17] Mobasher B., Peled A. and Pahilajani J. Distributed Cracking and Stiffness Degradation in Fabric Cement Composites. *Materials and Structures* 2006;39:317-331.
- [18] Mobasher B., Stang H., Shah S.P. Microcracking in fiber reinforced concrete. *Cement and Concrete Research* 1990;20(5):665–676.
- [19] Stang H., Mobasher B, Shah S.P. Quantitative damage characterization in polypropylene fiber reinforced concrete. *Cement and Concrete Research* 1990;20(4): 540–558.
- [41] Mobasher B., Castro-Montero A., Shah S.P. A Study of Fracture in Fiber Reinforced Cement-Based Composites Using Laser Holographic Interferometry. *Experimental Mechanics*, 1990;30:286-294.
- [42] Soranakom C. and Mobasher B. Correlation of tensile and flexural responses of strain softening and strain hardening cement composites. *Cement and Concrete Composites*, 2008;30:465-477.

ARTIGO F - Silva F.A., Mobasher B. and Toledo Filho R.D. Degradation Mechanisms in Sisal fiber Cement Composites Systems with Low Contents of Calcium Hydroxide. To be submitted, 2009.

**Degradation Mechanisms in Sisal fiber Cement Composites Systems with Low
Contents of Calcium Hydroxide**

Flávio de Andrade Silva^a, Barzin Mobasher^b, and Romildo Dias de Toledo Filho^a

^aCivil Engineering Department, COPPE, Universidade Federal do Rio de Janeiro, P.O.
Box 68506, CEP 21941-972, Rio de Janeiro – RJ, Brazil.

^bDepartment of Civil and Environmental Engineering, Arizona State University, Tempe,
AZ 85287-8706

To be submitted to an international journal

2009

Abstract

In the present paper the durability of sisal fiber reinforced cement composites was investigated. Matrix with low content of calcium hydroxide was used by replacing 50 % of cement by calcined clays. Composite systems were subjected to accelerated aging cycles of wetting and drying and then mechanically characterized by direct tension and four-point bending. Inverse analysis of the bending data was performed to compare with the experimental tension results. Aged fibers were investigated by means of TGA to verify possible degradation of cellulose and hemi-cellulose. It was found that the composites with low content of calcium hydroxide promoted a proper environment for the sisal fibers. No signs of degradation in the fibers was noticed through TGA and microstructural observation. Cracking spacing was measured during the tension tests by image analysis and correlated to the composite's strain as a function of age. It was found no difference in crack spacing with accelerated aging.

1. Introduction

The use of long aligned natural (sisal) fiber to reinforce cement based thin elements has been proved to be a promise alternative to other synthetic fibers [1-4]. This is a new family of material and the assessment of durability poses a challenge task. Moisture movements, freeze-thaw, attacks by chemicals are just some examples of deterioration that a fiber reinforced concrete can suffer individually or combined. The long aligned sisal fiber reinforced composite presents an average direct tension response of 12 MPa and four-point bending of 25 MPa with ultimate strain capacity in tension that can reach 1.5 % [2]. Although high mechanical performance can be reached the natural fiber undergoes an embrittlement and degradation process if exposed to environments with high contents of calcium hydroxide (CaOH_2). Due to the nature of the natural fibers that are composed by several micro-tubes (i.e. fiber-cells[see Figure 1 a]) linked together by hemicellulose and lignin, calcium hydroxide can precipitate inside these tubes (i.e. lumens). Using an environmental SEM it is shown in Figure 1 a & b that moisture can penetrate the outside layer of the fiber going all the way inside the lumens. The aging problem of sisal fibers led to the development of several measures such as the fiber treatment by blocking and water repellent agents [5], sealing the matrix pore system [6], and addition of pozzolanic materials to react with calcium hydroxide [3,5,7,8,9]. The use of a matrix that was free of calcium hydroxide at 28 days (showed by thermal

analysis) avoided the degradation and embrittlement of sisal fibers after 100 cycles of wetting and drying [3].

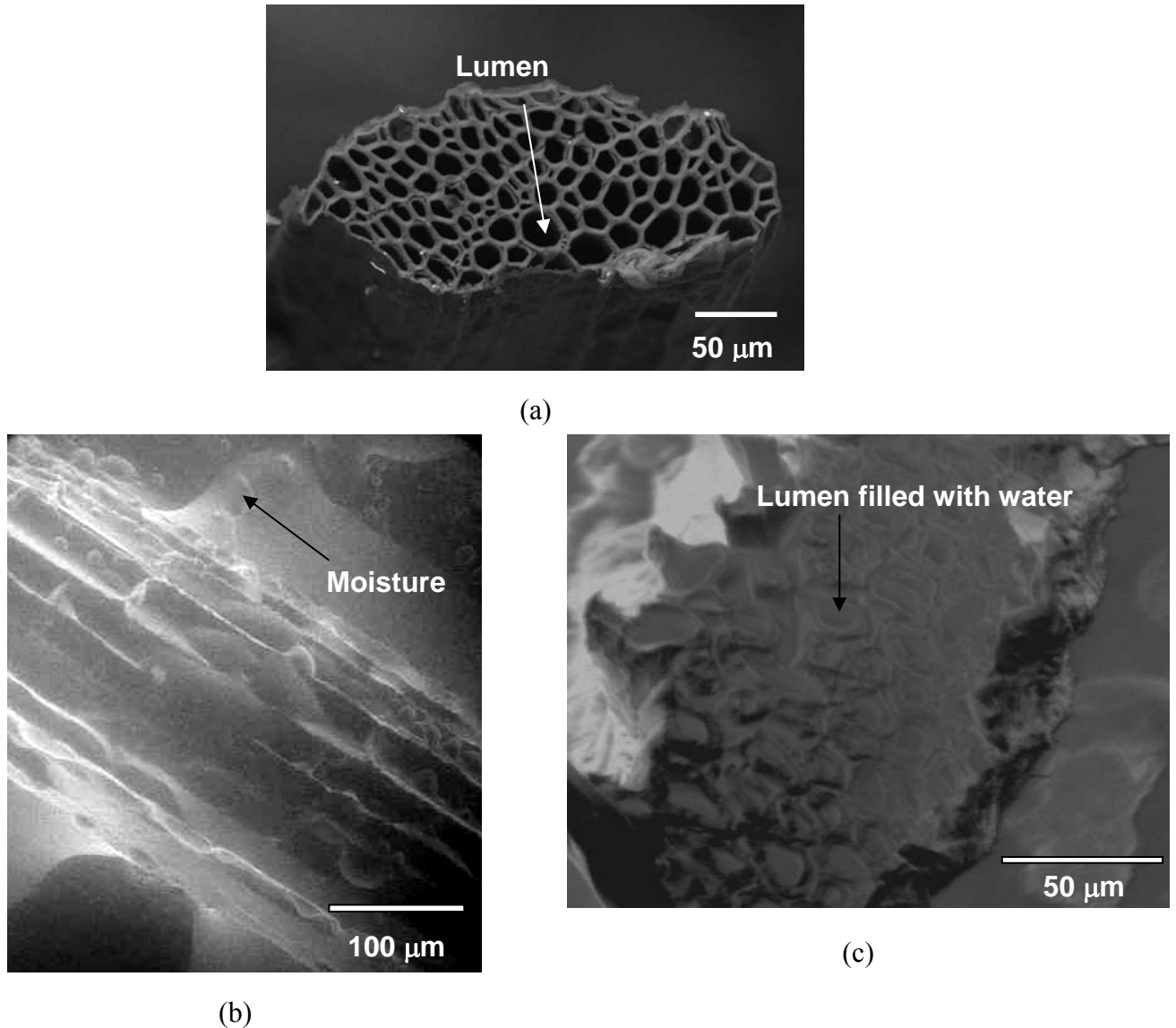


Figure 1. SEM images of the sisal fiber: a) cross section view using low vacuum chamber (Jeol SEM), b) lateral view at 100 % RH and c) cross section view at 100% RH (using ESEM).

The purpose of the present investigation is to evaluate the mechanical performance and identify the degradation mechanisms of the sisal fiber reinforced composite with low content of CaOH_2 after accelerate aging of wetting and drying. Direct tension and bending tests were performed after aging. An analytical model previously developed by Soranakom and Mobasher [10] was used to do an inverse analysis of the bending data in order to establish direct tension parameters. The results were compared to the

experimental direct tension data. Moment curvature diagram was calculated for aged and non-aged composites. Crack spacing was measured during the tension testing as a function of strain and correlated as a function of aging. A thermal analysis investigation was performed in fibers extracted from the aged composites to investigate degradation of cellulose, hemi-cellulose and lignin.

2. Experimental Program

2.1. The sisal Fiber

The sisal fibers used in this investigation were characterized by Silva et al. in a previous work [11]. It presented mean elastic modulus and tensile strength of 19 GPa and 400 MPa, respectively. These fibers were extracted from the sisal plant in a farm located in the city of Valente, state of Bahia – Brazil. The sisal plant leaf is a functionally graded composite structure which is reinforced by three types of fibers: structural, arch and xylem fibers. The first occurs in the periphery of the leaf providing resistance to tensile loads. The others present secondary reinforcement, occurring in the middle of the leaf, as well as, a path for nutrients.

Sisal fibers contain numerous elongated fiber-cells which are about 6 to 30 μm in diameter (see Figure 1). The individual fiber-cells are linked together by means of the middle lamella, which consist of hemicellulose and lignin. Each individual fiber-cell is made up of four main parts, namely the primary wall, the thick secondary wall, the tertiary wall and the lumen.

2.2. Matrix Modification

The matrix was produced using the Portland cement CII F-32 defined by the Brazilian standard [12] as composed with filler (in mass: 85%<clinker<91%; 3%<gypsum<5%; 6%<filler<10%) with a 28 days compressive strength of 32 MPa. The metakaolin (MK) obtained from Metacaulim do Brasil Industria e Comércio LTDA, and calcined waste crushed clay brick (CWCCB) from an industry located in Itaboraí – RJ, Brazil, calcined at 850 °C were used as cement additives. River sand with maximum diameter of 1.18 mm and density of 2.67g/cm³ and a naphthalene superplasticizer Fosroc Reax Conplast SP 430 with content of solids of 44% were also used. Following the recommendations

of previous studies, in order to increase the durability of the composites, the Portland cement was replaced by 30% of MK and 20% of CWCCB [3].

The mortar matrix used in this study presented a mix design 1:1:0.4 (cementitious material:sand:water by weight). Wollastonite fiber (JG class), obtained from Energyarc, were used as a micro-reinforcement in the composite production.

2.3. Composite manufacturing

The matrix was produced using a bench-mounted mechanical mixer of 20 liters capacity. The cementitious materials were homogenized by dry mixing for 30 seconds prior to addition of sand and 5% by volume of wollastonite. The powder material was mixed for an additional 30 seconds prior to addition of superplasticizer and water. The mixture was blended for 3 minutes. For the production of the laminates, the mortar mix was placed in a steel mold, one layer at a time, followed by single layers of long unidirectional aligned fibers (up to 5 layers). The samples were consolidated using a vibrating table operated at a frequency of 65 Hz, resulting in a sisal fiber volume fraction of 10%. After casting the composites were compressed at 3 MPa for 5 minutes. The specimens were covered in their molds for 24 hours prior to moist curing for 28 days in a cure chamber with 100% RH and 23 ± 1 °C. Two composite systems were produced: i) the first one was named CH free composite which had 50 % cement replacement by the mentioned calcined clays (i.e. MK and CWCCB), ii) the second was named PC composite and did not present cement substitution.

2.4. Mechanical Performance

Direct tension and four point bending tests that were performed before and after controlled cycles of wetting and drying. One cycle was defined as 1 day under water followed by 2 days of drying at 37 °C. These conditions were based in previous works [3].

Direct tensile tests were performed in an MTS 810 Instron universal testing machine with a load cell of 100 kN. The tests were controlled by the cross-head displacement at a rate of 0.1 mm/min. Five specimens measuring 400 mm x 50 mm x 12 mm (length x width x thickness) were tested using a gage length of 300 mm with fixed-fixed

boundary conditions. Aluminum thin sheets were glued on both ends of the specimen and the pressure of the hydraulic grips was adjusted to 1.37 MPa (200 psi) in order to minimize stress concentration and damage. The tensile load, cross head displacement and strain were recorded. The tensile strains were also measured by a strain gage glued on the center of the specimen, and also by the stroke displacement.

A Shimadzu UH-F 1000 kN testing machine was used to perform the four point bending tests. The tests were carried out at a crosshead rate of 0.5 mm/min. Three specimens with geometry of 400 mm x 100 mm x 12 mm (length x width x thickness) were tested under bending (300 mm span). Displacements at mid span were measured using electrical transducers (LVDT) and were continuously recorded, together with the corresponding loads, using a 32-bit data acquisition system taking four readings per second.

2.5. Thermal Analysis

Thermogravimetric analysis were used to determine the degradation of the sisal fibers after ageing. The tests were carried out in original fibers and in fibers extracted from the composites after 25 and 75 cycles of wetting and drying. The tests were performed at a heating rate of 10.0 °C/min until a maximum temperature of 1000 °C under a Helium atmosphere. It was used a platinum crucible with sample weight of approximately 24 mg.

2.6. Crack Spacing Measurements

By evaluating cracking patterns at regular time intervals, the crack development throughout the loading cycle of tensile was recorded. A digital Pulnix camera with a 10X macro zoom lens and frame grabber captured images at 30 second intervals. These images were used to measure the crack formation during bending and tension tests.

Image processing was done by the digital processing toolbox of MATLAB. To quantitatively measure the crack spacing as a function of the applied strain, a two step approach was used. During the first step, newly formed cracks of each image were traced and added to data from previous loading increment. The second step measured the crack spacing from the traced cracks using the following procedure:

An image consisting of a series of parallel lines was generated. By conducting a binary “AND” operation the points of intersection of the series of parallel lines with the cracks were identified. A second binary operation of “OR” between the intersection points and the parallel spacing lines, broke up the straight lines into segments representing crack spacing distribution. The next step was to compute the distribution of the length segments and statistical parameters of crack spacing. More information of this technique can be obtained elsewhere [13]. The crack spacing was measured in pixels, and the image was calibrated using conventional techniques to convert the size of a pixel to length measures [14-16].

2.7. Moment curvature and Inverse analysis

In the present work closed form solution for moment curvature diagram developed by Soranakom and Mobasher was used [10]. Moment-curvature diagrams were determined for four-point bending tests of aged and non-aged samples.

In the mentioned model the neutral axis depth ratio k is found by solving equilibrium of forces. The moment capacity is then calculated from internal forces and the neutral axis location; the corresponding curvature is obtained by dividing the top compressive strain with the neutral axis depth. Finally, the moment M_i and curvature ϕ_i for each stage i are normalized with their cracking moment M_{cr} and cracking curvature ϕ_{cr} to obtain the normalized moment M_i' and curvature ϕ_i' , respectively. Expressions for calculating moment and curvature are given in Eqs. 1 & 2:

$$M_i = M_i' M_{cr}; \quad M_{cr} = \frac{1}{6} b d^2 E \varepsilon_{cr} \quad (1)$$

$$\phi_i = \phi_i' \phi_{cr}; \quad \phi_{cr} = \frac{2 \varepsilon_{cr}}{d} \quad (2)$$

More information on how to obtain the neutral axis and detailed information of the above equations can be obtained elsewhere [10].

The inverse analysis of four-point bending data to obtain direct tension results was performed by using an algorithm written in MATLAB code developed by Soranakom and Mobasher [10]. First the Young's modulus was adjusted until the initial slopes of

the predicted and experimental flexural stress deflection responses were fitted. Next, the first cracking strain and post cracking tensile modulus E_{cr} were adjusted until the predicted post crack response matched the proportional limit (LOP) of the experiments. Finally, the strain at peak stress ε_{tm} (or transition strain) was adjusted until the predicted and experimental peak stresses were coincident.

2.8. Microstructural Analysis

The scanning electron microscopy was performed in a Phillips environmental scanning electron microscope (ESEM) model FEI-XL30 and in a Jeol JSM 6460 LV. In the ESEM the Peltier heating/cooling stage was used so it was possible to achieve 100 % RH (in the sample surface) by a combination of low temperature and high water vapor pressure. No precoating with carbon or gold, as is done for standard high vacuum SEM, was required and all the micrographs were taken under the backscattered electrons mode.

The Jeol was operated under low vacuum chamber to remove the high vacuum constraint in the sample environment. The Jeol microscope was operated under an accelerating voltage ranging from 10 kV to 20 kV and chamber pressure was adjusted to values ranging from 25 to 80 Pa. No precoating with carbon or gold was required. All the micrographs were taken under the backscattered electrons mode.

Micrographs showing the condition of the sisal fibers, in the two composite systems, before and after the controlled cycles were taken.

4. Discussion and Analysis

4.1. Mechanical tests

Figure 2 presents direct tension and four-point bending tests performed in aged and non-aged composites. For the composite made with a CH-free matrix it can be seen that the multiple cracking behavior in tension and bending is maintained with the accelerated aging (Figure 2 a and c). The cracking space was measured during the tension tests for aged and non-aged CH-free specimens and presented in Figure 3. It can be seen that there is no difference in the cracking mechanisms throughout the cycles. A crack saturation occurs at a deformation level of 1 % and the crack spacing stabilizes at 20 mm for all cycles. This behavior indicates that the capacity of load transfer between

matrix and fiber was not affected by the accelerated aging. Figure 8 shows that there is no difference in the pull-out length for the CH free composites through the cycles which agrees with the cracking mechanism behavior. The summary of results is presented in Table 1.

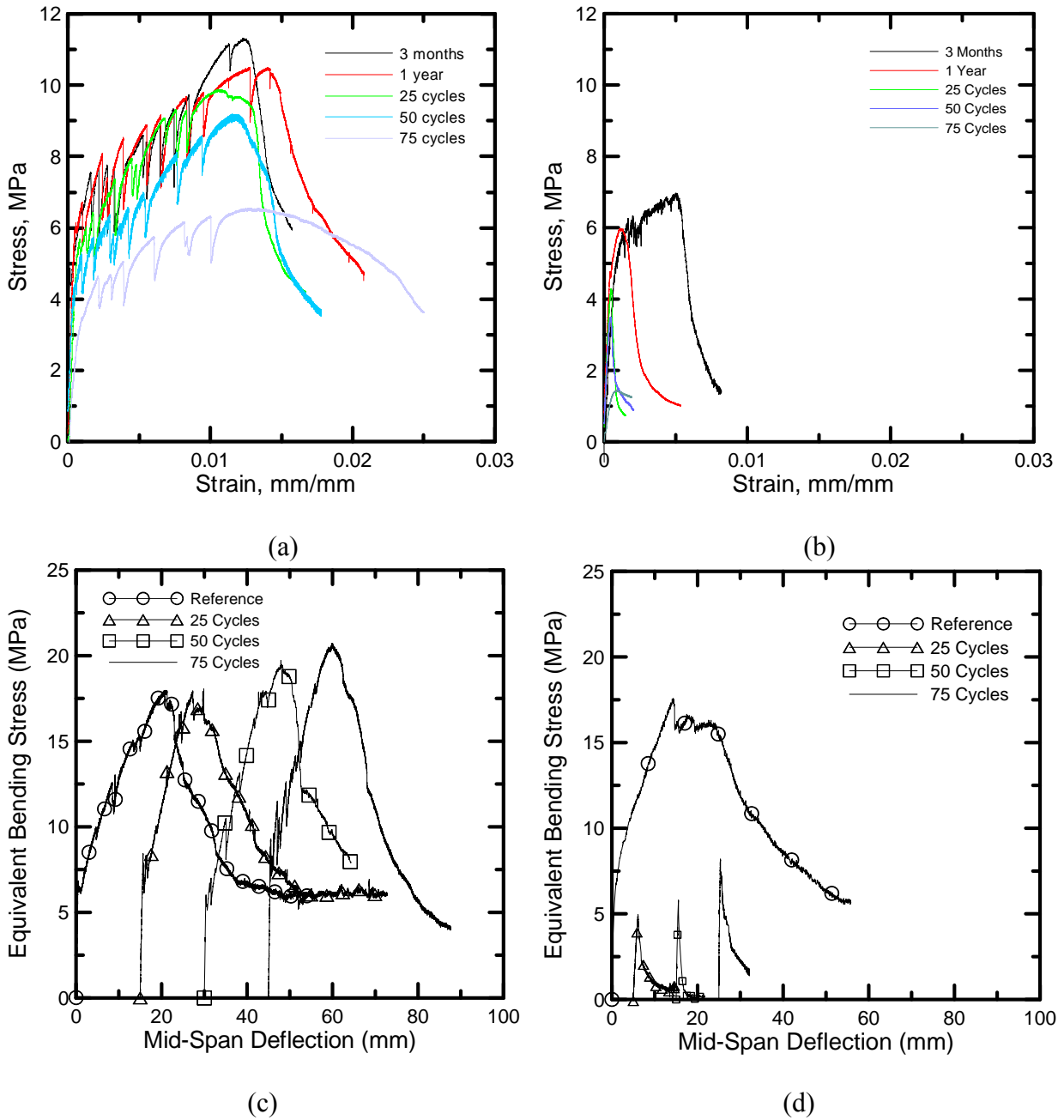


Figure 2. Effect of aging on mechanical response of sisal fiber reinforced cement composite. Tensile response: a) low content of CH matrix, b) Portland cement matrix and bending response: c) low content of CH matrix, d) Portland cement matrix.

Analyzing the four-point bending tests (Figure 2 c and d) it is noticed a post-cracking modulus increase and no effect with age in the modulus of rupture (MOR) and toughness (see Table 2). No significant changes in the limit of proportionality (LOP) is observed. Looking at the direct tension graphs at Figure 2 a and b it can be seen that despite the fact that there was no effect on the cracking mechanisms it was noticed a reduction in both ultimate tensile stress (UTS) and toughness. A reduction in UTS and toughness from 12 to 6 MPa and from 40 to 22 kJ/m² was observed, respectively.

Table 1. Summary of the direct tension tests for aged and non-aged composites.

Aging time	Matrix	UTS (MPa)	$\sigma_{BOP(-)}$ (MPa)	$\sigma_{BOP(+)}$ (MPa)	Young's Modulus (GPa)	Toughness (kJ/m ²)
3 months	CH free	12.00 ± 1.75	4.57 ± 0.30	5.20 ± 0.36	8.92 ± 1.75	40.13 ± 4.93
1 year		11.04 ± 0.70	4.42 ± 0.24	5.93 ± 0.20	12.71 ± 0.46	44.68 ± 5.00
25 cycles		8.45 ± 1.22	4.07 ± 0.19	4.86 ± 0.45	9.58 ± 1.01	30.09 ± 5.78
50 cycles		8.46 ± 0.74	4.76 ± 0.48	5.29 ± 0.23	10.17 ± 1.57	30.17 ± 5.47
75 cycles		6.07 ± 0.44	3.50 ± 0.33	4.24 ± 0.66	7.15 ± 1.36	22.96 ± 13.42
3 months	PC	6.13 ± 0.81	4.69 ± 0.60	5.46 ± 0.69	10.06 ± 3.71	10.07 ± 1.07
1 year		5.45 ± 0.66	3.74 ± 0.50	5.00 ± 0.56	7.70 ± 1.79	3.94 ± 0.80
25 cycles		4.26 ± 0.28	3.74 ± 0.29	4.23 ± 0.28	9.26 ± 1.39	0.92 ± 0.15
50 cycles		3.45 ± 0.52	2.72 ± 0.67	3.29 ± 0.65	9.39 ± 1.72	1.31 ± 0.28
75 cycles		2.36 ± 0.74	2.13 ± 0.79	2.41 ± 0.86	4.66 ± 0.82	1.23 ± 0.96

Reasons for the difference in the mechanical response when comparing direct tension to bending can be explained as follows: i) the direct tension itself is a much more sensitive test than the bending. Some matrix degradation may not be detected in bending tests ii) the fact that the composite becomes brittle with aging makes the positioning of the sample in the hydraulic jacks a tough task. A small misalignment can crack the specimen decreasing the BOP and consequently decreasing the UTS and toughness.

Table 2. Summary of results from the four-point bending tests.

Aging time	Matrix	LOP (MPa)	MOR (MPa)	Toughness (kJ/m ²)
Reference	CH free	6.23 ± 0.23	17.82 ± 0.66	21.70 ± 3.36
25 cycles		7.88 ± 0.52	19.70 ± 3.03	19.26 ± 3.98
50 cycles		6.81 ± 1.01	19.25 ± 4.28	17.84 ± 1.50
75 cycles		9.5 ± 1.37	21.08 ± 3.77	16.10 ± 4.22
Reference	PC	5.33 ± 0.93	19.32 ± 2.07	22.54 ± 4.39
25 cycles		5.80 ± 1.08	5.80 ± 1.08	0.36 ± 0.048
50 cycles		5.46 ± 1.04	5.46 ± 1.04	0.10 ± 0.018
75 cycles		7.50 ± 1.42	7.50 ± 1.42	0.42 ± 0.15

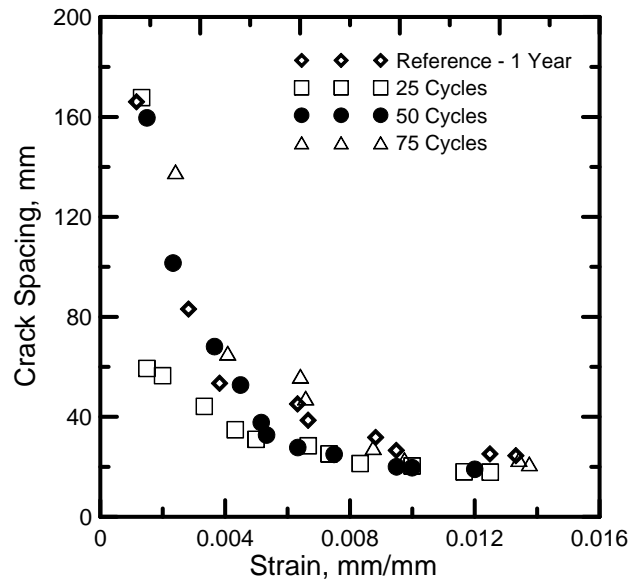


Figure 3. Influence of aging on the crack spacing.

The PC composites presented a severe degradation after 25 cycles for both tension and bending tests. After the accelerated aging only a single crack is formed. For the tension tests it was noticed degradation even before the aging. From 3 months to 1 year it was detected a reduction in toughness from 10 to 3.94 kJ/m². With the aging (comparing 1 year to 75 cycles) it was observed degradation in UTS and toughness from 6.13 to 2.36 MPa and from 2.10 to 1.23 kJ/m², respectively. In the bending tests it was noticed a degradation in MOR and toughness from 19.32 to 7.5 MPa and from 22.54 to 0.42 kJ/m², respectively. Nevertheless, the behavior of the CH free composites is much superior than the ones made with the PC matrix.

To better compare the tension to bending tests an inverse analysis of the bending tests was performed and the results were compared to the direct tension results for the CH free composites. Figure 4a shows the predicted and experimental bending curves and Figure 4b the obtained tension model from the inverse analysis, showing that the shape of the tension model follows the shape of equivalent flexural stress but the magnitudes are lower by as much as 50%. The initial slope of the unaged and 75 cycle responses are almost the same but the post-cracking modulus increases. The UTS remains the same with the cycles but the maximum strain decreases (see Table 3). This trend shows an embrittlement of the matrix with cycles.

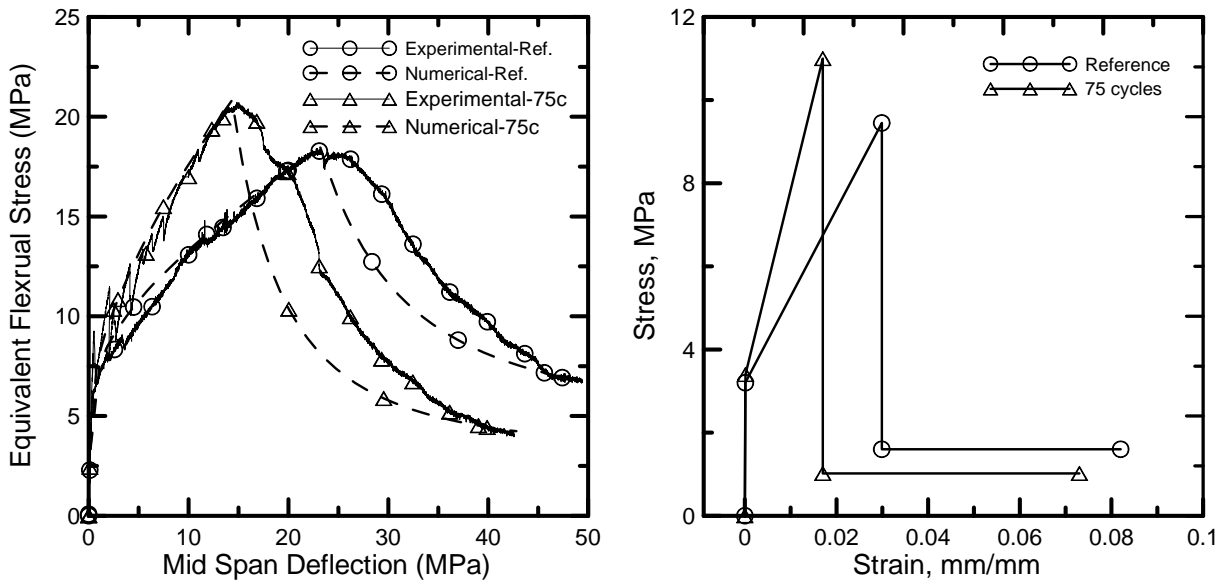


Figure 4. Inverse analysis from bending response.

Post-cracking modulus, first crack strength and strain and maximum strain were computed from inverse analysis and experimental tensile data. Figure 5 shows the comparison of experimental versus inverse analysis of the computed parameters. The post-cracking modulus shows a similar tendency from both calculations. There is an initial increase up to a point where the bonding strength reaches its maximum value followed by a degradation. The ultimate strain also shows a tendency of decreasing in both experimental and inverse analysis. That tendency confirms the fact that the matrix becomes more brittle with the accelerated aging. First crack strength and strain computed from inverse analysis both decrease up to 40 cycles and then shows a tendency of increasing. From experimental data there is no significant changes with aging for these two parameters and a tendency can not be determined.

Table 3. Parameters computed from inverse analysis.

Aging time	Matrix	UTS (MPa)	Ultimate Strain (%)	σ_{BOP} (MPa)	BOP Strain (%)	$E_{Initial}$ (GPa)	$E_{degraded}$ (GPa)	Max. Strain (%)	Residual strength (MPa)
1 year	CH free	9.09 ± 0.3	2.9 ± 0.13	3.17 ± 0.21	0.0105	30	0.2 ± 0.01	2.9 ± 0.13	1.47 ± 0.1
25 cycles		12.42 ± 2.84	1.6 ± 0.37	2.07 ± 0.12	0.0068	30	0.64 ± 0.02	1.6 ± 0.37	1.37 ± 0.6
50 cycles		10.10 ± 1.72	1.9 ± 0.01	2.2 ± 0.2	0.0073	30	0.40 ± 0.06	1.97 ± 0.1	2.23 ± 0.67
75 cycles		10.91 ± 2.37	1.5 ± 0.21	3.83 ± 0.45	0.0127	30	0.47 ± 0.11	1.49 ± 0.21	1.23 ± 0.43

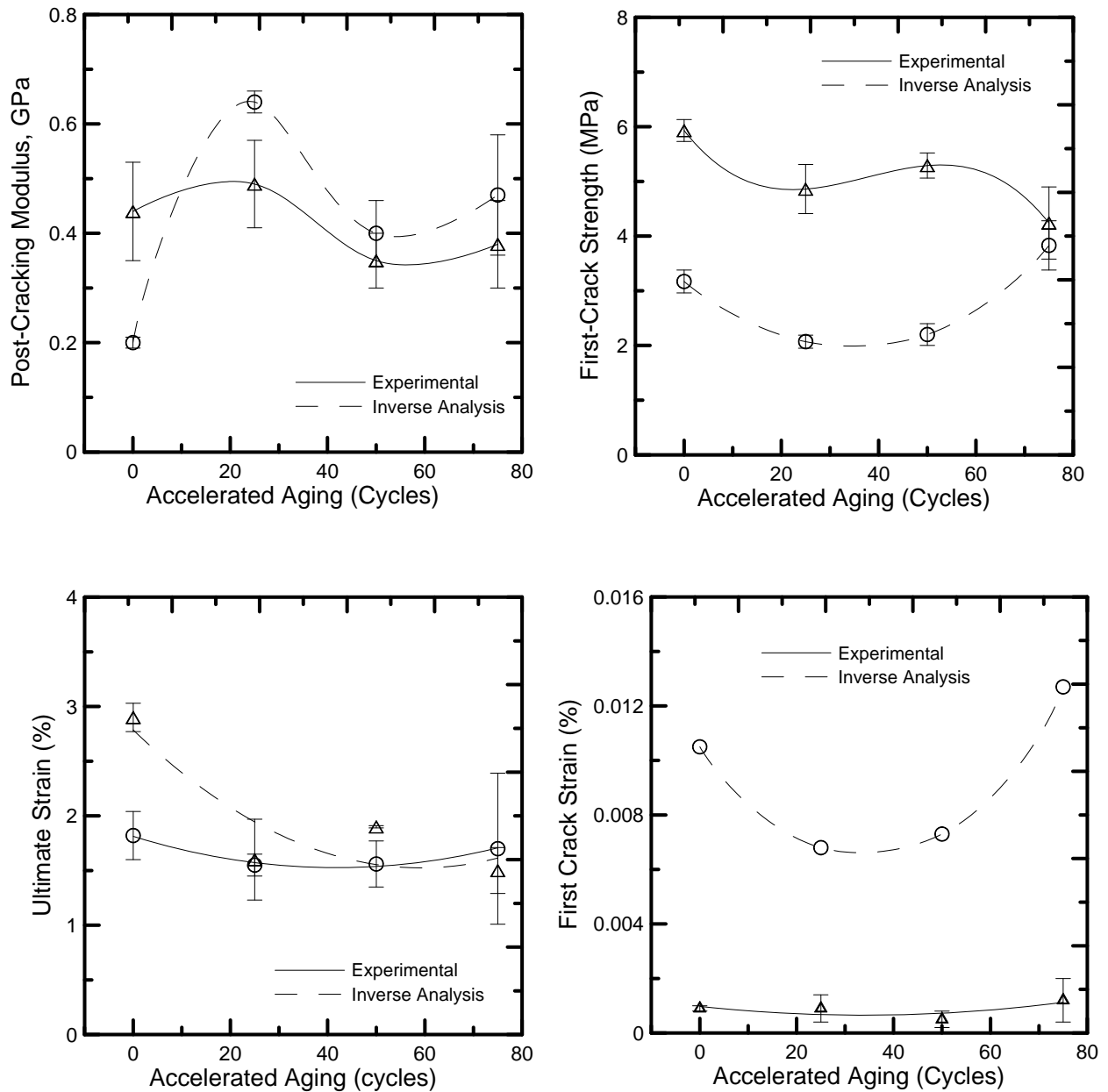


Figure 5. Effect of aging on time dependent parameters for the low CH content composite.

Moment-curvature diagrams were computed from four-point bending data using Soranakon and Mobasher model [10]. A maximum moment of 50 kN.mm is reached at a curvature of 0.002 mm^{-1} for the CH free composites. No difference is noticed for aged composites. For the non aged PC composite a moment of 60 kN.mm was observed with a degradation after 25 cycles that dropped the moment to 20 kN.mm (see Figure 6).

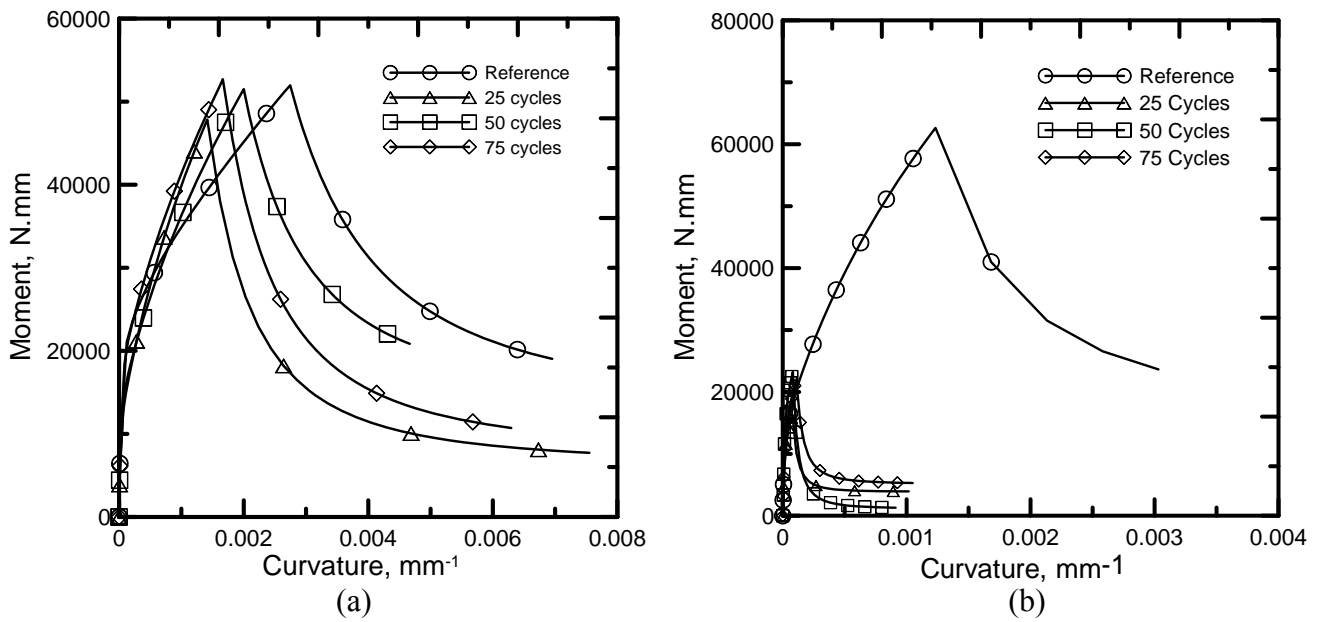


Figure 6. Moment curvature: a) CH free composites and b) PC composites.

4.2. Thermal analysis

Sisal is composed by cellulose (~70%), hemicellulose (~18%), lignin (~10%) and a small amount of pectin, waxes and fat (~2%). The hemicellulose was pyrolyzed in the ranges of 150 to 300 °C (see Figure 7) due to a cleavage of α - and β -aryl-alkyl-ether linkage from the thermal degradation reactions of the lignin [17,18,19]. As the temperature increases from 300 to 380 °C (refer to Figure 7), the degree of polymerization of cellulose decreases further, radicals appear and carbonyl, carboxyl and hydroperoxide groups are formed. Thermal degradation rates increase as heating constituents. Depolymerization takes place when the cellulose structure has absorbed enough energy to activate the cleavage of the glycosidic linkage to produce glucose, which is then dehydrated to levoglucosan (1,6-anhydro- β -Dglucopyranose) and oligosaccharides [17].

The TGA in Figure 7 shows a reduction, when compared to the non-aged fiber, in the amount of both hemi-cellulose and cellulose for the aged fibers extracted from the PC composite possible due to a calcification mechanism. No significant reduction in the amount of cellulose and hemi-cellulose was observed for fibers extracted from CH-free composites as can be seen in Figure 7b.

Silva [20] and d'almeida et al. [21] presented similar TGA plots for original (i.e. non treated) sisal and coroa fibers, respectively.

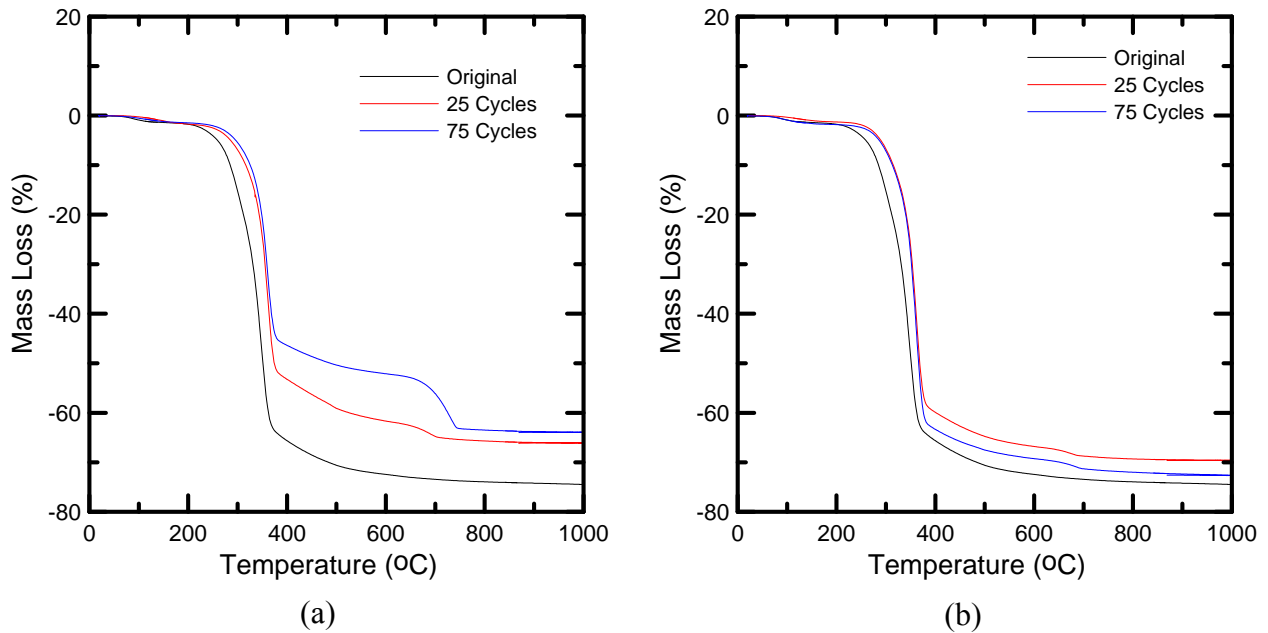


Figure 7. Effect of aging on the chemical properties of sisal fibers. (a) Fibers extracted from PC aged composites and (b) fibers extracted from CH free composites.

4.3. Microstructure

Evidence of calcium hydroxide precipitation can be observed in micrographs of fibers extracted or inside of aged PC composites. It can be seen in Figure 9b that a fiber extracted from a PC composite subjected to 25 cycles presents its lumen filled up with calcium (note the difference from a non-aged fiber [Figure 9a]). That is another evidence of the phenomenon shown by the ESEM at 100% RH (see Figure 1b and c). The moisture is able to penetrate the cell walls and is able to carry calcium to the lumen. The precipitation of calcium inside the lumen makes the fiber more brittle and also degrades the cellulose and hemi-cellulose as shown by TGA. On the other hand the fibers inside the aged CH free composite (see Figure 9c) do not present any sign of degradation neither any material inside the lumens or in the fiber-matrix interface. This behavior confirms the higher UTS, MOR and toughness obtained for the CH free composites. Figure 9d shows again calcium in a sisal fiber inside a PC composite subjected to 75 cycles. Note the difference between the two composite systems (Figure 9 c and d). It is clear that the fibers inside aged PC composite presents calcium precipitation and the fibers inside the aged CH free composites does not.

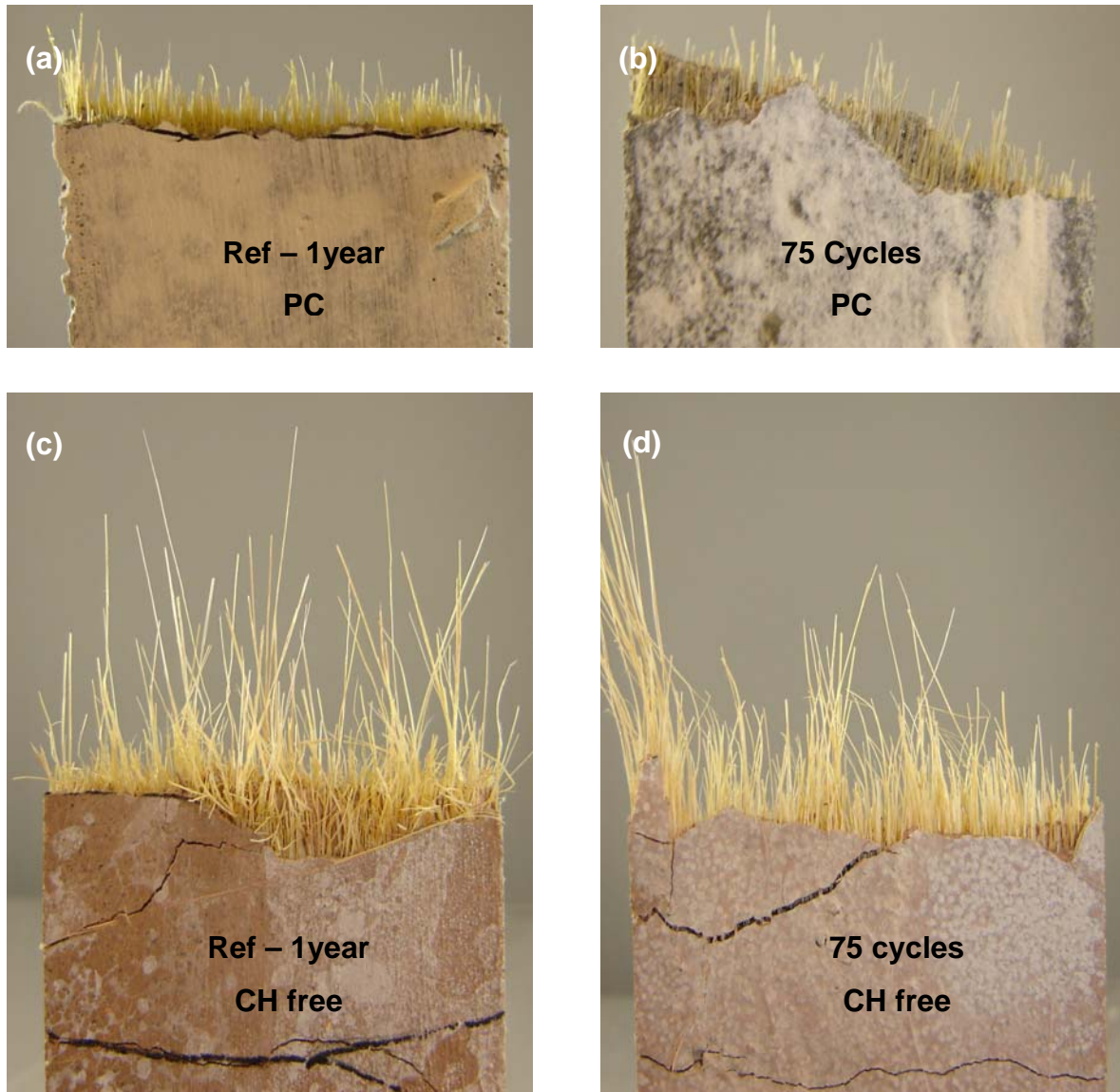


Figure 8. Pull-out length of the fibers in non aged PC specimens (a,b) PC composites and (c,d) CH free composites.

The higher pull out length observed for CH free composites in Figure 8 is another evidence that the ductility of the sisal fiber is maintained after aging for this composite system.

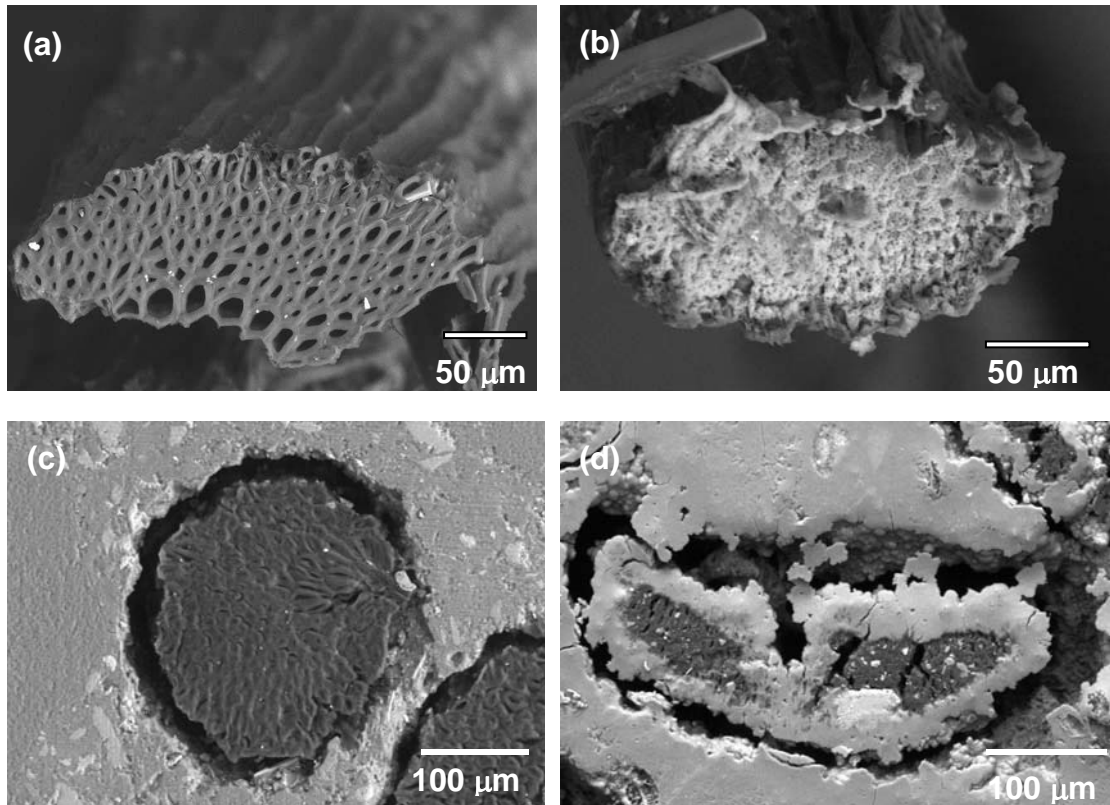


Figure 9. Effect of accelerated aging on sisal fibers: a) non-aged fiber, b) fiber extracted from a PC composite subjected to 25 cycles, c) fiber inside a CH free composite subjected to 75 cycles and d) fiber inside a PC composite subjected to 75 cycles.

Conclusion

The present work addressed the durability of sisal fiber reinforced cement composites. The composites were aged through cycles of wetting and drying and then mechanically characterized by direct tension and four-point bending. TGA analysis on aged fibers and microstructural analysis were performed. The main findings are described below:

- The CH free composites preserved its original multiple-cracking behavior in tension even after 75 cycles of wetting and drying. Cracking saturation occurs at a deformation level of 1 % and the crack spacing stabilizes at 20 mm for all cycles. Observation of the pull-out length after the tension tests supported this behavior. PC composites presented a single crack formation after the cycles.

- Despite the fact that the CH free composite presented no alteration on the cracking mechanisms a reduction in UTS and tensile toughness was observed after 75 cycles.
- No reduction in the MOR and toughness was observed for the CH free composites after 75 cycles of wetting and drying whereas the PC composite presented reduction from 19.32 MPa to 7.5 MPa and 22.54 to 0.42 kJ/m².
- TGA on sisal fibers showed significant reduction in the amount of cellulose and hemi-cellulose in fibers extracted from PC composites after aging.
- Microstructural observation demonstrated the mineralization of sisal fibers in aged PC composites. No signs of mineralization or degradation was observed for fibers inside aged CH free composites.

Acknowledgements

The authors would like to thank the CNPq for partial financial support and to acknowledge the LeRoy Eyring Center for Solid State Science at ASU for using the FEI-XL30-ESEM and TGA. Special gratitude is given to Timoty Karcher who performed the TGA tests, to David Wright who kindly provided facilities for sample preparation and to Zhenquan Liu and Sisouk (Si) Phrasavath for helping with ESEM.

References

- [1] Silva FA, Toledo Filho RD. Sisal fiber reinforcement of durable thin walled structures – a new perspective. In: Proceedings of international workshop on cement based materials & civil infrastructure. Karachi, Pakistan; 2007. p. 575–86.
- [2] Silva FA, Mobasher B, Toledo Filho RD. Recent Advances in High Performance Natural (Sisal) Fiber Cement Composites. In: Seventh International Rilem Symposium on Fibre Reinforced Concrete: Design and Applications (BEFIB 2008), Rilem Publications S.A.R.L., 2008, p. 105-113.
- [3] Toledo Filho RD, Silva FA, Fairbairn EMR, Melo Filho JA. Durability of compression molded sisal fiber reinforced mortar laminates. *Construction and Building Materials* (2008), doi:10.1016/j.conbuildmat.2008.10.012.
- [4] Silva FA, Melo Filho JA, Toledo Filho RD, Fairbairn EMR. Mechanical Behavior and Durability of Compression Moulded Sisal Fiber Cement Mortar Laminates

(SFCML). In: 1st International RILEM Conference on Textile Reinforced Concrete (ICTRC), Rilem Publications S.A.R.L., 2006, p. 171-180. doi:10.1617/2351580087.017.

[5] H.-E Gram, Durability of natural fibers in concrete, Swedish Cement and Concrete Research Institute, Research Fo. 1983.

[6] Z. Berhane. Performance of natural fiber reinforced mortar roofing tiles, *Materials and Structures* 27 (1999) 347-352.

[7] Mohr B.J., Biernacki J.J., Kurtis K.E. Supplementary cementitious materials for mitigating degradation of kraft pulp fiber-cement composites. *Cement and Concrete Research*, Volume 37, Issue 11, 2007, p. 1531-1543.

[8] R.D. Toledo Filho, K. Ghavami, G.L. England, K. Scrivener, Development of vegetable fiber-mortar composites of improved durability, *Cement & Concrete Composites* 25 (2003) 185-196.

[9] R.D. Toledo Filho, K. Scrivener, G.L England, K. Ghavami, Durability of alkali-sensivite sisal and coconut fibers in cement mortar composites, *Cement & concrete composites* 22 (2000) 127-143.

[10] Soranakom C., and Mobasher B., Correlation of Tensile and Flexural Responses of Strain Softening and Strain Hardening Cement Composites, *Cement and Concrete Composites*

[11] Silva F.A., Chawla N., Toledo Filho R.D. Tensile behavior of high performance natural (sisal) fibers. *Composites Science and Technology* 68 (2008) 3438-3443.

[12] NBR 11578, Cimento Portland Composto. Associação Brasileira de Normas Técnicas (ABNT), Julho, 1991 (In Portuguese).

[13] Silva FA, Mobasher B, Toledo Filho RD. On the Cracking Mechanisms in Durable Sisal Fiber Reinforced Cement Composites. *Cement and Concrete Composites*, 2008, in review.

[14] Mobasher B., Peled A. and Pahilajani J. Distributed Cracking and Stiffness Degradation in Fabric Cement Composites. *Materials and Structures* 2006;39:317-331.

[15] Mobasher B., Stang H., Shah S.P. Microcracking in fiber reinforced concrete. *Cement and Concrete Research* 1990;20(5):665-676.

- [16] Stang H., Mobasher B, Shah S.P. Quantitative damage characterization in polypropylene fiber reinforced concrete. *Cement and Concrete Research* 1990;20(4): 540–558.
- [17] White R.H., Dietsberger M.A. Wood products: thermal degradation and fire *Encyclopedia of materials: science and technology*. Elsevier Science Ltd, 2001: Pages 9712-9716
- [18] d’Almeida ALFS, Farreto DW, Calado V and d’Almeida JRM *Polymers and Polymer Composites* 14 (2006) 73.
- [19] Wielage B Lampke Th, Marx G , Nestler K and Starke D *Thermochimica Acta* 337 (1999) 169
- [20] Silva FA. Toughness of non-conventional materials. Masters thesis, Department of Civil Engineering PUC-RJ, 2004.
- [21] d’Almeida JRM, d’almeida ALFS and Carvalho LH. Mechanical, Morphological, and structural characterization of caroá (*Neoglaziovia variegata*) Fibres. *Polymers and Polymer Composite*, v. 16, n. 9, 2008 p.589-595.

ARTIGO G -Silva F.A., Mobasher B. and Toledo Filho R.D. Pull-out mechanism in sisal fiber cement composites. To be submitted, 2009.

Pull-Out Mechanism in Sisal Fiber Cement Composites

Flavio de Andrade Silva^a, Barzin Mobasher^b, and Romildo Dias de Toledo Filho^a

^aCivil Engineering Department, COPPE, Universidade Federal do Rio de Janeiro, P.O.
Box 68506, CEP 21941-972, Rio de Janeiro – RJ, Brazil.

^bDepartment of Civil and Environmental Engineering, Arizona State University, Tempe,
AZ 85287-8706

To be submitted to an international journal

2009

Abstract

An experimental investigation was performed to understand the sisal fiber pull-out behavior from a cement matrix. The effect of curing age and fiber embedded length on the fiber-matrix interface was studied. Sisal fiber presents irregular cross section with different shapes that may be beneficial for the bond strength. A scanning electron microscope coupled with image analysis was used to measure the area of every single tested fiber and to determine and classify its morphology. The results were correlated to the fiber morphology. Direct tension tests were performed in composites reinforced by 10% in volume of sisal fiber. A finite difference model developed by Soranakon and Mobasher was used to determine the bond strength vs. slip constitutive relation from experimental data and to predict the composite tensile behavior and crack spacing.

1. Introduction

Cement composites reinforced with unidirectional aligned sisal fibers present a tension-hardening with multiple cracking behavior [1]. This type of composite system is reinforced with 5 layers of fibers resulting in a total volume fraction of 10 %. A special matrix that has 50 % of cement replacement by calcined clays has been previously designed [2]. This newly developed matrix gives to the composite enhanced durability and also presents adequate rheology for the used fiber volume fraction. The multiple cracking behavior achieved by this composite is governed by interfacial bond characteristics between fiber and matrix.

A great amount of experimental and analytical investigation on the synthetic fiber-matrix bond adhesion for cementitious composites have been performed but yet no data has been presented for natural fibers [3-15]. Most of these works were performed on steel fibers. Naaman [3] states that there are 4 main factors that influence the bond adhesion: (i) physical and chemical adhesion, (ii) mechanical component of bond such as deformed, crimped and hooked end fibers, (iii) fiber-to-fiber interlock, and (iv) friction. Peled and Bentur [4] investigated the pull-out behavior of straight and crimped polyethylene yarns. They found that increasing the crimps density enhances the mechanical anchoring and the equivalent adhesion bond strength increases from 1 to 1.84 MPa (10 mm embedded length). Markovich et al. [5] studied the pull-out behavior of hooked end steel fibers for different types of matrices and it was found that the average frictional stress varied from 2.76 to 4.97 MPa depending on the mixture. The

bond properties of carbon in cementitious matrices were investigated by Katz et al. [6]. Carbon fibers with diameters of 10 and 46 μm were tested. Different matrices were used and the mean bond strength for 10 and 46 μm ranged from 0.52 to 1.29 MPa and 0.39 to 3.02 MPa, respectively. Kim et al. [7] investigated steel hooked ended and Torex fibers. Equivalent bond stresses was calculated from experimental pullout work data and it was found that hooked end fibers and Torex presented 4.73 and 14.49 MPa, respectively.

Sisal fibers are naturally modified by nature presenting different mechanical components of bond. Sisal is a flexible fiber as can be seen in Figure 1d that presents irregular cross-section area. They can be divided into 3 types of bond mechanical components: (i) horse-shoe shape – these represents the majority of the fibers that can be found in the sisal plant leaf and present small areas (see Figure 1a); (ii) arch shape – present larger areas and are found in a less content than the horse-shoe shape; (iii) twisted arch shape – a result of the fiber extraction process. The sisal fibers are extracted from its leaf by a mechanical process called decortication. In this process, sometimes, the arch shape fibers can brake and twist resulting in the type (iii) shape. Besides the different shape the sisal fibers also present a corrugated surface that may be beneficial to the fiber-matrix adhesion (see Figure 1d).

Several models have been used for prediction and characterization of pull-out behavior in fiber reinforced cement composites. Naaman [8] proposed an analytical model for smooth fibers or bars with a idealized bond-stress-slip relationship of the interface. The solution led to the prediction of the bond shear stress versus slip curve assuming the pullout load versus slip curve is given. Sueki et al. [9] modified Naaman's model to analyze pullout test results and quantify the equivalent bond properties of several fabrics. Banholzer et al. [10] proposed another analytical model to simulate the pull-out response of a fiber-matrix system in which an N-piecewise linear bond stress versus slip relation is adopted and the number N of the linear intervals assumed is not limited.

In the present research single fiber pullout tests were performed in sisal fibers for curing ages ranging from 3 to 28 days. Embedded lengths of 10, 20, 30 and 40 mm were tested for samples with 3 days of age. Microstructure characterization coupled with image analysis was performed to compute the sisal fiber area of each test and to investigate the effect of the fiber shape on the bond strength. A non-linear finite difference model developed by Soranakon and Mobasher [11,12] for 2-D bi-directional fabric reinforced composites was used to simulate the pull-out response and predict direct tensile and

crack spacing of sisal fiber reinforced composites based on its interface properties. The numerical analysis was compared to experiments. Small modifications were made to model to fit the response of unidirectional aligned fibers.

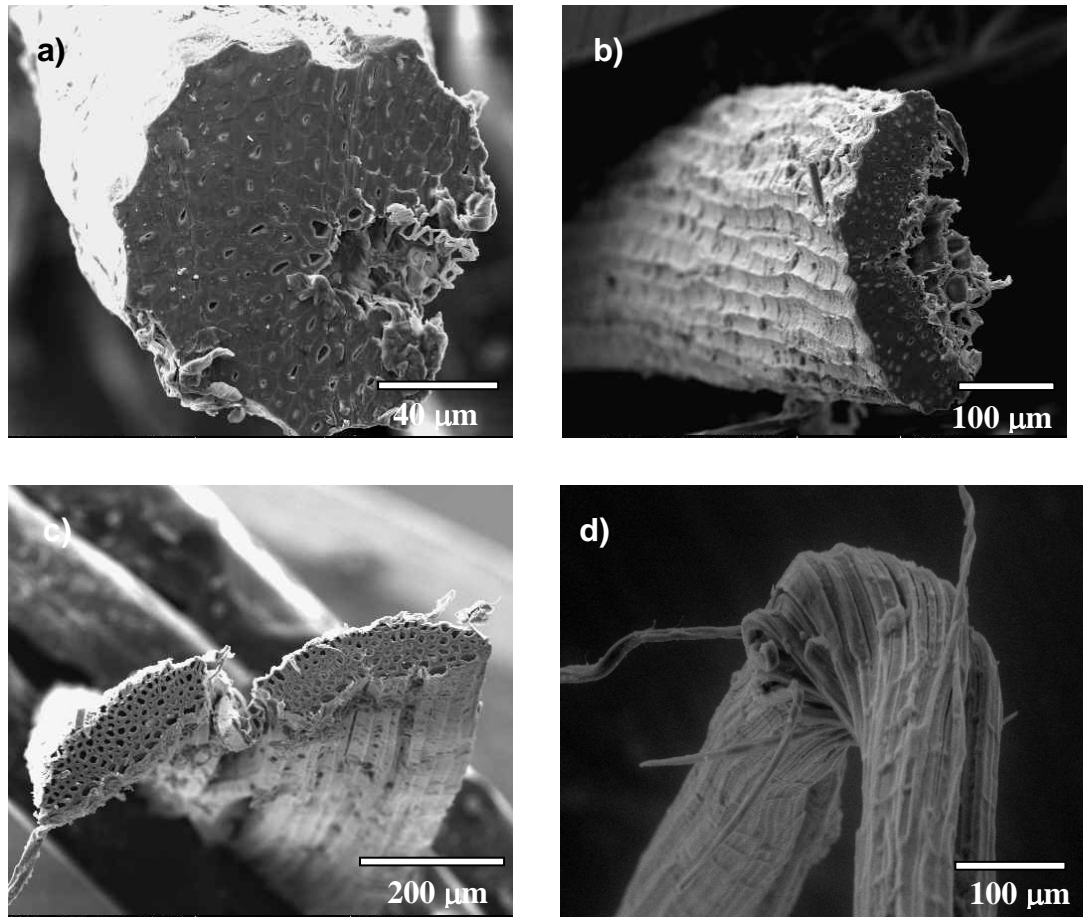


Figure 1. Different morphologies of the sisal fiber: a) horse-shoe shape, b) arch shape, and c) twisted arch shape. The different type of morphologies affects the fiber-matrix bond strength. The rough surface and flexibility of the fiber is observed in d.

2. Experimental Program

2.1. Materials and processing

The sisal fibers used in this investigation were of Brazilian production. Their mechanical properties were characterized by Silva et al. [16]. Silva and his co-workers found that the sisal fiber presented a mean elastic modulus and tensile strength of 19 GPa and 400 MPa, respectively. These fibers were extracted from the sisal plant in a farm located in the city of Valente, state of Bahia – Brazil. The Wollastonite fiber (JG class), obtained from Energyarc, were used as a micro-reinforcement.

The matrix used in the present work was based on past research [2]. It was produced using the Portland cement CII F-32, river sand with maximum diameter of 1.18 mm and density of 2.67g/cm^3 , 5% of wollastonite (in volume) and a naphthalene superplasticizer Fosroc Reax Conplast SP 430 with content of solids of 44%. Metakaolin (MK) from Metacaulim do Brasil Industria e Comércio LTDA and calcined waste crushed clay brick (CWCCB) from an industry located in Itaboraí – RJ, Brazil, burned at $850\text{ }^\circ\text{C}$, were used as cement replacements. The cement was replaced by 30% of MK and 20% of CWCCB following previous studies [2]. The mortar matrix used in this study presented a mix design 1:1:0.4 (cementitious material: sand: water by weight).

The matrix was produced using a bench-mounted mechanical mixer of 5 liters capacity. The cementitious materials, sand and wollastonite fibers were dry mixed during 5 minutes (for homogenization). The super plasticizer diluted in water were slowly poured in the running mixer and then mixed for 5 minutes. Special molds were designed for casting single filament pullout specimens (see Figure 2).

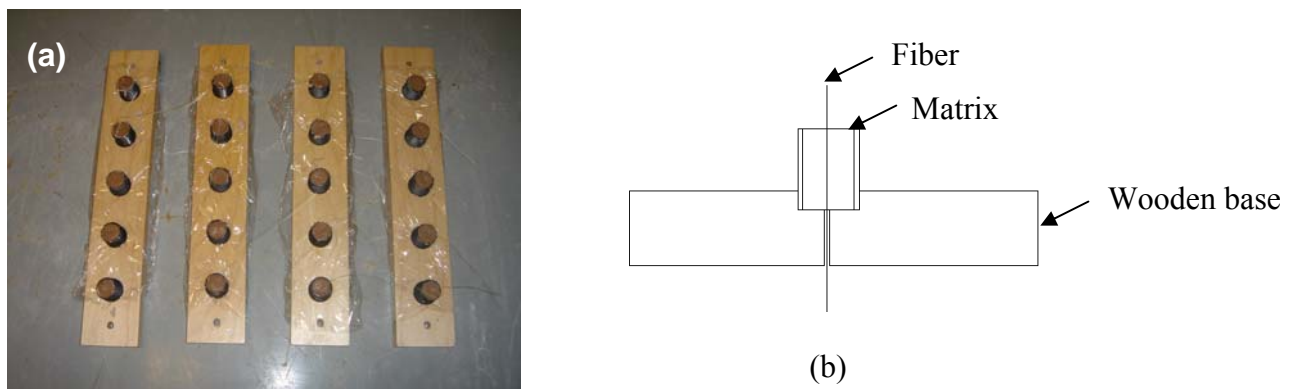


Figure 2- Molds for casting pullout specimens: (a) picture of four of the molds, (b) schematic drawing showing the alignment of the fiber.

PVC tubes were used as the formwork while wooden bases were used to guarantee the accuracy of the sisal fiber orientation at the centroidal axis of the mold through a hole drilled at the center of the circular embeddings of the base. The sisal fiber was inserted through the eye of a needle, which was then contrived through the wooden mold. The mix was then poured into the PVC tubes in three layers followed by manual compaction.

The specimens were covered in their molds for 24 hours and after this time they were demolded and cured in water.

Sisal fiber reinforced cement composites with fiber volume fraction of 10% were produced following previous works [2].

2.2. Testing

2.2.1 Single fiber pull-out tests

An electromechanical MTS (model SINTECH 1/S) was used for the pullout tests. The test setup is shown in Figure 3. The PVC mold was connected to a 0.44 kN (100 lb) load cell that was hold at the crosshead. The bottom part consisted of a pinch grip where the free end of the fiber was tightened. The test was conducted under constant crosshead displacement control at a rate of 0.1 mm/min. Six specimens of embedment length ranging from 10 to 40 mm were tested at 3 days of age. To investigate the influence of curing age on the fiber-matrix bond strength specimens with embedment length of 20 mm were tested at ages ranging from 3 to 28 days.

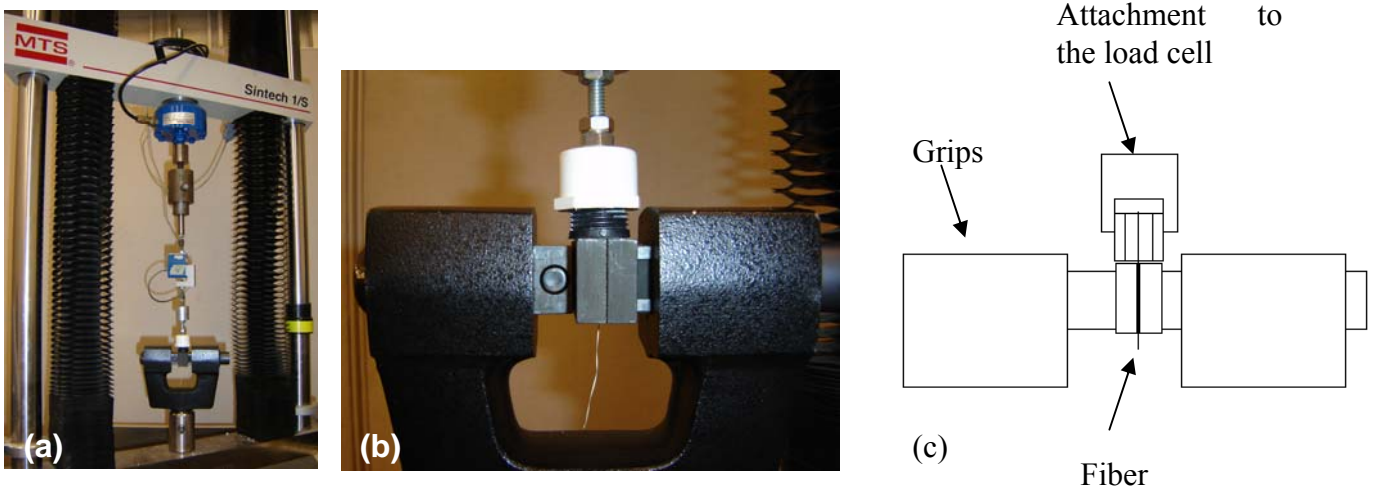


Figure 3- Details of pullout test set-up: (a) MTS Sintech machine, (b) detail of grips and (c) schematic drawing of (b).

2.2.2 Direct tension tests in sisal fiber reinforced composite

Direct tensile tests were performed in an Instron servo hydraulic universal testing machine with a capacity of 500 kN. The tests were controlled by the cross-head displacement at a rate of 0.1 mm/min. Six specimens measuring 400 mm x 50 mm x 12 mm (length x width x thickness) were tested using a gage length of 300 mm with fixed–fixed boundary conditions. Aluminum thin sheets were glued on both ends of the specimen and the pressure of the hydraulic grips was adjusted to 1.37 MPa (200 psi) in order to minimize stress concentration and damage. The tensile load, cross head displacement and strain were recorded. The tensile strains were measured by a strain gage glued on the center of the specimen, and by the stroke displacement.

Cracking space during the tensile tests was measure by image analysis and correlated to strain following the procedure described elsewhere [1].

2.2.3 Microstructure

The sisal fiber’s microstructure was investigated using a Low Vacuum SEM (Jeol JSM 347 6460 LV) and an Environmental SEM (Philips FEI-XL 30).

The scanning electron microscopy was under low vacuum chamber to remove the high vacuum constraint in the sample environment. The microscope was operated under an accelerating voltage ranging from 10 kV to 20 kV. No precoating with carbon or gold, as is done for standard high vacuum SEM, was required. The specimen chamber pressure was adjusted to values ranging from 25 to 80 Pa. All the micro-graphs were taken under the backscattered electrons mode.

In order to measure the fiber’s cross-sectional area, for each single fiber pull-out test, an adjacent piece of the fiber (immediately next to the one tested) was kept for future measurement and morphology characterization using the SEM. The obtained images were post-processed using ImageJ, a Java-based image processing program.

3. Results and discussion

A typical pull-out force-slip curve is shown in Figure 4a. Four distinct regions are indentified by roman numerals. Region I corresponds to the elastic-linear range with a rapid increasing of the load. As the load increases beyond the linear region a certain

degree of nonlinearity is observed. Region II starts at this non-linearity and defines the initial point of fiber debonding. The peak response is reached at region III. At this point the pull-out force reaches a maximum value (P_{au}). The slip of the fiber at this point is known as the slip at the peak and can be considered as the critical length of the debonded fiber. The peak pull-out force depends on the embedded length, diameter of the fiber and the curing period, the mix design being constant. The shear strength computed at P_{au} is defined as the adhesional strength (τ_{au}). In region IV the load drops to a fixed value after which it remains quite constant. The immediate post-peak region is governed by the shear strength of the fiber and continues till the fiber is completely debonded from the interface. The shear strength at this region is defined as frictional resistant strength (τ_{fu}).

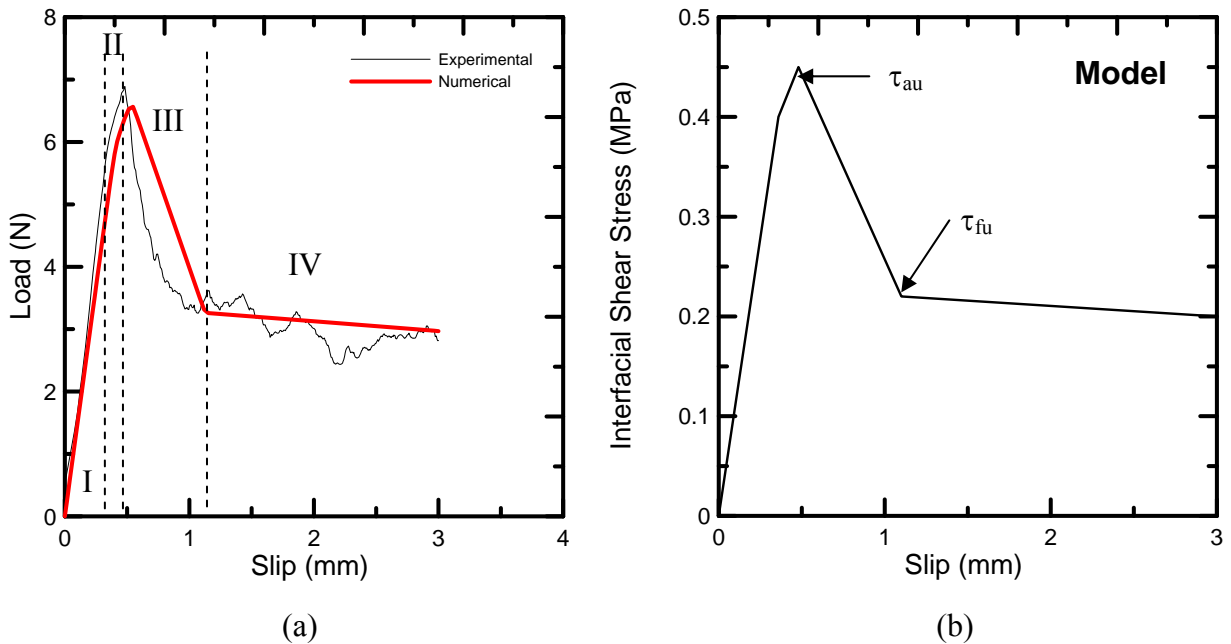


Figure 4. Fiber pull out test results of a sample tested a 3 days of curing with a embedded length of 20 mm. a) Comparison of the experimental and numerical result from the finite difference model and b) Interface constitutive relation obtained from the model.

The adhesional and frictional components were quantified in terms of stress τ_{au} and τ_{fu} , respectively. These parameters calculated using Soranakon and Mobasher's finite difference model using as first input for shear stress the following equation:

$$\tau = \frac{P}{2\pi rl} \quad (1)$$

where τ = fiber-matrix bond strength, P is the pull-out force, r = fiber radius, and l = embedded length.

In Soranakon and Mobasher's model the interfacial bond constitutive law and the tensile

stress-strain response of the fiber are described as piecewise linear functions. For the present work the restraint at the cross junction of longitudinal and transverse fibers used in the model was not considered since only longitudinal fibers are being used. Therefore the non-linear spring model that represents the stiffness of the transverse fibers was not used.

The model equilibrium equations are derived from free body diagrams of the nodes. The equations are expressed as coefficient and the unknown variable slip s , defined as the relative difference between the elongation of the longitudinal yarn and matrix

$$s = \int_{x_i}^{x_{i+1}} (\varepsilon_y - \varepsilon_m) dx \quad (2)$$

where ε_y and ε_m are fiber and matrix strains, respectively, dx is a finite length between two consecutive nodes i and $i+1$ along the longitudinal x -axis. For typical low fiber volume fraction, the axial stiffness of the yarn $A_y E_y$ is considerably lower than the matrix term $A_m E_m$ and the contribution of matrix elongation to slip is ignored. Thus, the slip s and fiber strain σ_y are simplified to:

$$s = \int_{x_i}^{x_{i+1}} \varepsilon_y dx \quad \text{and} \quad \varepsilon_y = s' = \frac{ds}{dx} \quad (3)$$

The embedded length L is discretized into “ n ” nodes with equal spacing of h . The bond stress is assumed constant over the small spacing h for each node within each linear domain. At the left end force in the fiber is imposed to be zero, simulating stress free condition, implying that the fiber strain or derivative of slip vanishes. At the right end the nodal slip is prescribed incrementally, simulating displacement control. As the loading progresses, the part of the fiber that slips out of the matrix has no frictional bond resistance; thus, fiber elongation is the only term in that section. The extruding part can be easily implemented by checking the amount of slip versus the embedded length of each node. If the slip is greater than the embedded length, zero bond stress is

applied to that node. Refer to Soranakon and Mobasher [11] for more detailed information about the model. The used model has shown good correlation with experimental sisal fiber pull-out behavior as can be seen in Figure 4a. The interfacial constitutive relation was determined from the model and presented in Figure 4b. The points where the adhesional and frictional bond strength were calculated are shown by arrows in the Figure 4b.

Pull-out tests were carried out on embedded lengths of 10, 20, 30, and 40 mm after 3 days of curing. The results are shown in Figure 5.

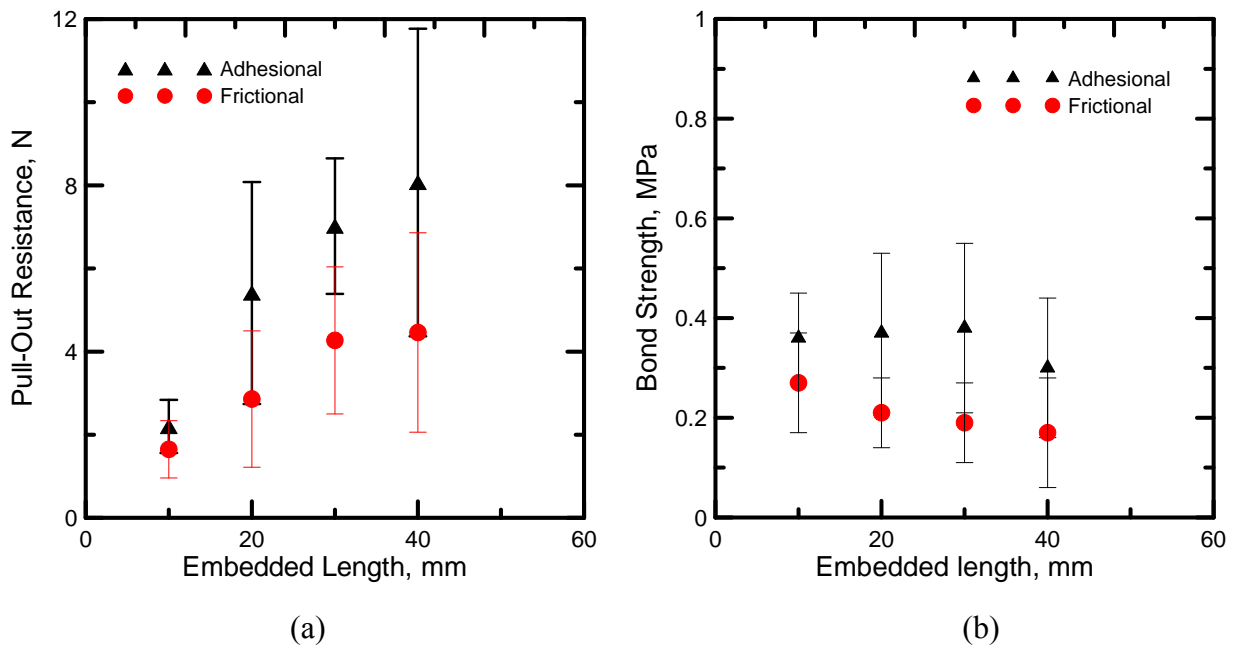


Figure 5. Influence of embedded length on the fiber-matrix interfacial bond strength: a) pull out resistance increase with increasing embedded length and b) bond strength does not improve when increasing embedded length.

It was found that increasing the embedded length the pull-out force increased from approximately 2 to 8 N. At an embedded length of 40 mm no significant increase was observed in the pull-out force related to adhesional and frictional bond. Note that the standard deviation of the fibers tested at 30 mm was in the range as of those tested with 40 mm. The adhesional bond strength computed based on the Pull-out force using Soranakon and Mobasher model showed a constant value for the studied embedded lengths (see Table 1). For frictional bond strengths a slight decrease was observed when increasing the embedded lengths.

Table 1. Summary of the results for pull-out samples tested with different embedded lengths. Values in parenthesis are standard deviation.

Embedded Length (mm)	Type of fiber	P_{au} (N)	τ_{au} (MPa)	P_{fu} (N)	τ_{fu} (MPa)	P_{au} Average (N)	τ_{au} Average (MPa)	P_{fu} Average (N)	τ_{fu} Average (MPa)
10	(i)	2.23	0.37	1.38	0.23	2.2 (0.64)	0.36 (0.09)	1.65 (0.69)	0.27 (0.10)
	(ii)	2.23	0.35	1.88	0.30				
	(iii)	-	-	-	-				
20	(i)	4.41	0.31	3.07	0.22	5.41 (2.67)	0.37 (0.16)	2.86 (1.64)	0.21 (0.07)
	(ii)	5.29	0.36	2.21	0.17				
	(iii)	7.06	0.45	3.21	0.23				
30	(i)	6.00	0.40	2.99	0.14	7.02 (1.63)	0.38 (0.17)	4.27 (1.77)	0.19 (0.08)
	(ii)	7.97	0.36	6.32	0.29				
	(iii)	7.14	0.38	4.03	0.15				
40	(i)	6.5	0.25	3.39	0.13	8.07 (3.7)	0.30 (0.14)	4.46 (2.4)	0.17 (0.11)
	(ii)	7.53	0.30	3.23	0.12				
	(iii)	9.49	0.34	6.00	0.23				

Comparing the present investigation to others found in the literature it is interesting to notice that similar behavior was found for polypropylene and steel fibers. Singh et al. studied the pull-out behavior of polypropylene fibers from cementitious matrix for embedded lengths of 19, 25 and 38 mm [17]. They found that despite the fact that the pull-out force increase with an increase in embedded length the adhesional bond strength was found to be almost constant with a value around 0.5 MPa. Shannag et al. investigated the pull-out behavior of steel fibers from cement composites for 6, 12, and 18 mm [18]. They also found that by keeping the other variables constant but increasing the embedded length from 6 to 18 mm resulted in significant increase in the pull-out adhesional load. Shannag et al. computed the frictional bond strengths for densified small particle (4.4 MPa) and conventional mortar matrices (1.4 MPa) and found no improvement when increasing the embedded length.

The effect of curing time was investigated for ages ranging from 3 to 28 days and their results are presented in Figure 6. The bond strength reaches its maximum capacity at 14 days and the further curing of the matrix shows no effect on ages of 21 and 28 days (see Table 2). The average adhesional bond strength after 15 days ranged from 0.59 to 0.67 MPa. Individual values of adhesional bond strength at 14 days ranged from 0.35 to 1.29 MPa. Frictional bond strength presented less scatter values in which main values varied from 0.37 to 0.44 MPa after 14 days. The obtained fiber-matrix bond strength results are in the range of some synthetic fibers. Carbon fibers embedded in different cement matrices were studied and the mean adhesional bond strength for diameters of 10 and 46

μm ranged from 0.52 to 1.29 MPa and 0.39 to 3.02 MPa, respectively [6]. Polypropylene fibers presented adhesional bond strength of 0.5 MPa [17].

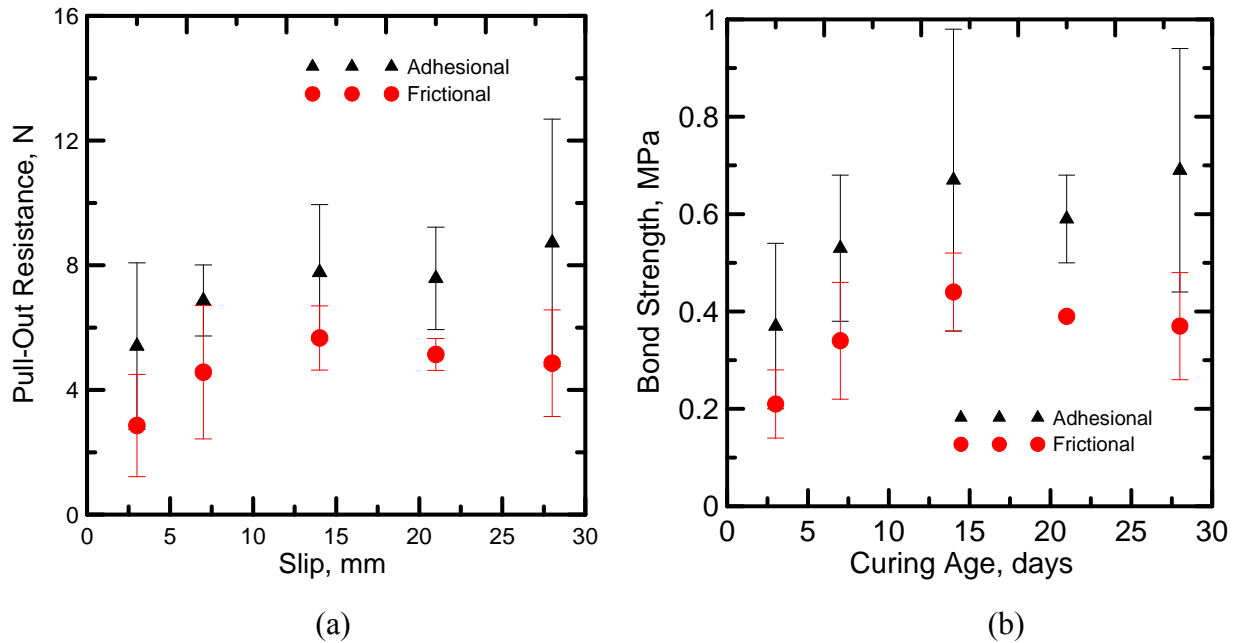


Figure 6. Influence of curing age on the fiber-matrix interfacial bond strength. After 14 days there is no further increase in a) pull out resistance and b) bond strength.

The pull-out tests results were separated in terms of the fiber morphology. As mentioned in the introduction the fiber can be divided in 3 types of mechanical bond components. As can be seen in Table 1 and 2 these different morphologies make a difference in the bond strength. It can be observed that fiber type (iii) presented the highest values. For example at 28 days of curing its adhesional bond strength was 0.92 MPa whereas fiber type (ii) and (i) presented values of 0.56 and 0.48 MPa, respectively. The influence on frictional bond was not as noticed as in the adhesional. Fiber type (ii) shows, especially in the curing age investigation, a tendency of presenting higher values than type (i).

The influence of bond strength on the sisal fiber critical length was computed using equation 4 [19]:

$$L_c = \frac{r\sigma_f}{\tau_{fu}} \quad (4)$$

where L_c = fiber critical length, r = fiber radius, σ_f = fiber ultimate tensile strength, and τ_{fu} = fiber frictional bond strength.

Table 2. Summary of the results for pull-out samples tested at different curing time. Values in parenthesis are standard deviation.

Age (days)	Type of fiber	P_{au} (N)	τ_{au} (MPa)	P_{fu} (N)	τ_{fu} (MPa)	Average P_{au} (MPa)	Average τ_{au} (MPa)	Average P_{fu} (MPa)	Average τ_{fu} (MPa)
3	(i)	4.41	0.31	3.07	0.22	5.41 (2.67)	0.37 (0.16)	2.86 (1.64)	0.21 (0.07)
	(ii)	5.29	0.36	2.21	0.17				
	(iii)	7.06	0.45	3.21	0.23				
7	(i)	5.46	0.47	3.38	0.29	6.87 (1.14)	0.52 (0.06)	4.57 (2.14)	0.34 (0.12)
	(ii)	8.34	0.59	7.04	0.48				
	(iii)	6.82	0.51	3.28	0.24				
14	(i)	6.64	0.52	5.06	0.35	7.77 (2.18)	0.62 (0.12)	5.67 (1.03)	0.44 (0.08)
	(ii)	6.39	0.58	5.10	0.46				
	(iii)	10.28	0.75	6.86	0.50				
21	(i)	-	-	-	-	7.58 (1.64)	0.59 (0.09)	5.14 (0.51)	0.39 (0.005)
	(ii)	7.06	0.51	5.51	0.40				
	(iii)	7.72	0.61	4.78	0.39				
28	(i)	5.54	0.48	2.31	0.2	8.72 (3.97)	0.67 (0.25)	4.86 (1.71)	0.37 (0.11)
	(ii)	7.01	0.56	5.57	0.46				
	(iii)	12.76	0.92	5.79	0.42				

Figure 7 shows the influence of bond strength on the critical fiber length using a fiber radius of 0.1 mm and fiber UTS of 400 MPa. If a frictional average bond strength selected from curing ages above 14 days is to be chosen (around 0.4 MPa) it can be obtained from Figure 7 a L_c of approximately 100 mm.

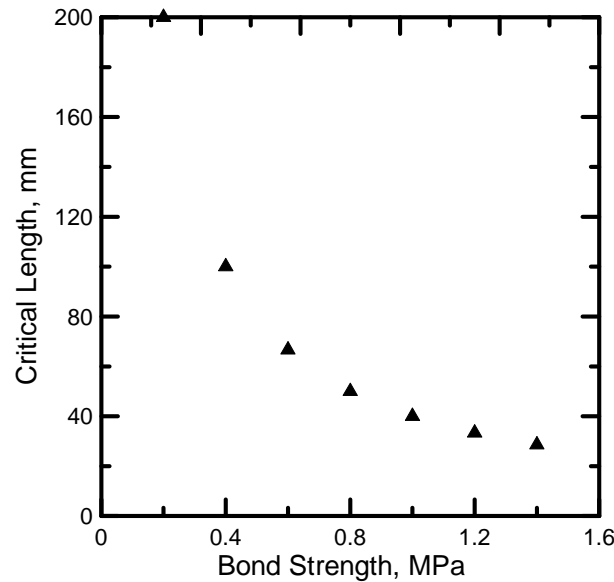


Figure 7. Influence of bond strength on the fiber critical length.

Direct tensile tests were performed in long aligned sisal fiber reinforced cement composites with a volume fraction of 10%. An average UTS of 12 MPa was obtained with individual results ranging from 10.56 to 14.70 MPa. A multiple cracking behavior

with ultimate strain of 1.53 % was observed with average cracking spacing of 23 mm in the crack saturated zone. More information on the tensile behavior and cracking mechanisms of sisal fiber reinforced composites can be obtained elsewhere [1]. To simulate the tensile behavior and crack spacing of the composites a model developed by Soranakon and Mobahser was used [12]. The simulation was done under load control and the procedure can be summarized as follow:

- The length of specimen is discretized into N nodes with equal spacing. The nodes are divided into two groups, those in the end grip zone which are not allowed to crack, and those within the clear length.
- Either uniform matrix strengths with predetermined sequential cracking locations or random matrix strengths at nodes along the length of specimen are generated and used as cracking criterion. This results in deterministic or stochastic crack pattern. The used cracking criterion in the present research was random matrix strengths.
- As long as the applied load is less than the first cracking limit, the tensile response is calculated by the rule of mixtures and strain compatibility;
- When the first crack appears, the section is divided into two parts and each segment is modeled as a pull-out problem and solved independently. As the load increases, additional cracks form at locations where the strength criterion is satisfied. The cracked specimen represented by a number of pull-out segments, each is solved independently and the solutions are combined to represent the entire specimen;
- The analysis is terminated if the stress in yarn reaches its ultimate tensile strength or a solution is not found due to slip instability (very large slip value).

To simulate the tensile behavior of the sisal fiber reinforced composite it was first selected an interfacial fiber-matrix and fiber model as shown in Figure 8a. This interface model was obtained from a pull-out test performed in a fiber type (iii) with curing age of 3 days and embedded length of 20 mm (Figure 4a). A fiber modulus of 19 GPa and UTS of 400 MPa was used as shown in the fiber model in Figure 8a. Matrix average tensile strength of 6 MPa and modulus of 35 GPa was selected. First it was studied the influence of an efficiency factor (μ) on the modulus and UTS of the fiber since in the composite the fiber may not present the same properties as those observed in a single fiber filament test.

It is observed from Figure 8b that by decreasing the values of η the total strain of the composite increases up to a point that the fiber starts to fracture. Fiber failure occurs

when η equals 0.3. It was selected an efficiency factor of 0.6 which presented ultimate strain of approximately 1.5 % (close to experimental results). The crack spacing has decreased when increasing η .

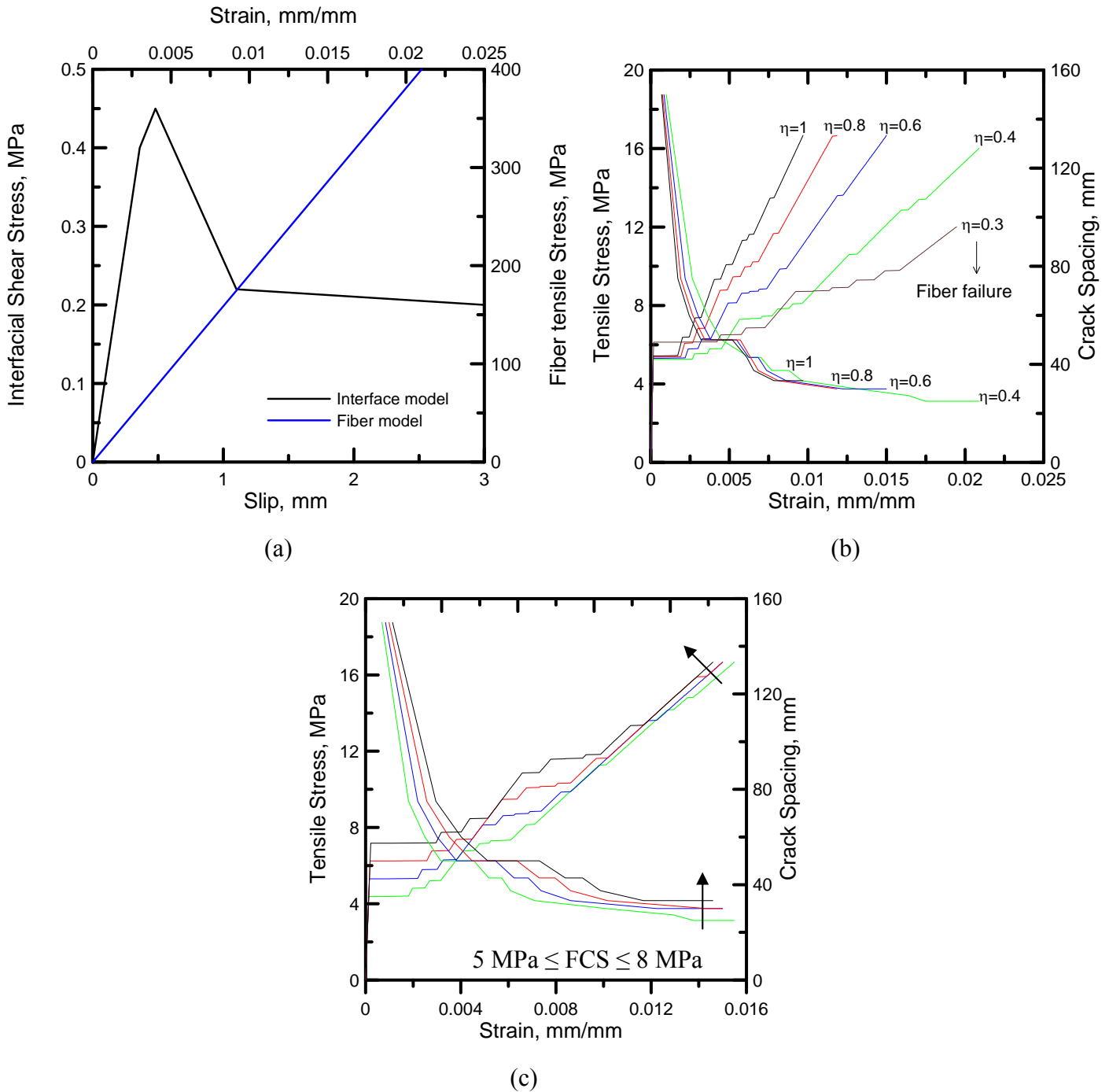


Figure 8. Prediction of tensile response and crack spacing: a) Interface and fiber model used in the finite difference simulation, b) effect of efficiency factor of fiber modulus and strength, and c) effect of matrix first crack strength.

In a second step the influence of the matrix first crack strength on the tensile and crack spacing was investigated (see Figure 8c). It was noticed a slight decrease in ultimate strain and increase in crack spacing when increasing the matrix first crack strength. No effect on the UTS was noticed.

Finally the influence of the fiber-matrix interfacial model was studied. A model that is presented in Figure 9 a and b obtained from a pull-out test performed at 21 days was used.

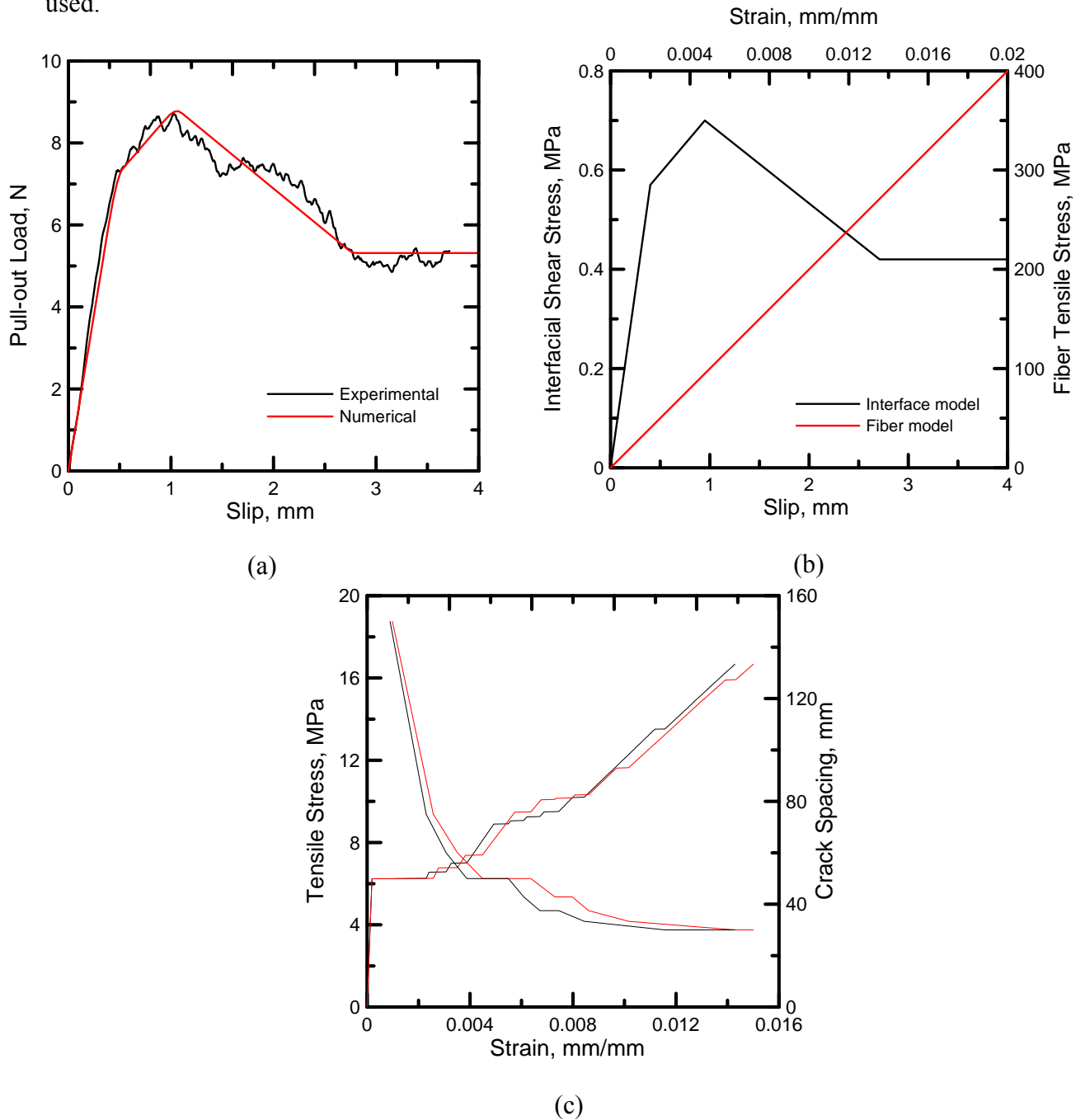


Figure 9. Study on the effect of the interface model on the tensile response and crack spacing: a) experimental and numerical pull-out response of a sample tested at 21 days

of curing with an embedded length of 20 mm, b) Interface and fiber model used in the simulation, and c) Prediction of the composite tensile behavior and crack spacing.

This specific test resulted in higher adhesional and frictional bond strengths than the one previously used. It was noticed a slight decrease in ultimate strain and no effect on crack spacing and UTS when using an interfacial model with higher bond strengths.

Figure 10 shows the comparison between experimental and predicted tension and cracking spacing behavior. It was used a η of 0.6, matrix first crack strength of 7 MPa and the interfacial bond model presented in Figure 8a. An accurate correlation with the strain gage response is seen in the linear elastic region up to the first crack formation (see Figure 10b). In the beginning of the multiple cracking zone the model correlates well with a lower bound experimental curve up to a strain of 0.4 %. After that point it fits the upper bound experimental curve overestimating the UTS. The numerical crack spacing shows an accurate prediction up to a strain value of 0.005 %. At the region of crack saturation a crack spacing of approximately 30 mm is obtained using the model and 23 mm for experiment. The model has satisfactory predicted the crack spacing and tensile behavior which can be a useful tool for design purposes.

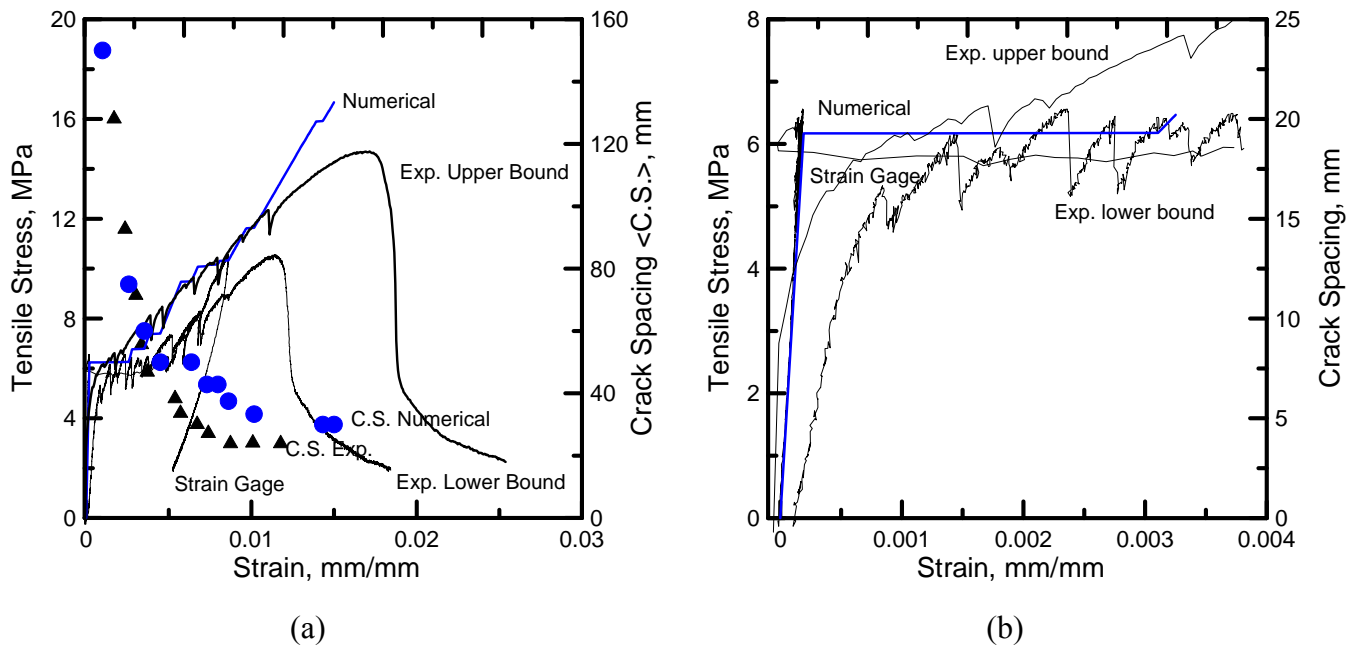


Figure 10. Comparison of experimental and numerical results of the composite tensile response and crack spacing. a) Two experimental tensile curves are shown: a lower and upper bound. b) Numerical simulation shows a perfect fit with the strain gage response in the linear elastic range up to the first crack formation.

4. Conclusion

The present work investigated the pull-out behavior of the sisal fiber from a cement matrix. The effect of curing age and embedded length were investigated and a finite difference model was used to determine the interfacial bond constitutive relation and to predict the sisal fiber reinforced composite tensile behavior and crack spacing. The following conclusions can be drawn:

- The bond strength reaches its maximum capacity at 14 days and the further curing of the matrix shows no effect on ages of 21 and 28 days. The average adhesional bond strength after 15 days ranged from 0.59 to 0.67 MPa.
- It was found that increasing the embedded length the pull-out force increased from approximately 2 to 8 N. At an embedded length of 40 mm no significant increase was observed in the pull-out force related to adhesional and frictional bond. No improvement in the bond strength was observed by increasing the embedded length.
- An influence on the bond strength was noticed for different fiber morphologies. It was observed higher values of bond strength for the twisted arch fiber type.
- The finite difference model showed to be efficient for predicting the pull-out response of the sisal fiber from cement matrices. The simulation of the composite tensile response showed good correlation with the strain gage readings up to the first cracking strength. A good correlation with a lower bound experimental value up to a 0.4 % strain was observed. After that point it fits the upper bound experimental curve overestimating the UTS. A final crack spacing of approximately 30 mm is obtained using the model and 23 mm for experiment.

Acknowledgements

The authors acknowledge Dr. Dallas Kingsbury (IMTL-ASU) for assisting with the set-up of the pull-out tests and Mr. Jeffrey Long (CEE-ASU) for helping in the production of the molds. This research was partially funded by CNPq (Brazilian National Science Agency).

References

- [1] Silva F.A., Mobasher B., Toledo Filho R.D. Cracking mechanisms in durable sisal reinforced cement composites. *Cement and Concrete Composites*, in Press, 2009.
- [2] Toledo Filho R.D., Silva F.A., Fairbairn E.M.R., Melo Filho J.A. Durability of compression molded sisal fiber reinforced mortar laminates. *Construction and Building Materials* 2008, in Press. doi:10.1016/j.conbuildmat.2008.10.012.
- [3] Naaman A. E., Najm Husamuddin. Bond-slip mechanisms of steel fibers in concrete. *ACI Materials Journal* 88 (1991) 135-145.
- [4] Peled A. and Bentur A. Quantitative description of the pull-out behavior of crimped yarns from cement matrix. *Journal of Materials in Civil Engineering* 15 (2003) 537-544.
- [5] Markovich J.G.M., Mier V. and Walraven J.C. Single fiber pullout from hybrid fiber reinforced concrete. *Heron* 46 (2001) 191-200.
- [6] Katz A., Li V.C., Kazmer A. Bond Properties of Carbon Fibers in Cementitious Matrix. *Journal of Materials in Civil Engineering* 7 (1995) 125-128.
- [7] Kim D.J., El-Tawil S., and Naaman A. Correlation between single fiber pullout and tensile response of FRC composites with high strength steel fiber. *High Performance Reinforced Cement Composites (HPRCC5) 2007*, 67-76.
- [8] Naaman A.E., Namur G.G., Alwan J.M., Najm H.S. Fiber pullout and bond slip I: Analytical Study. *Journal of Structural Engineering* 117 (1991) 2769-2790.
- [9] Sueki S., Soranakom C., Mobasher B, Peled A. A pullout-slip response of fabrics embedded in a cement paste matrix. *Journal of Materials in Civil Engineering* 104 (2007) 933–941.
- [10] Banholzer B., Brameshuber W., jung. Analytical simulation of pull-out tests—the direct problem. *Cement & Concrete Composites* 27 (2005) 93–101
- [11] Soranakom C., Mobasher B. Geometrical and mechanical aspects of fabric bonding and pullout in cement composites. *Materials and Structures* 2008.
- [12] Soranakom C., Mobasher B. Modeling of tension stiffening in reinforced cement composites: Part I -Theoretical Modeling, 2009, In preparation.
- [13] Peled A, Sueki S, Mobasher B. Bonding in fabric-cement systems: effects of fabrication methods. *Cement and Concrete Research* 36 (2006) 1661–1671.
- [14] Sujivorakul C., Waas A.M., Naaman A.E. Pullout response of a smooth fiber with an end anchorage. *Journal of Engineering Mechanics* 126 (2000) 986-993.

- [15] Shao Y., Ouyang C., Shah S. Interface behavior in steel fiber/cement composites under tension. *Journal of Engineering Mechanics* 124 (1997) 1037-1044.
- [16] Silva F.A., Chawla N., and Toledo Filho R.D. Tensile behavior of high performance natural (sisal) fibers. *Composites Science and Technology* 68 (2008) 3438-3443.
- [17] Singh S., Shukla A., Brown R. Pullout behavior of polypropylene fibers from cementitious matrix. *Cement and Concrete Research* 34 (2004) 1919-1925.
- [18] Shannag M.J., Brincker R., Hansen W. Pullout behavior of steel fibers from cement-based composites. *Cement and Concrete Research* 27 (1997) 925-936.
- [19] Kelly A. *Strong Solids*. Clarendon Press, Oxford 1966.

ARTIGO H - Silva F.A., Mobasher B. and Toledo Filho R.D. Fatigue behavior of sisal fiber cement composites. To be submitted, 2009.

Fatigue Behavior of Sisal Fiber Reinforced Cement Composites

Flavio de Andrade Silva^a, Barzin Mobasher^b and Romildo Dias Toledo Filho^a

^aDepartment of Civil Engineering, COPPE/ Universidade Federal do Rio de Janeiro,
P.O. Box 68506, CEP 21941-972, Rio de Janeiro – RJ, Brazil.

^bDepartment of Civil and Environmental Engineering, Arizona State University, Tempe,
Arizona.

To be submitted to an international Journal

2009

Abstract

The tensile fatigue behavior of long aligned sisal fiber reinforced cement composites was investigated. The fatigue behavior was examined in terms of the stress versus cycles and stress-strain hysteresis behavior of the composites. Composites were tested at stress-levels ranging between 4 to 9.8 MPa. The composites did not fatigue below a maximum fatigue level of 6 MPa up to 10^6 cycles. Monotonic tensile testing was performed for composites that survived 10^6 tests to determine its residual strength. Crack spacing was measured for these composites by image analysis technique. There was no observed loss in strength, but a decrease in Young's modulus and an increase in first crack strength was observed with increasing fatigue stress. Fluorescent optical microscopy was performed to investigate the micro crack formation in composites subject to fatigue loading.

1. Introduction

Long aligned sisal fiber reinforced cement composites have been investigated under static tension and bending tests in previous studies [1-4]. Continuous sisal fiber reinforced cement based composites are a new class of sustainable construction materials with superior tensile strength and ductility. These materials are strong enough to be used as load bearing structural members, therefore, they can be used in different types of applications such as structural panels, impact & blast resistance, repair and retrofit, earthquake remediation, and strengthening of unreinforced masonry walls. Although high ultimate tensile strength (UTS) and modulus of rupture (MOR) was obtained no information regarding to its fatigue resistance is known.

Fatigue can be defined as a permanent, localized, and progressive structural change that occurs in a material subjected to cyclic strains [5]. Those strains are created by loads smaller than the UTS of the material in a static test. In practice, fatigue affects all of the known engineering materials. Many structures are often subject to repetitive cyclic loads. Examples of such cyclic loads include machine vibration, sea waves, wind action and automobile traffic [6]. Fatigue failure occurs when a concrete structure fails at less than design load after being exposed to a large number of stress cycles [7]. The exposure to repeated loading results in a steady decrease in the stiffness of the structure, which may eventually lead to fatigue failure [6]. According to Hsu the interest in the fatigue of concrete started with the development of concrete railroad bridges which

were exposed to millions of cycles during their entire life [8]. Hsu summarized the ranges of interest of fatigue in a spectrum as shown in Table 1.

Table1. Relationship between ranges of fatigue cycles and types of applications.

Classification	Low-cycle	High-cycle		Super high-cycle	
Application	Structures subjected to earthquake	Airport pavements and bridge	Highway and highway bridges, highway pavements and concrete railroad ties	Mass rapid transfer structures	Sea structures
Number of cycles	0-10 ³	10 ³ -10 ⁵	10 ⁵ -10 ⁷	10 ⁷ -5x10 ⁷	5x10 ⁷ -5x10 ⁸

There is still a lack in understanding of the fatigue behavior of concrete materials and this is even more pronounced for fiber reinforced concrete (FRC). Although natural fibers such as cotton [9], wood pulp [10] and sisal [11] have been tested under fatigue load, cement composites reinforced with those fibers have not yet been investigated.

Most of the fatigue tests in concrete or FRC have been performed under bending loads [12-17]. Naaman [14] found that fiber reinforced concrete mixtures containing 2% of hooked steel fibers can sustain bending fatigue stresses more than twice of the plain concrete. This type of FRC (pre-cracked specimens) presented average fatigue lives of the order of 10 cycles for loads ranging between 10 and 90% of their static strength, 8000 cycles for loads ranging between 10 and 80%, and more than 2.7×10^6 cycles for loads ranging between 10 and 70%. Parant et al. [13] tested multi scale steel fiber cement composite (MSCC) under bending fatigue and observed that below a loading ratio of 0.88 (maximum fatigue stress ranging from 35.9 to 40.8 MPa for a MOR of 61.5 MPa), specimens do not fail by fatigue before 2 million cycles. Just a few works in the literature are related to fatigue in uniaxial compression [18,19] and tension loads [20-22].

In this paper we investigate the stress versus cycles fatigue behavior of sisal fiber reinforced composites. The composites were subjected to tensile fatigue load with maximum stresses ranging from 4 to 9.6 MPa at a frequency of 2 Hz. These stress levels represents approximately 30% and 80% of the UTS, respectively. Monotonic tensile tests were performed in previous works [3]. The fatigue tests were stopped either at 10^6

cycles or complete failure of the composite, whichever occurred first. Composites that survived 10^6 cycles were tested under monotonic tension to establish its residual strength. Optical and fluorescent microscopy was performed to investigate the composites microstructure after fatigue tests.

2. Experimental Program

2.1. Materials and Processing

Continuous sisal fibers were obtained from an agricultural farm located in the city of Valente, state of Bahia – Brazil. Their mechanical properties of bulk fibers defined in terms of young's modulus and tensile strength of 18 GPa and 400 MPa, respectively were reported by Silva et al. [23]. The sisal fibers are extracted from the plant leaf which is a functionally graded composite structure reinforced by three types of fibers: structural, arch and xylem fibers [23]. The first occurs in the periphery of the leaf providing resistance to tensile loads. The others present secondary reinforcement, occurring in the middle of the leaf, as well as, a path for nutrients. These fibers present different geometries as shown in Figure 1 which may result in different fiber-matrix bond strengths. The Wollastonite fiber (JG class), obtained from Energyarc, were used as a micro-reinforcement in the composite production.

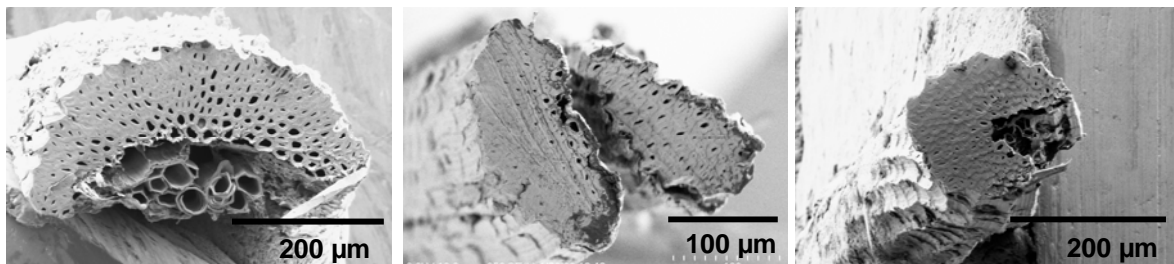


Figure 1. Sisal fiber morphology. The diverse geometry may result in different fiber-matrix bond adhesion

The matrix was produced using the Portland cement CII F-32, Metakaolin (MK) from Metacaulim do Brasil Industria e Comércio LTDA, calcined waste crushed clay brick (CWCCB) from an industry located in Itaboraí – RJ, Brazil, burned at 850 °C, river sand with maximum diameter of 1.18 mm and density of 2.67g/cm³ and a naphthalene superplasticizer Fosroc Reax Conplast SP 430 with content of solids of 44%. The mortar matrix used in this study presented a mix design 1:1:0.4 (cementitious

material:sand:water by weight). The Portland cement was replaced by 30 % of MK and 20 % of CWCCB following recommendations of a previous work [1] to increase the durability of the composite system.

The matrix was produced using a bench-mounted mechanical mixer of 20 liters capacity. The cementitious materials were dry mixed during 30 seconds (for homogenization) with the subsequent addition of sand and then a volume fraction of 5% wollastonite. The powder material was mixed for more 30 seconds when the superplasticizer diluted in water were slowly poured in the running mixer and then mixed for 3 minutes. The production of the laminates was achieved by placing the mortar mix in a steel mould one layer at a time, followed by one layer of unidirectional aligned fibers (up to 5 layers) and vibration resulting in a sisal fiber volume fraction of 10%. The vibrating table was used at a frequency of 65 Hz. After casting the composites were compressed at 3 MPa during 5 minutes. The specimens were covered in their molds for 24 hours and after this time they were demolded and fog cured for 28 days in a cure chamber with 100% RH and 23 ± 1 °C.

2.2 Fatigue tests

The composites were tested under tensile fatigue loading at a stress ratio (R ratio = $\sigma_{\min}/\sigma_{\max}$) of 0.2 and frequency of 2 Hz. Testing was conducted on a MTS 810 testing system under force control. Figure 2 shows a typical sinusoidal waveform of force versus time measured from the MTS testing system for a maximum stress level of 4 MPa. Note the high accuracy and control of the applied loading. The experiment was conducted in samples with a 300 mm gage length at five different stress levels: 4, 4.8, 6, 7.2, and 9.6 MPa which presented mean static UTS of 12 MPa [3]. Three samples were tested for each stress level and they presented exactly the same geometry (400 mm x 50 mm x 12 mm – length x width x thickness) than the ones used in the authors previous works [3]. The tests were stopped after 10^6 cycles or after failure, whichever occurred first.

Specimens that survived 10^6 cycles were tested under monotonic tensile load using the same testing system (MTS 810). The monotonic tests was controlled by the cross-head displacement at a rate of 0.1 mm/min. Crack spacing was measured during the monotonic tests following the same procedure of a previous work [3].

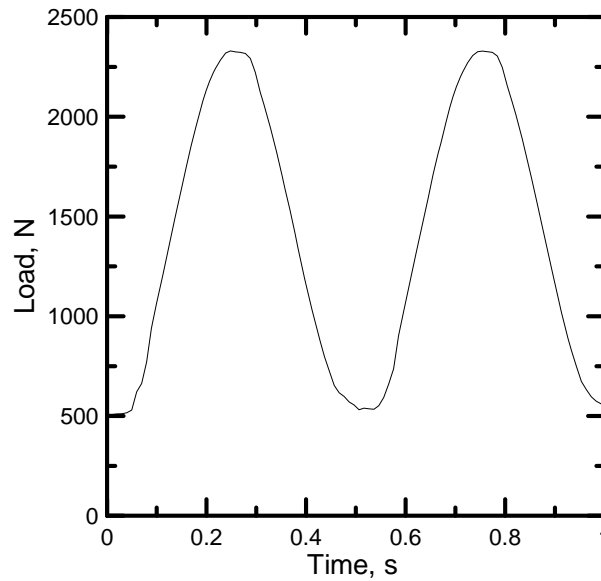


Figure 2. Load control of the fatigue test performed using MTS 810 at stress level of 4 MPa. A high accuracy is obtained by the system at the applied stress level.

2.3 Microstructural investigation

The microstructural analysis was performed using a Nikon Elipse TE300 Inverted Video Microscope. Samples that were tested under fatigue up to 10^6 cycles were preloaded to 0.4% strain and then glued with epoxy so the cracks remained open. These samples were then embedded in a polymer mixed with fluorescent dye in order to be analysed using the Nikon Inverted microscope. This microscope is outfitted with two cameras; a low light level CCD camera (Quantix) and also a standard CCD camera that allows realtime image capture. A fluorescent light (including both Phase and DIC contrast enhancement capabilities) was used. Images were captured and processed by Inovision's hardware/software interface on a SGI O2 R5000 computer.

3. Discussion and Analysis

Figure 3 shows the stress versus cycles behavior of the sisal reinforced cement composite tested at various maximum stresses (4 MPa-9.8 MPa). It can be seen that the composites can survive 10^6 cycles up to 6 MPa, which represents 50% of its UTS. The stress level of 6 MPa can be considered a threshold limit where composites may present

fatigue failure at cycles close 10^6 . Beyond 6 MPa all the composites failed below reaching 10^3 cycles. It was observed that for high stress levels (i.e. > 6 MPa) all the cracks are formed at the first cycles. The number of cracks (12) were the same as the ones observed in monotonic tensile tests. After the crack formation cracks started to widen. The cycles at these high stress levels caused a degradation process in the fiber-matrix interface which increased the rate of cracking opening leading the composite to complete failure at low cycles (i.e. $< 10^3$).

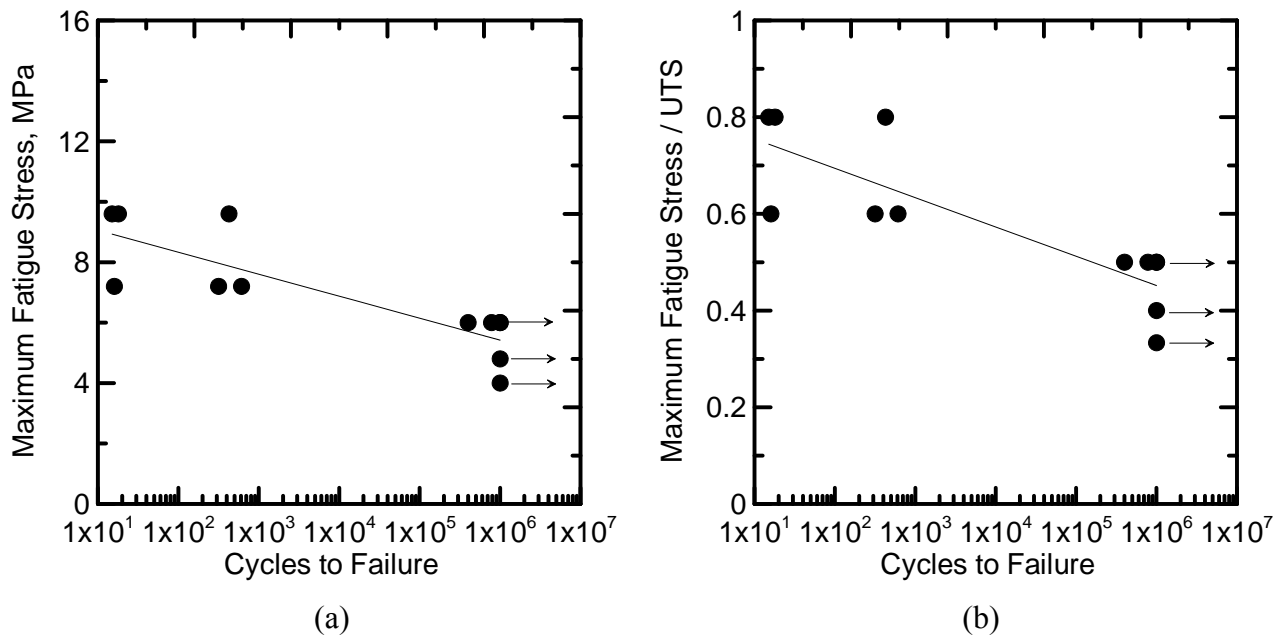


Figure 3. Stress versus cycles fatigue curve for composites subjected to maximum stress levels ranging from 4 to 9.8 MPa at constant R ratio of 0.2. Fatigue runout was taken at 10^6 cycles. The maximum stress was normalized by the ultimate tensile stress (UTS) of the composites in (b).

Composites that survived 10^6 cycles were tested under monotonic tensile load and the results are presented in Figure 4. When comparing the UTS from monotonic to post-fatigue tensile tests a slight decrease was observed. Nevertheless, this decrease lies in the standard variation range of the monotonic tests and no significant variation among the post-fatigue UTS for different stress levels was observed. Stiffness degradation was observed when calculating the modulus for the post-fatigue tensile tests. Figure 4b shows that samples subjected to a maximum fatigue stress level of 4 MPa presented higher modulus as the one calculated for the monotonic tensile tests. Above 4 MPa the modulus started to decrease from approximately 11.5 to 2 GPa. It is important to

mention that these modulus were calculated from cross-head displacement data. First crack strength was also computed for post-fatigue tensile tests. The composites presented increased first crack strength for higher maximum fatigue stress levels (see Figure 4 b).

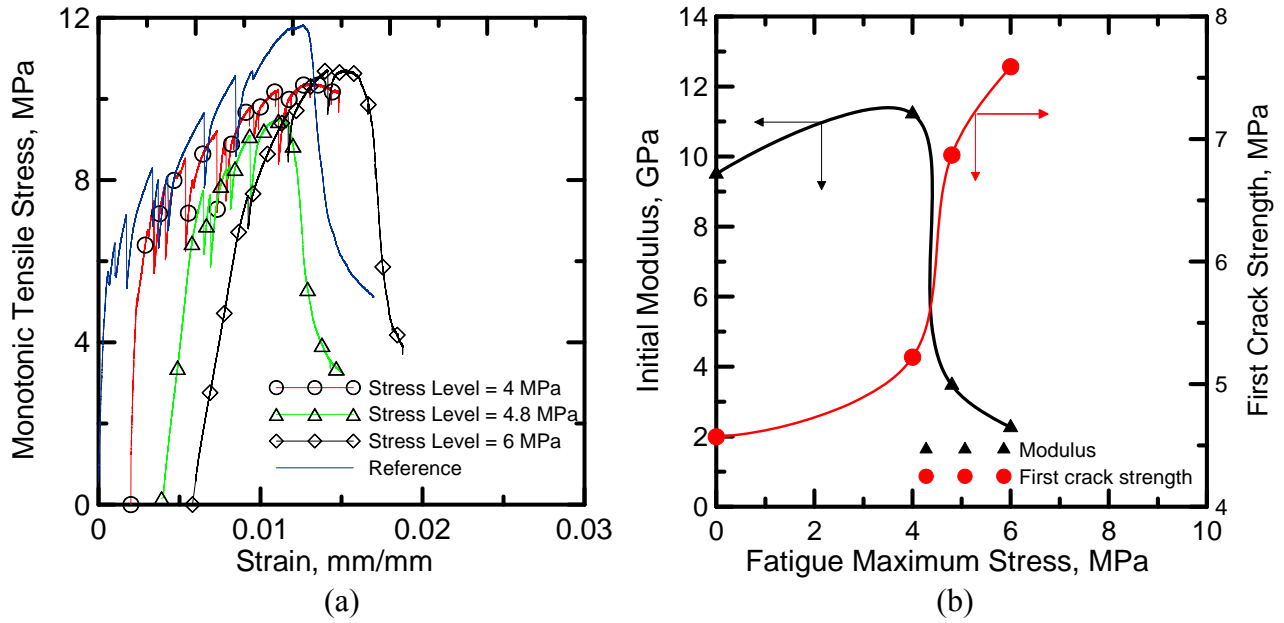


Figure 4. Monotonic tensile behavior of composites that have survived 10^6 cycles: (a) stress-strain curves of composites subjected to maximum fatigue stresses of 4, 4.8 and 6 MPa and (b) effect of the cycles on modulus of elasticity and first crack strength.

The crack spacing was measured during a post-fatigue monotonic tensile test on the sample that survived 10^6 cycles at a stress level of 6 MPa. Figure 5 show a significant difference in the cracking space behavior of a monotonic when compared to a post-fatigue test. To understand this difference one should first understand the crack spacing behavior in this composite system. The decrease in crack spacing can be empirically represented as a function of three parameters and its initiation is represented by parameters S_0 , S_1 , α , and σ_{mu} (Equation 1).

$$S(e_i) = S_1 + S_0 e^{-\alpha(e_i - e_{mu})} \quad e_i > e_{mu} \quad (1)$$

where, $S(e_i)$ = crack spacing as a function of strain, e_{mu} = average strain at the first cracking level, or where the first set of measurements were obtained, e_i = independent

parameter, S_0 and α = constants representing the initial length of the specimen and rate of crack formation as a function of strain, and S_1 = Saturation crack spacing.

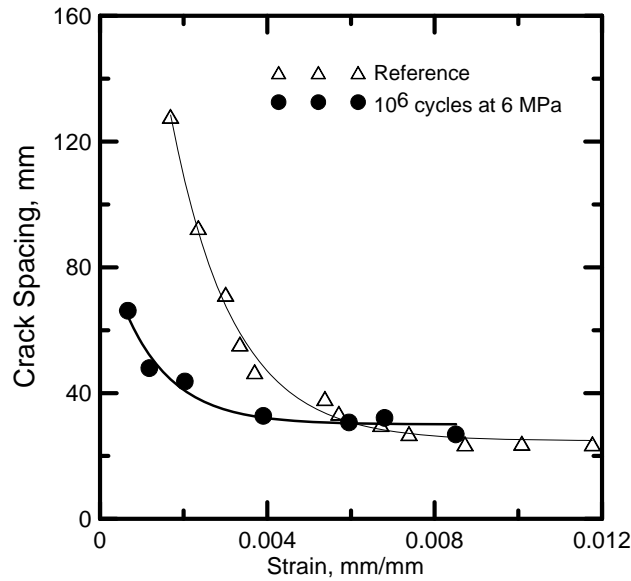


Figure 5. Effect of the cycles on the crack spacing of composites tested to monotonic tensile load after being subjected to maximum fatigue stress of 6 MPa for 10^6 cycles.

A decrease in S_0 and increase in α parameter was observed for the cycled specimen (see Table 2). This can be explained due to the fact that for the specimen subjected to fatigue load almost all the cracks were formed during the cycles. Therefore, when the specimen previously subjected to fatigue was tested under monotonic load the majority of cracks appeared in the first few minutes of the test (i.e. at low strain levels). Nevertheless, the composites presented the same saturation crack spacing, approximately 20 mm.

Table 2. Crack spacing versus strain equation for monotonic tension (reference) and post-fatigue monotonic tension.

Tests	$S_1 + S_0 * \exp^{-a(e_i - e_{mu})}$			
	S_1	S_0	α	ϵ_{mu} (mm/mm)
Reference	25.2	321.8	673.5	0.00155
10^6 cycles at 6 MPa	30.02	60.76	854.7	0.00066

Specimens were tested at maximum fatigue stress level of 6 MPa up to 45000, 200000 and 10^6 cycles. These specimens were then tested under monotonic tensile load up to complete failure. The results are shown in Figure 6. A slight decrease in the UTS is observed for the post-fatigue specimens when compared to non-fatigued ones. This decrease is in the error range of the non-fatigue UTS. More information on the monotonic UTS of the sisal fiber reinforced cement composite can be obtained elsewhere [3]. A decrease in the modulus from 12 GPa to 2 GPa is observed (see Figure 6b). Although a slight increase in the first crack strength is observed when comparing samples fatigued to 45000 and 10^6 cycles significant higher values were obtained if compared to monotonic tensile tests.

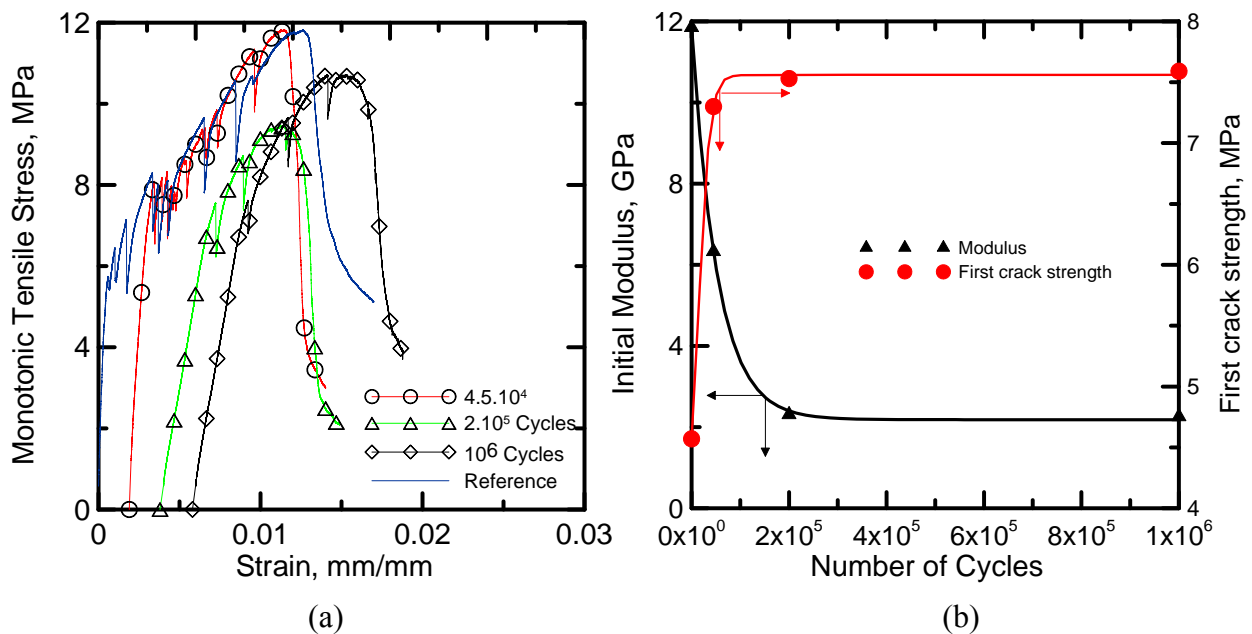


Figure 6. (a) Monotonic tensile behavior of composites cycled at maximum stress level of 6 MPa. The fatigue tests were stopped at 4.5×10^4 , 2.10^5 and 10^6 cycles. (b) Effect of the cycles on the modulus of elasticity and first crack strength.

To understand the evolution of damage, stress-strain hysteresis measurements were conducted at various stress levels. These are shown in Figure 7. These plots were obtained from composites that survived 10^6 cycles at maximum stress levels of 4, 4.8 and 6 MPa. The Young's modulus was computed from the linear unloading portion of the cycle for several cycles. For the maximum stress level of 4 MPa the thickness of the individual hysteresis loops, a measure of inelastic damage or energy during a given

cycle, was not significant and did not change with cycles. No stiffness degradation was observed for this stress level.

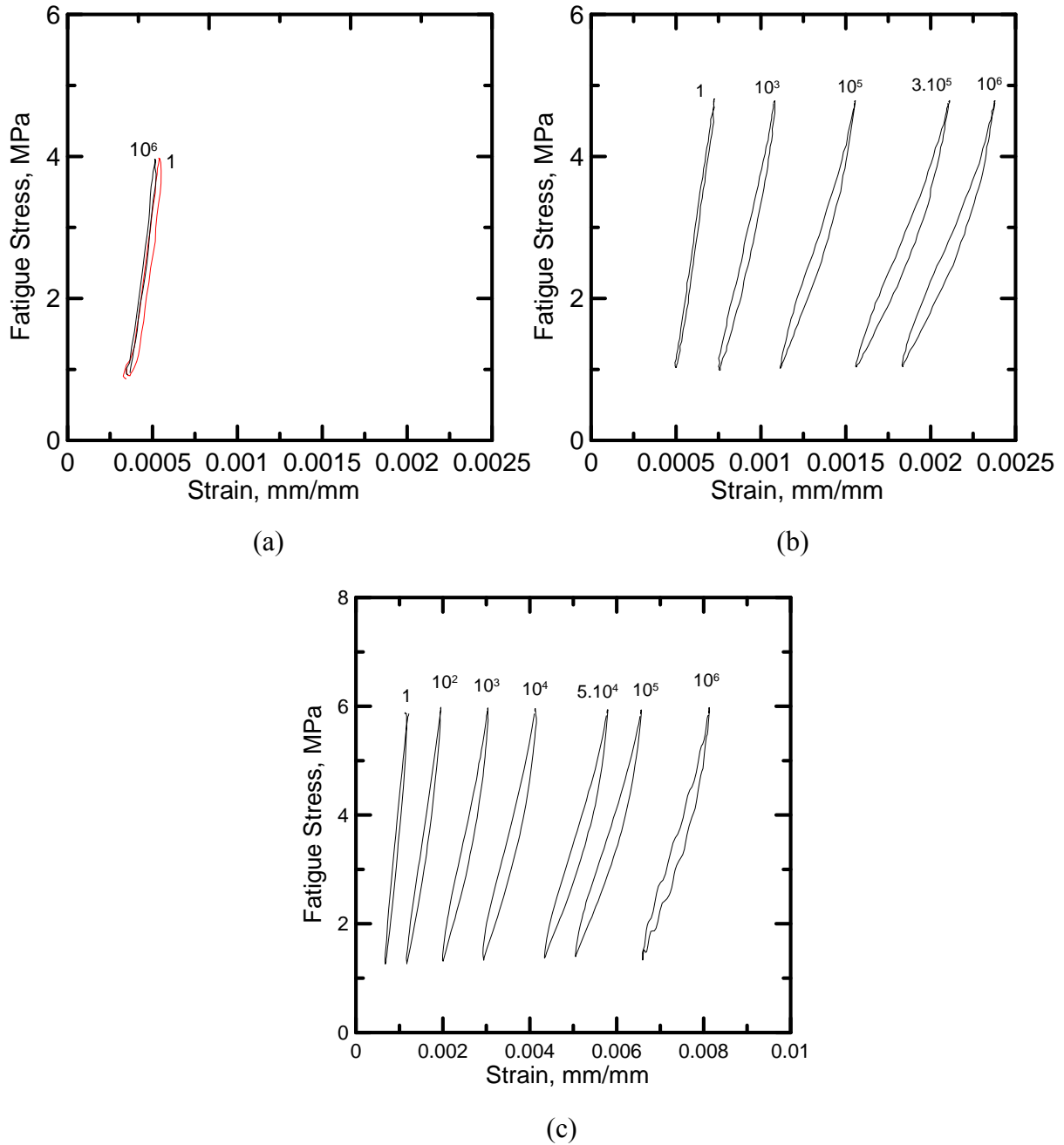


Figure 7. Hysteresis stress-strain behavior of composites subjected to 10^6 cycles. Maximum stress levels of (a) 4 MPa, (b) 4.8 MPa and (c) 6 MPa.

When increasing the maximum fatigue stress to 4.8 and 6 MPa a different behavior was observed. An increase in the thickness of the hysteresis loops as a function of cycles was observed for both levels. This behavior can be explained due to the formation of several cracks in the first cycles and posterior widening of these cracks. Stiffness

degradation and increment in strain was observed and is presented in Figure 8. Higher degradation was observed for the composites cycled at a maximum stress of 6 MPa as can be seen in Figure 8. At 10^6 cycles the maximum strain was 0.8 % and young's modulus of 4.2 GPa. For the 4.8 MPa stress level the maximum strain was 0.23% and young's modulus of 2 GPa at the 10^6 cycles. It was observed a change of shape in the hysteresis loops above 10^3 cycles for maximum fatigue tensile stresses of 4.8 and 6 MPa. The hysteresis loop changes to an “s” shape due to a continuous degradation process in the fiber-matrix interface.

Therefore for the studied composites and using the applied test methodology four stages in the fatigue cycles can be observed and classified:

- (i) Maximum fatigue stress (MFS) \leq 4 MPa – characterized by no fatigue and no damage to the material;
- (ii) $4 \text{ MPa} < \text{MFS} < 6 \text{ MPa}$ – characterized by no fatigue with moderate damage to the material;
- (iii) MFS = 6 MPa – characterized by fatigue at high cycles (close to 10^6) or no fatigue with high damage to the material;
- (iv) MFS $>$ 6 MPa – characterized by fatigue at low cycles (i.e. < 1000 cycles).

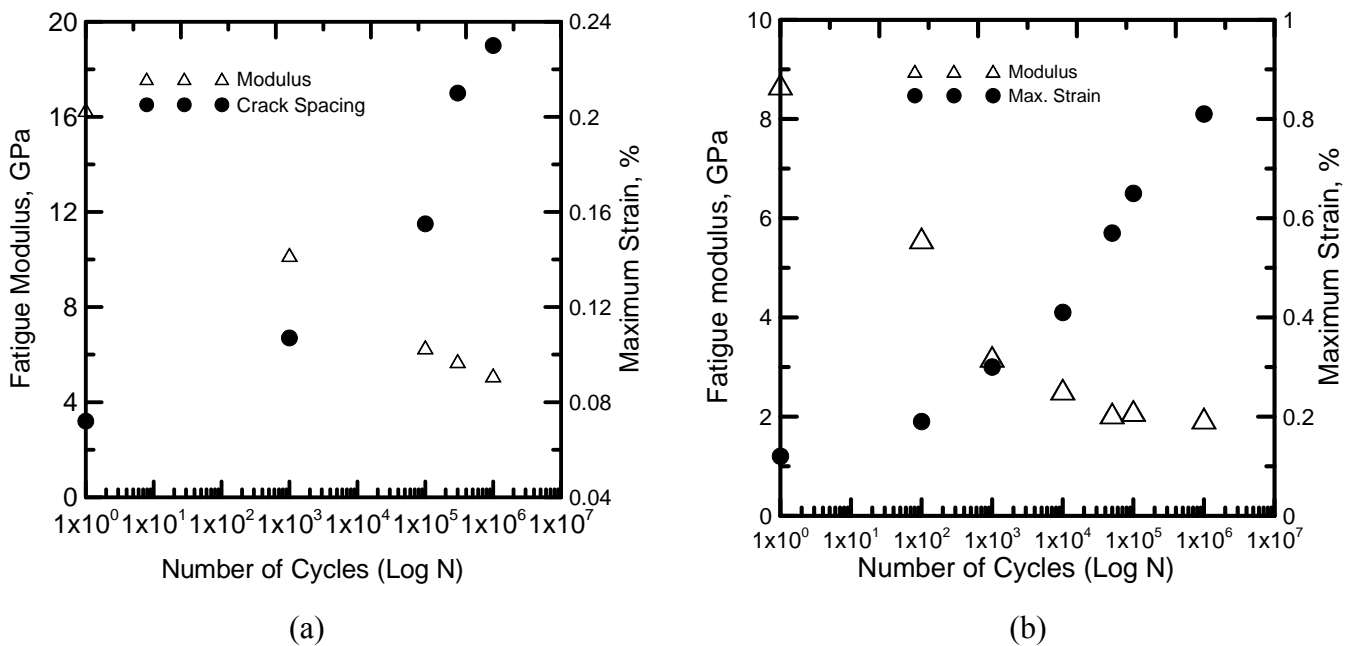


Figure 8. Effect of the cycles on the fatigue modulus and maximum strain of composites subjected to maximum stresses of (a) 4.8 MPa and (b) 6 MPa.

Samples that survived 10^6 cycles at a stress level of 6 MPa were investigated using fluorescent optical microscopy. Figure 9 shows the capacity of the fibers to arrest and bridge the cracks formed during fatigue cycles in lateral (Figures 9 a,c,d) and front (Figure 9 b) cross section views. This behavior attests the high efficiency in the fiber matrix bond adhesion of the composite system even when subjected to 10^6 cycles at a maximum stress of 6 MPa. Two ranges of crack widths were observed in the micrographs: (i) from 1 to 20 μm and (ii) from 150 to 200 μm at a deformation of 0.4%. The use of fluorescent dye possibilities the visualization of micro cracks with width less than 20 μm that were not observed in conventional optical microscopy. The enhancement in contrast was also achieved with the fluorescent microscopy. Only the cracks, voids and fibers are green while the matrix is black.

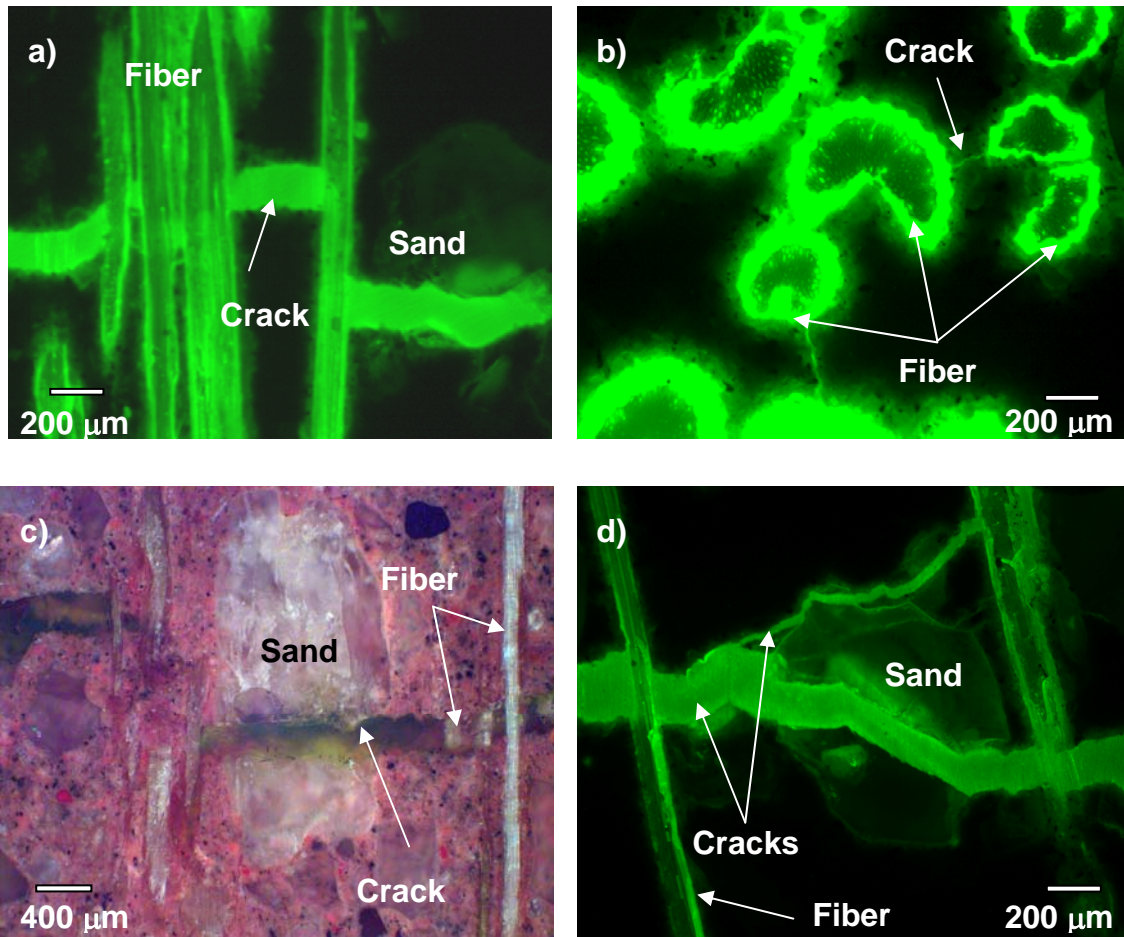


Figure 9. Cracks on composites subjected to 10^6 cycles at maximum fatigue level of 6 MPa. Fluorescent and conventional optical microscopy. Note the higher contrast in the fluorescent optical microscopy that allows the visualization of small cracks ($< 20\mu\text{m}$).

4. Conclusion

Long aligned sisal fiber reinforced cement composites were tested under tensile fatigue loading and the main findings are described below:

- Composites did not fatigue up to 10^6 cycles when subject to maximum stress level below 6 MPa. Above this stress the composites presented fatigue below 10^3 cycles.
- Composites that survived 10^6 cycles and were tested under monotonic tension did not present significant reduction in UTS but presented decrease in young's modulus. The first crack strength increased when increasing the fatigue stress levels.
- From the hysteresis stress-strain curves it was noticed no signs of degradation for maximum stress level of 4 MPa. For maximum stress levels of 4.8 and 6 MPa there was noticed an increase in the hysteresis area and decrease in the young's modulus.
- The use of fluorescent optical microscopy resulted in high contrast images. The sisal fibers were able to arrest and bridge the cracks even when subjected to 10^6 cycles at 6 MPa of maximum stress.

Acknowledgements

The authors acknowledge the W.M. Keck Bioimaging Laboratory at ASU for the use of the Nikon inverted microscope. The first author acknowledge financial support from CNPq (Brazilian National Science Foundation).

References

- [1] Toledo Filho R.D., Silva F.A., Fairbairn E.M.R., Melo Filho J.A. Durability of compression molded sisal fiber reinforced mortar laminates. *Construction and Building Materials* 2008, in Press. doi:10.1016/j.conbuildmat.2008.10.012.
- [2] Silva F.A., Melo Filho J.A., Toledo Filho R.D., Fairbairn E.M.R. Mechanical behavior and durability of compression moulded sisal fiber cement mortar laminates

- (SFCML). In: 1st International RILEM Conference on Textile Reinforced Concrete (ICTRC), Aachen, Proceedings, p. 171-180, 2006.
- [3] Silva F.A., Mobasher B., Toledo Filho R.D. Cracking mechanisms in durable sisal reinforced cement composites. *Cement and Concrete Composites* 2009.
- [4] Silva F.A., Melo Filho J.A., Toledo Filho R.D., Fairbairn E.M.R. Effect of Reinforcement Ratio on the mechanical response of compression molded sisal fiber textile reinforced concrete. In: *High Performance Fiber Reinforced Cement Composites (HPFRCC5)*, Mainz, p. 175-182, 2007.
- [5] Revuelta D. and Miravete A. Fatigue damage in composite materials. *International Applied Mechanics*, 38 (2002) 121-134.
- [6] Lee M.K. and Barr B.I.G. An overview of the fatigue behavior of plain and fibre reinforced concrete. *Cement & Concrete Composites* 26 (2004) 299-305.
- [7] Li H, Zhang M-H. Ou J-p. Flexural fatigue performance of concrete containing nano-particles for pavement. *International Journal of Fatigue* 29 (2007) 1292-1301.
- [8] Hsu T.C. Fatigue of Plain Concrete. *ACI Journal* 78 (1981) 292-304.
- [9] Hkarlk JWS and Sparrow JT. Tensile Fatigue of Cotton Fibers. *Textile Research Journal* 49 (1979) 242-243.
- [10] Hamad WY. Some microrheological aspects of wood-pulp fibres subjected to fatigue loading. *Cellulose* 4 (1997) 51-56.
- [11] Silva F.A., Chawla N., Toledo Filho R.D. The fatigue behavior of sisal fibers. *Materials Science and Engineering A* 2009.
- [12] Hernández-Olivares F., Barluenga G., Parga-Landa B., Bollati M. , Witoszek B. Fatigue behavior of recycled tyre rubber-filled concrete and its implications in the design of rigid pavements. *Construction and Building Materials* 21 (2007) 1918-1927.
- [13] Parant E., Rossi P. and Boulay C. Fatigue behavior of a multi-scale cement composite. *Cement and Concrete Research* 37 (2007) 264-269.
- [14] Naaman A.E. and Hammoud H. Fatigue characteristics of high performance fiber-reinforced concrete. *Cement and Concrete Composites* 20 (1998) 353-363.
- [15] Johnston CD, Zemp RW. Flexural fatigue performance of steel fiber reinforced concrete-influence of fiber content, aspect ratio and type. *ACI Materials Journal* 88(4) (1991) 374-383.
- [16] Zhang J, Stang H. Fatigue performance in flexure of fiber reinforced concrete. *ACI Materials Journal* 95(1) (1998) 58-67.

- [17] Ramakrishnan V., Lokvik BJ. Flexural fatigue strength of fiber reinforced concretes. In: Reinhardt H.W., Naaman AE, editors. High Performance Fiber Reinforced Cement Composites: Proceedings of the International RILEM/ACI workshop. London: E&FN SPON:1992. p. 271-287.
- [18] Gao L. ,Hsu T.C.C. Fatigue of concrete under uniaxial compression cyclic loading. *ACI Materials Journal* 95(5) (1988) 575-581.
- [19] Rafeez AS, Gupta A, Krishnamoorthy S. Influence of steel fibers in fatigue resistance of concrete in direct compression. *Journal of Materials in Civil Engineering* 12(2) (2000) 172-179.
- [20] Xianhong M. and Yupu S. Residual tensile strength of plain concrete under tensile fatigue loading. *Journal of Wuhan University of Technology-Mater. Sci. Ed.* 22:564-568.
- [21] Zhang J, Stang H, Li VC. Experimental study on crack bridging in FRC under uniaxial fatigue tension. *J Mater Civil Eng* 12 (2000) 66–73.
- [22] Saito M. Characteristics of microcracking in concrete under static and repeated tensile loading. *Cem Concr Res* 17 (1987) 211–8.
- [23] Silva F.A., Chawla N., and Toledo Filho R.D. Tensile behavior of high performance natural (sisal) fibers. *Composites Science and Technology* 68 (2008) 3438-3443.

ARTIGO 1 - Silva F.A., Zhu D., Mobasher B. and Toledo Filho R.D. Impact behavior of sisal fiber cement composites under flexural load. Composites Part A, submitted, 2009.

Impact Behavior of Sisal Fiber Cement Composites under Flexural Load

Flávio de Andrade Silva^a, Deju Zhu^b, Barzin Mobasher^b, and Romildo Dias de Toledo Filho^a

^aCivil Engineering Department, COPPE, Universidade Federal do Rio de Janeiro, P.O. Box 68506, CEP 21941-972, Rio de Janeiro – RJ, Brazil.

^bDepartment of Civil and Environmental Engineering, Arizona State University, Tempe, AZ 85287-8706

Composites Part A

2009

Abstract

The impact response of unidirectional continuous sisal fiber reinforced cement composites is studied. An impact test set up based on a free-fall drop of an instrumented hammer on a three point bending configuration test was used. The effect of impact energy was investigated by using three different drop heights. The hammer and specimen accelerations were recorded during the impact event. The impact load was measured by conventional and piezoelectric load cells. Furthermore, damage mechanisms were investigated by characterizing the cracking patterns during the impact event using a high speed digital camera. Mechanical properties obtained under impact loading were compared with static three point bending tests. It was observed that while the maximum flexural stress values were in the same range for static and impact tests, the absorbed energy increased up to a maximum level of 13.89 kJ/m² for input impact energy of 15.83 J. The damage process was initiated by tensile and shear cracks. Delamination of the plies within the continuous fiber composites was only observed when the impact energy was 21.1 J.

Keywords: Sisal Fiber (A), Cement composites (A), Impact test (D).

1. Introduction

Proper design of a composite system subjected to high loading rates can be accomplished only if strain rate sensitivity of the material has been measured and the modes of failure and energy absorption are well characterized. One of the characteristics of fiber reinforced cement based composites is their high ductility which makes them ideal for use under blast, impact, and dynamic loads. Since cement based composites are rate-dependent, their mechanical properties such as Young's modulus, ultimate strength, and fracture toughness are highly dependent on the loading rate. Proper knowledge of the constitutive relationship for a wide range of strain rates is therefore required to develop realistic material laws. During the life span of a structure, impact events by debris during a hurricane event, wind and seismic loads, and ballistic projectile can be expected to occur. In some cases impact velocities may be relatively low, but a high projectile mass may cause significant damage [1]. In addition, the potential for use of cement composites as a tool to withstand the high energy explosives cannot be

overlooked. Characterization of the impact response of the concrete is important for planning this activity [2].

Impact resistance of fiber reinforced concrete has been measured by several test methods: Charpy, Izod, drop-weight, split Hopkinson bar (SHB), explosive, and ballistic impact [3, 4]. These tests can be either instrumented or heuristically based and the resistance can be measured by means of fracture energy, damage accumulation, and/or measurement of the number of drops to achieve a determined damage or stress level. The results depend on many variables such as size of specimen, machine compliance, strain rate, type of instrumentation and test set-up.

Silva et al. performed Charpy impact tests (strain rate = 14.4 s^{-1}) and static three point bending tests in sisal pulp fiber reinforced cement composites with a fiber mass fraction of 14%. No significant difference between maximum force obtained from static (0.21 kN) and impact (0.19 kN) were observed [4, 5]. A modified SHB was used by Romano and Silva et al. to characterize steel fiber reinforced concrete (SFRC) [6]. SHB results showed an increase in both toughness and ultimate strength compared to static compression tests. Figure 1 shows the damages caused by the modified SHB impact tests in a SFRC ($V_f = 1\%$) compared to unreinforced concrete. The SFRC can absorb the energy through multiple cracking and therefore demonstrates a higher tolerance for damage.

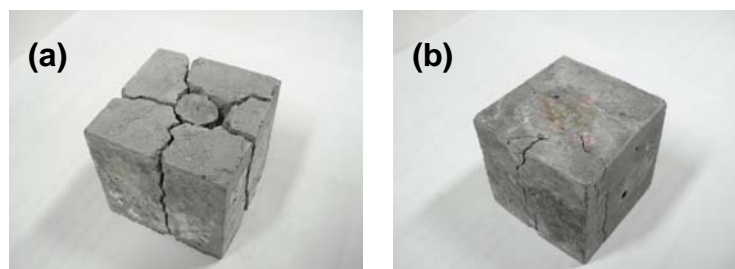


Figure 1. Comparison of damage in unreinforced (a) and steel fiber reinforced concrete (FRC) (b) after impact test using a modified Hopkinson bar [6]. Steel FRC can absorb more energy resulting in less damage.

Wang et al. identified two different damage mechanisms for fiber reinforced concrete (FRC) drop weight impact. For fiber fractions lower than the critical fiber volume (CFV), fiber fracture dominates the failure mechanism; while for values higher than the

CFV, the fiber pull-out mechanism dominates the response [7]. The critical value for the hooked steel fibers was found to be between 0.5% and 0.75%.

Lok and Zhao observed that the dynamic compressive strength of SFRC when tested using a SHB increases very slowly from quasi-static to a relatively low strain rate [8]. Up to strain rates between 10 and 20 s⁻¹, the increase is insignificant. For example, the average uniaxial compressive strength of cubes was 91 MPa and the specimen labeled Zh07^a tested under a strain rate of 32 s⁻¹ presented a dynamic strength of 91.8 MPa.

Flexural impact tests of cement based composites reinforced by Alkali Resistant (AR) glass and polyethylene fabrics have been performed [9, 10]. Zhu et al. reported for cement composites reinforced with AR glass fabrics flexural strengths as high as 29.9 MPa for plate specimens when subjected to potential energies in the range of 7-14 J [9]. The absorbed energy increased with drop height while the ratio of absorbed energy to potential energy decreased with drop height. Interlaminar shear was the dominant failure mode.

The flexural static and impact strength of long aligned sisal fiber reinforced cement composite was determined in this work. This composite system presents enhanced strength and ductility which is primarily governed by the composite action when matrix cracks and the fibers bridge them to transfer the loads, allowing a distributed microcrack system to develop [11]. These materials are strong enough to be used as load bearing structural members, in applications such as structural panels, impact & blast resistance, repair and retrofit, earthquake remediation, strengthening of unreinforced masonry walls, and beam-column connections.

An impact test set up based on a free-fall drop of an instrumented hammer on a three point bending specimen was developed. The hammer assembly weighing 134 N was dropped on specimens of 160×50×12 mm (length × width × thickness) in dimension from three different heights of 101.6 mm (4 in) 152.4 mm (6 in) and 203.2 (8 in). Accelerometers were mounted on both the impact hammer and specimen. The impact force and mid-span deflection of specimen were measured by piezoelectric and conventional load cells and LVDT, respectively. Data collection was accomplished by a high speed data acquisition unit. A high speed digital camera (Phantom v.7) was used to capture pictures at a sampling rate of 10,000 frames per second (fps) during the impact tests.

2. Experimental Program

2.1 Material properties and mix design

To increase the durability of the Sisal fibers in the alkaline environment, a cementitious matrix consisting of 50% Portland cement, 30% metakaolin (MK) and 20% calcined waste crushed clay brick (CWCCB) developed in earlier studies was used [12, 13]. The matrix was produced using the Portland cement CII F-32 with a 28 days compressive strength of 32 MPa. Metakaolin (MK) was obtained from Metacaulim do Brasil Industria e Comércio LTDA, and calcined waste crushed clay brick (CWCCB), obtained from a plant located in Itaboraí – RJ, Brazil, was calcined at 850 °C. River sand with maximum diameter of 1.18 mm and density of 2.67g/cm³ and a naphthalene superplasticizer Fosroc Reax Conplast SP 430 with content of solids of 44% were also used.

The mortar matrix used in this study presented a mix design 1:1:0.4 (cementitious material:sand:water by weight). Wollastonite fiber (JG class), obtained from Energyarc, were used as a micro-reinforcement in the composite production ($V_f = 5\%$).

The sisal fibers were characterized as having an irregular cross section with mean area ranging from 0.04 to 0.05 mm² and a mean density, elastic modulus, and tensile strength of 0.9 g/cm³, 19 GPa and 400 MPa, respectively [13]. These fibers were extracted from the sisal plant in a farm located in the city of Valente, state of Bahia – Brazil. More information on the sisal fibers mechanical properties and its morphology can be obtained elsewhere [14].

The matrix was produced using a bench-mounted mechanical mixer of 20 liters capacity. The cementitious materials were homogenized by dry mixing for 30 seconds prior to addition of sand and 5% by volume of wollastonite. The powder material was mixed for an additional 30 seconds prior to addition of superplasticizer and water. The mixture was blended for 3 minutes. For the production of the laminates, the mortar mix was placed in a steel mold, one layer at a time, followed by single layers of long unidirectional aligned fibers (up to 5 layers). The samples were consolidated using a vibrating table operated at a frequency of 65 Hz, which resulted in a sisal fiber volume fraction of 10%. After casting the composites were compressed at 3 MPa for 5 minutes. The specimens were covered in their molds for 24 hours prior to moist curing for 28 days in a curing chamber with 100% RH and 23±1 °C.

2.2 Impact Test procedure

An impact test set-up based on a free-fall drop of an instrumented hammer on a three point bending specimen was developed. The schematic and picture of the system is presented in Figure 2. The drop heights range from 1 to 2000 mm, and can be controlled by means of an electronic hoist and release mechanism. An anti-rebound system consisting of pneumatic brakes triggered by a contact type switch was used to stop the hammer after the duration of impact was completed.

The experimental set-up consisted of several components described as follows. The entire moving part that impacts the specimen included the free weight, frictionless bearings along the drop columns, load cell, connection plate, and a set of threaded rods. This entire assembly was referred to as the hammer and weighed 134 N. The hammer was released from a predetermined drop height by means of the electronic brake release mechanism. The impact force induced by the free fall weight was measured by two different means, the first a conventional resistance type strain gage based load cell with a range of 90 kN mounted on the hammer between the blunt shaped impact head and the hammer mass. An alternative piezoelectric load washer was also used to measure the load. A second strain gage based load cell with 90 kN capacity was mounted beneath the support plate and measured the force transmitted to the equipment base. A linear variable differential transformer (LVDT) with a range of ± 10 mm was connected to the specimen by means of a lever arm. Two accelerometers were used to document the acceleration-time history of the hammer and specimen. The accelerometers with a capacity of ± 500 g were mounted on the top load cell and tension zone of the specimen. The data acquisition system consisted of a PC based National Instruments PCI acquisition card and LABVIEW VI's with trigger function which can record signals from load cells, accelerometers, and the LVDT at sampling rates of 20 kHz. The entire duration of the test lasted from approximately 40 to 60 milliseconds. A MATLAB program was developed for data processing to filter and smooth the raw data with a low-pass filter, and calculate the mechanical properties. A high speed digital camera (Phantom v.7) was used to capture pictures of the samples during the impact tests. The damage caused in the samples for the different drop heights were then compared by visual examination.

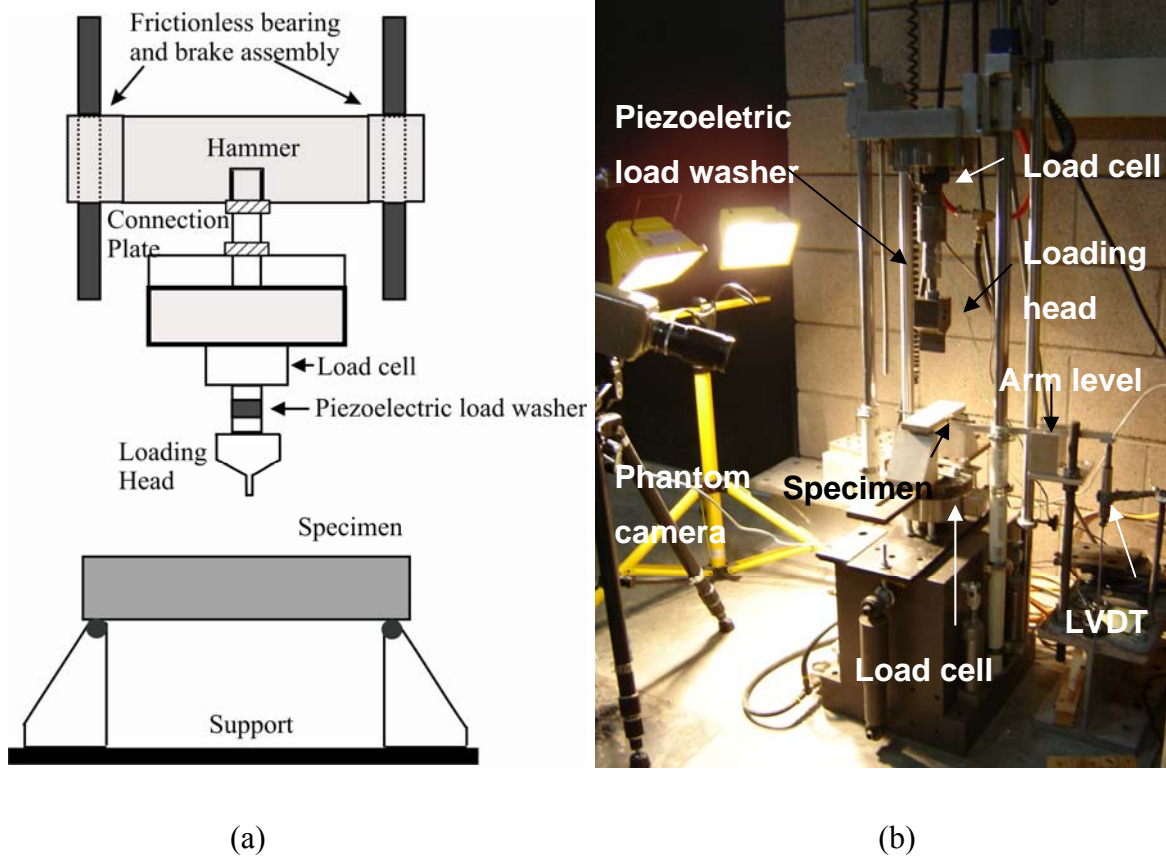


Figure 2. Schematic diagram (a) and actual picture (b) of the impact test set-up. The tests were performed in three drop heights: 101.6, 152.4 and 203.2 mm.

2.3 Dynamic Calibration for Impact Testing

The signal acquisition during a dynamic test is strongly conditioned by the nature of the test procedures [15]. Rapid variation of the kinematical quantities excites vibrations depending on the stiffness and mass of the specimen, support, or the hammer, resulting in signal disturbances. Interpretation of raw signals without prior knowledge of the dynamic characteristics of the system would therefore be questionable. After the system dynamics are identified, it is essential to filter the data to retain the material responses [16].

In order to evaluate the measurement accuracy of the conventional strain gage based load cell, a Kistler 9041A piezoelectric load washer with a capacity of 90 kN and rigidity of 7.5 kN/ μm was installed between the conventional load cell and blunt shaped impact head. The response frequency of the load washer is 33 kHz. The load signal was

amplified through a Kistler 5010B dual mode charge amplifier. The signals were filtered by a low-pass filter with cutoff frequency of 2 kHz to eliminate high frequency noise during data processing. Figure 6(a) compares the force measured by the conventional load cell and the piezoelectric load washer. The force measured by the piezoelectric load washer has more oscillations than the conventional load cell during the initial loading range. This behavior is due to the frequency response of the system and the specimen and the hammer reacting to the impact by oscillating at their natural frequencies. Since the piezoelectric load washer has a higher response frequency than the conventional load cell, it is able to acquire details of the oscillation. In consideration to the absorbed energy, negligible differences between them based on the impact forces measured by these two load transducers were observed. Therefore, results listed are based on the conventional load cell and were used in the analysis.

The potential energy of the hammer is the input energy and depends on its drop height and mass, and the amount of energy lost during the free fall drop of the hammer such as friction. Some of the input energy is absorbed by the test specimen, while the remaining energy is either dissipated by friction, or transferred to the test set-up through the supports after the impact event.

The input potential energy of the hammer, U_i , was defined as the follows:

$$U_i = mgH = \frac{1}{2}mv_0^2 + U_d = U_k + U_f + U_d \quad (1)$$

Where m is same as above, g is the acceleration of gravity, H is the drop height of hammer, v_0 represents the hammer velocity prior to impact, U_d represents the frictional dissipated energy between the time of release of the hammer until just prior to the impact event, U_k represents the absorbed energy by the specimen, and U_f represents the energy remaining in the system after the failure of the specimen has taken place. This energy may be elastically stored in the sample, and result in the rebound, or transmitted through the specimen to the support.

The total absorbed energy (kinetic energy dissipated in the specimen), U_k , was defined as the follows:

$$U_k = \int_{t=0}^{t=t^*} P(t)v(t)dt \approx \sum P(t)\Delta d(t) \quad (2)$$

Where $P(t)$ and $v(t)$ represent the force and velocity history of the impact event, t^* represents the impact event duration, $\Delta d(t)$ represents the deflection increment history of test specimen. The total absorbed energy was evaluated using the area under the load-deflection curves and obtained from equation 2. Peak absorbed energy was computed as the area under the load-deflection curve up to the peak load. The computed individual absorbed energies were parameterized with the respective samples cross section areas. The load-deflection curves were then analyzed to measure the flexural stress and the absorbed energy for all samples.

The maximum flexural stress, σ_f , was measured using the following linear elastic small displacement bending equation:

$$\sigma_f = \frac{3 P_m L}{2 b h^2} \quad (3)$$

Where P_m is the maximum load recorded during testing, b and h are the width and thickness of the test specimen, respectively, L is the specimen span.

The strain rate for three point bending test was computed in a method based on continuous mechanics proposed by Land [17,18]. The general equation of the model is:

$$\varepsilon_{\max} = \frac{2h(N+2)y}{(L-a)[L+a(N+1)]} \quad (4)$$

where h and L are same to the above, N is the creep exponent and y is the deflection. For a three point bending configuration and elastically deflected material: $a = 0$ and $N = 1$ and differentiating with respect to time, hence:

$$\dot{\varepsilon} = \frac{d\varepsilon}{dt} = \frac{6hV}{L^2} \quad (5)$$

where t is time and V is the velocity.

The impulse was computed using equation 6:

$$I = \int_0^{t_{\max}} F(t)dt \quad (6)$$

where I is the impulse, $F(t)$ is the force as a function of time.

2.4 Static Tests

Static three point bending tests were performed using a MTS 810 universal testing machine with a load cell capacity of 100 kN, and controlled by the cross-head displacement at a rate of 0.5 mm/min (strain rate = $3.7 \times 10^{-5} \text{ s}^{-1}$, computed from equation 5). Six specimens with dimension of 160×50×12 mm (length × width × thickness) were tested using a span of 127 mm. Strain gages were glued at the center of the specimen in order to compute the extreme fiber strain. Deflections at mid span were measured using an electrical transducer (LVDT) and were continuously recorded, together with the bending load and cross head displacement.

3. Discussion and Analysis

3.1 Static Tests

Typical static bending curves are presented in Figure 3. Cross-head, LVDT and strain gage measurements are compared. The sisal fiber reinforced cement composite bending behavior is characterized by a multiple cracking behavior with strain hardening. The curve can be divided into 5 regions identified by roman numerals. Zone I corresponds to the elastic-linear range where both matrix and the fibers behave linearly. The lower and upper bounds of the limit of proportionality (LOP) define the range of Zone II. In this region cracks initiate and propagate across the cross sectional areas of the specimen. Mean values of 9.86 and 11.46 MPa for $\sigma_{\text{LOP-}}$ and $\sigma_{\text{LOP+}}$, respectively, were obtained. These values are in the same range of values obtained in earlier work for similar specimens tested with a span of 300 mm [9]. The post LOP range (zone III) is characterized by multiple cracking formation that results in strain hardening. Only 4-5 cracks develop in the span of 127 mm. For the span of 300 mm, as many as 20 cracks were observed [9]. The crack spacing saturates at the end of Zone IV at a deflection of approximately 2.2 mm for cross-head and 0.8 mm for LVDT measurements. Zone V is characterized by the strain softening response due to the localization and widening of a major crack. No new cracks appear at this stage. The average modulus of rupture (MOR) of 23.88 MPa and initial elastic modulus of 36.86 GPa shows that the replacement of cement by calcined clays and the use of long sisal fiber as reinforcement resulted in a composite of sufficiently high stiffness and elevated strength. Table 2

shows individuals tests results as well as average and standard deviations of static tests. It can be seen that MOR varies from 19.2 to 27.3 MPa.

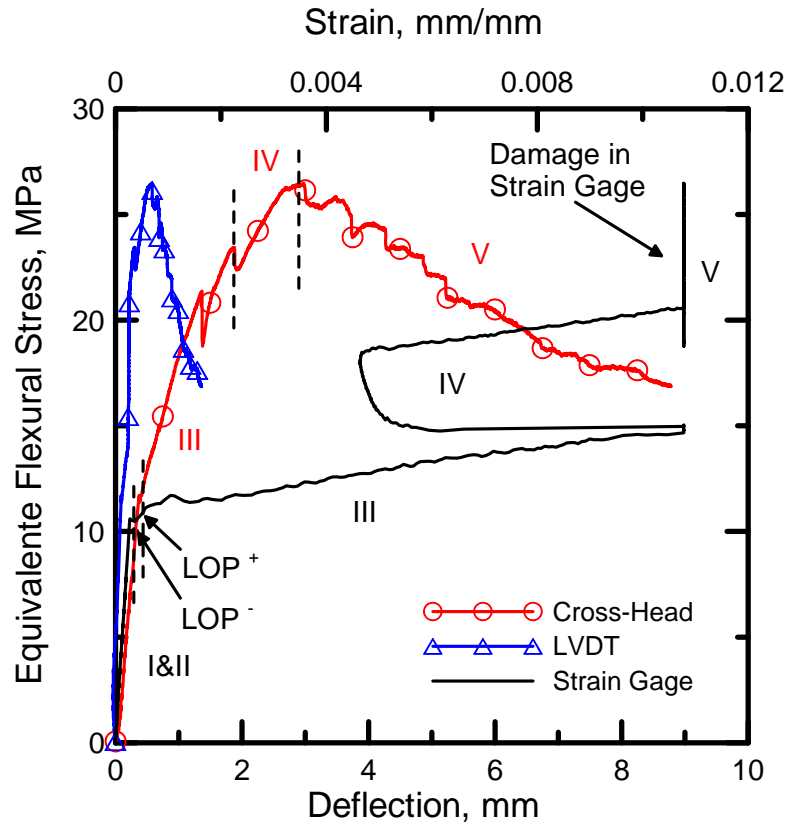


Figure 3. Response of sisal fiber reinforced composite under static three point bending. Mid-span deflection was measured by LVDT while bottom face strain was measured by strain gages.

The tensile region of the flexural sample measured by the strain gage experiences five ranges of behavior (see Figure 3). Zone I is characterized by a linear-elastic response. After the complete formation of the first crack, Zone II begins. Stiffness degradation is caused by the crack formation, and results in a significant drop in the modulus from 38.99 to 0.41 GPa. A decrease in tensile strain occurs in zone IV as a result of crack formations in the vicinity of the strain gage and shear lag mechanisms which result in stress decay in matrix. Note that the resistance type strain gage measurements are not uniquely related to the uncracked material as the strain recorded in the matrix is dependent on the relative position of a strain gage between two parallel cracks. This stage characterizes the degraded matrix's contribution to the composite overall response. After the localized unloading recorded by the strain gage caused by the crack

formation, the modulus of the matrix (at the strain gage location) is recorded as much as 6.90 GPa as the loading progresses. With the formation of new cracks the modulus reduces again to only 0.38 GPa with an increase in strain. Zone V is the unloading region. At this region the strain gage fails to measure due to a damage caused by a crack formation.

The three types of instrumentation used in the present work showed no significant difference for the σ_{LOP} region. Nevertheless, a huge distinction can be observed when comparing the deflection levels for the cross head and LVDT measurements. Total absorbed energy values of 15.1 and 2.03 kJ/m² was computed from cross-head and LVDT measurements, respectively. This range indicates the large magnitude of energy due to spurious deformations recorded by the cross head measurement. Results from LVDT measurements were used to compare static and impact test behaviors in section 3.2.

Table 1. Summary of static three point bending tests. Results in parenthesis are standard deviation.

Specimen id	MOR (MPa)	σ_{LOP-} (MPa)	σ_{LOP+} (MPa)	Young's Modulus from Strain Gage (GPa)	Cross Head Peak Absorbed Energy (kJ/m ²)	Cross Head Total Absorbed Energy (kJ/m ²)	LVDT Peak Absorbed Energy (kJ/m ²)	LVDT Total Absorbed Energy (kJ/m ²)
1	19.19	10.10	10.10	-	4.11	12.92	-	-
2	23.99	9.50	13.34	32.26	9.77	18.17	-	-
3	26.47	7.96	11.56	38.99	5.72	18.16	0.67	3.57
4	27.30	10.63	11.06	35.36	3.61	15.48	0.37	0.90
5	25.39	10.31	10.81	41.58	5.87	14.52	0.95	1.62
6	20.96	10.63	11.86	36.00	1.66	11.52	-	-
Average	23.88 (3.20)	9.86 (1.0)	11.46 (1.1)	36.86 (3.6)	5.12 (2.7)	15.13 (2.7)	0.66 (0.3)	2.03 (1.4)

3.2 Impact tests

The acceleration time history of hammer and specimen were recorded by two individual accelerometers. As shown in Figure 4(a), the acceleration of hammer at three different drop heights of 101.6 mm, 152.4 mm, and 203.2 mm indicates that the peak acceleration of hammer during impact does not significantly increases with drop height. Average values of acceleration were reported to range from about 10.6 m/s² at 101.6 mm to 12.5 m/s² at 203.2 mm. Standard deviation for hammer accelerations was about ± 1.5 m/s²

which indicates that the input energy generate from the different drop heights did not change the hammer acceleration behavior during impact. The average velocity increased from 856.31 mm/s ($h=101.6$ mm) to 1307.98 mm/s ($h=203.2$ mm). Figure 4(b) shows the accelerations of specimens during impact at the three different drop heights cited before. The transient peak acceleration that the specimen experienced during impact increases from about 100 m/s^2 at a drop height of 101.6 mm to about 170 m/s^2 at drop height of 203.2 mm. The deceleration of the specimen was found to be increasing with increasing the drop height.

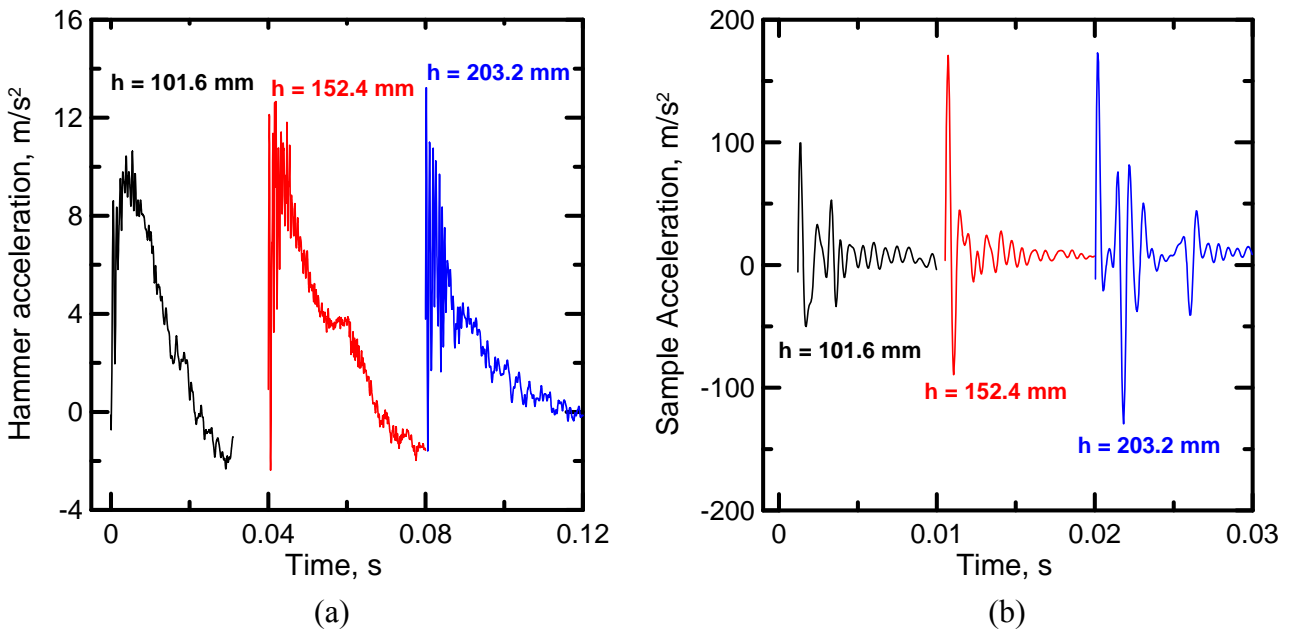


Figure 4. Effect of the drop height on the striker (a) and sample (b) acceleration.

The system can then be idealized by a single degree of freedom model, if the damping effect is neglected, the equation of dynamic equilibrium is:

$$ma(t) + F_{specimen}(t) = F(t) \quad (7)$$

where $F_{specimen}(t)$ is the impact force on the specimen, m is mass, a is acceleration and t is time.

The sample mass is around 230 g and according to Newton's second law, for a drop height of 101.6 mm, the inertial force is about 23 N. This inertial force is approximately 2.7% of the force measured by load cell. At the highest impact height used in the present work (203.2 mm), the inertial force is about 39 N which is about 4.5% of the

force measured by load cell. The inertial force on the specimen during impact was therefore neglected.

Figure 5 represents a time-history of acceleration, deflection and force response of a composite subjected to impact at drop height of 101.6 mm. Both the acceleration and deceleration response of the hammer and the specimen indicate that the specimen may accelerate after the initial contact to as high as 100 m/s^2 , and experience loads of up to 850 N. There is a phase lag in the deflection signal due to loading of the specimen as the maximum deflection is achieved while the load drops significantly; the specimen decelerates and comes to rest as the load and deflection signals stabilize after the impact event; however permanent deflection and post-failure oscillations exist after the impact event.

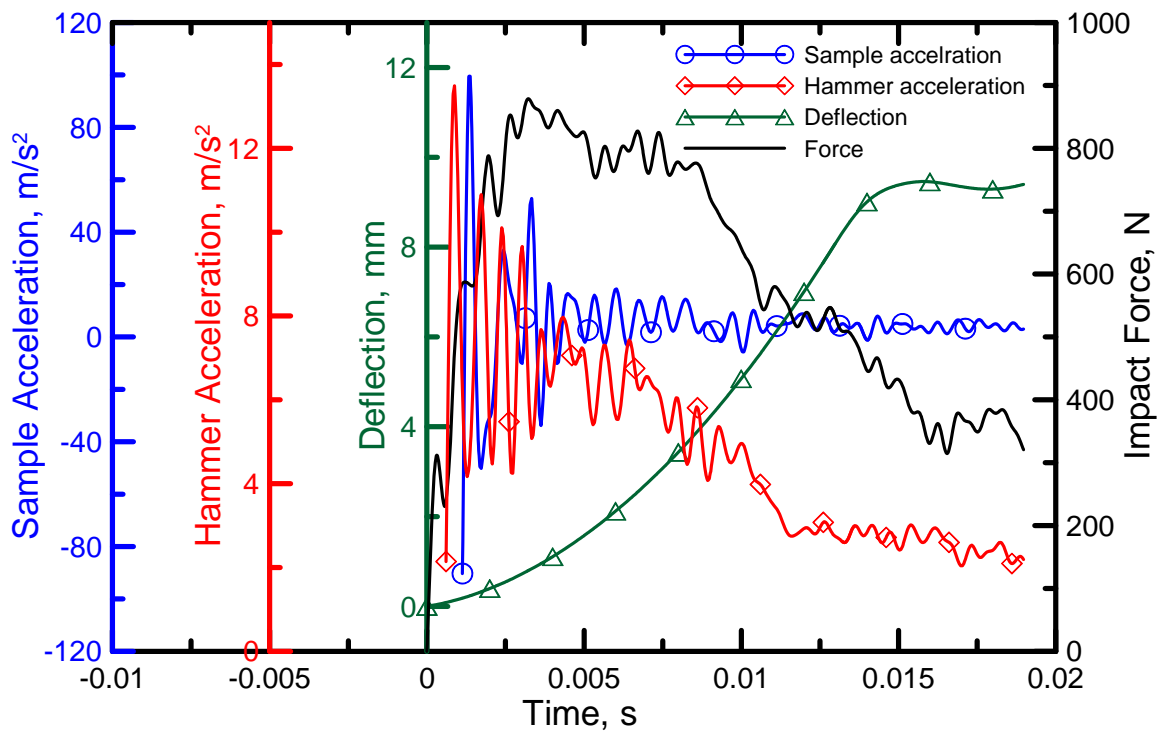


Figure 5. Time history of sample, hammer, deflection and impact force for a sample tested with impact energy of 10.55 J (or drop height of 101.6 mm).

Figure 6 (a) compares typical responses of impact forces obtained from conventional load cell and piezoelectric load washer; indicating that a similar behavior and values are obtained. The upper conventional load cell results were used for computing stress values and for further analysis due to the fact that it recorded less oscillations as explained in section 2.3.

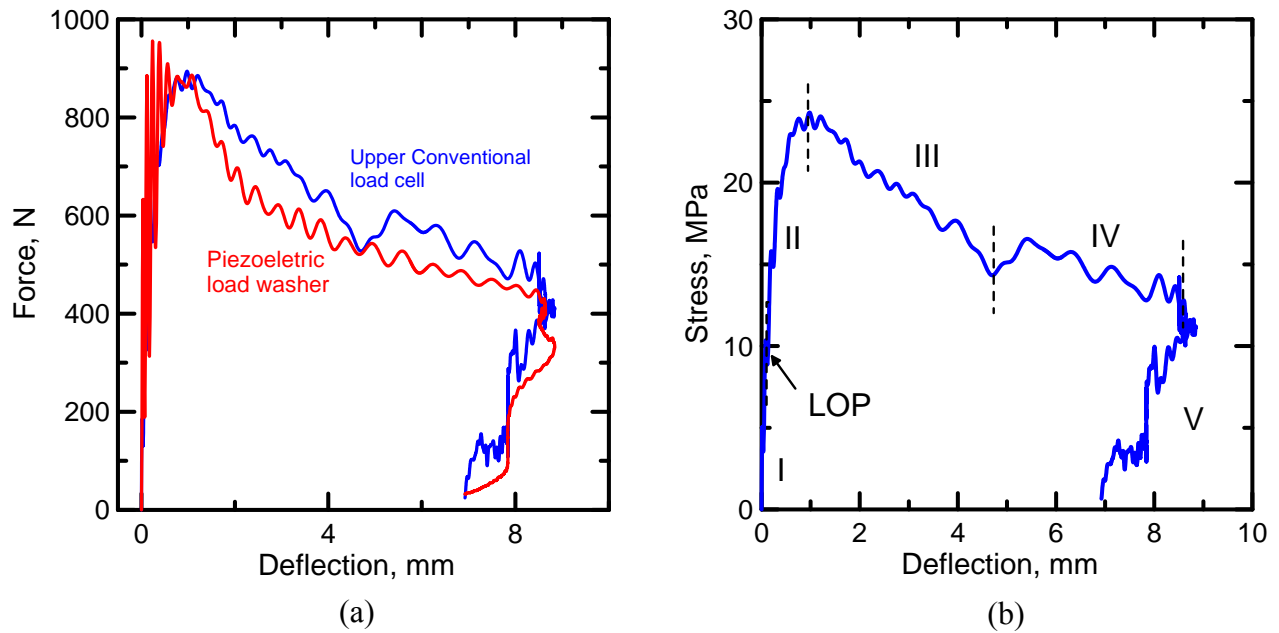


Figure 6. Comparison of piezoelectric load washer and upper conventional load cell responses (a) and different zones in a typical stress vs. deflection impact curve (b). Note the less oscillation measured from the conventional load cell.

A typical flexural stress vs. deflection behavior is presented in Figure 6 (b) for drop height of 101.6 mm. Five distinct zones are represented by roman numerals. Zone I is the linear elastic range that ends at the formation of the first crack (LOP region). The LOP range is similar to those obtained by the static tests. Zone II starts after the LOP and is characterized by multiple cracking behavior with strain hardening. An average of four parallel cracks was observed at this zone. Stiffness degradation takes place during Zone II as presented in Figure 8, and maximum flexural stress values are obtained at the end of this region. Strain softening behavior characterizes zones III and IV. Damage that takes place in the matrix and fiber-matrix interface is a function of drop height and deflection level. Depending on the nature of available energy, if there is sufficient ductility in the sample to absorb the applied energy, some of the stored energy release causes a rebound that is characterized by a reduction in deflection of the sample as the load is decreased. Zone V characterizes the rebound of the specimen.

Comparisons of flexural stress vs. deflection responses for hammer drop height ranging from 101.6 to 203.2 mm, representing an input potential energy from 10.55 to 21.1 J, are presented in Figure 7 (a). Note that the strain rates calculated from equation 5 resulted in rates ranging from 3.82 to 5.83 s^{-1} . These tests can be characterized as low

velocity impact. No significant effect in the ultimate strength was noticed with the increase in drop height. The average strength decreased from 23 (h=101.6 mm) to 18 MPa (h=203.2mm) with standard deviations ranging from 3.3 to 4.6 MPa, respectively, as shown in Table 2. These values are in the same range of the MOR for static bending tests. It is observed that the maximum deflection increases with increasing drop height. The post peak stiffness seems to decrease with increasing input potential energy which may be possibly attributed to a reduction in bond characteristics of fiber-matrix interface. The frictional nature of the bond has been shown to be affected by the loading rate [19, 20]. Force vs. time curves are presented in Figure 7b. It can be noticed that the duration of the impact is between 4 to 6.5 ms depending on the drop height and the maximum load capacity is around 850 N.

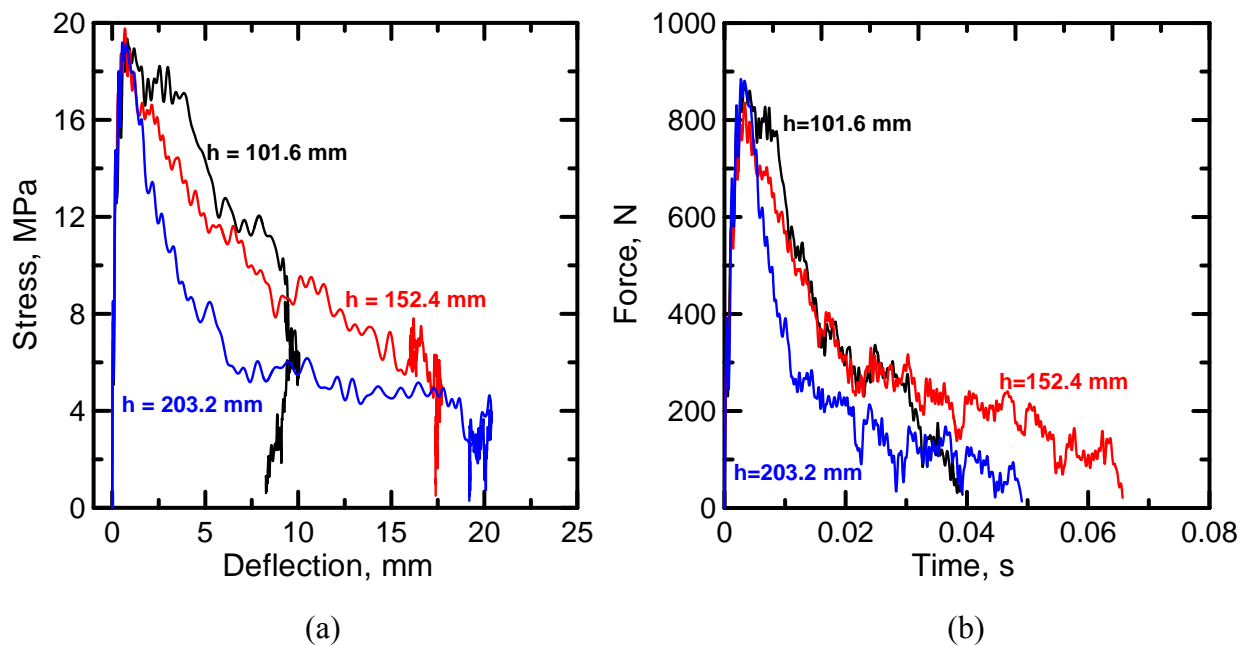


Figure 7. Effect of drop height on the stress vs. deflection (a) and stress vs. time (b) response of the sisal fiber reinforced composite.

The initial stiffness decreases from 4.5 to 2.2 kN/mm with increasing drop height (see Figure 8a). Stiffness degradation also takes place after the first crack formation as presented in Figure 8b. No significant difference is noticed for stiffness degradation as a function of drop height.

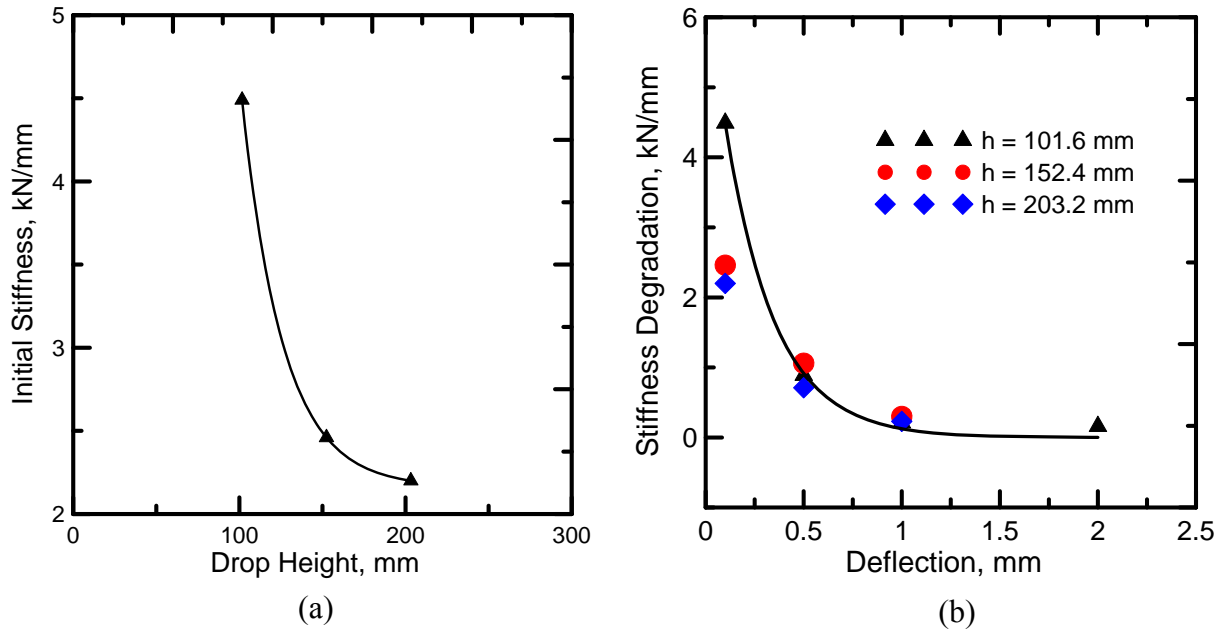


Figure 8. Effect of drop height on the initial stiffness (a) and degraded stiffness (b).

The total absorbed energy increases from static test to impact achieving its maximum value of 13.9 kJ/m^2 at drop height of 152.4 mm (see Figure 9a). By normalizing the total absorbed energy to the input energy, it is observed a constant ratio of 0.5 from a height of 101.6 to 152.4 mm with a posterior drop to 0.3. This indicates that the drop height of 152.4 mm (15.83 J) is a threshold level. The impulse follows similar behavior of absorbed energy. There is an increase from 18 to 20 N·s by increasing the drop height from 101.6 to 152.4 mm with a posterior decrease to 14 N·s (see Figure 9b).

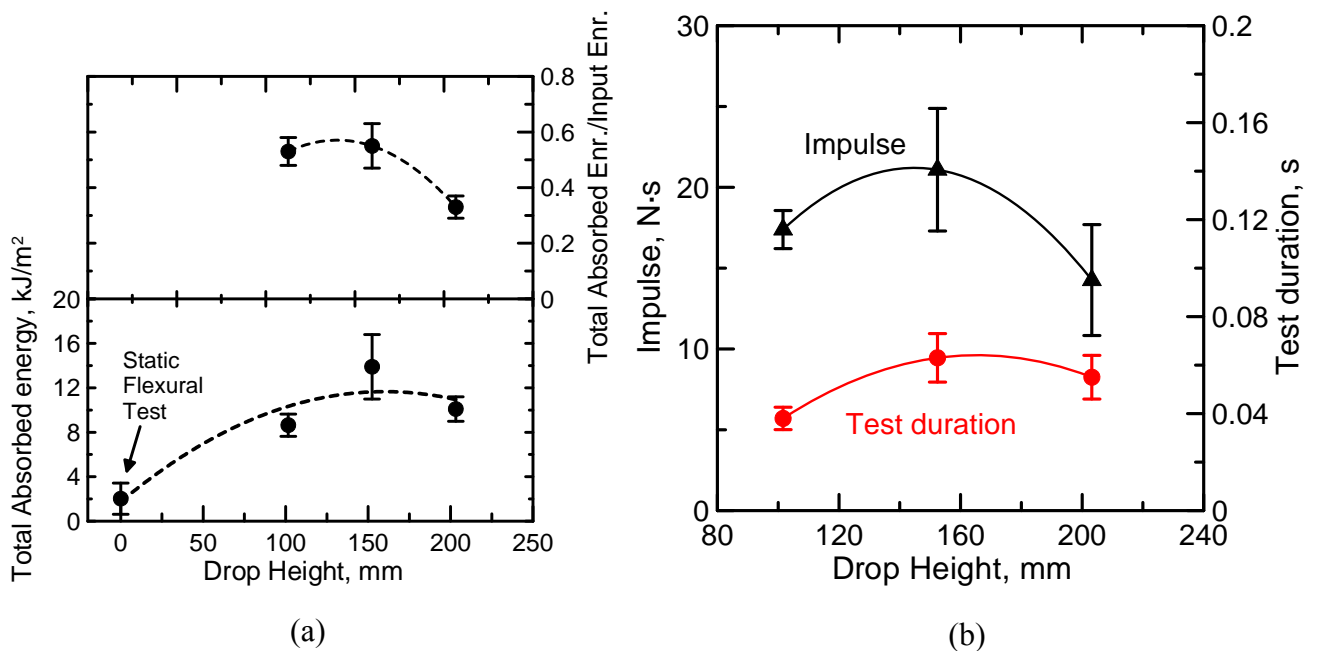


Figure 9. Effect of drop height on toughness (a) and impulse (b). Total absorbed energy was normalized in respect to the impact energy (input energy) in (a).

Pictures showing the composite deflection at four distinct stages of loading are shown in Figure 10 for specimen id 04 impacted at a drop height of 152.4 mm. Note the high ductility of the material. The image sequence shows deflection levels ranging from 0.06 mm (load = 296 N) (Figure 10a) to 13.9 mm (load = 313 N) (Figure 10d). The maximum load (823 N) is reached in Figure 10b at a deflection of 0.72 mm.

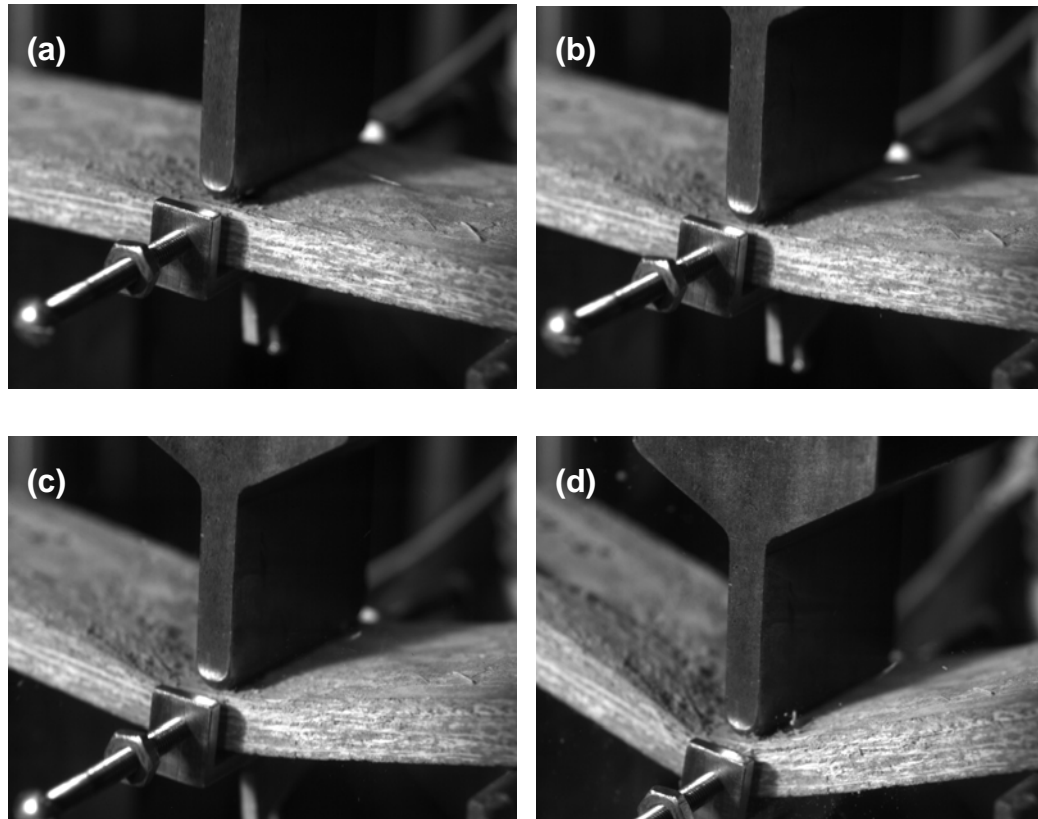


Figure 10. Effect of impact load on the deflection of sisal fiber composites subjected to impact at drop height of 152.4 mm. Note the high ductility of the material.

Figure 11 shows the damage in the composite caused by various input energies. The damage is generally associated with matrix cracking and delamination, and is initiated by the formation of tensile flexural cracks which may be deflected to shear cracks due to bridging fibers. Tensile cracks are introduced when in-plane normal stresses exceed the transverse tensile strength of the matrix layer (see Figures 11 (a) and (b)) at the bottom surface of the composite, but may not lead to material failure. Shear cracks start as flexural matrix cracks away from the mid-center, and convert to delamination cracks as they intersect the continuous fibers. This indicates that transverse shear stresses play

a role in their formation. Shear cracks were only observed when the drop height was 152.4 mm or superior (see Figure 11b). Delamination which is the debonding between adjacent layers is of most concern since it can reduce the strength of the composite. Damage caused by delamination was only observed at the drop height of 203.2 mm and resulted in a complete material failure. It can be seen from Figure 12 that shear cracks (initiated after 5000 μ s) started the delamination process. Nevertheless, even with the formation of shear cracks the composites presented ductility and strength similar to the lower drop heights reaching MOR of 18.06 MPa at deflection of 0.85 mm.

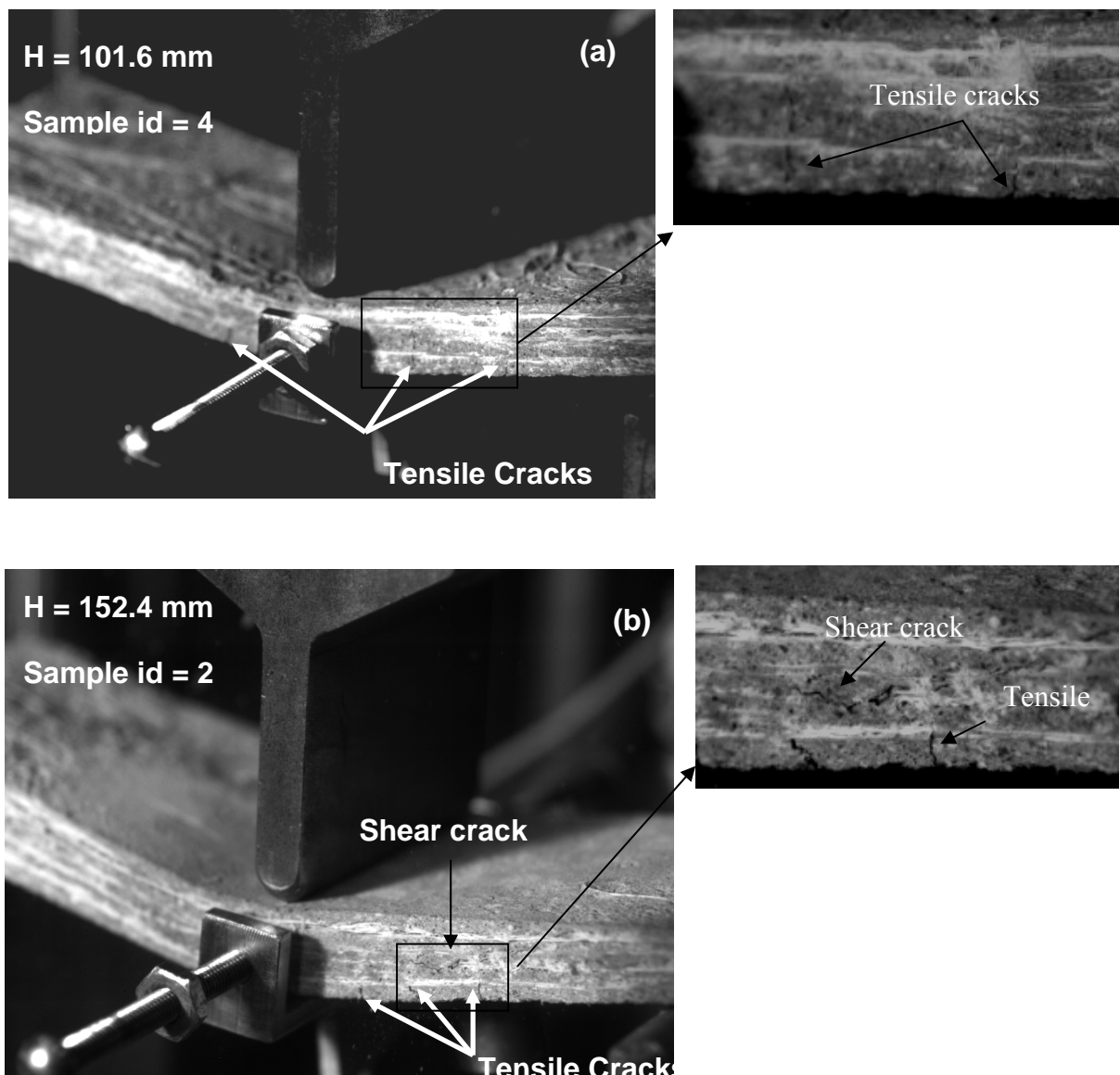


Figure 11. Damage mechanisms in composites subjected to impact: (a) drop height = 101.6 mm and (b) 152.4 mm. Tensile cracks were observed in the bottom face and shear cracks in the midplane.

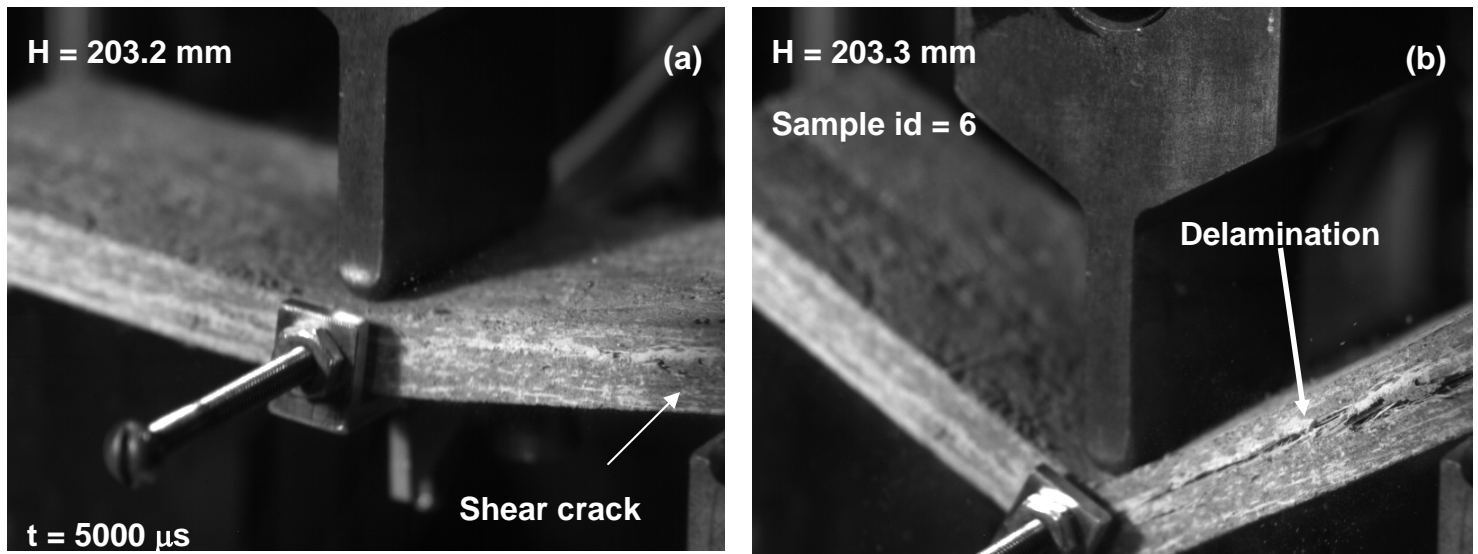


Figure 12. Damage mechanisms in sample subjected to impact height of 203.2 mm. Shear crack (a) initiated the delamination process in (b).

Table 2. Summary of impact test results. Results in parenthesis are standard deviation.

Height (mm)	Potential Energy (J)	Strain Rate (s ⁻¹)	Specimen id	Max. Flexural Stress (MPa)	Deflection at Max. Stress (mm)	Max. Deflection (mm)	Initial Stiffness (N/mm)	Velocity (mm/s)	Peak Absorbed Energy (kJ/m ²)	Total Absorbed Energy (kJ/m ²)
101.6	10.55	3.82	1	28.01	2.51	7.26	9173.65	725.15	3.40	9.19
			2	21.56	1.11	10.13	3248.37	987.76	1.18	10.45
			3	25.16	1.96	7.62	1716.01	870.17	-	7.53
			4	24.30	0.97	8.84	1969.07	693.72	1.08	8.19
			5	19.43	0.49	9.56	5541.15	995.81	0.93	7.94
			6	19.35	0.80	10.04	5344.04	865.23	0.78	8.49
			Average	22.97 (3.4)	1.31 (0.76)	8.91 (1.2)	4498.72 (2805.78)	856.31 (127.0)	1.48 (1.1)	8.64 (1.0)
52.4	15.83	5.46	1	27.57	2.40	13.99	2037.61	952.56	1.53	17.87
			2	18.78	0.40	18.19	2845.54	1503.49	0.29	15.94
			3	23.40	1.08	17.03	1942.58	1275.94	1.28	15.41
			4	19.76	0.68	17.69	2205.83	972.00	1.11	11.19
			5	19.22	0.38	20.14	3043.39	1329.89	0.95	10.53
			6	14.08	2.23	19.77	2703.13	1312.76	1.34	12.36
			Average	20.47 (4.6)	1.20 (0.9)	17.81 (2.2)	2463.02 (460.17)	1224.44 (217.7)	1.09 (0.4)	13.89 (2.9)
203.2	21.1	5.83	1	16.26	0.44	20.07	3983.30	1368.54	0.98	10.69
			2	21.86	0.79	20.37	1840.03	1212.66	0.97	13.14
			3	21.53	1.80	20.40	1189.04	1184.41	-	9.17
			4	13.74	1.07	20.46	1784.69	1461.84	0.70	8.40
			5	15.78	0.48	20.11	2012.50	1290.98	0.60	10.41
			6	19.18	0.55	20.40	2409.00	1329.43	1.19	8.51
			Average	18.06 (3.3)	0.85 (0.5)	20.30 (0.2)	2203.09 (975.40)	1307.98 (102.4)	0.89 (0.2)	10.09 (1.1)

4. Conclusion

An experimental study has been performed to investigate the impact response of sisal fiber reinforced cement composites under a three point bending configuration. The acceleration and deceleration response of the hammer and the specimen indicate that the specimen may accelerate after the initial contact to as high as 100 m/s^2 , and experience loads of up to 850 N for an input energy of 10.55 J. For higher input energies (15.83 J and 21.1 J) the sample acceleration increased to 170 m/s^2 but no significant difference was noticed for the load. The maximum flexural stress ranged from 22.97 MPa (input energy of 10.55 J) to 18.06 MPa (21.1 J) with standard deviation ranging from 3.3 to 4.6 MPa. The average static MOR was about 24 MPa. The absorbed energy increased from static test to impact achieving its maximum value of 13.89 kJ/m^2 at input energy of 15.83 J.

Initial stiffness decreases from 4.4 to 2.2 kN/mm when increasing the input energy from 10.55 to 21.1 J. Stiffness degradation takes place after the first crack formation and no significant difference was noticed between stiffness degradation as a function of impact energy.

The damage morphology consisted of matrix cracking and delamination. The damage process is initiated by the formation and distribution of flexural cracks. Tensile and shear cracks were observed. Delamination resulting in total failure was only observed when the impact energy was above 21.1 J.

References

- [1] Abrate S. Impact on Composite Structures. Cambridge University Press, Cambridge, UK, 1998.
- [2] Romano GQ, Silva FA, Toledo Filho RD, Fairbairn EMR, Battista R. On the Removal of Steel Fiber Reinforced Refractory Concrete from Thin Walled Steel Structures Using Blast Loading. In: Unified International Technical Conference on Refractories (Unitecr 07), Dresden, 2007, p. 509-512.

- [3] Balaguru PN and Shah SP. Fiber-reinforced cement composites. McGraw-Hill, Singapore, 1992.
- [4] Silva FA. Toughness of non conventional materials. M.Sc. thesis, Department of Civil Engineering, PUC-Rio, 2004.
- [5] Silva FA, Ghavami K, d'Almeida JRM. Toughness of Cementitious Composites Reinforced by Randomly Sisal Pulps. In: Eleventh International Conference on Composites Engineering - ICCE-11, Hilton Head Island – SC, 2004
- [6] Romano GQ, Silva FA, Toledo Filho RD, Tavares LM, Battista R., Fairbairn EMR. Impact Loading Behavior of Steel Fiber Reinforced Refractory Concrete Exposed to High Temperatures. In: Fifth International Conference on Concrete under Severe Conditions: Environment and Loading, Tours, France. v. 2, 2007, p. 1259-1266.
- [7] Wang N, Mindess S and Ko K. Fibre Reinforced Concrete Beams Under Impact Loading. Cement and Concrete Research 1996; 26: 363-376.
- [8] Lok T S and Zhao PJ. Impact Response of Steel Fiber-Reinforced Concrete Using a Split Hopkinson Pressure Bar. Journal of Materials In Civil Engineering 2004;16:54-59.
- [9] Zhu D, Gencoglu M, Mobasher B. Low Velocity Flexural Impact Behavior of AR Glass Fabric Reinforced Cement Composites. Cement and Concrete Composites, in review, 2009.
- [10] Gencoglu M, Mobasher B. Static and impact behavior of fabric reinforced cement composites in Flexure. In: High Performance Fiber Reinforced Cement Composites (HPRCC5), Mainz, Germany, RILEM Publications S.A.R.L., PRO 53, 2007, 463-470.
- [11] Silva FA, Mobahser B, Toledo Filho RD. Cracking mechanisms in durable sisal fiber reinforced cement composites. Cement and Concrete Composites, in Press, 2009.

- [12] Silva FA, Melo Filho JA, Toledo Filho RD, Fairbairn EMR. Mechanical behavior and durability of compression molded sisal fiber cement mortar laminates (SFCML). In: 1st International RILEM Conference on Textile Reinforced Concrete (ICTRC), Aachen, p. 171-180, 2006.
- [13] Toledo Filho RD, Silva FA, Fairbairn EMR, Melo Filho JA. Durability of compression molded sisal fiber reinforced mortar laminates. *Construction and Building Materials* 2009; 23:2409-2420.
- [14] Silva FA, Chawla N, and Toledo Filho RD. Tensile behavior of high performance natural (sisal) fibers. *Composites Science and Technology* 2008; 68:3438-3443.
- [15] Cheresch MC and McMichael S. Instrumented Impact Test Data Interpretation. In: Kessler S.L. et. al., (editors). Instrumented impact testing of plastic and composite materials. Philadelphia. STP: ASTM, 963, 1987.
- [16] Cain PJ. Digital Filtering of Impact Data. In: Kessler S.L. et al., (editors). Instrumented impact testing of plastic and Composite Materials. Philadelphia. STP: ASTM, 963, 1987.
- [17] Land PL. Strain rates for three and four point flexure tests. *Journal of Materials Science* 1979; 14:2760-2761.
- [18] Silva FA, Ghavami K, d'Almeida JRM. Strain Rate Behavior of Fiber-Reinforced Cement Composite Materials. In: Fifth International Symposium on Natural Polymers and Composites-ISNAPOL, São Pedro, São Paulo, 2004. p. 205-207.
- [19] Sueki S, Soranakom C, Peled A, and Mobasher B. Pullout-Slip Response of Fabrics Embedded in a Cement Paste Matrix. *ASCE Journal of Materials Engineering* 2007; 19:718-727.

[20] Pacios A, Ouyang C and Shah SP. Rate effect on interfacial response between fibres and matrix. *Materials and Structures* 1995; 28:1359-5997.

ARTIGO J - Silva F.A., Zhu D., Mobasher B. and Toledo Filho R.D. High speed tensile behavior of sisal fiber cement composites. To be submitted, 2009.

High Speed Tensile Behavior of Sisal Fiber Cement Composites

Flávio de Andrade Silva^a, Deju Zhu^b, Barzin Mobasher^b, and Romildo Dias de Toledo Filho^a

^aCivil Engineering Department, COPPE, Universidade Federal do Rio de Janeiro, P.O. Box 68506, CEP 21941-972, Rio de Janeiro – RJ, Brazil.

^bDepartment of Civil and Environmental Engineering, Arizona State University, Tempe, AZ 85287-8706

To be submitted to an international Journal

2009

Abstract

The experimental behavior of sisal fiber reinforced cement composites subjected to high speed tension load have been investigated and reported in this paper. High strain rates were achieved by using a high rate servo-hydraulic testing machine. The effect of strain rate was investigated by comparing static and dynamic tensile tests which were performed at strain rates ranging from $5.5 \times 10^{-6} \text{ s}^{-1}$ to 24.6 s^{-1} , respectively. It was found strain rate sensitivity for ultimate tensile strength and strain capacity. A dynamic increase factor of 1.26 was computed. An enormous strain capacity of 0.67 mm/mm was reported for dynamic tension tests. A state of the art high speed Phantom camera was used to take images from the specimen during high speed tension tests. The images were used in a digital image correlation model to determine the displacement fields and to calculate the strain.

1. Introduction

Long aligned sisal fiber reinforced cement composites are a new class of sustainable construction material with superior tensile strength and ductility. This composite system presents a strain hardening behavior with multiple cracking formation. The enhanced strength and ductility is primarily governed by the composite action that exists such that the fibers bridge the matrix cracks and transfer the loads, allowing a distributed microcrack system to develop [1]. These materials are strong enough to be used as load bearing structural members, in applications such as structural panels, impact & blast resistance, repair and retrofit, earthquake remediation, strengthening of unreinforced masonry walls, and beam-column connections. Thus, the response to impulse loading, for applications in extreme loading condition, becomes of great importance.

The dynamic tensile response of cement based material is a difficult experiment to perform, therefore only a few results are published. Most of the available literature on the dynamic tensile behavior of concrete regards to investigations on plain concrete. It has been reported, for plain concrete, an increase in the dynamic tensile strength with increase in strain rate [2-8]. For example, Xiao et al. [2] reported that compared to the quasi-static tensile strength of concrete (strain rate of 10^{-5} s^{-1}), the dynamic tensile strengths of concrete at strain rates of 10^{-4} , 10^{-3} and 10^{-2} s^{-1} increase by 6%, 10% and 18%, respectively. Birkimer and Lindemann [3] conducted dynamic tensile tests using

plain concrete cylinders. The dynamic strength at a strain rate of 20 s^{-1} was between 17.2 MPa and 22.1 MPa, while the static tensile strength was 3.4 MPa at the quasi-static strain rate of $0.57 \times 10^{-6} \text{ s}^{-1}$.

Dynamic tensile data on fiber reinforced concrete is even more limited. Kim et al. [9] investigated the strain rate effect on the tensile behavior of high performance fiber reinforced cement composites (HPFRCC) using two deformed high strength steel fibers, namely hooked fibers and twisted (Torex) fibers. The strain rate ranged from pseudo static (strain rate of 0.0001 s^{-1}) to seismic (strain rate of 0.1 s^{-1}). The results showed that the tensile behavior of HPFRCC with twisted fibers is sensitive to the strain rate, while hooked fiber reinforced specimens show no rate sensitivity. It was also observed that lower fiber volume fraction ($V_f = 1\%$) reinforced specimens show higher sensitivity than higher fiber volume fraction ($V_f = 2\%$) reinforced specimens. Maalej et al. [10] performed dynamic tensile tests in Engineered Cement Composites (ECC) containing 0.5 % steel and 1.5 % polyethylene fibers (in volume). The applied strain rate ranged from 2×10^{-6} to $2 \times 10^{-1} \text{ s}^{-1}$. The results indicate that there is a substantial increase in the ultimate tensile strength from 3.1–6 MPa with increasing strain rate. The strain capacity does not appear to be affected by the strain rate.

In the present work, a new sustainable material, namely long aligned sisal fiber reinforced composite was characterized under high speed direct tension. To achieve high strain rates a MTS high rate servo-hydraulic testing machine was used. The effect of strain rate was investigated by comparing static and dynamic tensile tests which were performed at strain rates ranging from $5.5 \times 10^{-6} \text{ s}^{-1}$ to 24.6 s^{-1} , respectively. A state of the art high speed Phantom camera was used to take images from the specimen during high speed tension tests. The images were used in a digital image correlation model previously developed in MatLab code [11] to determine the displacement fields and calculate the true strain during high strain rate tension tests. Failure behavior and cracking pattern were also observed using the Phantom camera images.

2. Experimental Program

2.1 Materials and Processing

To increase the durability of the composites, the cementitious matrix consisted on 50% Portland cement, 30% metakaolin (MK) and 20% calcined waste crushed clay brick (CWCCB) following previous works [12]. The matrix was produced using the Portland cement CII F-32 defined by the Brazilian standard [13] as composed with filler (in mass: 85%<clinker<91%; 3%<gypsum<5%; 6%<filler<10%) with a 28 days compressive strength of 32 MPa. The metakaolin (MK) was obtained from Metacaulim do Brasil Industria e Comércio LTDA, and calcined waste crushed clay brick (CWCCB) from an industry located in Itaboraí – RJ, Brazil, calcined at 850 °C. River sand with maximum diameter of 1.18 mm and density of 2.67 g/cm³ and a naphthalene superplasticizer Fosroc Reax Conplast SP 430 with content of solids of 44% were also used.

The mortar matrix used in this study presented a mix design 1:1:0.4 (cementitious material:sand:water by weight). Wollastonite fiber (JG class), obtained from Energyarc, were used as a micro-reinforcement in the composite production ($V_f = 5\%$).

The sisal fibers were characterized earlier to have an irregular cross section with mean area ranging from 0.04 to 0.05 mm² and a mean density, elastic modulus, and tensile strength of 0.9 g/cm³, 19 GPa and 400 MPa, respectively [14]. These fibers were extracted from the sisal plant in a farm located in the city of Valente, state of Bahia – Brazil. More information on the sisal fibers mechanical properties and its morphology can be obtained elsewhere [14].

The matrix was produced using a bench-mounted mechanical mixer of 20 liters capacity. The cementitious materials were homogenized by dry mixing for 30 seconds prior to addition of sand and 5% by volume of wollastonite. The powder material was mixed for and additional 30 seconds prior to addition of superplasticizer and water. The mixture was blended for 3 minutes. For the production of the laminates, the mortar mix was placed in a steel mold, one layer at a time, followed by single layers of long unidirectional aligned fibers (up to 5 layers). The samples were consolidated using a vibrating table operated at a frequency of 65 Hz, resulting in a sisal fiber volume fraction of 10%. After casting the composites were compressed at 3 MPa for 5 minutes.

The specimens were covered in their molds for 24 hours prior to moist curing for 28 days in a cure chamber with 100% RH and 23 ± 1 °C.

2.2 High Speed Tensile Test Procedure

The dynamic tensile tests were conducted using a MTS high rate servo-hydraulic testing machine. Six samples were tested with a geometry of 152.4 mm x 25.4 mm x 12 mm (length x width x thickness) under a span of 50.8 mm. According to the manufacture's specification, the machine can reach a maximum speed of 14 m/s with a load capacity of 200 kN. The machine can operate in closed-loop and open-loop. In close-loop tensile and compression, measurements can be conducted with testing rates lower than 0.25m/s. Open-loop condition can be used for tensile testing only at rates higher than 0.25 m/s. The speed of the actuator is controlled by the opening and closing of the servo-valve of hydraulic supply. By manually turning the servo-valve, the rate of flow of hydraulic fluid can be controlled, resulting in different actuator speed. In addition to the loading frame, MTS Flex SE control panels and a high speed data acquisition card were used. Also, the crack pattern and failure behavior of the composites were captured during loading by a Phantom v.7 high speed digital camera at a sampling rate of 10000 fps (frame per second).

The setup of the dynamic tensile testing is presented in Figure 1. Acceleration is imposed on the lower grip through the slack adaptor until the constant velocity is achieved. The slack adaptor has a hollow tube and a sliding bar. When the machine is in operation, the hollow tube travels freely with the actuator over a distance to reach a specified velocity before making contact with the cone-shaped surface of the sliding bar. The slack adaptor eliminates the inertia effect of the lower grip and actuator in its acceleration stage. In this work, the grips were made of stainless steel, as shown in Figure 1b. The weight of grip is about 1.5 kg. A specimen was installed between two steel wedges whose faces were serrated in order to improve the contact between the specimen and wedges (see Figure 1c). The grip was tightened by turning the screw stud that pushed the wedges against the slanted interior surface of hollow socket. Figure 2 shows a picture of the set-up before and after the high speed test.

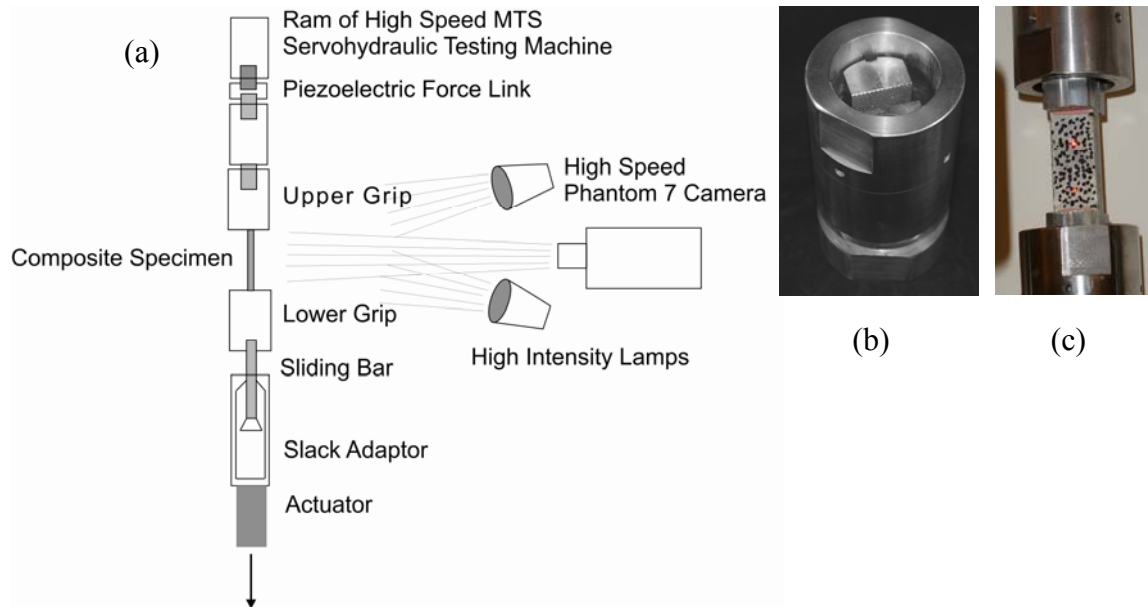
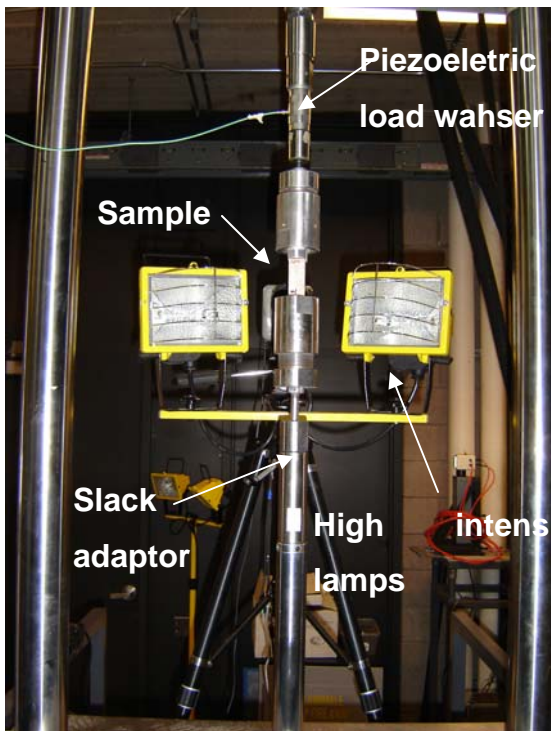


Figure 1. Schematic diagram of test set-up for high speed tensile testing (a). The grip can fit different specimen widths by changing the internal wedge grips (b) and the sample in place before the dynamic test (c).

In high rate testing, the response of the load cell should be a concern. Piezoelectric load washers are recommended for dynamic tests [15-18] because conventional load cell has much lower response frequency. In this work, the load was measured by a Kistler 9041A piezoelectric force link (load washer) with a capacity of 90 kN and rigidity of 7.5 kN/ μm . The response frequency of the load washer is 33 kHz. The load signal was amplified through a Kistler 5010B dual mode charge amplifier. A high speed digitizer was used to collect the signal from the LVDT actuator; this was to measure the deformation of the specimen and the force signal from the piezoelectric force link.



(a)



(b)

Figure 2. Dynamic test set-up before (a) and after (b) the test.

2.3 Data Processing Method for High Speed Tensile Test

It's quite cumbersome to process the data in dynamic testing as the data is not as clean as in static test. In this work, the signals from the load washer and internal LVDT of actuator were recorded at sampling rate of 250 kHz. The signals contain high frequency noises which require taking certain measures to clean up the signals in order to obtain the response of the test specimen. During the data processing, a low-pass filter with cut-off frequency of 3 kHz was used to eliminate high frequency noise.

An example of the recorded responses without filtering generated by the servo-hydraulic high rate testing setup is given in Figure 3. The figure presents the recorded force, displacement of stroke and its corresponding velocity versus the time history of a sisal fiber reinforced cement composite. The test duration was around 20 milliseconds within the range of nearly constant velocity of actuator. A nominal actuator velocity of 1180 mm/s is obtained by linearly fitting the section of displacement history curve which has nearly constant velocity just prior to loading the specimen. This velocity corresponds to a strain rate of 24.6 s^{-1} for the used span.

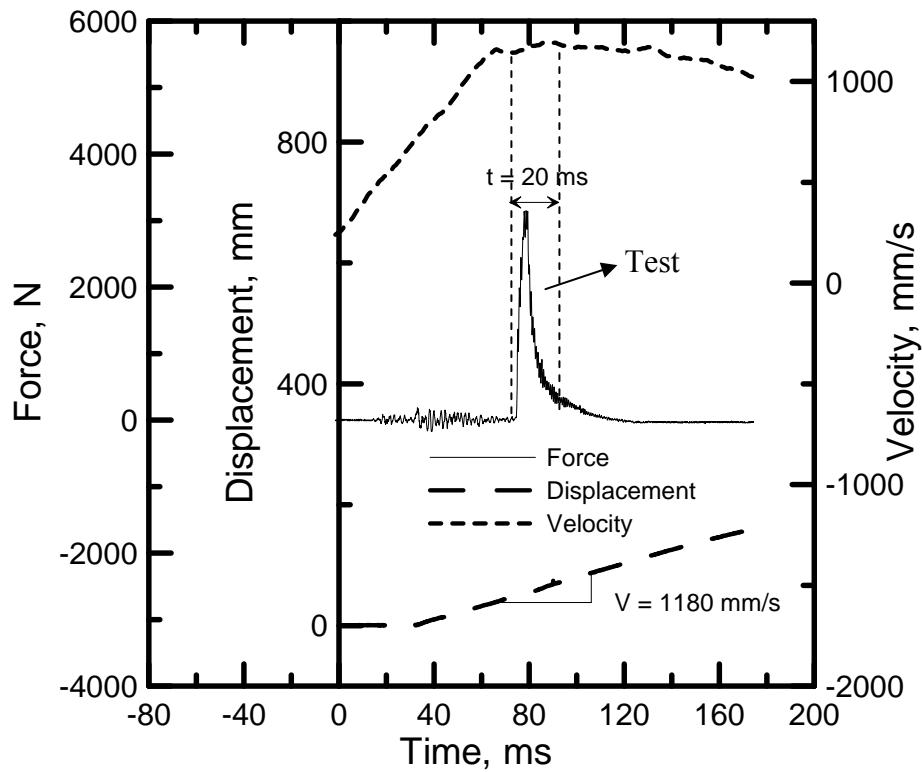


Figure 3. Force history, displacement history of actuator, and its corresponding velocity history curves at nominal velocity of 1180 mm/s, generated by the servo-hydraulic high rate testing setup.

2.4 Image Analysis - Digital Image Correlation (DIC) Method

Images can be acquired using a variety of commercially available frame grabbers and digital cameras. White light illumination is used to obtain B&W images. The most convenient method for expressing locations in an image is using picture elements or pixels. Both continuous, or discontinuous deformations between any two points within an image can be measured by means of an image matching technique commonly known as cross correlation technique (also known as template matching). This technique relies on tracking two sequential images to estimate relative motion of surface structures imaged under different applied stresses. After obtaining the displacement fields, the function can be subjected to a derivative operation in order to obtain the strain. The use of cross-correlation for template matching is motivated by the distance measure (squared Euclidean distance) [19,20].

$$d_{f,t}^2(u, v) = \sum_{x,y} [f(x, y) - t(x - u, y - v)]^2 \quad (1)$$

where “ f ” is the reference image defined as intensity as a function of location at a specified strain level. The sub-set image “ t ” is obtained at a higher strain level and positioned at unknown displacement (u, v) with respect to image “ f ”. The sum is over the coordinates (x, y) of pixels contained in the sub-set image “ t ” which may be a 5x5, 7x7, or generally any arbitrary sub-set of the original image. Expanding d and eliminating constant terms yields the following expression as a cross correlation function, “ c ” that is a measure of the similarity between the image and the feature.

$$c(u, v) = \sum_{x,y} [f(x, y) * t(x - u, y - v)] \quad (2)$$

In this procedure, the value of an output pixel is computed as a weighted sum of neighboring pixels. The matrix of weights is called the *correlation kernel*.

One technique for measuring the displacement vector (u, v) is to first compute the normalized cross correlation of the interference images of the pre-stressed and stressed medium within a pre-defined window, and then estimate the displacement from the maximum of the resultant cross-correlation function. The choice of normalization of the cross correlation function and the size of the window where the function has to be evaluated on a case by case basis depending on the relative extent of deformation.

Using the displacement vectors (u, v) , one can calculate the principal strains at any point on the surface. In the present study, images obtained using the Phantom high speed camera was used to determine the displacement field and to measure the strain during the high speed tensile tests. Random dots were generated in the composites to create a contrast in the uniform specimen face (see Figure 1c).

The processing steps used to derive displacement and strain information from images of a specimen at two different stress levels are as follows:

- (1) A pair of images from data acquired in the sequential steps is processed using the first image as the template and the second image as the current position.
- (2) The central pixel $(i_0; j_0)$ within a 10x10 block of pixels from the template serves as the center-point around which the cross-correlations are computed. To

compute the cross correlation function, a discretized form of Eqn. (1) which allows the parameters u and v to assume up to 10 pixel shifts is used.

- (3) The cross correlation function is evaluated for 100 points of the template. This function is maximized to obtain the values of u and v as defined in Eqn. (1). Quadratic interpolation is then used to calculate the displacements at which the cross-correlation is largest within a given block.
- (4) The total displacement at the given pixel is computed as the vector sum of the displacement estimates for each image pair. The dimension of the block over which the cross-correlation calculation is performed was optimized by trial and error to obtain the best estimates, as judged by the ratio of the mean and standard deviation of the displacements obtained.

The above procedure developed by Mobasher et al. was implemented in a MATLAB code [11] and used in the present investigation to calculate the displacement field and strain of the composite tested under high speed tension.

2.5 Static Tests

Direct tensile tests were performed in an electromechanical Instron universal testing machine model 4411 with a load cell of 1000 lbs (4.44 kN). The tests were controlled by the cross-head displacement at a rate of 0.016 mm/min (strain rate of $5.5 \times 10^{-6} \text{ s}^{-1}$). Four specimens measuring 152.4 mm x 25.4 mm x 12 mm (length x width x thickness) were tested using a gage length of 50.8 mm with fixed–hinged boundary conditions. Aluminum thin sheets were glued on both ends of the specimen and a set of mechanical grips were used. The tensile load and cross head displacement were recorded.

3. Discussion and Analysis

3.1 Static Test

In the present research the span and width of the tested specimens were reduced in relation to those used in the author's previous works [1]. That was done to facilitate the high speed tensile tests and to increase the resolution for the image analysis. Figure 4 shows the static tensile behavior of the sisal fiber reinforced cement composite (span = 50.8 mm). The stress-strain curve can be divided in five distinct zones and these are labeled with roman numerals. Zone I is the linear elastic range. The modulus computed

from the cross-head displacement data resulted in an average value of 0.75 GPa. This takes into account the machine and grip compliance resulting in a much smaller value. The correct modulus was calculated before [1] from strain gage measurements (see Figure 5 b) and it was found a value of 35 GPa. The linear zone is terminated by initial crack formation in the matrix phase (reported as of σ_{BOP-} from experiments) as shown in Figure 4. After the initiation of cracks in the matrix, its load carrying capacity does not vanish as the cracks are bridged by the longitudinal fibers.

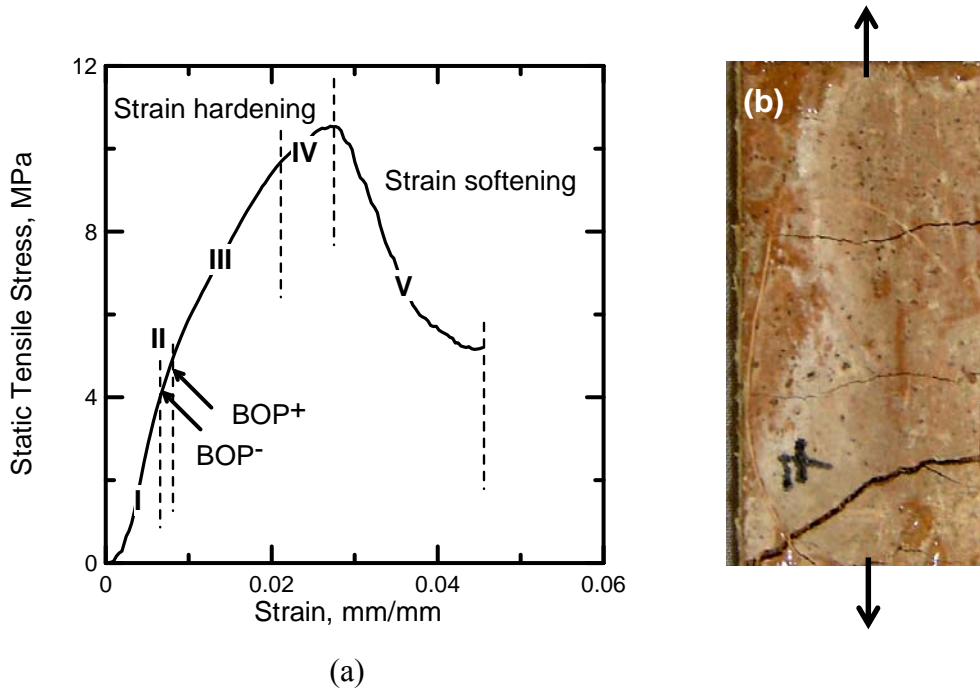


Figure 4. Static stress-strain behavior of the sisal fiber cement composite (50.8 mm span) (a) and a tested sample showing only 3 cracks (b). Both tensile and shear cracks can be observed.

The strain range within Zone II is associated with formation of matrix cracks; however, no single crack has traversed the entire width. The term defined as BOP+ corresponds to the stress level at which the first matrix crack completely propagates across the width. As indicated in the experimental results shown in Figure 4 the linear behavior terminates at the $\sigma_{BOP-} = 4.19-5.79$ MPa. The bend over point ranges from the beginning of non-linearity at 4.79 MPa to a point where the slope drastically decreases ($\sigma_{BOP+}=4.79-6.17$ MPa). Zone II is therefore defined as the stable cracking range between the two stress levels of σ_{BOP-} and σ_{BOP+} . The BOP values obtained for the span of 50.8 mm are in the same range of those reported for a 300 mm span. Individual values and averages are presented in Table 1. Zone III is characterized by a multiple

cracking formation with strain hardening. For the reduced span used (50.8 mm) it was observed only 3 cracks (see Figure 4). It was also noticed shear cracks as can be seen in Figure 4. For specimens with 300 mm span tested in the author's previous work [1] it was observed an average of 12 cracks (see Figure 5). Only tensile cracks were reported as can be seen in Figure 5. It can also be noticed that the drops in the stress-strain curve for the 300 mm span (Figure 5) which are related to the crack formation. For the span of 50.8 mm no drops were reported in the stress-strain curve which suggests either smaller crack opening or less sensitivity in the used testing system.

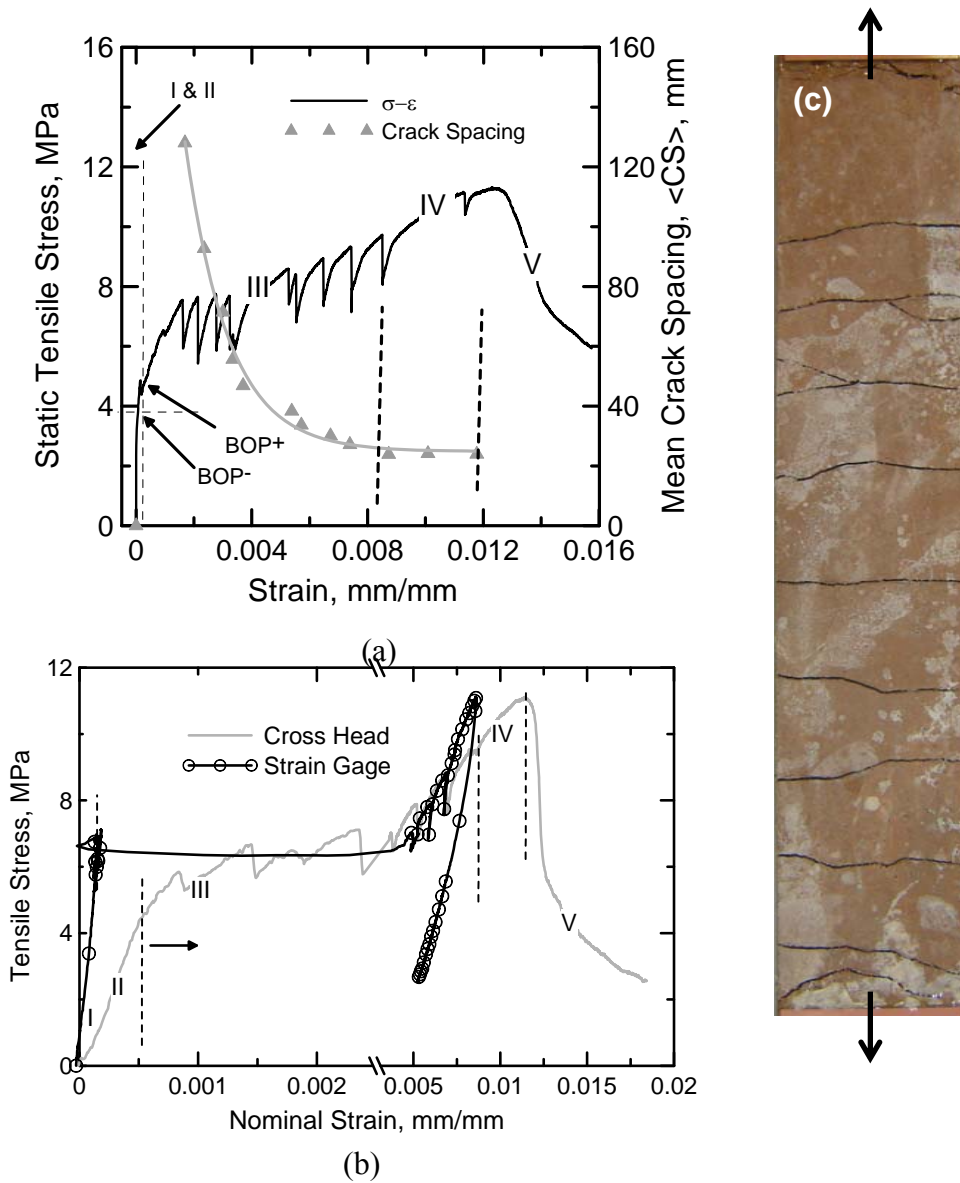


Figure 5. Static stress-strain response of the sisal fiber cement composite for a span of 300 mm [1]. Note in (a) the drops in the curve that correspond to the crack formation and in (b) the difference in the stiffness in the linear elastic zone obtained from strain gage and cross head measurements. Parallel tensile cracks in a total of 12 were observed (c).

Zone IV corresponds to the completion of cracking phase and initiation of debonding. As the cracking saturates in the specimen, Zone IV is dominated by progressive damage and characterized by a crack widening stage ultimately leading to failure by fiber pullout. The average ultimate strain of the composite is 3% (measured from cross-head displacement) which shows the capacity of the sisal fibers to cause crack distribution. The average ultimate strength was found to be 11 MPa. For specimens with span of 300 mm an ultimate strain of 1.53 % was measured. This can be explained by the difference compliances in the machines used for the static tensile tests. The UTS is in the same level for both tested spans.

The post peak response occurs in Zone V and is characterized by a strain softening behavior. Peak and total toughness values were found to be 8.27 and 14.20 kJ/m², respectively.

Table 1. Summary of static tensile test results.

Sample id	UTS (MPa)	$\sigma_{BOP(-)}$ (MPa)	$\sigma_{BOP(+)}$ (MPa)	*Ultimate Strain (mm/mm)	*Max. Strain (mm/mm)	*Static Modulus (GPa)	*Peak Toughness (kJ/m ²)	*Total Toughness (kJ/m ²)
1s	10.59	4.43	6.04	0.026	0.029	0.77	7.47	9.08
2s	9.04	4.66	5.62	0.020	0.037	0.72	3.66	11.76
3s	13.69	5.79	6.17	0.033	0.045	0.81	12.51	19.57
4s	10.56	4.19	5.78	0.027	0.040	0.69	9.43	16.40
Average (Standard dev.)	11.00 (1.9)	4.96 (0.7)	5.94 (0.4)	0.03 (0.01)	0.04 (0.01)	0.75 (0.06)	8.27 (3.7)	14.20 (4.7)

Strain rate ($\dot{\epsilon}$) = $5.5 \times 10^{-6} \text{ s}^{-1}$ (* measured from cross-head LVDT data).

3.2 High Speed Tension Test

A typical high speed stress-strain response of the sisal fiber reinforced composite is presented in Figure 6. The tests were performed at a strain rate of 24.6 s^{-1} . Using the same methodology as per the static stress-strain behavior, the dynamic tensile curve can also be divided in five zones. Zone I is the elastic region and its average dynamic modulus calculated from the Actuator LVDT was 1 GPa. Zone II is characterized by the formation of the first crack. The BOP⁻ ranged from 5.05 to 10.22 MPa while the BOP⁺ varied from 5.14 to 10.58 MPa. A higher scatter for BOP values was obtained when comparing to static results. As in the static tests, zones III and IV are marked by the formation of three cracks with a strain hardening behavior. A distinction between zones III and IV can not be draw from the stress-strain curve. Nevertheless, the widening of the cracks, which happens in zone IV, was observed in the images taken during the high

speed tests. Strong strain rate dependence was noticed for strain capacity. An average ultimate strain value of 10 % was reported. A different behavior regarding to strain capacity was found in the work of Yang and Li [21]. They observed that for ECC the tensile strain capacity decreases from 3% to 0.5% when the loading rate increases from quasi-static (10^{-5} s^{-1}) to seismic strain rate (10^{-1} s^{-1}). In contrast Maleej et al. [10] reported that the tensile strain capacity in their tests was insensitive to strain rate.

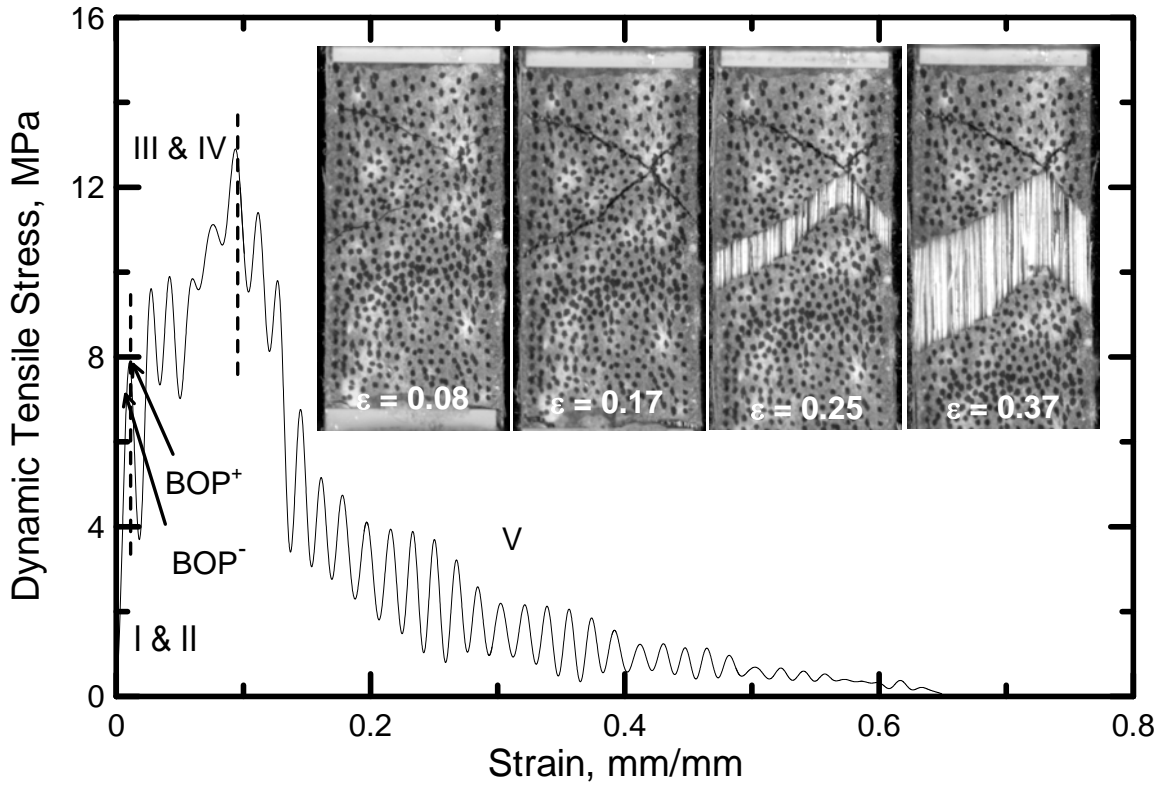


Figure 6. Dynamic stress-strain behavior of the sisal fiber cement composite. Images obtained from high speed Phantom camera shows the formation of shear cracks and the pull-out failure; therefore, resulting in high energy absorption.

In general it was observed an increase in UTS, BOP and toughness when compared to static tests. Individual results, average and standard deviation are presented in Table 2.

A Dynamic Increase Factor (DIF), which is the ratio between dynamic response and static response (in UTS), is computed to illustrate the strain rate effect. It was reported a DIF of 1.26. Images at several strain levels during the high speed tension tests are presented in Figure 6. Tensile and shear cracks were observed resulting in an average of 3 cracks. From the images it can be seen that the composite failure is a result of crack widening leading to fiber pull-out. Even at high strain levels (e.g. $\epsilon = 0.25 \text{ mm/mm}$) it can be observed a residual strength of 2 MPa due to high interfacial fiber-matrix bond

strength. This behavior results in enormous energy absorption capacity. Peak and total toughness values of 45.5 and 102.64 kJ/m² were reported, respectively.

Table 2. Summary of dynamic tensile test results.

Sample id	UTS (MPa)	$\sigma_{BOP(-)}$ (MPa)	$\sigma_{BOP(+)}$ (MPa)	*Ultimate Strain (mm/mm)	*Max. Strain (mm/mm)	*Dynamic Modulus (GPa)	*Peak Toughness (kJ/m ²)	*Total Toughness (kJ/m ²)
1d	11.66	5.05	5.14	0.09	0.56	0.94	38.27	74.55
2d	12.60	9.30	9.47	0.05	-	1.00	-	-
3d	12.90	7.54	7.73	0.09	0.65	0.90	44.59	103.86
4d	14.35	7.61	7.71	0.12	0.73	1.09	58.02	93.68
5d	14.60	7.64	7.75	0.21	0.78	0.73	56.37	132.42
6d	14.10	10.22	10.58	0.05	0.61	1.61	30.23	108.68
Average (Standard dev.)	13.37 (1.2)	7.89 (1.77)	8.06 (1.85)	0.10 (0.06)	0.67 (0.09)	1.04 (0.3)	45.50 (11.8)	102.64 (21.2)

Strain rate ($\dot{\epsilon}$) = 24.6 s⁻¹ (* measured from actuator LVDT data).

A comparison of static and dynamic tension behavior is presented in Figure 7. The BOP levels for the dynamic tests were twice as those reported for static tests. Note in Figure 7 the increased capacity of energy absorption for the high speed tension test. The increase in energy absorption is due mainly to the strain softening region which is prolonged in the dynamic test.

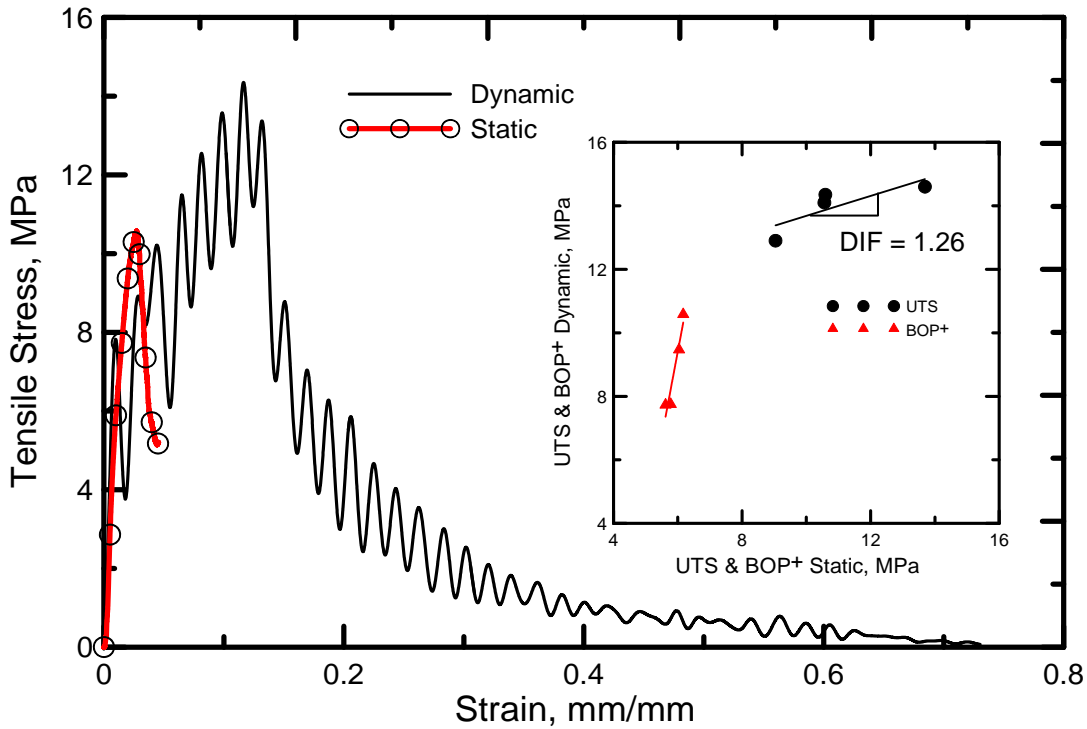


Figure 7. Comparison of dynamic and static tests. The inset plot shows an increase in UTS and BOP level for dynamic tests.

The displacement field generated by the digital image correlation method is presented in Figures 8 and 9 for two different types of crack formation: shear and tension, respectively.

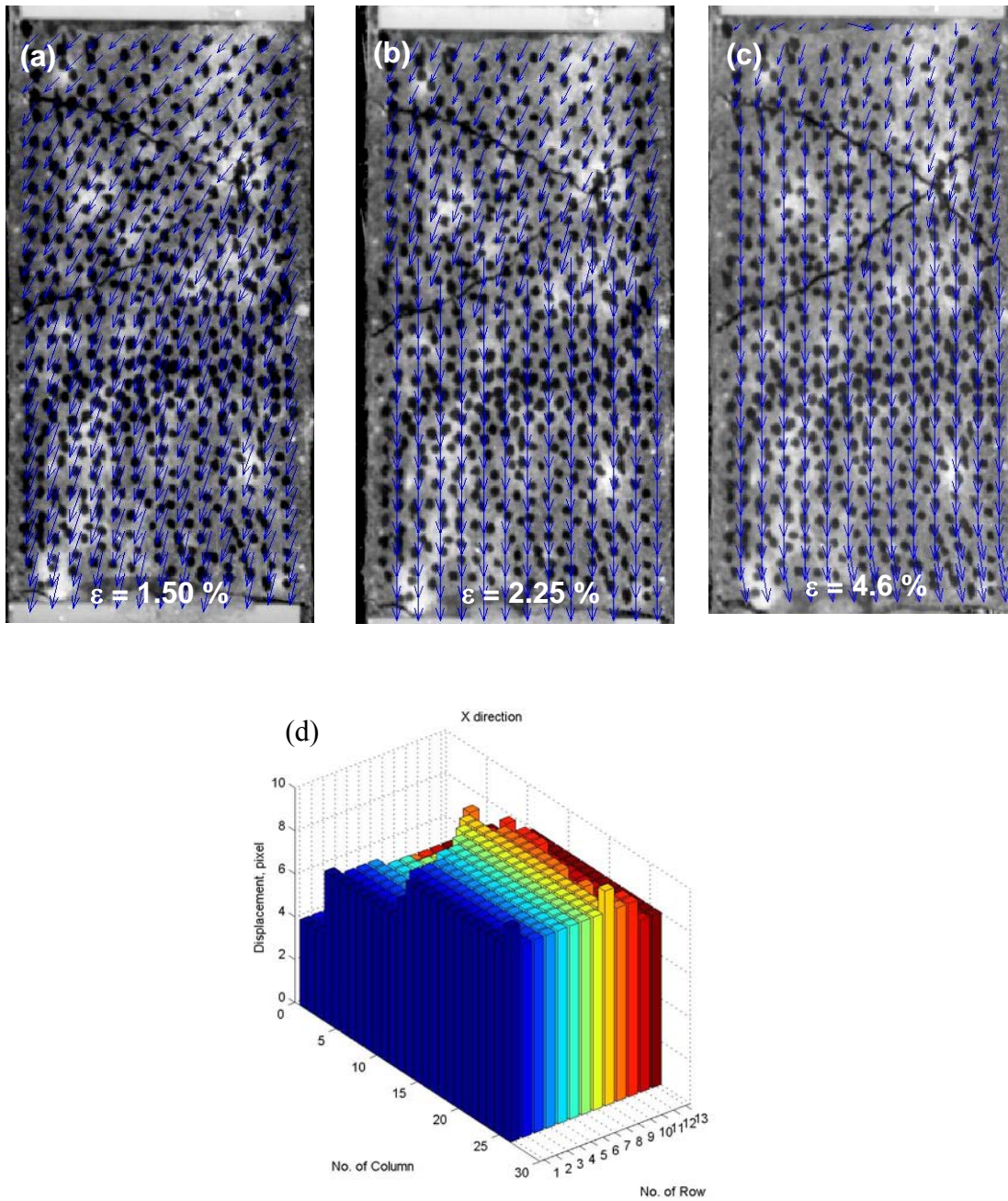


Figure 8. Displacement fields generated by the DIC method for a sample with shear cracks (a-c). The displacement level in pixels is shown by the bar graph (d) for a strain of 1.5%. This displacement values corresponds to different locations in the composite. Each row and column corresponds to a width of 10 pixels.

The arrows represent the displacement direction from the current deformation level in relation to the samples non deformed regime. In Figure 8a it can be seen that as the

shear crack opens at the top region of the sample, a rotation is imposed. This rotation, showed by the 45° arrows in the top region, leads to a lower level of deformation which is reported in the bar graph (see Figure 8d). Below the shear cracks a more uniform displacement field is reported (see Figure 8a) with the arrows closer to 0° . This behavior resulted in a larger deformation level for that specific region (bottom part of the specimen) as can be seen in the bar graph. As the strain level increases (Figure 8b and c) the rotation decreases resulting in pure uniaxial tension after a strain level of 4.6 %.

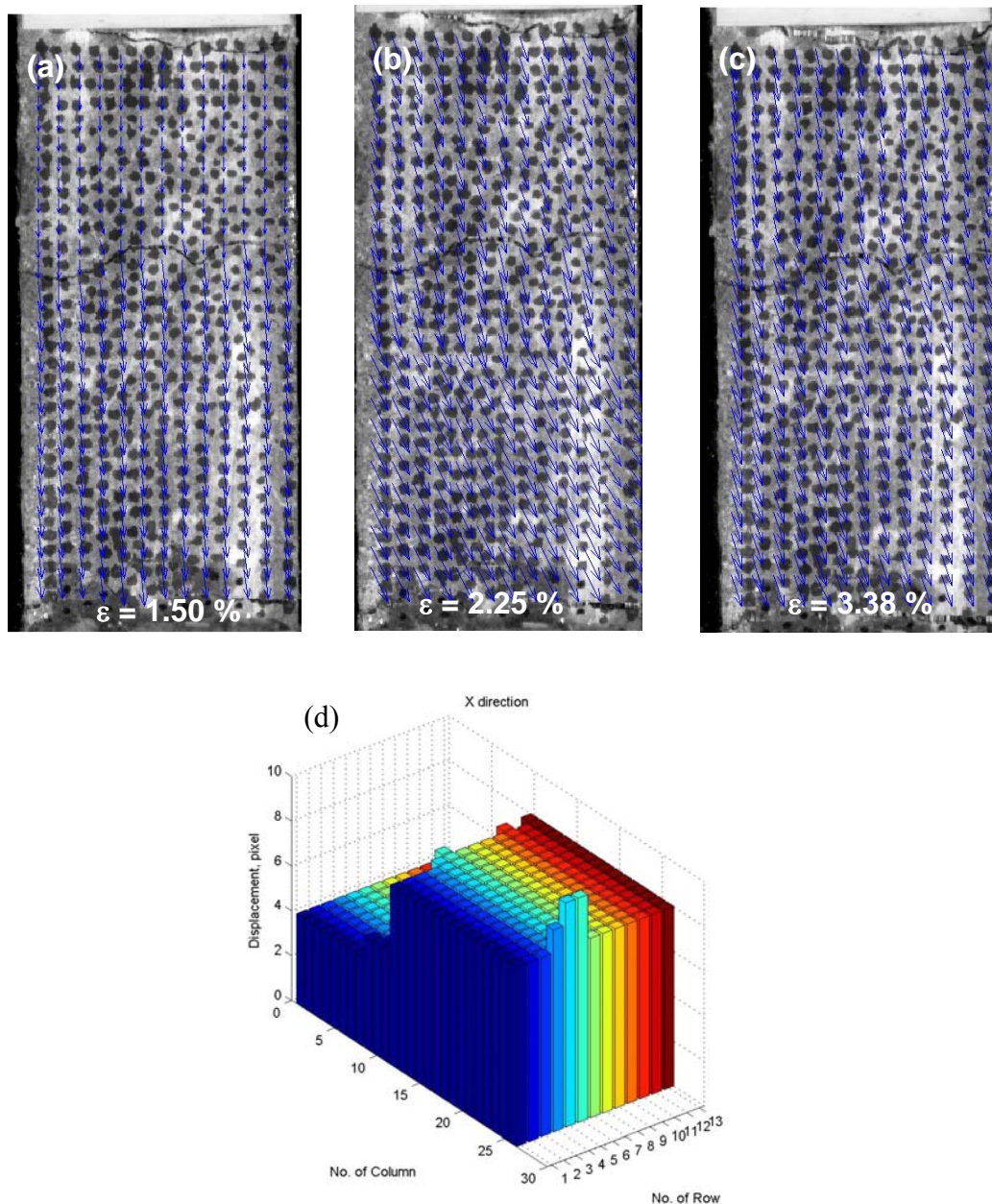


Figure 9. Displacement fields generated by the DIC method for a sample with tensile cracks (a-c). The displacement level in pixels is shown by the bar graph (d) for a strain of 1.5%. This displacement values corresponds to different locations in the composite. Each row and column corresponds to a width of 10 pixels.

For the samples in which only tensile cracks were observed, as shown in Figure 9, rotation was observed after larger strain levels (i.e. $\epsilon = 2.25\%$). Nevertheless, the rotation tends to decrease for larger strain levels. Different displacement levels for the same specimen was also observed after the first crack formation. Figure 9d shows a distinct displacement level for the region below and above the crack.

A comparison of the stress-strain behavior calculated from image analysis and from the actuator LVDT data is presented in Figure 10. Note that for strain above 10% the image analysis method fails to compute the deformation. It was reported smaller values of ultimate and maximum strains, therefore resulting in reduced toughness values when comparing to those values computed from LVDT actuator data. The dynamic modulus of elasticity obtained from image analysis was 3.44 GPa, approximately 3 times larger than the one obtained from LVDT actuator data. If comparing to the true static modulus computed from strain gage measurements a decrease of 10 times is observed for the dynamic modulus.

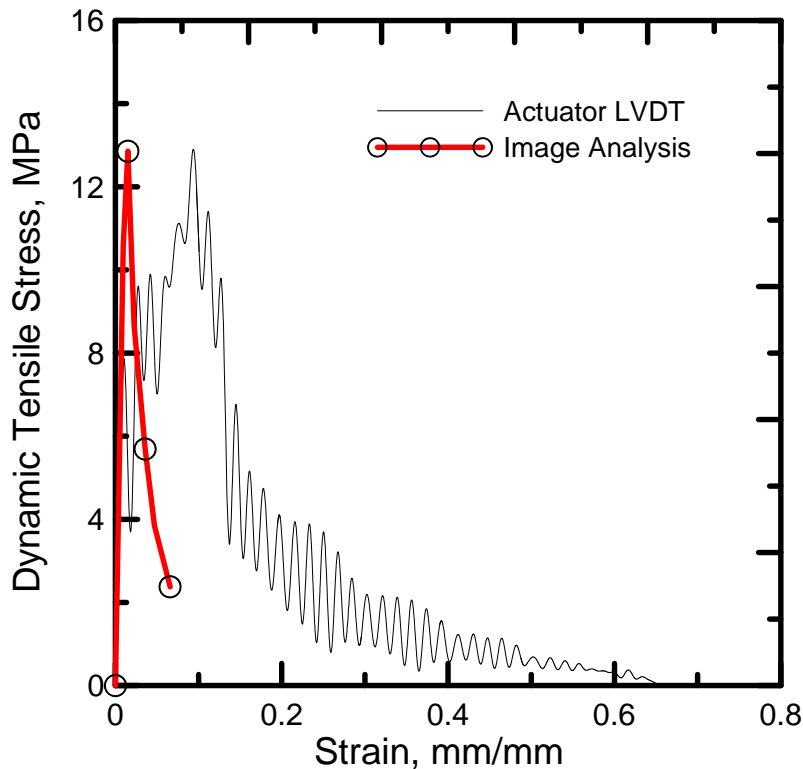


Figure 10. Comparison of a typical stress-strain curve obtained from the Actuator LVDT data and image analysis.

Table 3. Summary of dynamic tensile test results obtained from image analysis technique.

Sample id	UTS (MPa)	$\sigma_{BOP(-)}$ (MPa)	$\sigma_{BOP(+)}$ (MPa)	*Ultimate Strain (mm/mm)	*Max. Strain (mm/mm)	*Dynamic Modulus (GPa)	*Peak Toughness (kJ/m ²)	*Total Toughness (kJ/m ²)
3d	12.90	7.54	7.73	0.015	0.065	1.12	6.15	21.92
4d	14.35	7.61	7.71	0.0263	0.0394	4.30	13.06	21.17
5d	14.60	7.64	7.75	0.0187	0.048	4.90	10.48	25.62
Average (Standard dev.)	13.95 (0.9)	7.59 (0.05)	7.73 (0.02)	0.02 (0.005)	0.05 (0.01)	3.44 (2.03)	9.90 (3.5)	22.90 (2.4)

4. Conclusions

The following conclusions can be drawn from the present work on the tensile behavior of sisal fiber reinforced cement composites under low and high strain rates:

- There is a significant increase in UTS for the dynamic tensile test. A tensile strength DIF of 1.26 was computed. The dynamic stress-strain behavior was similar to the static with a multiple cracking formation followed by a strain hardening behavior. Both tensile and shear cracks were observed.
- The first crack strength was found to be sensitive to strain rate. It was observed an increase of BOP⁺ from 5.94 to 8.06 MPa when comparing static to dynamic tests, respectively.
- A strain rate sensitivity was noticed for the strain capacity. Ultimate strain increased from 3 % in static to 10 % in dynamic tensile tests. The main failure mechanism was fiber pull-out.
- The digital image correlation method has proven to be a powerful tool to determine the displacement field in cement composites. It was observed that during the crack formation part of the composite may rotate resulting in different strain levels at different regions of the material.
- The dynamic modulus calculated from image analysis was found to be approximately 3 times higher than that obtained from actuator LVDT measurements. The dynamic modulus was found to be approximately 10 times lower than the static.

References

- [1] Silva F.A., Mobahser B., Toledo Filho R.D. Cracking mechanisms in durable sisal fiber reinforced cement composites. *Cement and Concrete Composites*, in Press, 2009.
- [2] Xiao S., Li H. and Lin G. Dynamic behaviour and constitutive model of concrete at different strain rates. *Magazine of Concrete Research* 2008;60:271–278.
- [3] Birkimer D.L. and Lindemann R. Dynamic tensile strength of concrete materials. *ACI Journal* 1971;68:47–49.
- [4] Oh B.H. Behavior of concrete under dynamic tensile loads. *ACI Materials Journal*, 1987;84:8–13.
- [5] Rossi P., Van Mier J.G.M., Toutlemonde F., Le Maou F., Boulay C. Effect of loading rate on the strength of concrete subjected to uniaxial tension. *Materials and Structures* 1994;27:260–264.
- [6] Rossi P. and Toutlemonde F. Effect of loading rate on the tensile behaviour of concrete: description of the physical mechanisms. *Materials and Structures*, 1996;29:116–118.
- [7] Cadoni E., Labibes K. and Albertini C. Strain-rate effect on the tensile behaviour of concrete at different relative humidity levels. *Materials and Structures* 2001;34: 21–26.
- [8] Malvar L.J. and Ross C.A. Review of strain rate effects for concrete in tension. *ACI Materials Journal* 1998;95:735–739.
- [9] Kim D.J., El-Tawil S., Naaman A.E. Rate-dependent tensile behavior of high performance fiber reinforced cementitious composites. *Materials and Structures* 2009;42:399–414.
- [10] Maalej M., Quek S.T., Zhang J. Behavior of hybrid fiber engineered cementitious composites subjected to dynamic tensile loading and projectile impact. *J Mater Civil Eng* 2005;17:143–152
- [11] Mobasher B. and Rajan S.D. *Image Processing Applications for the Study of Displacements and Cracking in Composite Materials*. American Society of Civil Engineers, 2004.

- [12] Toledo Filho R.D., Silva F.A., Fairbairn E.M.R., Melo Filho J.A. Durability of compression molded sisal fiber reinforced mortar laminates. *Construction and Building Materials* 2008, in Press. doi:10.1016/j.conbuildmat.2008.10.012.
- [13] Brazilian Standard NBR 11578, Cimento Portland Composto. Associação Brasileira de Normas Técnicas (ABNT), 1991 (In Portuguese).
- [14] Silva F.A., Chawla N., and Toledo Filho R.D. Tensile behavior of high performance natural (sisal) fibers. *Composites Science and Technology* 2008;68:3438-3443.
- [15] Xiao X.R. Dynamic Tensile Testing of Plastic Materials. *Polymer Testing* 2008;27: 164-178.
- [16] Hill S. and Sjöblom P. Practical Considerations in Determining High Strain Rate Material Properties, SAE, 981136, 1998.
- [17] Fitoussi J., Meraghni F., Jendli Z., Hug G., and Baptiste D. Experimental Methodology for High Strain Rates Tensile Behavior Analysis of Polymer Matrix Composites. *Composite Science Technology* 2005;65:2174–2188.
- [18] Hill S.I. Standardization of High Strain Rate Test Techniques for Automotive Plastics Project, UDRI: Structural Test Group, UDR-TR-2004-00016, 2004.
- [19] Duda R.O. and Hart P. E. *Pattern Classification and Scene Analysis*, New York: Wiley, 1973.
- [20] Gonzalez R.C., Woods R. E. *Digital Image Processing* (third edition), Reading, Massachusetts: Addison-Wesley, 1992.
- [21] Yang E., Li V.C. Rate dependence in engineered cementitious composites. In: *Proceedings, HPRCC-2005 international workshop*. Honolulu, Hawaii, USA, 2005.

Livros Grátis

(<http://www.livrosgratis.com.br>)

Milhares de Livros para Download:

[Baixar livros de Administração](#)

[Baixar livros de Agronomia](#)

[Baixar livros de Arquitetura](#)

[Baixar livros de Artes](#)

[Baixar livros de Astronomia](#)

[Baixar livros de Biologia Geral](#)

[Baixar livros de Ciência da Computação](#)

[Baixar livros de Ciência da Informação](#)

[Baixar livros de Ciência Política](#)

[Baixar livros de Ciências da Saúde](#)

[Baixar livros de Comunicação](#)

[Baixar livros do Conselho Nacional de Educação - CNE](#)

[Baixar livros de Defesa civil](#)

[Baixar livros de Direito](#)

[Baixar livros de Direitos humanos](#)

[Baixar livros de Economia](#)

[Baixar livros de Economia Doméstica](#)

[Baixar livros de Educação](#)

[Baixar livros de Educação - Trânsito](#)

[Baixar livros de Educação Física](#)

[Baixar livros de Engenharia Aeroespacial](#)

[Baixar livros de Farmácia](#)

[Baixar livros de Filosofia](#)

[Baixar livros de Física](#)

[Baixar livros de Geociências](#)

[Baixar livros de Geografia](#)

[Baixar livros de História](#)

[Baixar livros de Línguas](#)

[Baixar livros de Literatura](#)
[Baixar livros de Literatura de Cordel](#)
[Baixar livros de Literatura Infantil](#)
[Baixar livros de Matemática](#)
[Baixar livros de Medicina](#)
[Baixar livros de Medicina Veterinária](#)
[Baixar livros de Meio Ambiente](#)
[Baixar livros de Meteorologia](#)
[Baixar Monografias e TCC](#)
[Baixar livros Multidisciplinar](#)
[Baixar livros de Música](#)
[Baixar livros de Psicologia](#)
[Baixar livros de Química](#)
[Baixar livros de Saúde Coletiva](#)
[Baixar livros de Serviço Social](#)
[Baixar livros de Sociologia](#)
[Baixar livros de Teologia](#)
[Baixar livros de Trabalho](#)
[Baixar livros de Turismo](#)